UNIVERSITÀ
DI PAVIA
Università degli Studi di Pavia

Dipartimento di Fisica

Dottorato di Ricerca in Fisica - XXXVI Ciclo

Understanding functional properties of spinel oxide nanoparticles and thin films by static and dynamic experimental approaches

Simone Restelli

Submitted to the Graduate School of Physics in partial fulfillment of the requirements for the degree of *Dottore di Ricerca in Fisica* at the University of Pavia

Supervisor: Prof. Pietro Galinetto
Co-supervisor: Prof. Giulia Fulvia Mancini

Understanding functional properties of spinel oxide nanoparticles and thin films by static and dynamic experimental approaches

Simone Restelli

Ph.D Thesis - University of Pavia
Pavia, Italy, September 2023

Certainty Of Death? Small Chance Of Success? What Are We Waitin' For?

Gimli, son of Glóin *The Lord of the Rings*

Contents

Chapter 1

Introduction

1.1 Functional oxides: General aspects and applications

In material science, the historical classification broadly categorizes materials into two main groups based on their intended use: *structural* materials and *functional* materials. The first category encompasses substances primarily used or studied for their mechanical properties. This involves understanding how a material responds to applied forces, whether it exhibits elasticity or plasticity, and assessing its hardness and strength [1]. The second category comprises materials which can perform a function or produce a signal as a response to external stimuli [2]. Functional materials can be designed, synthesized and engineered to expose tailored properties at variance, for example, with doping, crystalline structure or external parameters such as temperature, electric and magnetic fields *etc.*

Among the broad class of functional materials, the focus will be narrowed down to Functional Oxides and, in particular, Transition Metal Oxides (TMOs). As the name states, these latter are composed mainly of oxygen anions and transition metal cations with an overall complex chemical structure. This is due to electronic bonds that form compounds dominated by the hybridization of the $2p$ electrons in oxygen and d-f electrons in the transition metals which, in turn, favour, for example, non-trivial spatial arrangements of cations and anions generating novel lattice structures. In this arrangement, the spin degree of freedom plays also an extremely significant role. Indeed, most TMOs exhibit cross-interactions between spin, lattice and electrons which are able to form materials with a huge plethora of of characteristic behaviours [3]. These can range from the most common ones *i.e.*, Metallic, Insulating conductivity or Antiferro-, Ferro-, Para- and dia- magnetism; to skirmions [4, 5], complex spin ordering [6, 7], charge and spin density waves [8,

9, 10].

One example of the complexity of TMOs is found in magnetite (Fe_3O_4). This compound has a metallic cubic inverse spinel structure at Room Temperature (RT) and its magnetic behaviour has been known since ancient Greece. Indeed, it is ferrimagnetic with Curie temperature $T_C \approx 853\,\mathrm{K}$ ($580\,^\circ\mathrm{C}$). In the last century, Verwey found a structural and electronic transition at $T_V \approx 120\,\mathrm{K}$ through which magnetite becomes a monoclinic insulator [11]. Below T_V, a new long-range orbital order is established with the insurgence of three-site small polaron states, the so-called trimeron [12, 13]. Trimerons result from multiple cooperative effects, such as charge, orbital orderings, and strong electron-phonon coupling [14]. Furthermore, soft modes linked to the trimeron network can be triggered and detected by ultrafast experiments with photons in the THz region [15].

The main reasons that bring such systems to be extensively studied are: (i) it is not always possible to disentangle the strong correlation between the various degrees of freedom, (ii) there are only a few general considerations that can be valid for all the TMOs, and (iii) the huge amount of different exotic effects arising from these systems can be exploited in most of the applications both industrial (*e.g.* microelectronics) [16, 17, 18] and still under research (*e.g.*, spintronics [19, 20] or all-optical switching [21]).

1.1.1 Importance of functional oxides: some examples

Functional oxides hold paramount importance from both practical and fundamental perspectives. In terms of practical applications related to this thesis work, the most significant ones encompass areas such as photocatalysis and magnetic-related applications, including magnetic hyperthermia. Photocatalysis or photo-assisted catalysis is a property of a substance (the photocatalyst) to start or increase the rate of a chemical or photo-chemical reaction upon absorption of photons in the Ultraviolet (UV), Visible (Vis) or Infrared (IR) energy ranges. This happens because the excited state of the photocatalyst repeatedly interacts with the reaction partners forming intermediates or products and then regenerates itself after each cycle of such interactions [22]. An example of this behaviour was seen in $ZnFe_2O_4$ composites which are able to split water into hydrogen and oxygen molecules, following the two-step reaction [23, 24, 25, 26]:

$$6\,\mathrm{ZnFe_2O_4(s)} + E_{\text{photo-thermal}} = 6\,\mathrm{ZnO\,(g)} + 4\,\mathrm{Fe_3O_4(g)} + \mathrm{O_2(g)} \tag{1.1}$$

$$\mathrm{H_2O\,(l)} + 3\,\mathrm{ZnO\,(g)} + 2\,\mathrm{Fe_3O_4(s)} = 3\,\mathrm{ZnFe_2O_4(g)} + \mathrm{H_2(g)} \tag{1.2}$$

involving an intermediate transformation of $ZnFe_2O_4$ into magnetite.

Magnetic hyperthermia exploits the magnetic interactions of TMOs for medical purposes, such as cancer treatment, as follows. It is known that the micro-

scopic exchange interactions give rise to long-range magnetic orders with Ferromagnetic, Antiferromagnetic or more complex character [3]. When TMOs are nanostructured, only short-range magnetic interactions are possible, therefore, the system must behave as a standard paramagnet. However, if one applies a magnetic field the short-range interactions allow for magnetic moment polarization of each nanostructure along the magnetic field axis. This effect is called superparamagnetism [27] and will be more extensively treated in the next sections. If properly designed, core-shell superparamagnetic nanoparticles capped with sugar molecules can bind to cancer cells. The nanoparticles enter the membrane and are heated up to 40-60°C through an applied alternate magnetic field causing the death of the tumor cells [28, 29]. Limitations are however to be expected in these applications calling for further studies. Indeed, in photocatalysis, the photoinduced degradation and the stability of the samples need to be addressed to have the most efficient recombination steps possible [30, 31, 32, 33]. Magnetic hyperthermia limitations are mainly linked to the aggregation of nanostructure and/or low biocompatibility of the compounds. One example of a strategy to overcome these issues is to dope superparamagnetic nanoparticles with other transition metal ions to ensure more biocompatibility and possibly decrease the surface energy [34, 35].

From a fundamental perspective, most of the work was devoted to understanding, disentangling and possibly controlling the electronic, structural and spin responses. In particular, coherently excited electronic modes and their coupling with other degrees of freedom (*e.g.*, polarons) can be exploited to prepare, engineer, and manipulate the quantum states in a material and even steer chemical reactions into a pre-defined target channel [36, 37, 38]. The electronic modes may give information on eventual charge ordering or phase transitions in the samples [15, 39, 40, 41]. In addition, the exploitation of coherent electronic modes and polarons is crucial also for applicative purposes. In fact, collective excitations in Charge Density Wave (CDW) materials can be exploited for data storage, processing and search [42]; electronic modes can increase the parametric gain in photonic crystal cavities for all-optical switching applications [43]; and modifications of the polaron order by coherent tailored light pulses can generate hidden phases with high durability (more than one week) [44]. In this framework, TMOs represent the perfect playground due to their complex electronic, lattice and spin arrangements. For example, an all-optical switch is a device able to control an optical signal by means of another optical trigger. In general, all-optical switches are nonlinear media with $\chi^{(3)}$ (third−order) processes and have to satisfy the following requirements: (i) ultrafast switching time, (ii) low control power (intensity less than $1\,\mathrm{kW/cm^2}$), (iii) high switching efficiency (ideally 100 %), and (iv) nano-, micrometric dimensions [45]. A limitation in this field may be given by the contradiction between the low control power and ultrafast response time [46, 47]. An example of a valuable

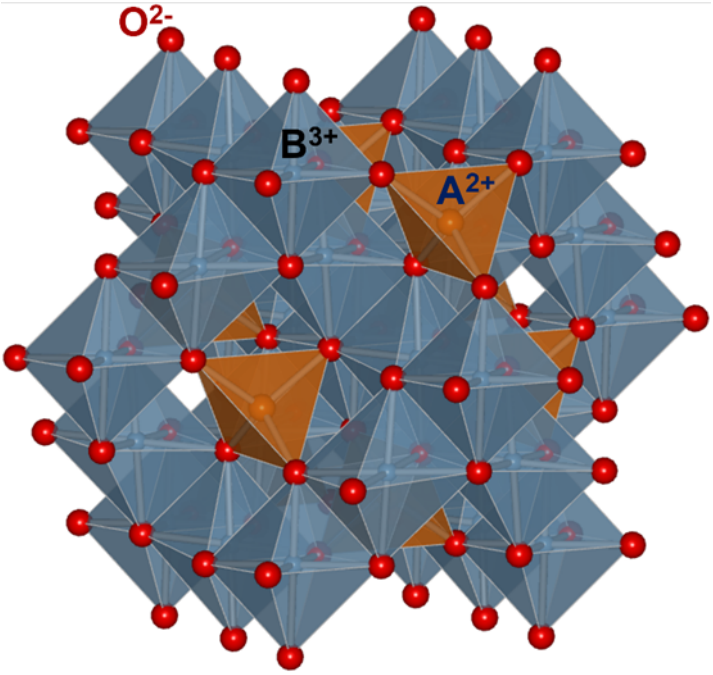

Figure 1.1: Sketch of the spinel structure with chemical formula AB_2O_4. This is characterized by tetrahedrons (A) and octahedrons (B) with O^{2-} ions vertices and divalent and trivalent metal cations occupying A-site and B-site interstices, respectively.

TMO platform for all-optical switching is Aluminum-doped Zinc oxide in its epsilon near-zero region [21]. Indeed, it has a picosecond response when controlled by an interband pump, and a femtosecond response when controlled by an intraband pump [48, 49]. In addition, Al-doped ZnO works in the telecommunication wavelength range (1300-1500 nm) giving rise to huge applications in future integrated photonic devices. However, the low control power requirement is not strictly satisfied. In fact, pump incident fluences of about $5\,\mathrm{mJ/cm^2}$ and $14\,\mathrm{mJ/cm^2}$ were employed in the ultraviolet and NIR ranges, respectively [49]. Therefore, research on possible ultrafast switches with low activation power and high nonlinearity is still ongoing.

1.2 Spinel oxides

1.2.1 Structure of spinel oxides

In this thesis work, the focus is on spinel oxides. Spinel oxides are a subset of TMOs belonging to the $O_h^7 - Fd\bar{3}m$ space group and with stoichiometric chemi-

cal formula AB_2O_4 [50]. Their structure is characterized by tetrahedrons (A) and octahedrons (B) with O^{2-} ions vertices and divalent and trivalent metal cations occupying A-site and B-site interstices, respectively (Fig. 1.1). The chemical formula can be detailed as $(A)^{tet}[B]_2^{oct}O_4$. Examples of these systems are: $ZnFe_2O_4$, Co_3O_4, and Fe_3O_4, with detailed chemical formula $(Zn)^{2+}[Fe]_2^{3+}O_4$, $(Co)^{2+}[Co]_2^{3+}O_4$, and $(Fe)^{3+}[Fe]^{3+}[Fe]^{2+}O_4$. The complex cationic distribution hereby presented (Fig. 1.1) allows for the strong interplay between electronic, structural and spin degrees of freedom. Consequently, a huge variety of optical and magnetic properties are detected. For example, the electronic transitions following the absorption of a photon with a given energy can be ascribed to excitations between two d levels of the same transition metal ion but also to charge transfer processes between different metallic cations or between O^{2-} and the metallic cations. These transitions can be found in the UV visible or NIR ranges giving semiconducting or insulating character to the considered systems allowing for the aforementioned applications in photocatalysis and photovoltaics. In addition, the spin configuration allows for long-range magnetic orders and/or other complex phenomena as will be discussed in the following.

1.2.2 Magnetic properties

An example of the importance of the complex cation distribution in spinel oxides is given by their magnetic properties due to the microscopic spin interactions. Among these, the main magnetic interaction is superexchange which is sketched in Figure 1.2 for the simple case of MnO rock salt $Fm\bar{3}m$ bulk system. A rock salt MnO system is chosen to simplify the description of the interaction. However, a similar mechanism is valid for spinel $Fd\bar{3}m$ systems. The superexchange interaction is well known in oxides literature and was the object of theoretical treatment firstly by Kramers [51] and later by Anderson [52, 53]. The first examples of experimental results hinting at this interaction come from neutron diffraction on MnO and other similar compounds [54, 55, 56]. The mechanism through which magnetic order is reached is given by an exchange spin-coupling mediated by a non-magnetic ion (O^{2-} in the case of most oxides). This can be seen in Figure 1.2 where the magnetic ions are represented by Mn^{2+} and their antiferromagnetic interaction is mediated by O^{2-}. For simplicity, only two electrons in the same $p-$state of O^{2-}, magnetic ions (Mn^{2+}) possessing only one electron in the $d-$state bonded with O^{2-}, and no orbital momentum (or quenched orbital momenta) shall be considered. By hypothesis, no direct overlap between the two d wave functions is established but there is a finite probability of a O^{2-} electron to jump to *e.g.*, an $s-$orbital of one of the magnetic ions. The latter state must be coupled *via* exchange interaction with the $d-$electron already considered on the magnetic ion. Let the first $d-$orbital of Mn^{2+} be in a spin down $|\downarrow>$ state. A first exchange spin-coupling

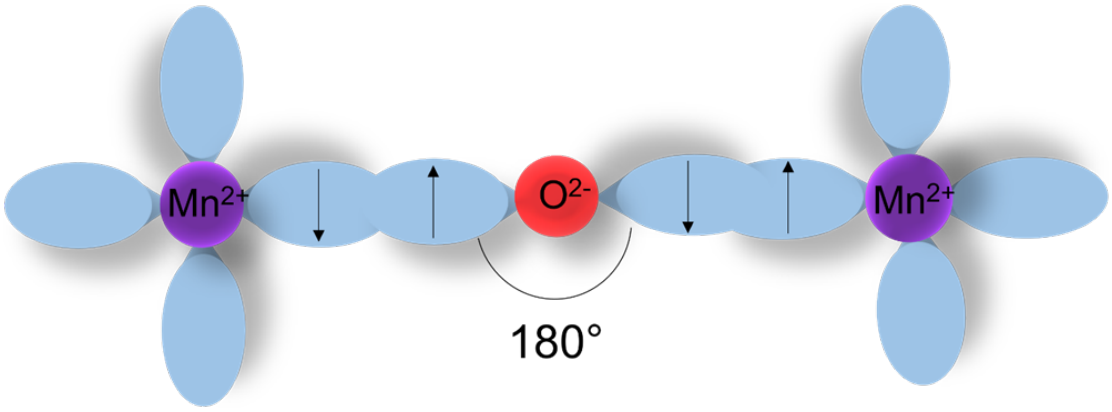

Figure 1.2: Sketch of the superexchange interaction in bulk MnO with the orbital configurations of manganese ions (Deep Blue) and the oxygen ligands (Red).

Spin direction of added electron	Coupling p-electron $\rightarrow$ d-electron	Resulting coupling
Parallel	FM	AFM
Parallel	AFM	FM
Antiparallel	FM	FM
Antiparallel	AFM	AFM

Table 1.1: Rules for the determination of the sign of superexchange interaction

is established between the $d-$orbital and O^{2-} $p-$orbital with the latter acquiring a spin up $|\uparrow>$ state. Due to orbital occupancy rules given by fermionic statistics on electrons, a second electron in the $p-$orbital of O^{2-} must be in the $|\downarrow>$ state. Because of the exchange interaction between the second electron in the $p-$orbital of O^{2-} and the $d-$electron on the second Mn^{2+}, the latter acquires a spin up $|\uparrow>$ state. Due to this mechanism, antiferromagnetic (AFM) coupling is achieved in most of the cases, but also Ferromagnetic (FM) order was reported [57]. Indeed, by looking at the superexchange interaction constant J sign, it is possible to construct a table to predict the outcoming magnetic order as shown in Tab. 1.1, generalizing to the case of ions with spins greater than $\frac{1}{2}$. In this case, one starts guessing the spin direction of an extra electron added to the first magnetic ion (first column). Then, based on the exchange coupling between the p-electron and the other ion the general coupling can be retrieved. Assuming that other magnetic interactions are not disturbing this picture, the outcoming magnetic order can be predicted.

The superexchange interaction can be treated starting from an effective Heisenberg Hamiltonian [3]:

$$\mathcal{H}_{eff} = J \sum_{<i,j>} S_i \cdot S_j \tag{1.3}$$

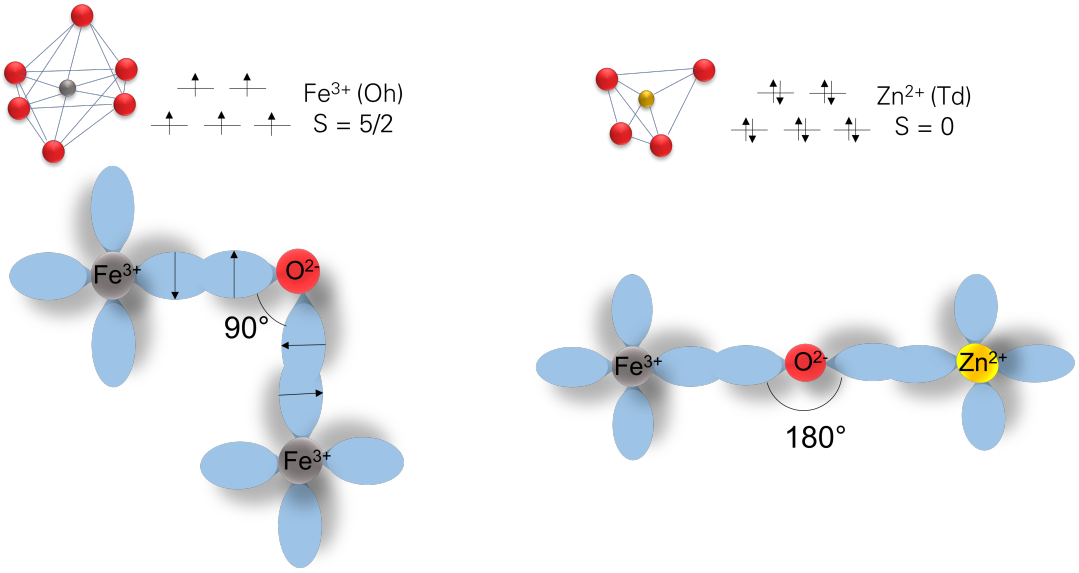

Figure 1.3: Sketch of the superexchange interaction in an example of spinel oxide, bulk $ZnFe_2O_4$. (left) orbital configuration between two octahedral cages containing iron and the oxygen ligand. The Fe^{3+}-ion spin configuration is indicated above. (right) orbital configuration between an octahedral cage containing Fe^{3+} ion and a tetrahedral site containing Zn^{2+} mediated by O^{2-} ligand. No superexchange interaction is possible because Zn^{2+} is a nonmagnetic ion as evidenced by its spin configuration indicated above.

with i and j corresponding to the magnetic ion sites and

$$J = \frac{2t^2}{U} \tag{1.4}$$

where t is the hopping term of an electron from a magnetic ion to an Oxygen (t^2 because two hoppings are described), while U is the Hubbard term accounting for the Coulomb repulsion between electrons [3]. From the spin-spin product of eq. 1.3 one can look at the interaction dependence from the angle between the interacting $p-$orbitals [58] with the simple proportionality:

$$S_i \cdot S_j \propto \cos(\theta_{int}) \tag{1.5}$$

This latter formula indicates that when the interaction angle is $\theta_{int} = 180\,^\circ$, there will be a maximization of the superexchange while if $\theta_{int} = 90\,^\circ$, a minimum in the interaction energy shall be detected. This angular dependence is reflected in the magnetic ordering temperature (T_C or T_N) and is reported, for example for $ACuO_3$ (with A = Se, Te) [59] and $ACr_0 \cdot 99\,Fe_0 \cdot 1\,O_3$ (A = La, Nd, Sm, Gd, Dy, Y **etc**) [58]. Since the case of MnO brings to have $\theta_{int} \simeq 180\,^\circ$ the superexchange interaction will be maximized and the magnetic AFM ordering will present a high

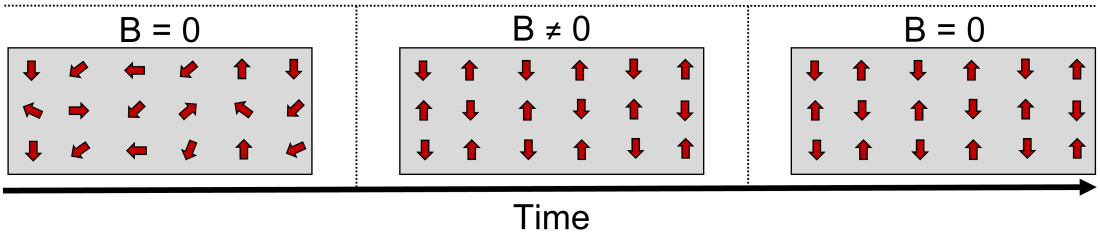

Figure 1.4: Sketch of the Antiferromagnetic order. An external magnetic field B is applied in the central panel while it is set to zero in the first and third panels.

transition temperature ($T_N \simeq 122\,\mathrm{K}$). However, it is important to look at systems with the opposite behaviour ($\theta_{int} \simeq 90\,^\circ$) and perhaps also with multi-valence metallic ions. An example is shown in Fig. 1.3 in the case of $ZnFe_2O_4$ bulk system. This structure is composed by two metallic ions *i.e.*, magnetic Fe^{3+} ($S = \frac{5}{2}$) and nonmagnetic Zn^{2+} ($S = 0$) bonded together by O^{2-} anions with $\theta_{int} \simeq 90\,^\circ$ and $\theta_{int} \simeq 180\,^\circ$, respectively. Such geometric arrangement leads to a weak AFM order in the system due to small $Fe^{3+} - O^{2-} - Fe^{3+}$ interaction. The ordering cannot be reached between Fe^{3+} and Zn^{2+}, the latter being nonmagnetic. In this case of unfavoured superexchange the transition temperature of the system should be low ($10\,\mathrm{K}$) [60]. Another example of superexchange interaction is given by Co_3O_4. Neutron diffraction [61] and susceptibility [62] studies indicated that the magnetic contributions arise from the Co^{2+} ion on the A site, while Co^{3+} on the B site has almost zero magnetic moment due to huge crystal field splitting. The superexchange interaction in this case is non tri*vial* since it may involve $Co^{2+} - O^{2-} - Co^{2+}$ interaction with an angle of $\theta_{int} \simeq 77\,^\circ$ but also $Co^{2+} - O^{2-} - Co^{3+} - O^{2-} - Co^{2+}$ next-to-nearest-neighbours superexchange. The $Co^{2+} - O^{2-} - Co^{3+} - O^{2-} - Co^{2+}$ interaction is hypothesized by *Roth* [61] based on the experimental discrepancies with the two sublattice model proposed by *Van Vleck* [63]. Indeed, neutron diffraction studies found that the ratio between the susceptibility at $T = 0\,\mathrm{K}$ and at $T = T_N$ is $\frac{\chi(T=0K)}{\chi(T=T_N)} \simeq \frac{2.025}{3}$ against the predicted $\frac{2}{3}$ and the ratio between the Curie-Weiss temperature θ_{CW} and T_N is $\frac{\theta_{CW}}{T_N} \simeq 1.3$ to be compared with the predicted value of 1. Considering the two above-mentioned interactions leads to a long-range magnetic order at a temperature $T_N \simeq 40\,\mathrm{K}$ and to the possibility of a spin-liquid phase below $100\,\mathrm{K}$ as suggested in a more recent work [64].

In Fig. 1.4 the mechanism of the AFM order in bulk materials is schematically highlighted. The system is originally composed of magnetic moments with a completely random direction. When an external magnetic field B is applied, these magnetic moments become aligned in the direction of B with alternating positive-negative signs. When the magnetic field is again set to zero, the system retains its alignment.

The unfavoured superexchange coupling in spinels can be increased by ideally exchanging some of the nonmagnetic and magnetic ions in their respective sites. Interestingly, the latter engineering is possible by introducing nanostructured systems as will be shown in the next section.

1.2.3 Nanostructures

In general, nanostructuring a material changes its optical, structural-vibrational and magnetic properties. A first example of size-dependent optical property is the bandgap which, in the case of Silicon nanoparticles, is blueshifting as the dimension of the particle is reduced [65]. Another example is found in nanosized metals where the optical properties show a variation of the plasmonic resonances at variance with dimension *e.g.*, in the case of Gold [66]. From the vibrational point of view, a decrease of the grain size to the nanometric scale causes a relaxation of the phonon momentum conservation rule ($\mathbf{q} \simeq 0$). A wider phonon reservoir can participate to the Raman events, leading to a broadening and shifting of the Raman peaks observed in bulk crystals. The extent of these effects depends on the nanometric dimensions, and they are sizeable below 20 nm. In this range the experimental features are often correctly interpreted by the so called Phonon confinment model (PCM) [67]. Considering structural and chemical properties, spinel oxides show size-dependent cation inversion *i.e.*, when the A- and B-cations are exchanged in the unit cell [32, 68]. If this happens, the overall nanostructured system will be a mixture of A- and B-cations in the tetrahedral and octahedral sites. This cation inversion strongly affects the overall magnetic response of materials. In particular, the magnetically ordered bulk materials become superparamagnetic when nanosized [27]. Consider nanoparticles as randomly oriented magnetic domains in space, in the absence of an external magnetic field (Fig. 1.5 left pane). When an external magnetic field is applied, the magnetic moment of each nanoparticle is oriented in the direction of the field (Fig. 1.5 central panel). However, when the external field is turned off again, the nanoparticles become again randomly oriented (Fig. 1.5 right panel). Therefore, the magnetic nanoparticles show an increased response typical of a ferromagnet in the presence of an applied external field but without the residual magnetization after the field is turned off. Such phenomenon is extremely important in various fields like medicine in which hyperthermia is studied as a potential cancer treatment with high success rate and low healthy tissue damage [69, 70, 71]. Another crucial point of superparamagnetism, for example in $ZnFe_2O_4$ is that it is seen even in RT conditions even if bulk material magnetic order is reached below 10 K. The origin of the RT superparamagnetism could again be given by the cation inversion. Consider a general AB_2O_4 spinel with A nonmagnetic and B magnetic ions, the B-O-B bond with an angle of $\theta_{int} \simeq 90\,^\circ$ and the A-O-B bond with $\theta_{int} \simeq 180\,^\circ$. In this situation, the superexchange

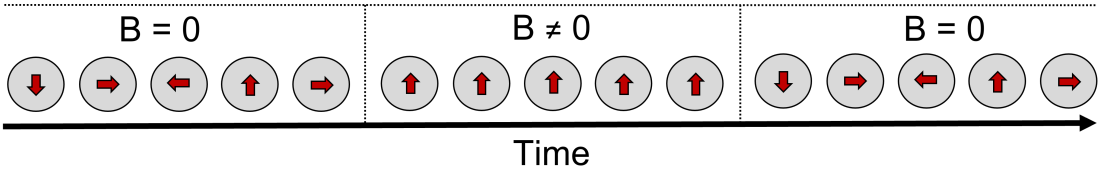

Figure 1.5: Sketch of the Superparamagnetic functional properties. An external magnetic field B is applied in the central panel while it is set to zero in the first and third panels.

interaction is only favoured at low temperatures but, by nanostructuring the system, the exchange of the sites of a partial amount of A and B ions is allowed. Therefore, there will be some situations in which the B-O-B bond has $\theta_{int} \simeq 180\,^{\circ}$ strengthening the magnetic interaction and justifying the superparamagnetism at RT.

1.3 Interplay between fundamental and applied physics in spinel oxides: aim of this work

Several crucial aspects of spinel oxides were grasped. These features closely depend on the ions involved and in particular, on their structural and electronic arrangement within the tetrahedral and octahedral sub-lattices. This arrangement plays an important role in charge trapping, transport and magnetic behaviour and is strongly dependent on external stimuli such as temperature, light, electric and magnetic fields, and so on. Furthermore, when managing nanostructured materials it is important to understand how the synthesis and growth procedures affect the chemical and structural properties to produce systems stable in time and when exposed to different ambient conditions and treatments. Such dependence on external stimuli and synthesis process is found, for example, in $ZnFe_2O_4$ nanoparticles and thin films. In nanoparticles, a high external temperature (around 1100 °C) in high vacuum atmosphere transforms $ZnFe_2O_4$ into magnetite thanks to Zn-sublimation [23, 24, 25]. In thin films, the presence of oxygen vacancies during the synthesis allows for magnetic behaviour tuning [72, 73, 74].

The problematics arising in the example case of the magnetic hyperthermia applications shall be described in a more quantitative manner. Some literature discrepancies and application drawbacks arise when understanding the superparamagnetic properties of, for example, $ZnFe_2O_4$ and Fe_3O_4 nanoparticles crucial for hyperthermia. Fe_3O_4 is the most studied and employed system for hyperthermia applications. However, it is not ideal in terms of biocompatibility and perma-

nent ferrimagnetic phases upon aggregation. Therefore, it is generally used to substitute it with zinc or other ferrite systems which are more biocompatible and paramagnetic in their bulk phase [34, 35, 75]. As reported in literature, the particle size required to achieve superparamagnetism in Fe_3O_4 nanoparticles is coarsely estimated to be below 20 nm [76, 77, 78], whereas the critical size for forming a multi-domain structure was theoretically estimated to be 76 nm for cubic [79] and 128 nm for spherical Fe_3O_4 NPs [80, 81]. However, other literature studies see a closed hysteresis loop typical of superparamagnetic particles even for particles with dimension 135 nm [82]. In addition, if one considers uncapped nanoparticles, their huge surface energy should be taken into account. This is caused by the pending ligands on the nanoparticle shell and increases as the dimension is reduced. A huge surface energy leads to nanoparticle aggregation in the end suppressing their superparamagnetic behaviour. Therefore, nanoparticles with higher dimensions (lower surface energy and lower aggregation) and high superparamagnetic effect are ideally wanted. A possible workaround is to cap the nanoparticles with a SiO_2 shell and/or organic ligands to ensure biocompatibility and to favour their injection in the body. Identical considerations are valid for $ZnFe_2O_4$ both on the dimensionality and on the aggregation problem [34, 35].

A complete and deep knowledge of the problematics and aspects presented above can be reached through a correlative approach combining different techniques (synthesis, characterization, theoretical calculations). This is because a magnetic, structural, and chemical characterization at variance with dimensionality and/or doping in spinel TMOs nanoparticles and thin films is required. In addition, the characterization of the complex interplay between the strongly correlated structural, charge and spin Degrees Of Freedom (DOF) is needed. Indeed, the comprehension of the intimate physical processes in spinel oxides allows one to achieve control and possibly be able to tune their functional properties.

My PhD work is devoted to deepening the knowledge of functional spinel TMOs by studying the aforementioned topics in two systems: (i) Zinc ferrite, starting from the nanoparticles characterization and thin film synthesis with a step-by-step approach and (ii) Cobalt Oxide (Co_3O_4), studying the strong correlation between the various DOF by looking at their transient dynamics. $ZnFe_2O_4$ is relevant for its magnetic and photocatalytic properties. The objective of the study was the synthesis and characterization of the multifunctional behaviour of thin films starting from nanoparticle precursors. Co_3O_4 shows applicative relevance for photovoltaics and photocatalysis. The objective of the study was the understanding of the Co^{2+} and Co^{3+} involvement in the electronic, structural, and magnetic dynamics upon photoexcitation. The steady-state techniques and data analysis protocols from the $ZnFe_2O_4$ project were harnessed to understand Co_3O_4 ground-state properties. Conversely, the unique knowledge gathered with the time-resolved methods

on Co_3O_4 shall be applied to $ZnFe_2O_4$ thin films after the synthesis and characterization protocol is validated. In both cases, I utilized thin film samples because of their importance in applications. In the case of $ZnFe_2O_4$, I also concentrated on the full characterization of nanoparticles since these constitute the starting point for the synthesis of the thin films. The correlative approach was possible by exploiting several synthesis, experimental, and theoretical techniques which are: Radiofrequency magnetron sputtering, Coprecipitation, Raman Spectroscopy from the Infrared to the Ultraviolet, Time-Resolved Reflectivity, Electron Paramagnetic Resonance, SQUID magnetometry, X-Ray Diffraction (both in laboratory and large scale facilities such as Free Electron Lasers), Profilometry, Ellipsometry, Fourier Transform IR spectroscopy, UV-Vis spectroscopy, and Density Functional Theory calculations. This huge combination of techniques was possible thanks to the expertise of the University of Pavia (UNIPV) and Italian and international collaborations with: École Polytechnique Fédérale de Lausanne (EPFL), Inelastic UV Scattering (IUVS) beamline at Elettra Sincrotrone Trieste, University of Austin Texas, European XFEL, and the Institute of Nuclear Physics of the Polish Academy of Sciences.

Chapter 2

$ZnFe_2O_4$ thin films from nanopowders precursors. Synthesis and characterization

2.1 General introduction on $ZnFe_2O_4$ nanostructures

$ZnFe_2O_4$ (ZFO) possesses a direct spinel structure with cubic symmetry in the O_h^7-Fd3m space group. It is composed of tetrahedral (A) and octahedral (B) coordination sites in a O^{2-} close-packed face-centred cubic units network. Low spin (S = 0) Zn^{2+} and high spin (S = 5/2) Fe^{3+} cations are located at the A and B interstices, respectively [83]. At the nanoregime a partial cation inversion occurs in the two sublattices and in turn nanostructured ZFO shows a mixed spinel structured in which Zn^{2+} and Fe^{3+} ions are distributed over the two sites: $(Zn_{1-x}Fe_x)^{2+}[Zn_{1-x}Fe_{2x}]^{3+}O_4$ where x is the inversion degree, *i.e.* the amount of Fe^{3+} ions in the tetrahedral site, while () and [] represent the A and B sites, respectively. The cationic redistribution over the two sublattices alters the strength of the interactions between ions adding novel functional properties crucial for the applicative fields as for instance, drug delivery, sensing [84], information storage [85], ferrofluids [86], magnetic resonance imaging (MRI) contrast agents and for radiofrequency magnetic hyperthermia (MH) [87]. More recently this compound seems to be also exploited as a possible theranostic system and as a substrate for water remediation [88] as well as in catalysis [89] and photocatalysis [90, 91]. Examples of the properties crucial for the possible applications [34] are room temperature superparamagnetism (instead of paramagnetism for the bulk system) [27] and strong photocatalytic activity [23, 92, 24].

In general, the functional properties of these systems are closely dependent on the composition, size and architecture of the nanoparticles or thin films as well

as on the synthesis methods. Indeed, by acting on the ionic environment with doping and/or by varying the synthesis methods, one can change the magnetic, optical and transport properties of the compounds. For example, it is possible to change the magnetic domains of both nanoparticles and thin films. In the case of nanoparticles, the magnetic domains are strictly related to the dimension and homogeneity since a lower size gives higher inversion. In the case of thin films instead, magnetic domains are generated by inter-atomic forces during the growth process which cause internal stresses and/or preferential alignment of the nanocrystalline grains and, again, may influence the local inversion [93, 94, 95]. Nevertheless, the cationic inversion *per sè* is not the only parameter to be considered because magnetic domains, optical and transport properties can be influenced by oxidation states, oxygen vacancies, compositional (dis-)homogeneity and so on. Therefore, different approaches would give different and seemingly contrasting results but also give an extremely high degree of engineering of the ZFO nanostructures depending on the specific applications. The strategy of doping or changing the growth process, oriented to obtain *e.g.*, a tuning of the magnetic behavior, requires a detailed and exhaustive understanding of the structural and chemical properties and their interplay in determining functional properties. Moreover, ZFO applications rely on the physico-chemical response when exposed to different atmospheres and/or in specific ambient conditions. As a matter of example, ZFO gas sensing properties rely on the change of resistivity upon adsorption of a specific gas (*e.g.* Acetone and H_2S) [96]. Another example is found in water splitting where the production of H_2 and O_2 is a consequence of photogenerated carriers' interaction with water [25]. Therefore, a fundamental requirement for nanostructured ZFO is the chemical, structural and morphological stability or better, the possibility to control these properties during the working operations. This, in turn, requires *ex-situ* and *in-situ* monitoring of basic properties of ZFO because of the close correlation between functional behavior with structural and defect-related properties. Indeed, some environmental-, treatment- or defect-related triggers might induce unwanted properties which, in turn, can be caused by a change in composition [97, 30] or structure and, in the end, may hinder their performance [73]. For example, a general issue for ZFO nanoparticles is to reveal the presence of pure iron oxides that may lead to extrinsic magnetic behaviour, causing problems in terms of stability and, possibly, biocompatibility if used for example in biomedical applications.

2.1.1 Open questions

In this framework of a functional oxide with a wide range of applications, several open questions need to be addressed. The general aim is to have a final control on the engineering of ZFO nanostructures starting from fast, cheap, highly repeatable and low failure synthesis methods and going towards a fine control over their

physico-chemical responses. To do this several open questions on both fundamental mechanisms and applications points of view must be solved. Some of these can be: (i) Is the estimation of the inversion degree by means of Raman spectral features effectively reliable? (ii) How does the inversion degree affect the magnetic response in ZFO? (iii) How does the composition change at the nanostructure surface? (iv) How do the operational atmosphere and irradiation affect the stability of ZFO nanostructures? (v) It is possible to produce thin films *via* sputtering starting from nanopowders of ZnO [98] and, for example, cesium tin bromides [99]. However, to date, no attempt to produce ZFO films from nanopowders has been made. Therefore, is it possible to produce a ZFO thin film using sputtering with a nanoparticle target? (vi) How does the treatment of the sputtered film affect its physical properties? (vii) What are the electronic relaxation pathways in a multi-cation, mixed-valence spinel such as ZFO? (viii) How do the lattice and spin degrees of freedom rearrange if an electronic transition is excited in ZFO?

Several literature studies tried to address the plethora of open questions on both nanoparticle and thin film samples. The first example regards the inversion degree and its influence on the optical and magnetic properties in ZFO. *Granone et al.* [100] studied the variation of the Raman and optical features with inversion degrees from 0.07 to 0.20. As the inversion degree is increased, they showed a seemingly strange behaviour of the Raman spectral response in the 600-700 cm^{-1} region. In this Raman shift range a double peak structure is observed, compatible with the totally symmetric A_{1g} vibration of the tetrahedral cages containing Zn (around 650 cm^{-1}) and Fe (around 690 cm^{-1}) ions. One should expect that increasing the inversion degree favours the increase of $Fe-$ions in the tetrahedral sites enhancing the signal as it is found for nanoparticles [101, 102, 103]. In this case, the opposite was observed with an enhanced Zn contribution as the inversion is increased. This is only one of the various contrasts regarding the inversion degree estimation from Raman spectral features which can be traced back to experimental approach drawbacks such as wrong peak assignment, presence of spurious compounds (like magnetite) induced in the samples by the laser irradiation, and unwanted doping during the growth process.

Another example regards the chemical and structural stability of ZFO nanoparticles. This has been studied in peculiar ambient conditions connected to specific applications. In particular, *Kaneko et al.* [23] while investigating $Zn-$ferrite systems as efficient solar energy material estimated that solar decomposition of the $Zn-$ferrite is triggered above 1500 K and takes less than 60 s for the $Zn-$ferrite powders to reach the O_2 generation reaction temperature of 1750 K at the insolation level of 840–980 W/m^2 in an Ar flux. More recently, *Kuciakowski et al.* [30] investigated the thermal decomposition of ZFO annealing nonstoichiometric nanoparticles in an inert atmosphere and 5 mbar vacuum up to a temperature

of 1443 K. They showed that the annealing leads to partial reduction of Fe ions, to magnetism enhancement, and to the increase of particle sizes independently on the atmosphere. Vacuum annealing, with high probability, produces a ZnO, Fe_3O_4, and Fe_2O_3 multiphase system with signs of amorphization, mainly on the surface. Instead, for what concerns the response of zinc ferrite nanoparticles to visible laser irradiation in air, it is known that, depending on the stoichiometry deficiency of the surfaces, a transition to hematite can be often observed [101]. This latter strongly depends on different factors such as the size of the nanoparticles, thermal dissipation (which is environment-dependent) and irradiation power. However, in general, ZFO nanoparticles are claimed to be stable in a wide range of experimental conditions.

From the ZFO thin film point of view, several studies were devoted to the magnetic and optical characterization of as synthesized and annealed thin films [93, 104, 105, 106, 107]. In particular, it is known that ZFO thin films exhibit superparamagnetic behavior. In particular, the study presented in *Yadav et al.* [104] at variance with thermal annealing time in air and hydrothermal conditions showed that the hydrothermal annealing favors the superparamagnetic behavior in the system by playing on the oxygen vacancies. In both cases, the films become more crystalline as the annealing time is increased. However, a fixed temperature of 180 °C was employed during the thermal treatment. Another study by Sultan and Singh [106] showed that increasing the oxygen atmosphere in the sputtering chamber increases the saturation magnetization of the films in partial contrast with the increased magnetization due to oxygen vacancies. *Sahu et al.* [105] demonstrated that increasing annealing temperature (with fixed annealing time 2 h) decreases the saturation magnetization thus the superparamagnetic behavior. These seemingly contrasting aspects could be reconciled by accounting for the cation inversion and oxygen vacancies. Furthermore, it is possible that the films present both amorphous and crystalline environments, which may play different roles in determining the functional properties. A similar discussion can be made in EPR studies [93, 105] which showed uniaxial anisotropy of the films but did not investigate the effect of annealing. In addition, from the spectroscopic point of view, some studies were devoted to understanding the optical properties of ZFO films but only a few aimed to assign the reported features to precise electronic transitions in the system [107]. Moreover, *Fu et al.* [108] studied the time-resolved spectroscopic response in $ZnFe_2O_4$ nanocrystals. However, the interpretation given is based on a single colour pump-probe experiment without a clear indication of the fs-, ps-, ns-behavior of the transitions composing the probe energy region and on the possible coherent oscillatory response. Therefore, the complete picture of the fs-dynamics of ZFO after photoexcitation is still far from understood.

2.1.2 Goal of this thesis chapter

The goal of this chapter is the synthesis and complete characterization of ZFO thin films by RF sputtering starting from pure and doped nanopowders without any target pre-treatment (sintering, milling, *etc.*). All the work was possible thanks to a collaboration between the Physics and Physical Chemistry departments of the University of Pavia and of the Inelastic UV Scattering beamline at Elettra Synchrotron in Trieste. This collaboration involves: Dr. B. Albini, Dr. S. Bonomi, Dr. M.C. Mozzati, Prof. M. Bini, M. Patrini, Prof. L. Malavasi and Dr. F. D'amico.

To reach the aforementioned goal a complete and careful characterization of the pure and doped ZFO nanoparticles produced by the coprecipitation method is first needed. A comparison of the functional properties and stability with commercially available nanoparticles (Sigma Aldrich) is also required. The complete characterization was performed focusing on the structural properties by matching different methodologies, combining short- and long-range probes, optical, magnetic spectroscopies, *etc.* This approach is time-consuming and costly; thus, it is extremely important to define protocols able to quickly assess the quality of the sample. Among the different techniques, high relevance to Raman spectroscopy (RS) shall be given. RS is certainly widely used to characterize different microscopic features of the general class of iron oxide compounds. Indeed, by RS it is possible to distinguish between hematite, maghemite, magnetite and wurtzite [109]; it is possible to evaluate the stability of ZFO under different laser treatments or thermal annealing in different atmospheres. In addition, and more specifically for the spinel type structure, RS can be used to extract (semi)-quantitative information on the cationic distribution *i.e.*, the inversion degree of the spinel. Thus, considering the sensitivity of the technique, its versatility for different sample shapes and forms, and its ability to reveal unwanted spurious compounds, RS is a valid candidate for quick and robust validation of the zinc ferrite sample quality once verified that spectral parameters derived from Raman experiments are directly related to functional properties. The doping was performed on both the cationic sites by substituting Mg on the Zn site and/or Ga on the Fe site. At first, the structural homogeneity was tested within the samples. Their Raman response was evaluated by varying the incident laser wavelength using 266 nm, 533 nm, 633 nm and 785 nm sources. Semi-quantitative analyses on the ZFO Raman modes are also needed in order to get information about the cationic disorder of the spinel structure.

Moreover, the nanoparticles' structural and chemical stability under irradiation in different atmospheres was monitored in view of evaluating the thermal and laser-induced stability of thin films. The Raman responses of pure and doped ZFO nanoparticles were studied acquiring the scattering light before and after laser-induced heating, keeping the powders both at ambient atmosphere and in

vacuum at different pressures. Thermal and photoinduced effects were generated by the same 632.8 nm laser used for Raman measurements exciting the powders just below the optical bandgap ($E_g \approx 2\,\text{eV}$) [110, 111]. Furthermore, to demonstrate the effectiveness of the Raman technique in the study of zinc ferrite, the obtained results are discussed and validated taking into account the information obtained from complementary analysis, like X-ray powder diffraction (XRPD), Electron Paramagnetic Resonance (EPR) spectroscopy and SQUID measurements, which were performed to evaluate the magnetic response.

After the complete characterization of ZFO nanoparticles the ZFO thin films were synthesized starting from the nanopowder targets. In this step, the synthesis and complete characterization of ZFO thin films was performed starting from Sigma Aldrich nanopowders. The results obtained so far also serve to find the perfect synthesis receipt that will be applied to pure and doped coprecipitated nanoparticles. These latter have, as advantages, a very narrow dimension distribution and, of course, the possibility of easy cation substitution and realization of core-shell architectures which will constitute one of the perspectives of this work.

During this research path, it would be possible to get answers to some of the questions reported above. A possible interpretation is provided taking into account the differences arisen in literature and bridging their interpretations. However, the solution to some of the questions here presented still remains calling for a further improvement of the complexity of the techniques employed. Indeed, one important perspective of this work concerns the evaluation of the time-resolved response of zinc ferrite thin films. This is needed in order to fully understand the behaviour of the intertwined electronic, structural and magnetic degrees of freedom which should help the engineering of future multifunctional oxide-based devices. Furthermore, $ZnFe_2O_4$ is a multi-valence multi-centre compound, therefore, a complex plethora of lattice, magnetic and possibly electronic excitations would be expected. These excitations would give fundamental information on the energy transfer processes upon photoexcitation of the system. To understand this, it is firstly necessary to use the same approach in other benchmark systems without a multi-cation composition, Co_3O_4 that will be investigated in full in the next chapter.

2.2 Materials and methods

In the next pages, the synthesis and characterization methods used for ZFO-related activities are presented. Firstly, the two synthesis methods employed *i.e.*, coprecipitation route and Radiofrequency (RF) magnetron sputtering are described. These methods are used to grow ZFO nanoparticles and thin films, respectively. Then, the general principles of Raman spectroscopy, Electron Paramagnetic Resonance,

Superconducting Quantum Interference Devices (SQUID), and Optical absorption are described. Raman spectroscopy will have high relevance because it will be extensively employed in this and the next chapters. X-Ray Diffraction (XRD) data will also be shown. The XRD technique is not described in this section because it shall be mainly treated in its time-resolved implementation, thus, its basic principles shall be presented in Chapter 3.

2.2.1 Synthesis of the samples

2.2.1.1 The coprecipitation method

The coprecipitation process has been known since the beginning of the 20th century [112] and it has evolved to be one of the most affordable and reliable chemical synthesis methods for nanoparticles of metals and alloys (for catalysts), ceramic, metal-oxides and/or mixed nanoparticles. It is defined as the simultaneous precipitation of more than one compound from a solution and is generally divided into two steps: chemical synthesis in the liquid phase and post-synthesis thermal treatment [113, 114]. The first determines the chemical composition while the second determines the crystal structure and morphology. The synthesis of compounds by coprecipitation depends on several factors like the precursor material (metal oxides, metal halides, or organometallic), the solvents used (water, organic solvents, or polyols), and reaction energy (mechanical *e.g.*, stirring, thermal or radiation *e.g.*, microwave, ultrasonication, *etc*). Indeed, this method has been widely used for the production of transition metal oxide nanoparticles, *e.g.* magnetite [115], Ferrites (Zn, Mg, Co) [116, 75, 117], ZnO with Rare earth doping [118] and TiO_2 [119]. It can be used also for radionuclides separation in radiochemistry [120, 121], production of catalysts [122] and can be adapted as a tool for protein-encapsulation [123]. The chemical synthesis begins with the mixing of precursor materials with various levels of stirring in a solution (aqueous or nonaqueous) at room or low temperature for several hours. Here, the chemical composition is controlled by several reactions such as reduction, oxidation, hydrolysis, *etc*. The addition of a precipitant like ammonium hydroxide, sodium hydroxide, or sodium carbonate results in the precipitation of the nanomaterial with low solubility in the solvent through several mechanisms such as initial nucleation (formation of small crystallites), growth (aggregation), coarsening, and agglomeration. The particles are then left to rest (age) for hours-days to increase their dimensions, and then the precipitates are collected (as metal hydroxides or metal complexes) *via* filtration or centrifugation. Capping agents such as hydroxypropyl cellulose and polyethylene glycol or electrostatic stabilization might be used to control the crystal growth. The post-synthesis thermal treatment begins with the washing of the precipitate with water or solvents and its drying which may be performed at temperatures above 100 °C or by freeze-drying.

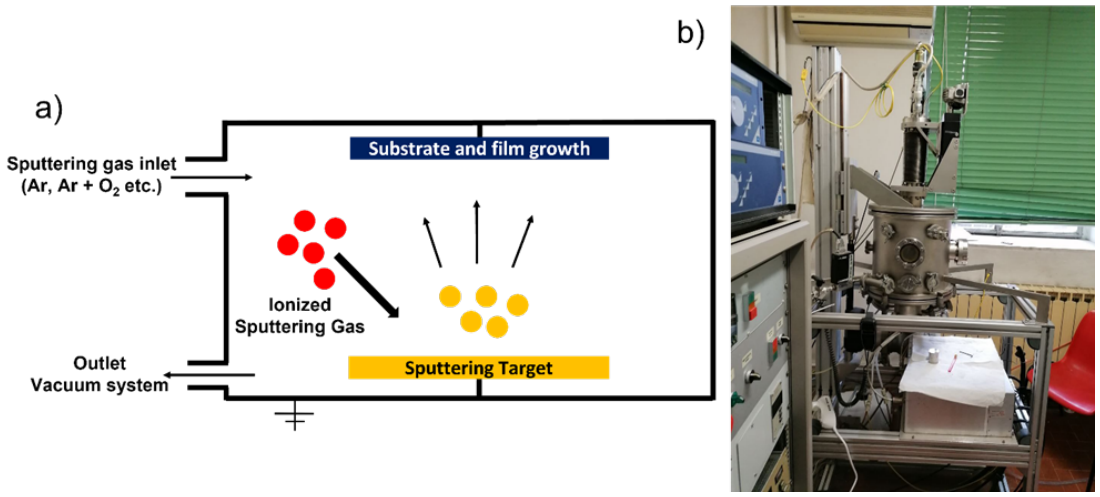

Figure 2.1: (a) Sketch of the sputtering chamber along with (b) the picture of the real chamber used for deposition.

The aforementioned process produces a precursor powder, which is often characterized by low crystallinity and compositional order. Therefore, thermal treatment (annealing, calcination, and sintering) at elevated temperatures must be carried out for several hours to achieve the final crystalline structure and morphology of the nanomaterial. The thermal treatment must be optimized on the sample in order to obtain nanoparticles of the desired dimension avoiding decomposition (too high temperatures) or micrometric dimensions (excessive thermal treatment duration).

2.2.1.2 The R.F. magnetron sputtering technique: basic principles and experimental realization

Radiofrequency (RF) magnetron sputtering was used for thin film deposition thanks to its huge advantages such as simple equipment, easy control of the chemical composition, large coating area, and strong adhesion [124]. This is a Physical Vapor Deposition (PVD) method largely used to prepare a variety of materials such as metals, semiconductors, insulators *etc*, even on an industrial scale. Firstly, a reaction chamber is filled with a controlled pressure of gas whose composition determines if the sputtering is reactive or non-reactive. The gas utilized in non-reactive sputtering is mostly Ar while, for reactive sputtering N_2, O_2, *etc.* are usually employed alone or in a mixture with Ar. A strong RF or Direct Current (DC) potential difference is then applied between the cathode covered with a target material and an anode usually a ferrule set at a defined distance. The electric field given by the potential difference ionizes the inert gas particles composing the

rarefied atmosphere of the chamber, causing their collision with the target and the following ejection of material (see Figures 2.1a,b). The ejected material is then deposited onto a substrate which can be manipulated during the whole process for example by heating or rotating it. The addition of a magnetron is crucial to allow for the deposition of relatively high purity, high speed, low temperature, and low-cost thin films [125, 126]. The magnetic field generated by such a component causes the electrons to spiral in the target surface proximity, thus increasing the collisions with the target. The main advantage of an RF source is that it does not require an electrically conductive target making it suitable for the deposition of any possible material [124]. Therefore, this technique has huge implications in fields like Renewable Energy (solar cells [127], batteries [128], fuel cells [129]), Optics (sensors [130], antireflective films [131], low-emissivity glass [132]), Microelectronics (coating films) [133], Machining industry (functional films, super hard coatings [134], self-lubricating films [135]), Decoration (total reflective or translucent films) [136] and Biomedical supports (cochlear implants, drug delivery [137]).

2.2.2 Raman spectroscopy: basic principles and setup

2.2.2.1 Classical mechanism of the Raman effect

By looking at the scattered radiation of a monochromatic light with frequency ω_1 impinging on a molecule, one can distinguish an elastically scattered component with the same ω_1 as the incoming wave but also other components with shifted frequencies $\omega_1 \pm \omega_s$. ω_s is associated with the transitions between rotational, vibrational and electronic levels. The generation mechanism of the elastically scattered component with ω_1 is called Rayleigh scattering whereas, the inelastically scattered component is generated *via* Raman scattering. In a classical electromagnetism view, the source of the Raman scattering is the presence of an induced oscillating dipole in the molecule, generated by the displacement in the distribution of the electron cloud with respect to the positive charges, in response to an applied external electric field. The associated dipole moment can be written as:

$$\mathbf{p} = \alpha \cdot \mathbf{E} + \frac{1}{2}\beta \cdot \mathbf{EE} + \frac{1}{6}\gamma \cdot \mathbf{EEE} \tag{2.1}$$

where α, β and γ are tensors indicating the polarizability, the hyperpolarizability and the second- hyperpolarizability, respectively. The first term, linear in E, accounts for the ordinary Raman scattering while the second and third terms are responsible for Hyper-Raman scattering effects. For the purpose of this thesis work, nonlinear Electric field terms of the polarization (second and third terms) are neglected. eq. 2.1 becomes:

$$\mathbf{p} = \alpha \cdot \mathbf{E} \tag{2.2}$$

By considering only vibrational transitions in the molecule and electrical harmonicity, the components of the polarizability tensor, $\alpha_{\rho\sigma}$ can be written as 1^{st}-order truncated Taylor expansion of the normal coordinates of vibration Q_k:

$$\alpha_{\rho\sigma} = (\alpha_{\rho\sigma})_0 + \sum_k \left(\frac{\partial \alpha_{\rho\sigma}}{\partial Q_k}\right)_0 Q_k \tag{2.3}$$

The electrical harmonicity assumption is included to avoid other terms in the expansion taking into account second-order Raman phenomena such as overtones (scattered frequency $\omega_1 \pm 2\omega_k$) or combinations (scattered frequency $\omega_1 \pm (2\omega_k + \omega_l)$. To restrict to the sole linear Raman the simple harmonic motion of the molecules must be assumed. This gives time-dependent Q_k of the form:

$$Q_k = Q_{k_0} \cos(\omega_k t + \delta_k) \tag{2.4}$$

By introducing eq. 2.3 and eq. 2.4 in eq. 2.2 and expressing the field frequency dependence as:

$$\mathbf{E} = E_0 \cos(\omega_1 t) \tag{2.5}$$

the linear induced electric dipole becomes:

$$\boldsymbol{p} = (\alpha_{\rho\sigma})_0 \boldsymbol{E}_0 \cos\omega_1 t + \left(\alpha'_{\rho\sigma}\right)_k \boldsymbol{E}_0 Q_{k_0} \cos(\omega_k t + \delta_k) \cos\omega_1 t \tag{2.6}$$

where now $\alpha_{\rho\sigma}$ represent the polarizability components at the equilibrium configuration while $\alpha'_{\rho\sigma}$

$$(\alpha'_{\rho\sigma})_k = \left(\frac{\partial \alpha_{\rho\sigma}}{\partial Q_k}\right)_0 \tag{2.7}$$

are the components of the k-derivative of the polarizability α'_k. With the help of some trigonometry eq. 2.6 can be written as:

$$\boldsymbol{p} = \boldsymbol{p}(\omega_1) + \boldsymbol{p}(\omega_1 - \omega_k) + \boldsymbol{p}(\omega_1 + \omega_k) \tag{2.8}$$

From eq. 2.8 one can retrieve three scattered light components: p(ω_1), p(ω_1 - ω_k) and p(ω_1 + ω_k) which represent the Rayleigh, Raman Stokes (S) and Raman Anti-Stokes (AS) radiations, respectively. Expressing the average dipole power and using eq. 2.6, the intensity of the Raman-shifted light turns out to be:

$$I = \frac{\omega_s^4 I_0 Q_k^2}{6\pi\epsilon_0^2 c^4} \left(\frac{\partial \alpha_{\rho\sigma}}{\partial Q_k}\right)_0^2 \tag{2.9}$$

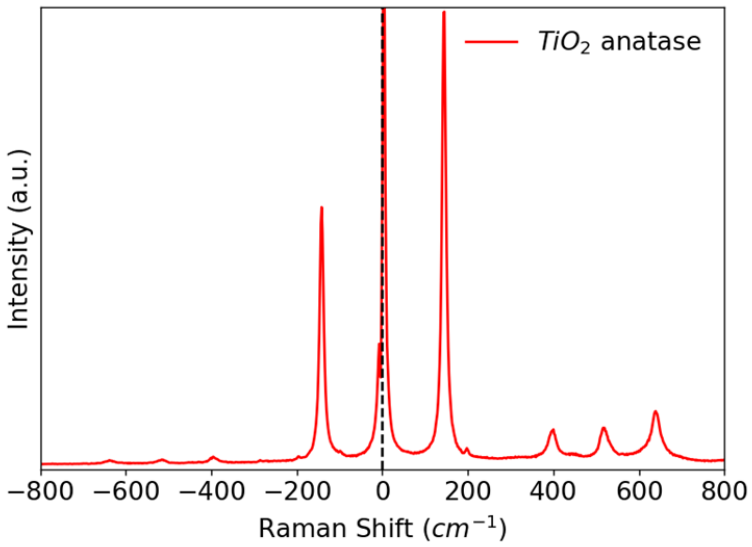

Figure 2.2: Raman Stokes and Anti-Stokes spectrum of TiO_2 with Anatase structure.

depending on the 4^{th}-power of the vibration frequency and on α'_k components. The latter dependence requires a non-zero polarizability change with respect to the normal coordinate of vibration. The Raman effect is well described by this change in polarizability both with the classical and quantum treatment. However, the classical electromagnetism description gives some results which are not physically observed in real cases. For example, the experimental evidence shows an S-AS intensity ratio different from the classical theoretical estimates. Indeed, as shown in Fig. 2.2 for the case of TiO_2 Raman spectrum, the AS lines are less intense than S ones by about one order of magnitude whereas the classical treatment would estimate the AS lines to be at higher intensity respect to the S ones.

2.2.2.2 Quantum mechanical treatment

The quantum mechanical treatment of the Raman effect is now introduced. Following the key steps of the reasoning reported in the book by Derek A. Long [138] the components ρ and σ of the transition electric dipole moment for S and AS scattering can be expressed through time-dependent perturbation theory. For example, the ρ component of p is expressed as:

$$(p_\rho)_{fi} = \frac{1}{2\hbar} \sum_{r \neq i,f} \left(\frac{\langle f | \hat{p}_\rho | r \rangle \langle r | \hat{p}_\sigma | i \rangle}{\omega_{ri} - \omega_1 - i\Gamma_r} + \frac{\langle f | \hat{p}_\sigma | r \rangle \langle r | \hat{p}_\rho | i \rangle}{\omega_{rf} + \omega_1 + i\Gamma_r} \right) \tilde{E}_{\sigma_0} e^{-i\omega_s t} + \text{c.c.} \tag{2.10}$$

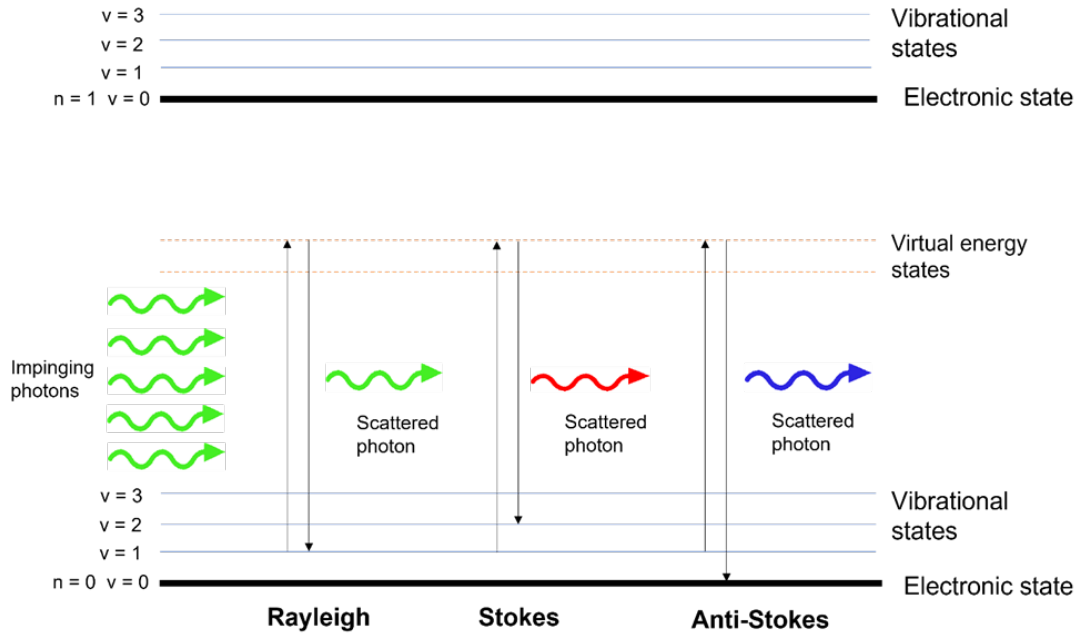

Figure 2.3: Simplified sketch of non-resonant Raman scattering mechanisms.

where f is the final state wavefunction while i and r are the wavefunctions of the unperturbed states, $\omega_S = \omega_1$-ω_{fi}, $E_{\sigma 0}$ is the complex amplitude of the σ component of the electric field, Γ_r is a damping term, and *c.c.* stands for complex conjugate. From $p_{\rho\sigma}$, the components of the polarizability tensor $\alpha_{\rho\sigma}$ are outlined:

$$(\alpha_{\rho\sigma})_{fi} = \frac{1}{\hbar} \sum_{r \neq i,f} \left(\frac{\langle f | \hat{p}_\rho | r \rangle \langle r | \hat{p}_\sigma | i \rangle}{\omega_{ri} - \omega_1 - i\Gamma_r} + \frac{\langle f | \hat{p}_\sigma | r \rangle \langle r | \hat{p}_\rho | i \rangle}{\omega_{rf} + \omega_1 + i\Gamma_r} \right) \tag{2.11}$$

This generalized formulation of the components of the polarizability tensor encloses all the possible Raman scattering processes.

A sketch of the Raman mechanism is presented in Fig. 2.3 in the case of non-resonant scattering ($\hbar\omega_1 << \hbar\omega(n=1) - \hbar\omega(n=0)$ *i.e.*, $\omega_1 << \omega_{ri}$ in the first term of eq. 2.11). In the following, the sole vibrational levels are considered but the treatment can be easily extended to rotations as well. Upon photon incidence, the system (molecule, crystal, *etc.*) undergoes a first transition from an initial stationary state $|n = 0,\ v = 1>$ to a virtual state (indicated by a dashed line) and a subsequent transition back from the virtual state to the final stationary one. This virtual state does not correspond to a well-defined value of energy. Therefore, the process is said to be a virtual absorption with a lifetime of the metastable state of the order of 10^{-15} s, 10^{-16} s (fs, as). For values of ω_1 approaching, matching or exceeding ω_{ri}, eq. 2.11 describes pre-resonance, resonance or continuum-resonance

Raman scattering. If the vibrational energetic level of the molecule is increased (final state $|n = 0,\ v = 2>$) in the process, the scattered photon will have $\hbar\omega_S < \hbar\omega_1$ defining the Stokes process (Fig. 2.3 middle). *Vice versa*, if the vibrational level is decreased (final state $|n = 0,\ v = 0>$) in the process, the scattered photon will have $\hbar\omega_S > \hbar\omega_1$ defining the Anti-Stokes process.

It is important to say that the second denominator in eq. 2.11 would give negligible contributions to the polarizability components, in particular when there are dominant components in the first term of $(\alpha_{\rho\sigma})_{fi}$. In addition, the first numerator of the equation is the product of two transition dipoles, one from a state $|i >$ to a state $|r >$ which is the photon absorption and the other from $|r >$ to $|f >$ which is the emission term, provided that $\omega_r > \omega_i$ and ω_f. The second term could be considered as a virtual process *i.e.*, the absorption of an incident photon following the emission of a scattered one. Taking eq. 2.11 as a starting point, the Born-Oppenheimer approximation (or adiabatic approximation) can be introduced. This considers the reaction of the electrons to be practically instantaneous with respect to the nuclei. Starting from a generic electronic-nuclear state $|j >= |e^j v^j R^j >$ with electronic, vibrational and rotational parts described by the e^j, v^j and R^j quantum numbers, respectively, this approximation allows to rewrite the state as:

$$|j\rangle = \left|e^j\right\rangle \left|v^j\right\rangle \left|R^j\right\rangle \tag{2.12}$$

with frequency (energy):

$$\omega_{e^j v^j R^j} = \omega_{e^j} + \omega_{v^j} + \omega_{R^j} \tag{2.13}$$

Again, the rotational part is neglected (rotations not resolved) considering only pure vibrational Raman scattering. Consider also the initial electronic state as a non-degenerate ground state, $e^i = e^g$ and ω_1 incident much greater than every vibrational absorption frequency (ω_{vib}) but much lower than electronic absorption ones (ω_e). In this case, the ρ and σ components of the polarizability tensor $\alpha_{\rho\sigma}(e^r, v^r)$ can be rewritten as:

$$(\alpha_{\rho\sigma})_{fi} = \left\langle v^f \left| \left\langle e^f \left| \hat{\alpha}_{\rho\sigma}\left(e^r, v^r\right)\right| e^g \right\rangle \right| v^i \right\rangle \tag{2.14}$$

Considering isotropic averaging *i.e.*, all molecular orientations are equally possible, $(\alpha_{\rho\sigma})_{fi}$ turns out to be:

$$\begin{aligned}(\alpha_{\rho\sigma})_{fi} = \frac{1}{\hbar}\sum_{r\neq i,f}\Bigg(&\frac{\left\langle v^f \left| \left\langle e^f \left| \hat{p}_\rho \right| e^r \right\rangle \right| v^r \right\rangle \left\langle v^r \left| \left\langle e^r \left| \hat{p}_\sigma \right| e^g \right\rangle \right| v^i \right\rangle}{\omega_{e^r e^g} + \omega_{v^r v^i} - \omega_1 - i\Gamma_{e^r v^r}} \\ &+ \frac{\left\langle v^f \left| \left\langle e^f \left| \hat{p}_\sigma \right| e^r \right\rangle \right| v^r \right\rangle \left\langle v^r \left| \left\langle e^r \left| \hat{p}_\rho \right| e^g \right\rangle \right| v^i \right\rangle}{\omega_{e^r e^f} + \omega_{v^r v^f} + \omega_1 + i\Gamma_{e^r v^r}}\Bigg)\end{aligned} \tag{2.15}$$

Now, the approximation of slight dependence of the electronic transition dipole moment on the normal vibrational coordinates Q is introduced, assuming $Q-$dependence as a perturbation of the electronic state within the Born-Oppenheimer regime. By evaluating the effect of the perturbation on the components of the electric transition dipoles in eq. 2.15 and considering again $\omega_1 >> \omega_{vib}$ and $\omega_1 << \omega_e$, the Taylor expansion to the second order of $\alpha_{\rho\sigma}(Q)$ can be rewritten:

$$\begin{aligned}(\alpha_{\rho\sigma})_{fi} = \left\langle v^f \left|\hat{\alpha}_{\rho\sigma}(Q)\right| v^i \right\rangle = (\alpha_{\rho\sigma})_0 \left\langle v^f \left| v^i \right.\right\rangle + \sum_k \left(\frac{\partial \alpha_{\rho\sigma}}{\partial Q_k}\right)_0 \left\langle v^f \left|Q_k\right| v^i \right\rangle \\ + \frac{1}{2}\sum_k \sum_l \left(\frac{\partial^2 \alpha_{\rho\sigma}}{\partial Q_k \partial Q_l}\right)_0 \left\langle v^f \left|Q_k Q_l\right| v^i \right\rangle\end{aligned} \tag{2.16}$$

where $(\alpha_{\rho\sigma})_0$, $(\frac{\partial(\alpha_{\rho\sigma})}{\partial Q_k})_0$ and $(\frac{\partial^2(\alpha_{\rho\sigma})}{\partial Q_k \partial Q_l})_0$ can be written in terms of $p_{\rho\sigma}$ as:

$$(\alpha_{\rho\sigma})_0 = \frac{1}{\hbar}\sum_{e^r \neq e^g} \left(\frac{(p_\rho)^0_{e^g e^r}}{\omega_{e^r e^g} - \omega_1} + \frac{(p_\sigma)^0_{e^g e^r}(p_\rho)^0_{e^r e^g}}{\omega_{e^r e^g} + \omega_1} \right) \tag{2.17}$$

$$\begin{aligned}\left(\frac{\partial \alpha_{\rho\sigma}}{\partial Q_k}\right)_0 = \frac{1}{\hbar}\sum_{e^r \neq e^g} \left(\frac{(p_\rho)^k_{e^g e^r}(p_\sigma)^0_{e^r e^g} + (p_\rho)^0_{e^g e^r}(p_\sigma)^k_{e^r e^g}}{\omega_{e^r e^g} - \omega_1} \right. \\ \left. + \frac{(p_\sigma)^0_{e^g e^r}(p_\rho)^k_{e^r e^g} + (p_\sigma)^r_{e^g e^r}(p_\rho)^0_{e^r e^g}}{\omega_{e^r e^g} + \omega_1} \right)\end{aligned} \tag{2.18}$$

$$\left(\frac{\partial^2 \alpha_{\rho\sigma}}{\partial Q_k \partial Q_l}\right)_0 = \frac{1}{\hbar}\sum_{e^r \neq e^g} \left(\frac{(p_\rho)^k_{e^g}(p_\sigma)^{k^r}_{e^g}}{\omega_{e^r e^g} - \omega_1} + \frac{(p_\sigma)^{k^r}_{e'}(p_\rho)^k_{e^g e^r}}{\omega_{e^r e^g} + \omega_1} \right) \tag{2.19}$$

The derivatives in eq. 2.18 and eq. 2.19 express the transition polarizability components for one specific transition where only the quantum number v_k changes.

2.2.2.3 Raman selection rule

Within the harmonic oscillator approximation and electrical harmonicity, eq. 2.16 can be truncated to the first order and the total vibration wave function ϕ can be written as the product of harmonic oscillator wave functions for each normal mode of vibration:

$$\begin{aligned}(\alpha_{\rho\sigma})_{fi} = (\alpha_{\rho\sigma})_0 \left\langle \prod_k \phi_{v_k^f}(Q_k) \left| \prod_k \phi_{v_k^i}(Q_k) \right.\right\rangle \\ + \sum_k \left(\frac{\partial \alpha_{\rho\sigma}}{\partial Q_k}\right)_0 \left\langle \prod_k \phi_{v_k^f}(Q_k) \left|Q_k\right| \prod_k \phi_{v_k^i}(Q_k) \right\rangle\end{aligned} \tag{2.20}$$

The first and second terms of eq. 2.20 represent Rayleigh and Raman scattering, respectively. With the help of harmonic oscillator properties, it is possible to determine the condition under which the two terms are non-zero:

$$\left\langle \phi_{v_k^f}(Q_k) \mid \phi_{v_k^i}(Q_k) \right\rangle = \begin{cases} 0 & \text{for } v_k^f \neq v_k^i \\ 1 & \text{for } v_k^f = v_k^i \end{cases} \tag{2.21}$$

$$\left\langle \phi_{v_k^f}(Q_k) \left| Q_k \right| \phi_{v_k^i}(Q_k) \right\rangle = \begin{cases} \left(v_k^i + 1\right)^{1/2} b_{v_k} & \text{for } v_k^f = v_k^i + 1 \\ \left(v_k^i\right)^{1/2} b_{v_k} & \text{for } v_k^f = v_k^i - 1 \\ 0 & \text{otherwise} \end{cases} \tag{2.22}$$

where:

$$b_{v_k} = \left(\frac{\hbar}{2\omega_k}\right)^{1/2} = \left(\frac{h}{8\pi^2 c_0 \bar{\nu_k}}\right)^{1/2} \tag{2.23}$$

With the help of eq. 2.21, and eq. 2.22 one can reasonably say that elastic scattering occurs only when there is no change in any vibrational quantum number ($v_k^f = v_k^i$). Instead, Raman scattering for the k^{th} vibrational mode occurs if the final vibrational quantum number of each mode is equal to its starting value except for v_k^f, which changes by unity *i.e.*, $v_k^f = v_k^i \pm 1$. Within the presented framework, the polarizability component for S and AS scattering can be written as:

$$\begin{aligned} \left(\alpha_{\rho\sigma}\right)_{v_k^i+1, v_k^i} &= \left(v_k^i + 1\right)^{1/2} b_{v_k} \left(\frac{\partial \alpha_{\rho\sigma}}{\partial Q_k}\right)_0 \\ \left(\alpha_{\rho\sigma}\right)_{v_k^i-1, v_k^i} &= \left(v_k^i\right)^{1/2} b_{v_k} \left(\frac{\partial \alpha_{\rho\sigma}}{\partial Q_k}\right)_0 \end{aligned} \tag{2.24}$$

with S and AS scattering associated to $v_{fk} = v_{ik} + 1$ and $v_{fk} = v_{ik} - 1$, respectively. In synthesis, the two necessary conditions to observe the Raman effect are: (i) at least one non-zero element of the derived polarizability tensor and (ii) $v_{fk} = v_{ik} \pm 1$ *i.e.*, the vibrational quantum number must be changed in the final state. In addition, by eq. 2.16 one can retrieve a general selection rule: at least one of the products $<v_f|\ \alpha_{\rho\sigma}\ |\ v_i>$ must belong to the totally symmetric representation Γ_1, namely $\Gamma_1 \subset \Gamma(v^f)$ x $\Gamma(\alpha_{\rho\sigma})$ x $\Gamma(v^i)$.

2.2.2.4 Raman scattered intensity

For the purpose of this work, it is also useful to introduce the Raman scattered intensity and retrieve a formulation for Raman thermometry. This will be useful in the results sections where the temperature of laser irradiated Zinc Ferrite nanoparticles will be estimated. Considering an ensemble of N molecules, the scattered

intensity is directly related to the occupancy of each vibrational mode through Boltzmann's statistics. For S and AS vibrational transitions from v_{ik} to $v_{ik}+1$ and $v_{ik}-1$, respectively, the scattered intensity is proportional to:

$$Stokes: \qquad N\sum_i \left(v_k^i+1\right) f_{v_k^i} = \frac{N}{1-e^{-hc_0\bar{\nu}_k/kT}} \tag{2.25}$$

$$Anti-Stokes: \qquad N\sum_i \left(v_k^i\right) f_{v_k^i} = \frac{N}{e^{hc_0\bar{\nu}_k/kT-1}} \tag{2.26}$$

Assuming S transition for k^{th} mode in a back-scattered geometry and incident light polarized along z axis of a fixed laboratory system, the intensity I is given by:

$$I = \frac{k_{\bar{\nu}} h N \bar{\nu}_S^4}{8\pi^2 c_0 \bar{\nu}_k (1-e^{-hc_0\bar{\nu}_k/kT})} \frac{45(\alpha_k')^2 + 7(\gamma_k')^2}{45} J \tag{2.27}$$

where $\nu_S = \nu_l - \nu_k$ is the Stokes shifted wavenumber, α'_k and γ'_k are the derived polarizability tensor invariants for the k^{th} mode and J is the irradiance of the incident radiation given by:

$$J = \frac{1}{2} c_0 \epsilon_0 E_{y0}^2 \tag{2.28}$$

A similar expression can be obtained for AS scattering replacing eq. 2.26 in eq. 2.27 with $\nu_{AS} = \nu_l + \nu_k$. In general, the Raman scattered intensity can be rewritten as:

$$I = \frac{d\sigma}{d\Omega} J \tag{2.29}$$

where $\frac{d\sigma}{d\Omega}$ is the differential Raman cross section. This latter is a property of the investigated molecule giving its scattering efficiency. Having introduced the scattering intensity for S and AS processes, the ratio between the S and AS intensities is calculated as follows:

$$\frac{I_S}{I_{AS}} = \frac{\bar{\nu}_S^4}{\bar{\nu}_{AS}^4} e^{\frac{hc_0\bar{\nu}_k}{kT}} \tag{2.30}$$

Eq. 2.30 allows us to see that the AS lines in a Raman experiment will always be weaker with respect to their S counterparts, consistently with the detected response in Fig. 2.2. Furthermore, the temperature of an investigated sample can be calculated if the intensity ratio between S and AS lines is given.

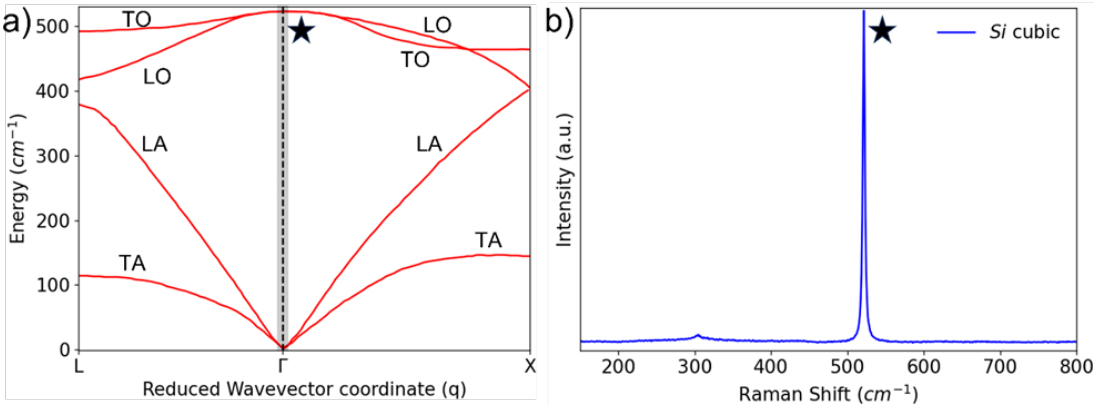

Figure 2.4: (a) Phonon dispersion of silicon crystal. The black shaded rectangle is used to indicate the region probed by Raman scattering. (b) Raman Stokes scattering of Si. The 522 cm^{-1} first-order Raman mode is evidenced and corresponds to the optical phonon at the Brillouin zone center.

2.2.2.5 Raman Selection rules in crystals

Passing from a molecular system to crystals with full translational symmetry both energy and momentum conservations must be considered through the equations:

$$Energy: \qquad \hbar\omega_i = \hbar\omega_S + \hbar\Omega \tag{2.31}$$

$$Momentum: \qquad \mathbf{k_i} = \mathbf{k_S} + \mathbf{q} \tag{2.32}$$

ω_i, $\mathbf{k_i}$ and ω_S, $\mathbf{k_S}$ represent the incident and scattered frequencies and wave vectors, respectively while Ω and $\mathbf{q}$ are the frequency and wave vector of the phonon, magnon, electronic or other mode involved in the scattering. In Raman experiments $\Omega \simeq 10 \times 10^{-13}$ Hz and $\omega_{i,S} \simeq 10^{14-15}$ Hz, thus $|\mathbf{k_i}| \simeq |\mathbf{k_f}|$ and the wave vector conservation becomes $|\mathbf{q}| = 2|\mathbf{k_i}| \sin(\frac{\theta}{2})$, where θ is the angle between the incident and scattered photons directions. The maximum excitation wave vector is $2|\mathbf{k_i}| \simeq 5 \times 10^4\,\mathrm{cm}^{-1}$, while the wave vector of the full phonon dispersion curve extended to the boundary of the Brillouin zone is $\frac{\pi}{a} \simeq 108\,\mathrm{cm}^{-1}$. Therefore, the only probed phonons are very close to the center of the Brillouin zone (Γ-point) giving the selection rule $\mathbf{q} \simeq 0$. A typical example of the Raman effect in crystals is silicon whose phonon dispersion and relative first-order Raman spectrum are reported in Fig. 2.4.

This scenario is further complicated by other selection rules introduced by the crystal symmetries. The general differential scattering cross section can be written as:

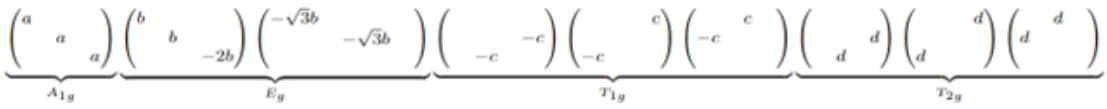

Figure 2.5: Allowed Raman tensors for the O_h cubic point group [104].

$$\frac{d^2\sigma}{d\Omega d\omega_s} = \frac{\omega_i \omega_s^3 V}{(4\pi)^2 c^4} \frac{n_s}{n_i} \left| \epsilon_s \cdot \frac{d\chi(\omega)}{d\omega} \cdot \epsilon_i \right|^2 \langle \chi(\mathbf{q},\omega)\chi^*(\mathbf{q},\omega) \rangle \tag{2.33}$$

where $\chi(\omega)$ is the susceptibility while n_i, ϵ_i and n_S, ϵ_S represent the refractive indexes and polarizations of the incident and scattered light, respectively [139]. With this formulation, the Neumann principle can be introduced. This governs the symmetry selection rules effectively acting on the $\left|\epsilon_S \cdot \frac{d\chi(\omega)}{d\omega} \cdot \epsilon_i\right|$ term. The principle requires that the physical properties of the illuminated crystal (incident field, induced polarization, and Raman susceptibility tensor) are invariant under all the symmetry operations of the crystal point group. Therefore, since ϵ_i and ϵ_S transform like polar vectors, the only non-zero $\frac{d\chi(\omega)}{d\omega}$ elements are those with symmetries Γ_x belonging to the $\Gamma^* \bigotimes \Gamma$, where Γ is the irreducible representation. Only some elements of the point group are zero and equal or related as shown for example in Fig. 2.5 for the O_h cubic point group [104]. The symmetries indicated are retrieved through polarized Raman measurements. Indeed, varying the polarization of the incident wave ϵ_i with respect to the crystal axes allows the selection of different elements of the susceptibility tensor determining the symmetry of the modes. In such experiments, it is required to indicate also the incoming and scattered polarization and wave vectors through the Porto notation $\mathbf{k_i}(\epsilon_i, \epsilon_S)\mathbf{k_S}$.

2.2.2.6 Influence of the crystal dimensions on the Raman linewidth

In the ideal case of an infinite crystal, the Raman signal can be thought of as given by a resonance between two vibrational levels, thus describable with a Lorentz peak function. However, the $\mathbf{q} \simeq 0$ condition is relaxed when the dimension of the crystal or of grain boundaries in a bulk system is nanometric. This occurs because the propagation of phonons is interrupted by the grain boundaries and, in the case of a single isolated grain, the phonon mode is reflected from the boundaries and confined within the grain. The uncertainty of the phonon wave vector at a crystal boundary (*e.g.*, nanocrystal surface, interspace between defects, *etc.*) with dimension d is $\Delta q \simeq \frac{\pi}{d}$ as a consequence of the Heisenberg uncertainty principle and the boundary conditions on the phonon wave function [140]. Therefore, the phonon modes with $\mathbf{q} \neq 0$ over the whole Brillouin zone can contribute to the first-order Raman spectrum with a broadening of the Raman lines as well as a shift in the peak positions. This phenomenon is called Phonon Confinement and,

as a rule of thumb, can be observed in crystals with dimensions smaller than 20 lattice parameters [141]. The theoretical description of this confinement is due to *Richter, Wang and Ley* [142, 141] and known as Phonon Confinement Model (PCM) or RWL model. The model begins considering a nanosphere with diameter d and a plane wave for the phonon of wave vector $\mathbf{q}$. This plane wave has to be multiplied by a confinement Gaussian function $W(r)$ expressed as:

$$W(r) = e^{\alpha r^2/d^2} \tag{2.34}$$

where α is a parameter which determines how fast the wavefunction decays approaching the boundary. Since the phonon amplitude, proportional to $|W(r)|^2$, decays of $1/e$ at the boundary, $r = d/2$ and $\alpha = 2$ for this case. The contributions of phonons away from the Brillouin zone centre can be estimated using the $C(\mathbf{q})$ weighting factor which is derived as the Fourier transform of the confinement function:

$$|C(q)|^2 = e^{-\frac{\mathbf{q}^2 d^2}{4}} \tag{2.35}$$

The integration of all the contributions over the whole Brillouin zone allows one to obtain the complete first-order Raman spectrum given by:

$$I(\omega) = \int_{BZ} \frac{|C(\mathbf{q})|^2 d^3\mathbf{q}}{[\omega - \omega(\mathbf{q})]^2 + (\Gamma_0/2)^2} \tag{2.36}$$

where Γ_0 is the linewidth of the zone-centred Raman mode while $\omega(\mathbf{q})$ is the phonon dispersion curve.

2.2.2.7 Raman setup

A basic Raman setup configuration is sketched in Fig. 2.6. It is composed of the following components:

1. Laser Source: This is the first part of the spectrometer shown in Figure 2.6(1). An He-Ne Laser at 632.8 nm and diode lasers at 638 nm, 785 nm, and 532 nm were employed.

2. Attenuator: The light is then passed through a wheel equipped with several neutral density filters. These have optical density OD4, OD3, OD2, OD1, OD0.6, OD0.3, OD0, thus, scale the power with a base-10 logarithmic law. Therefore, starting from a OD0 of 5 mW the OD1 filter will reduce the incidence power of 10^{-1}, giving 0.5 mW.

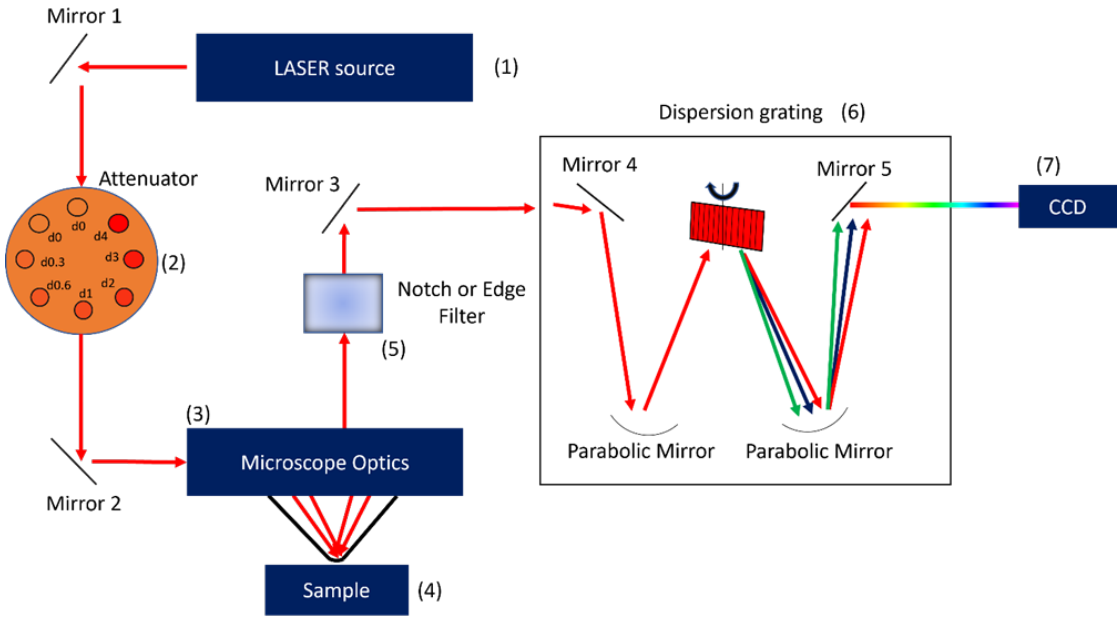

Figure 2.6: Sketch of the configuration of a basic Raman setup with its key components.

3. Microscope Optics: The light beam is focused on the sample thanks to the microscope optics (Fig. 2.6(3)). This is composed of four different magnification stages which are 10x, 20x, 50x, and 100x. Two 50x objectives can be employed: standard and long working distance.

4. Sample holder: The optics focus on the support in which the sample is placed (Fig. 2.6(4)). This is composed of a motorized stage that can move in any direction of the sample plane and two focus knobs for coarse and fine-tuning.

5. Filter: After hitting the sample the light beam is backscattered in the spectrometer passing through the optics and encounters a filter which can be holographic band-blocking (notch) or long-pass (edge) which cuts the Rayleigh line (notch filter) or the Rayleigh and Anti-Stokes lines (edge filter). The filter is visible in the sketch Fig. 2.6(5).

6. Dispersion grating (Fig. 2.6(6)): Passing through other optical components like mirrors, slits, and lenses the beam hits an elliptic mirror which focuses on a dispersion grating (with 600 lines/mm or 1800 lines/mm depending on the wanted resolution). Selected fractions of the dispersed spectra are sent on the detector depending on the angle of incidence (and therefore reflection) on the grating. The grating dispersion follows the Bragg law for incident plane waves at any angle:

$$d\,(\sin\theta_i - \sin\theta_m(\lambda)) = m\lambda \tag{2.37}$$

where d is the distance between adjacent lines, θ_m is the angle of m^{th} order diffraction with integer m (m = 1, 2, 3, ...), θ_i is the incidence angle and λ is the dispersed wavelength.

7. CCD Detector: The light is sent directly on a Charge Coupled Device (CCD) detector made out of silicon pixels Peltier cooled at about -41 °C. This allows for the simultaneous detection of a set of dispersed wavelengths after the dispersion grating step. The CCD detector is shown in Fig. 2.6(7).

8. Horiba LabSpec software: The detector sends the collected signal to the LabSpec software in which the integration time and the number of means can be set and spectra can be postprocessed by subtracting the possible environment contributions and possible substrate Raman scattering and/or luminescence. Typical integration times for the presented data are 10-20 s with 10-30 averages.

The nanoparticles Raman characterization was performed at room temperature (RT) using an automated and integrated confocal microRaman spectrometer, XploRA Plus HORIBA Scientific, equipped with an Olympus microscope BX43 and three different laser sources: 532 nm - 100 mW, 638 nm - 90 mW, and 785 nm - 100 mW. Neutral filters with different optical densities allowed to set incident laser power. The spectrometer was equipped with a motorized xy stage on which the investigated samples were positioned. Spectral resolution was about 1 cm^{-1}. An Open Electrode CCD camera, with a multistage Peltier air-cooling system, was used as a detector. The measurements were performed with all three excitation wavelengths and using a 50x magnification objective. Thermal cycles were performed by progressively increasing and decreasing the incident laser density power ranging from about 2.5×10^6 W/cm^2 to 2.5×10^7 W/cm^2. The spectra were acquired with a mean integration time of about 20 s and a number of accumulations equal to 10.

The in vacuum and in air ambient/atmosphere MicroRaman irradiation and measurements were carried out with a Horiba LabRAM spectrometer with 632.8 nm He-Ne laser excitation, a 50x long-working-distance objective and a CCD camera with a multistage Peltier air-cooling system as a detector. Two different optical sample chambers were used for Raman measurements at different ambient conditions: (i) a cold-finger cryostat (Oxford Instruments Microstat) connected to a turbomolecular pump with a backup scroll (Pfeiffer) used to keep the powders at around 3×10^{-6} mbar and (ii) a home-made optical chamber connected to a

diaphragm pump to irradiate the powders at a pressure around 1.5 mbar. During the irradiation steps, the laser power was varied in several different measurements from 0.5 mW to 5 mW with a minimum power density of about 125 mW/m^2 (12.5 kW/cm^2) on the sample. The Raman spectra, both before and after irradiation, were collected in an air atmosphere with 30 s and 60 s of CCD exposure time for the high-vacuum and home-made chambers, respectively. 5 and 30 averages were used to decrease the noise level of the spectra collected respectively before and after the irradiation since the Signal-to-Noise Ratio (SNR) of the in-vacuum irradiated compound was low. To estimate the temperature of the scattering volume reached during irradiation procedures the Stokes and anti-Stokes components were measured using a Horiba LabRAM HR Evolution equipped with a notch filter and a NdYAG laser with 532 nm excitation wavelength at the Experimental Mineralogy Lab. of the University of Pavia.

The UV Raman measurements were carried out with a benchtop Raman set-up at the IUVS beamline at the Elettra synchrotron in Trieste. A 266 nm light from an Nd:YAG laser was used as the excitation source. The samples were mounted on an oscillating stage to avoid photo-damaging. The incident power laser was set to 200 μW. A Czerny-Turner spectrometer equipped with a holographic dispersive element of 3600 lines/mm, coupled with a Peltier-cooled back-thinned CCD has been used to record the Raman signals. The calibration of the spectrometer was standardized using cyclohexane (Sigma-Aldrich). The Visible and UV Raman measurements have been carried on thanks to the collaboration with Dr. B. Albini of the Department of Physics at UNIPV and Dr. F. D'Amico of the Inelastic UV Scattering (IUVS) beamline at Elettra Sincrotrone Trieste.

2.2.3 Electron Paramagnetic Resonance (EPR)

2.2.3.1 Basic Principles

The basic principles of Electron Paramagnetic Resonance (EPR) here described are elaborated and synthesized starting from several reviews and introductory textbooks [143, 144, 145, 146]. For simplicity, only solid-state Continuous Wave (CW) EPR will be considered.

A single free electron with spin $S = \frac{1}{2}$ can be represented through the quantum numbers $|S,m_S>$ where $m_S = \pm\frac{1}{2}$. The application of a magnetic field B_0 splits the degeneracy of the m_S spin levels through electron Zeeman interaction which is expressed as:

$$\Delta E = h\nu = g_e \beta_B B_0 \tag{2.38}$$

The splitting of the levels is linearly proportional to the magnitude of the magnetic field producing the situation sketched in Fig. 2.7. Once the levels are

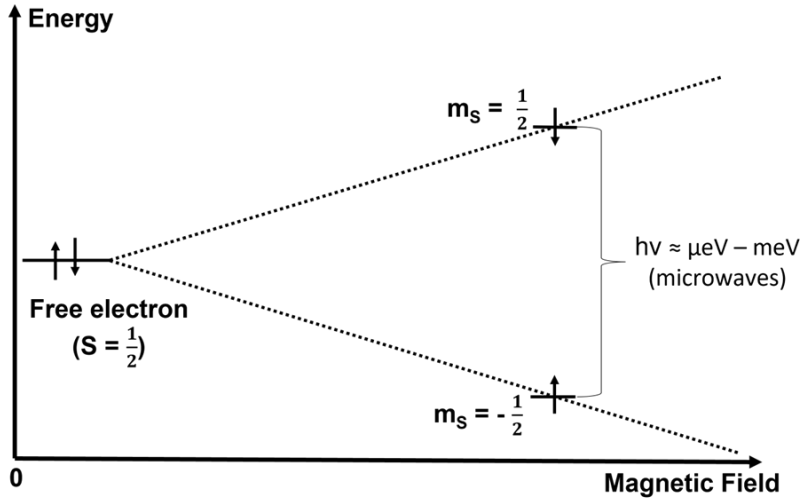

Figure 2.7: Sketch of the basic electron Zeeman interaction.

split, the electron can resonate in between $m_S = +\frac{1}{2}$ and $m_S = -\frac{1}{2}$ states upon absorption of photons usually in the microwave range (Fig. 2.7).

Such a simplified description shows only the basic concepts applied to an ideal system, but it already gives two important rules applicable to a real system: (i) the system must have one or more unpaired electrons and (ii) the transitions must increase or decrease the spin by 1 ($\Delta m_S = \pm 1$). In general, real samples are characterized by more complex spin interactions. These can be expressed through a spin Hamiltonian for a single unpaired electron of the form:

$$\begin{aligned} H_0 = H_{\mathrm{EZ}} + H_{\mathrm{NZ}} + H_{\mathrm{HF}} + H_{\mathrm{NQ}} + H_{\mathrm{NN}} = \beta_{\mathrm{e}}\mathbf{B}_0\mathbf{g}\mathbf{S}/\hbar - \beta_{\mathrm{n}}\sum_{k=1}^{l} g_{n,k}\mathbf{B}_0\mathbf{I}_k/\hbar \\ + \sum_{k=1}^{l}\mathbf{S}\mathbf{A}_k\mathbf{I}_k + \sum_{I_k>\frac{1}{2}}\mathbf{I}_k\mathbf{Q}_k\mathbf{I}_k + \sum_{i\neq k}\mathbf{I}_i\mathbf{d}_{ik}\mathbf{I}_k \end{aligned} \tag{2.39}$$

where:

1. H_{EZ} is the single electron Zeeman interaction which splits the electron spin energy levels. This depends on g values which can be used as identifier of given paramagnetic species since it is independent from the microwave frequency and designates the intrinsic resonance position of an ion in a particular environment rather than being given relative to a reference compound (like in NMR). For a free electron $g \simeq 2.0023$ and any deviation from this value depends on the molecular environment and spin-orbit interaction. For

a solid-state single crystal sample, g is not a pure number but a $3\,x\,3$ matrix. From this, the three principal components g_x, g_y and g_z and three Euler angles describing the orientation of the tensor in a given molecular frame can be extracted. For cubic symmetry $g_x = g_y = g_z$, for axial symmetry $g_\perp = g_x = g_y \neq g_z = g_\parallel$ while for rhombic symmetry $g_x \neq g_y \neq g_z$.

2. H_{NZ} is the nuclear Zeeman interaction analogous in mechanism to the electron Zeeman one but weaker in intensity since the nuclear magneton β_n scales inversely with the mass of the nucleus. It is described by a nuclear g_n and should be considered only in pulsed EPR.

3. H_{HF} is the electron-nuclear hyperfine interaction *i.e.*, the interaction between the magnetic dipoles of unpaired electrons and surrounding nuclei. It is composed of an isotropic and an anisotropic part which are linked to the probability of finding the electron in the nuclear position (typical orbitals with s character or of mechanisms that polarise the spin orientation of $p-$, $d-$, and $f-$ to inner $s-$orbitals) and a pure magnetic dipole-dipole interaction depending on the orientation and average distance between unpaired electron and nucleus, respectively.

4. H_{NQ} is the nuclear quadrupole interaction for nuclei with nuclear spin $I > \frac{1}{2}$. It is the interaction between the nuclear quadrupole moment and the electric field gradient generated by the asymmetric distribution of electron density. It is difficult to detect this contribution due to broadening effects but EPR spectra with narrow lines can often display discernible peak shifts.

5. H_{NN} is the nuclear-nuclear spin interaction which is generally not detected in CW EPR because of its small amplitude with respect to electron-electron or electron-nuclear interactions.

In this work, the multi-electron interactions are the only ones considered because they are the most important actors in TMOs. These are: the Zero-field splitting interaction (H_{ZFS}) and the dipolar and exchange interactions (H_{DD} and H_{ex}). The zero-field splitting interaction becomes important in the case of multiple strongly-coupled unpaired electrons for example located on the same transition metal ion thus the electron-electron coupling must be considered. Such systems are described by a total spin $S > \frac{1}{2}$ with a spin degeneracy $(2S + 1)$ which can be removed by dipolar interaction and spin-orbit coupling even in the absence of external contributions. The zero-field Hamiltonian is expressed as:

$$H_{\mathrm{ZFS}} = \mathbf{SDS} \tag{2.40}$$

where $\mathbf{D}$ is the symmetric and traceless zero-field interaction tensor:

$$\mathbf{D} = \begin{pmatrix} D_x & & \\ & D_y & \\ & & D_z \end{pmatrix} = \begin{pmatrix} -\frac{G}{3} + E & & \\ & -\frac{G}{3} - E & \\ & & \frac{2G}{3} \end{pmatrix} \tag{2.41}$$

Only two parameters $G = \frac{3D_z}{2}$ and $E = \frac{(D_x - D_y)}{2}$ describe $\mathbf{D}$ in the diagonal form. G and E depend on the average distance between the unpaired electrons and the deviation from the cubic symmetry, respectively. Indeed, for cubic symmetry $G = E = 0$ and the spin sublevels are degenerate, while $G \neq 0$, $E = 0$ for axial and $G \neq 0$, $E \neq 0$ for rhombic symmetries are obtained. When the photon energy exceeds the ZFS energy ($h\nu >> G$) multiple intra- and inter-manifold transitions are detected. If instead $G >> h\nu$ only intra-manifold transitions are observed. These latter can be treated with an effective $S = \frac{1}{2}$ spin system with g_{eff} values deviating from the "true" $S = \frac{1}{2}$ configuration.

Instead, if the electrons are weakly coupled, the system can be described as composed of individual spins with some interactions between them. Within this framework, the Hamiltonian of a system of two electrons with spins S_1 and S_2 is described as:

$$\begin{aligned} H_0 &= H_0(S_1) + H_0(S_2) + H_{\mathrm{DD}} + H_{\mathrm{EX}} \\ &= H_0(S_1) + H_0(S_2) + \mathbf{S}_1\mathbf{D}\mathbf{S}_2 + \mathbf{S}_1\mathbf{J}\mathbf{S}_2 \end{aligned} \tag{2.42}$$

where $H_0(S_1)$ and $H_0(S_2)$ are the single electron terms of eq. 2.42 while H_{DD} and H_{ex}, are the interactions between them. The electron dipole-dipole interaction H_{DD} provides information on the distance and orientation between the two weakly-coupled unpaired electrons since depends on the distance r between the two spins as $\frac{1}{r^3}$ and relative orientation. Indeed, the electron dipole-dipole coupling tensor $\mathbf{F}$ is expressed as:

$$\mathbf{F} = \frac{\mu_0}{4\pi\hbar}\frac{g_1 g_2 \beta_e^2}{{r_{12}}^3}\begin{pmatrix} -1 & & \\ & -1 & \\ & & 2 \end{pmatrix} = \begin{pmatrix} -\omega_{dd} & & \\ & -\omega_{dd} & \\ & & 2\omega_{dd} \end{pmatrix} \tag{2.43}$$

showing the aforementioned dependencies. The point-dipole approximation of $\mathbf{F}$ is not always valid especially in Transition Metal ions because of the large $g-$anisotropy and high electron spin delocalization. Furthermore, if there is an overlap between the wavefunctions of the two electron spins, an additional contribution arises, the electron exchange interaction H_{ex}. This is expressed with an exchange coupling tensor:

$$\mathbf{J} = \begin{pmatrix} -J & & \\ & -J & \\ & & 2J \end{pmatrix} \tag{2.44}$$

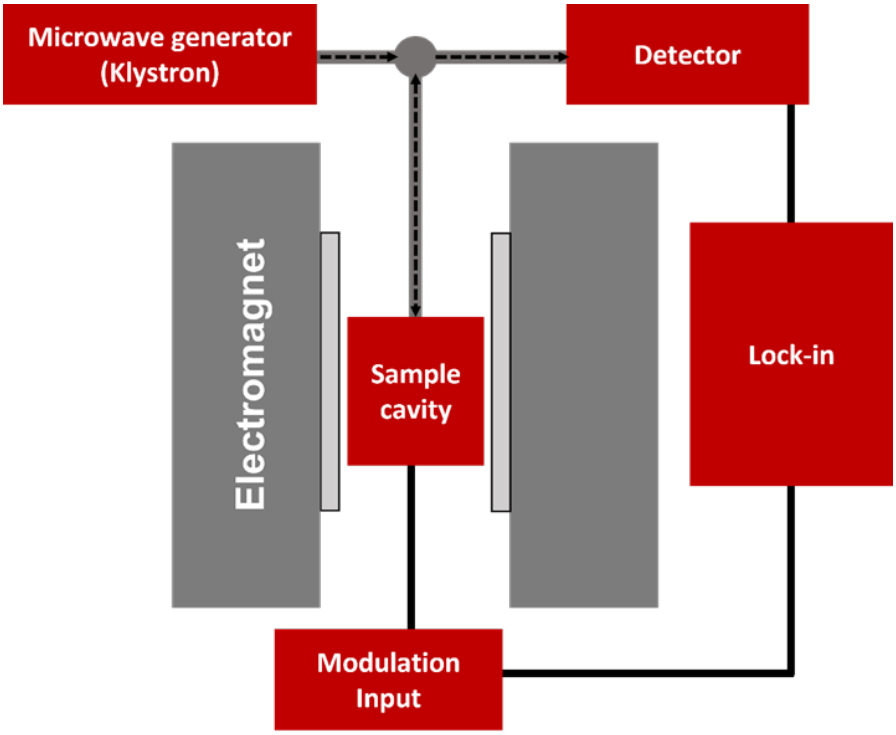

Figure 2.8: Sketch of the main components of an EPR spectrometer configuration.

which consists of an isotropic J_{iso} part and an anisotropic one. J_{iso} is usually sufficient to describe the exchange coupling, thus H_{ex} becomes:

$$H_{\text{ex}} = J_{iso}\mathbf{S_1}\mathbf{S_2} \tag{2.45}$$

In the case of two electrons with $S = \frac{1}{2}$ the sign of J_{iso} determines whether the ground state is a singlet ($J_{iso} > 0$) with an antiferromagnetic coupling or a triplet ($J_{iso} < 0$) with a ferromagnetic coupling. Moreover, the electron exchange interaction decays exponentially with distance, therefore, J_{iso} should go to zero in approximately 15 Å.

2.2.3.2 EPR Experimental setup

A sketch of an EPR spectrometer is shown in Fig. 2.8. The EPR measurements presented in this work have been conducted in collaboration with Dr. M. C. Mozzati. Microwaves generated from a source (typically a Klystron or a Gunn diode), are sent through an attenuator and directed onto the sample which is placed into a microwave cavity and surrounded by an electromagnet. The external magnetic field B_0 applied and the microwave frequency ν are closely related. Indeed, the higher the ν the higher the B_0 with typical values ranging in the X-band, thus $\nu =$

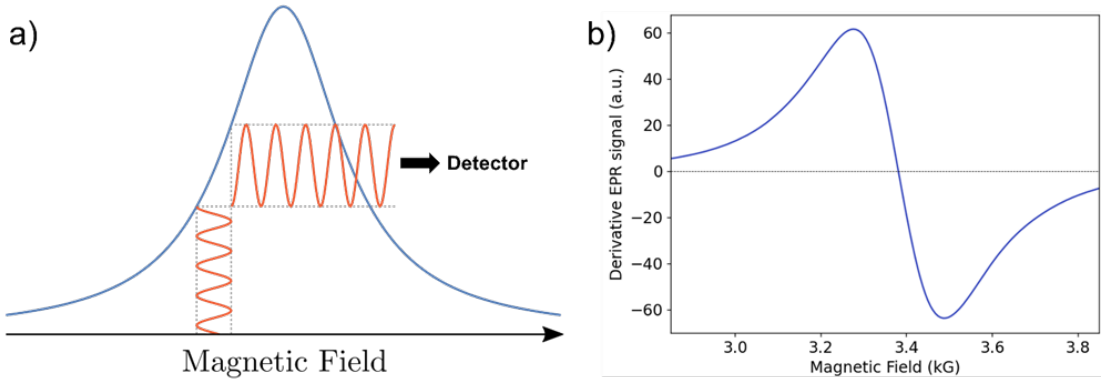

Figure 2.9: (a) Lock-in detection through field modulation. (b) Typical derivative EPR spectra.

9.4 GHz and $B_0 = 3000$ G (0.3 T). The microwaves are reflected from the sample and sent to the detector which is synchronized with a lock-in amplifier. EPR spectroscopy can be realized by either scanning the microwave frequency with a fixed external magnetic field or by scanning B_0 and impinging monochromatic microwaves. The last scheme was employed in this work.

The lock-in detection is based on field modulation which is sketched in Fig. 2.9a. It consists of the addition of a small oscillating magnetic field to the external B_0 at a typical frequency of 100 kHz and the use of a phase-sensitive detector. Therefore, only signals with the same modulation (100 kHz) are detected increasing the signal-to-noise ratio of the absorption measurement. However, this method retrieves the derivative of the real signal, therefore, a typical EPR spectra will be the derivative of the resonance peak as presented in Fig. 2.9b. The EPR setup employed in this work was an X-band ($\simeq$ 9.45-9.47 GHz) Bruker spectrometer, with a magnetic field in the range between 200-6000 G. A continuous nitrogen flow cryostat was used to carry out the investigation as a function of temperature in the range between 120 K and 500 K.

2.2.4 Superconducting Quantum Interference Devices (SQUID)

The description of the qualitative principles of SQUID magnetometry and its applications is based on the reviews made by *Fagaly* [147] and *Buchner et al.* [148]. SQUID magnetometry is a measure of external variations of the magnetic flux through Josephson junctions *i.e.*, devices based on the junction between two superconductors with a non-superconducting interface, usually an insulator a metal or a bottleneck region. This section is dedicated to the description of principles and basic implementations of Low-Temperature (LT) dc-SQUID magnetometers focusing on type-I superconductors and insulating interfaces in Josephson junc-

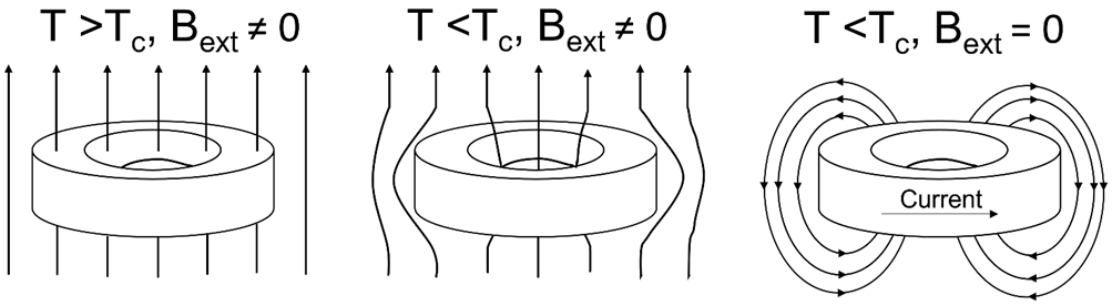

Figure 2.10: Meissner effect in a superconducting ring cooled in an externally applied magnetic field.

tions.

2.2.4.1 Basic principles

Superconductors are materials which exhibit zero resistivity and the complete expulsion of the magnetic field except for a thin superficial layer (Meissner effect) below a certain critical temperature (T_c). As described in *Bardeen, Cooper and Schriffer* (BCS) theory [149], the superconducting phase is possible thanks to phonon exchange between electron pairs which condensates in a weakly bound state (Cooper pairs) that moves in the material without scattering. Electrons in Cooper pairs can exchange partners and are decoupled by thermal (T_c), kinetic (critical current density, J_c) and magnetic (critical field, H_c) interactions. A ring of a superconducting material with an applied external magnetic field (Fig. 2.10) $H < H_c$ is now considered. If the ring is in its normal state, the external field penetrates the material but, when the ring becomes superconducting, the internal magnetic flux is trapped in the ring hole rather than expelled as in a continuous solid. When the magnetic field is turned off, a current is induced into the ring to maintain the internal constant flux without dissipation due to the zero-resistivity. Now, two half-rings of superconducting material, joined together with an insulating interface are considered. It is expected that the Cooper pairs wave function would decay in passing through the interface between the first half-ring and the insulator with a net decrease of the superconducting current. Instead, as predicted by *Josephson* [150], the electrons tunnel across the insulator and a superconducting current can be found also in the second half-ring. This is possible if the interface length is less than the coherence length of the superconducting material and the current is below I_c. The device here presented is called Josephson junction and was obtained for the first time by *Anderson and Rowell* [151]. If one applies a magnetic field $H < H_c$ to the junction a behaviour similar to the aforementioned superconducting ring is observed *i.e.*, H is trapped inside the device as long as it

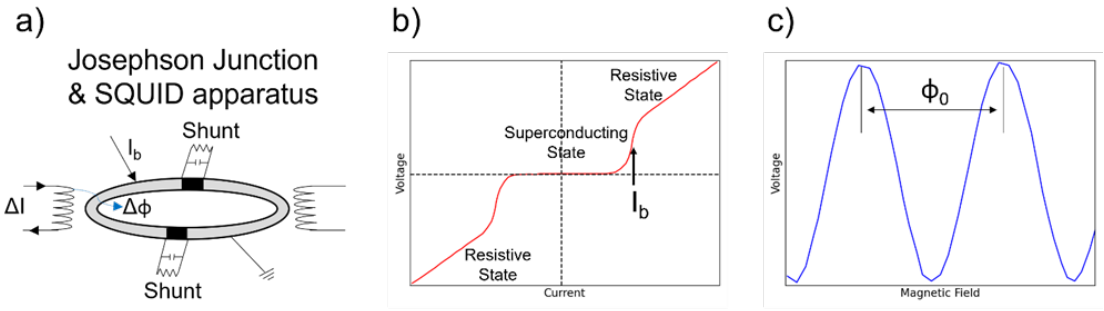

Figure 2.11: (a) Sketch of the SQUID magnetometer core components. A superconducting ring is interrupted by one or more Josephson junctions equipped with shunt resistors in parallel and properly grounded. Input and modulation coils are placed around the ring. (b) Current vs voltage curve of a shunted Josephson tunnel junction measured across the junction. (c) Voltage vs externally applied flux with constant bias current.

remains in its superconducting state. In addition, the level of magnetic flux in the ring cannot be changed in a continuous manner but rather, it is quantized existing only in multiples of $\phi_0 = 2.068$ x 10^{-15} $\frac{Wb}{m^2}$ where 1 $\frac{\mathrm{Wb}}{\mathrm{m}^2}$ = 1 T.

2.2.4.2 SQUID Experimental setup

The properties here presented allow the usage of Josephson junctions to measure extremely small variations of the magnetic field. The sketch of the experimental setup is reported in Fig. 2.11a. A superconducting ring is interrupted by one or more Josephson junctions and properly grounded. Considering the case of dc-SQUID, two bias currents of the same entity I_b are applied to the junctions setting the operational point in the I-V curve close to I_c (Fig. 2.11b) which means nearby the superconducting-resistive transition. To prevent $I - V$ hysteresis shunt resistors are placed [152]. Inductively coupling magnetic flux into the SQUID loop through input coils placed around the ring creates screening currents $I_L = \frac{\phi_L}{L_L}$ that will effectively increase or decrease I_c, depending on the direction of the induced flux. If I_b is slightly greater than I_c when an external magnetic field ($\phi_{ext} = B_{ext}A$, where A is the area considered to calculate the flux) is applied, a voltage drop change is detected in the junction. By increasing or decreasing the external flux a periodic modulation of the voltage is observed with a period related to the quantum of flux ϕ_0 (Fig. 2.11c). In practical implementations of SQUID magnetometry experiments, the sample position is varied through a step motor and its magnetization is measured. Static magnetic fields can be applied to the sample and are not detected by the Josephson junction. The temperature can be also varied through cold finger cryostats. In the most common dc-SQUID *apparati*, the superconducting wires are based on Niobium (Nb) and must be liq-

uid He cooled to ensure the desired performances. These temperature limitations can be overcome by using high-temperature SQUID which can be cryo-cooled with liquid nitrogen at 77 K since are based on type-II superconducting alloys such as cuprates like YBCO ($YBa_2Cu_3O_7$). In this work, the magnetic characterization was performed by acquiring Zero-field cooling (ZFO) - Field cooling (FC) magnetization curves and Hysteresis loops. ZFC-FC studies were performed with a 100 G applied magnetic field and temperatures in the range 5-305 K. Hysteresis loops were collected at room temperature with a magnetic field ranging between 0 and ± 30 kOe(*i.e.*, 30 kG) for the ZFO nanoparticles and between 0 and ± 8 kG for the ZFO films. The SQUID measurements presented in this work have been conducted in collaboration with Dr. M. C. Mozzati.

2.2.5 Optical absorption

The static NIR-Vis-UV optical absorption measurements allow one to characterize the optical behavior of newly synthesized samples. The method is based on the Lambert-Beer law which relates the intensity of the light impinging on a material with the transmitted one as an exponential decay depending on the thickness of the material d and on its absorption properties:

$$I(d) = I_0 e^{-\alpha d} \tag{2.46}$$

where $I(d)$ and I_0 are the transmitted and incident light intensities, respectively while α is the material's absorption coefficient which is dependent on the light energy (wavelength or frequency). To retrieve the absorption properties of a material eq. 2.46 should be inverted, obtaining:

$$-\frac{\ln(I(d)/I_0)}{d} = \alpha \tag{2.47}$$

If the thickness of the sample d is known, one can express the absorption coefficient $\alpha(h\nu)$. Otherwise, the optical density $OD = \alpha(h\nu)d$ is used. A simple sketch showing the essential components of a spectrometer for absorption measurements is reported in Fig. 2.12. Tungsten, halogen and deuterium discharge arc lamps are used as NIR, Vis and UV light sources, respectively. The light produced is passed through a dispersion grating, collimated and sent to a rotating chopper, which generates a reference and a probe beam. The probe beam is sent across the sample in transmission configuration giving $I(d)$ while the reference beam gives the I_0. The probe and reference beams are detected separately by the same detector operating at the double of the chopper rotation frequency. The probe beam is scaled to the reference by the simple ratio $\frac{I(d)}{I_0}$ for every wavelength and the absorption coefficient is extracted by applying eq. 2.47. In real cases, the sample and

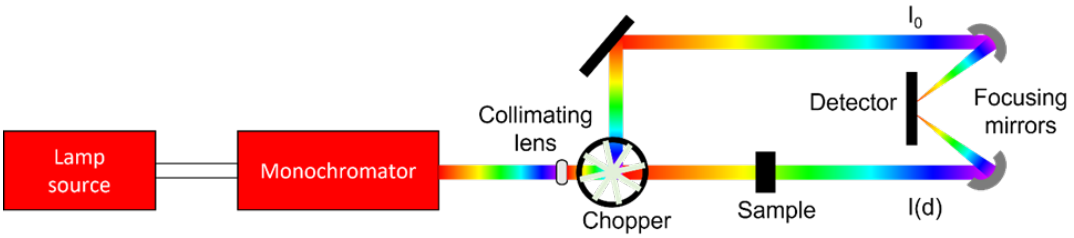

Figure 2.12: Sketch of the absorption spectrometer configuration.

instrumental responses such as the reflection, and wavelength dependence of optical components should be considered. A further "dark" branch is also included to account for the electronic noise. Therefore, both the $I(d)$ and I_0 terms in eq. 2.47, should become $I(d) - I_{dark}$ and $I_0 - I_{dark}$. The absorption measurements shown in this chapter have been conducted thanks to the collaboration with Prof. M. Patrini of the Department of Physics at the University of Pavia.

2.3 Chemical and structural characterization of pure and doped zinc ferrite nanoparticles

The following section is adapted from the articles:

> B. Albini, **S. Restelli**, M. Ambrosetti M. Bini, F. D'Amico, M. C. Mozzati & P. Galinetto "Raman spectroscopy in pure and doped zinc ferrites nanoparticles." *J Mater Sci: Mater Electron* 34, 1030 (2023). My contribution: Data acquisition, Data analysis, Manuscript Revision. Published in Open Access under Creative Commons 4.0 license. `http://creativecommons.org/licenses/by/4.0/`.
>
> **S. Restelli**, B. Albini, S. Bonomi, M. Bini, M.C. Mozzati, P. Galinetto, "Raman study of the laser-induced decomposition of $ZnFe_2O_4$ nanoparticles." *Materials Today Communications* (2023): 106405. My contribution: Data acquisition, Data analysis, Manuscript writing and Corresponding Author. Published in Open Access under Creative Commons CC-BY license. `http://creativecommons.org/licenses/by/4.0/`.

2.3.1 Introduction

In this section, we characterize pure and doped $ZnFe_2O_4$ (ZFO) nanoparticles functional response and stability. We perform a chemical and crystalline quality

assessment through XRD, Scanning Electron Microscopy (SEM) and EPR techniques. We also introduce ZFO nanoparticles Raman response and study their homogeneity. From the Raman mode analysis, we estimate the inversion degree and study its effect on the magnetic behaviour. After this first characterization, we study ZFO stability in air and vacuum atmospheres by local heating through laser irradiation and detecting the Raman mode changes. Within this extensive Raman study, we get access to the structural, vibrational, and chemical properties of zinc ferrite nanoparticles by exploiting the high sensitivity offered by the technique itself. The pure and doped nanoparticles studied are both commercially available (Sigma Aldrich) and synthesized in collaboration with Prof. Marcella Bini's group in the Physical Chemistry department of the University of Pavia. The nanopowder samples employed in this section are: (i) pure zinc ferrite nanoparticles with size $d \approx 6\,\text{nm}$ (ZFO-C) and $d < 100\,\text{nm}$ (Sigma Aldrich commercial sample, ZFO-SA), (ii) zinc ferrite nanoparticles doped with Ga ions at 10 atomic %, with the formula $ZnGa_{0.2}Fe_{1.8}O_4$ (ZGFO), (iii) zinc ferrite nanoparticles doped with Mg ions at 10 atomic %, with the formula $Mg_{0.1}Zn_{0.9}Fe_2O_4$ (MZFO) and (iv) zinc ferrite nanoparticles doped with both Mg and Ga ions at 10 atomic %, with the formula $Mg_{0.1}Zn_{0.9}Ga_{0.2}Fe_{1.8}O_4$ (MZGFO). The nanoparticles were synthesized through the coprecipitation route described in section 2.2.1.1. $Zn(NO_3)_2\ 6\,H_2O$ and $Fe(NO_3)_3\ 9\,H_2O$ were dissolved in 50 ml of water, adjusting the pH value at about 10 with the addition of NaOH 2M; in case of doping, the nitrates ($Mg(NO_3)_2\ 6\,H_2O$ or $Ga(NO_3)_3\ 8\,H_2O$) were added to the starting blend at the beginning of the coprecipitation procedure. The obtained solutions were maintained at 80 °C for about 2 h, cooled down to room temperature, then centrifuged 6000 rpm for 5 min two times with water and ethanol. The products were dried overnight at 80 °C in a muffle and finally treated at 300 °C for about 6 h to decompose the organic component.

2.3.2 Results and Discussion

2.3.2.1 Composition, structural and morphological characterization

$ZnFe_2O_4$ cubic spinel belongs to the $Fd\bar{3}m$ (O_h^7) space group. Its unit cell contains 8 molecules with a total of 56 atoms, while the Bravais cell contains 2 formula units with a total of 14 atoms. The synthesis procedure described in section 2.2.1.1 led to the formation of brownish powders with nanoparticles size of about 6-7 nm. Indeed, the XRPD patterns (Fig. 2.13a) display the typical peaks proper of the $ZnFe_2O_4$ cubic spinel structure (JCPDS card N. 89-7412, franklinite mineral). In Tab. 2.1 we show the main structural parameters obtained by Rietveld refinement. The doping slightly affected the XRPD patterns. Indeed, the lattice parameters are similar, even if slightly lower for the doped samples with respect to ZFO-C.

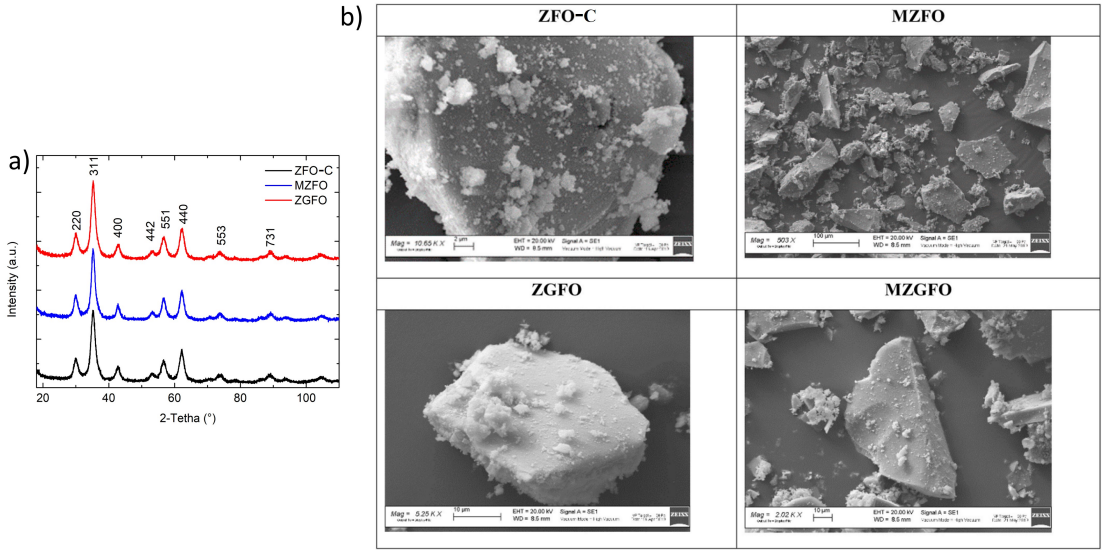

Figure 2.13: (a) XRPD patterns of the investigated samples with the Miller indices of the main reflections. From *Albini et al.* [103]; (b) SEM image of the aggregates of ZFO-C, MZFO, ZGFO and MZGFO nanoparticles. Reproduced with permission from *Gazzola et al.* [35].

	a (Å)	Cry size (nm)	R_{wp} (GoF)
ZFO-C	8.4472 (14)	6.2 (1)	8.03 (1.11)
MZFO	8.4349 (13)	7.2 (1)	7.63 (1.06)
ZGFO	8.4387 (13)	6.3 (1)	7.78 (1.09)

Table 2.1: The main structural parameters obtained from Rietveld refinements, together with the agreement indices R_{wp} and GoF. From *Albini et al.* [103].

This can be due to the differences in the ionic radii of Zn^{2+} (0.6 Å) and Mg^{2+} (0.57 Å) and Fe^{3+} (0.64 Å) and Ga^{3+} (0.62 Å). The refinements are all reliable, as demonstrated by the Goodness of Fit (GoF) values near 1.

In Fig. 2.13b we provide with the SEM images of the nanopowder clusters used in this study, previously published in *Gazzola et al.* [35]. We report the presence of extended blocks in all the samples. These are constituted by aggregates of small spherical nanoparticles as it is often described in literature [153]. From a morphological point of view, we do not appreciate differences between undoped and doped samples.

The ZFO unit cell composition (56 atoms, 2 formula units with 14 atoms) gives 42 modes (3 acoustic and 39 optical). The reduction of the 42-dimensional representation into irreducible representations of the O_h^7 factor group gives $\Gamma = A_{1g} + E_g + 3F_{2g} + 4F_{1u} + 2A_{2u} + 2E_u + 2F_{2u} + F_{1u}$. The Raman active modes

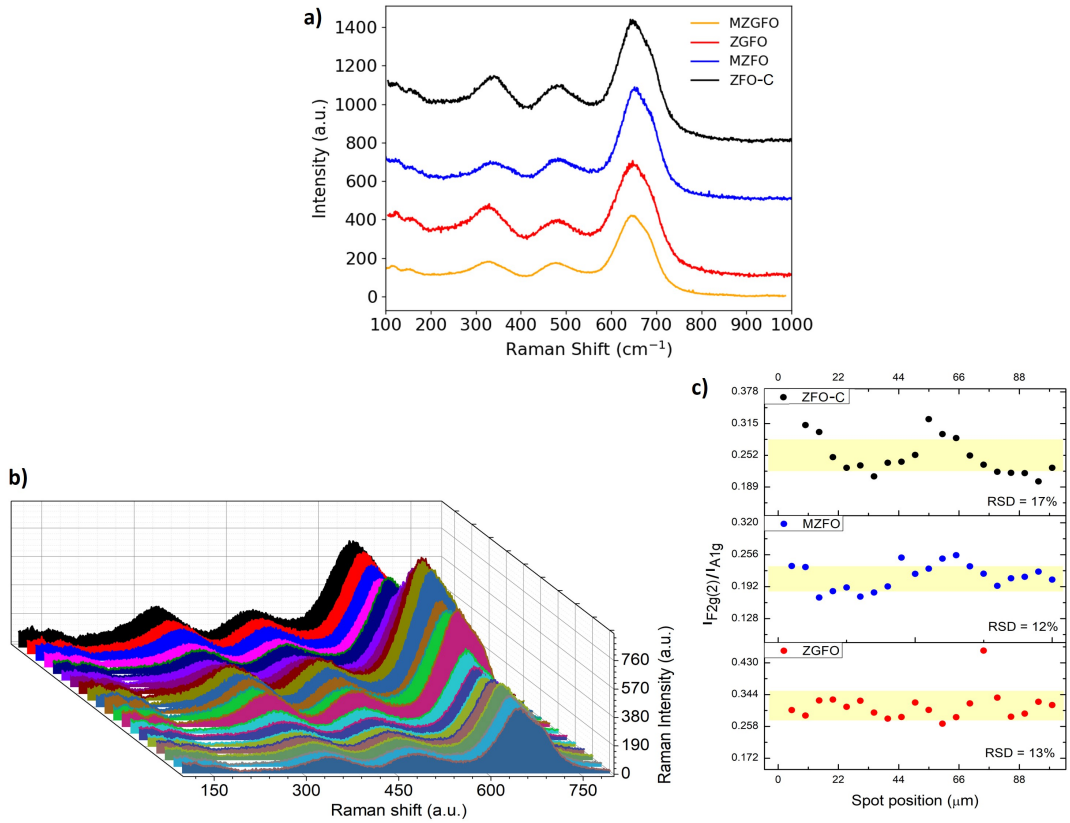

Figure 2.14: (a) Raman spectra of the investigated systems excited with a 638 nm laser wavelength. (b) Raman spectra of the pure sample (ZFO-C) recorded along a single linear scan of 100 μm. (c) Ratio between the intensities of the $F_{2g}(2)$ and A_{1g} modes, reported as a function of the laser spot position for the ZFO-C, MZFO, and ZGFO investigated samples. The value of the standard deviation for each of the investigated samples is reported. Adapted from *Albini et al.* [103]

have A_{1g}, E_g and $3F_{2g}$ symmetries but only the $F_{2g}(2)$, $F_{2g}(3)$ and A_{1g} ones have been considered in the following study since the detection of the two E_g and $F_{2g}(1)$ modes, falling below 300 cm^{-1}, is often difficult possibly because of poor Raman yield [102]. The total symmetric mode A_{1g} generally falls between 570-780 cm^{-1}, the $F_{2g}(3)$ and the $F_{2g}(2)$ at about 450-500 cm^{-1} and 350-400 cm^{-1}, respectively. The spectra of all the investigated samples, collected with a 638 nm laser source, are reported in Fig. 2.14a. As it is possible to observe, they all display the characteristic Raman features of the zinc ferrite spinel, revealing a good structural stability, also upon doping [68]. In particular, the spectra are dominated by the total symmetric A_{1g} mode that falls between 570-780 cm^{-1} while the $F_{2g}(3)$ and the $F_{2g}(2)$ can be found at about 450-500 cm^{-1} and 350-400 cm^{-1},

respectively. According to literature, the A_{1g} mode is associated to the symmetric breathing vibration of the tetrahedron AO_4 unit where the cation is surrounded by four oxygen atoms in the non-adjacent corners [154].

For the lower energy modes, a clearly stated assignment is still missing thus, in some cases, they are associated to the tetrahedral cage [155] and in others to the octahedral one [156]. More accordance is found on the assignment of the lowest energy mode, $F_{2g}(1)$, which is due to the translational motion of the whole AO_4 unit within the spinel structure [68]. By nanostructuring and/or doping the system, the presence of different cations involved in the same vibrational unit entails the broadening of the Raman features and it results in the presence of different contributions for each Raman mode. This behaviour is the so-called two-mode behaviour and it is particularly pronounced for the A_{1g} mode which is the result of the overlap of two different modes for the undoped samples: the vibration of the ZnO_4 tetrahedral unit that produces a signal at about $650\,cm^{-1}$ and the vibration of the FeO_4 one whose signal is generally located at about $690\,cm^{-1}$ [157].

The homogeneity of the zinc ferrite intra-sample was verified by collecting multiple automatic linear acquisition along an area of about $100\,\mu m$ in different portion of the samples as shown in Fig. 2.14b for ZFO-C. Only the Raman signatures of zinc ferrite spinel dominate the spectra, with a variation in the Raman yield due to a slight loss of focus as it generally occurs in an automatic scan. The homogeneity of the ZFO, MZFO and ZGFO samples is better highlighted in Fig. 2.14c, where the ratio between the intensities of the $F_{2g}(2)$ and A_{1g} modes, reported as a function of the laser spot position, points out relative standard deviation (RSD) values between 12 - 17%. We did not perform the same linear scan analysis on the MZGFO sample. However, we sampled the homogeneity of the nanopowders on 15 points in approximately $30\,\mu m$ from which we extracted a mean value of $I(F_{2g}(2))/I(A_{1g}) \simeq 0.18$. The resulting mean spectra and the homogeneity tests possibly demonstrate the purity of the spinel structure confirming XRPD findings.

The room temperature derivative EPR signals present the typical broadened spectra centred around $g \simeq 2.001$ proper of Fe^{3+} ions in paramagnetic nanostructured zinc ferrite at least for the ZFO-C and ZGFO samples (Fig. 2.15a). The MZFO sample is characterized by an EPR signal centred at $g \simeq 2.01$, so not negligibly shifted with respect to the other two samples as seen in the comparison between the room temperature spectra (Fig. 2.15a). In general, this behaviour could be ascribed to the presence of a magnetically ordered extrinsic phase or to a SPM behaviour with Paramagnetic-Superparamagnetic (PM-SPM) transition temperature above RT. We reasonably excluded the first hypothesis in favour of the second one since, by increasing the measuring temperature, the EPR signals of all the investigated samples are characterized by the same single broadened signal, observed at room temperature, without appreciable changing in the

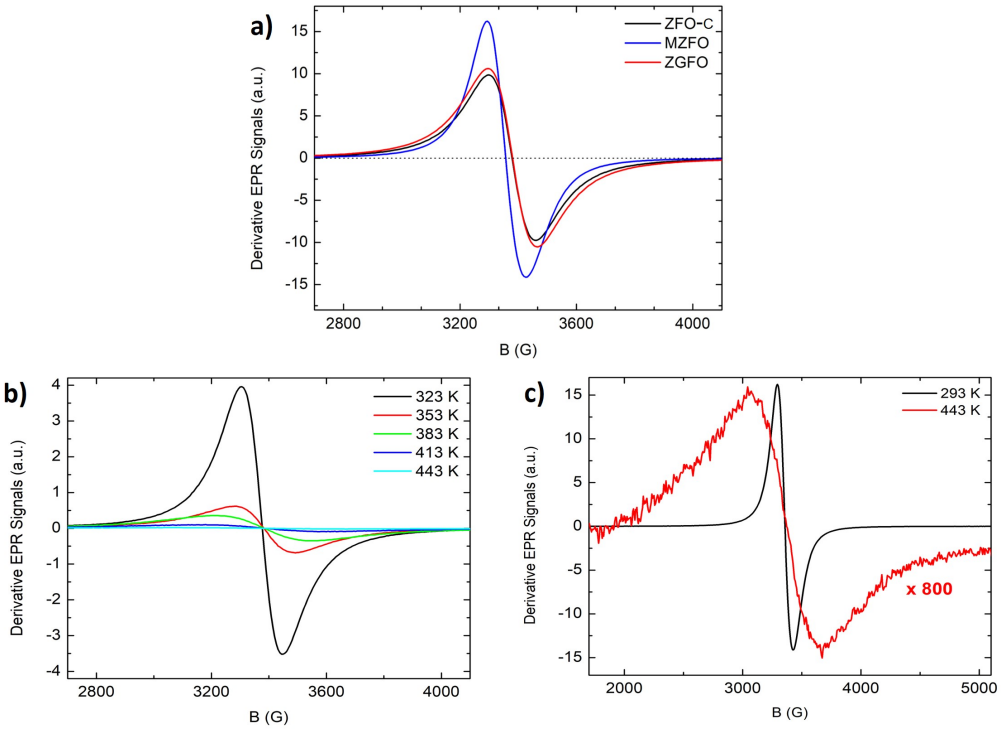

Figure 2.15: (a) Room temperature derivative EPR signals of the investigated samples. (b) Derivative EPR signals collected above room temperature for the MZFO sample; (c) comparison between the EPR signals of the MZFO sample collected at room temperature and at $T = 443\,\mathrm{K}$. From *Albini et al.* [103].

shape (Fig. 2.15b). Moreover, the trend of all the characteristic EPR parameters ($g-$factor, peak to peak linewidth, signal symmetry) is consistent with a ferrite system involved in a PM-SPM transition, as already shown for analogous samples in literature [35]. However, as an explanatory case, Fig. 2.15b reports the EPR signals collected at different temperatures for MZFO sample, while in Fig. 2.15c the comparison between the normalized EPR signals collected at room temperature and at 443 K is reported to highlight the lack of noticeable changes in the signal. This result corroborates the interpretation of the possible absence of other magnetically ordered iron oxides at least within the EPR detection limit [102].

2.3.2.2 Inversion degree estimation through Raman spectroscopy

In view of this and previous experimental evidence, we could reasonably state that our samples are not affected by the presence of other iron oxides, at least within the detection limits of the involved techniques, being EPR the most sensitive one.

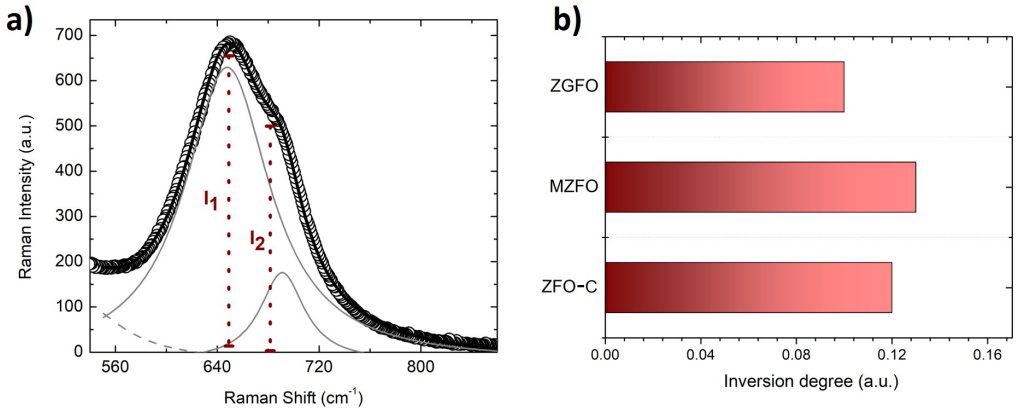

Figure 2.16: (a) Best-fitting procedure performed on the A_{1g} mode for the ZFO-C sample, using two Lorentzian functions (solid grey lines) and a Gaussian one (dashed grey line). The brownish dotted lines highlight the heights of the two principal components of the analysed mode. (b) Inversion degree value calculated with the simplified approach. From *Albini et al.* [103].

Thus, the combination of these techniques could be eligible for an in-depth study on the correlation between the magnetic behaviour and the cationic disorder as derived through the RS inspection. In fact, as previously described, RS allows also to characterize the cationic distribution between the two sublattices by exploiting the pronounced two-mode behaviour of the A_{1g} mode to calculate the inversion degree of the samples through the following formula:

$$i.d. = 1 - \frac{I_{Zn}}{I_{Zn} + I_{Fe}} \tag{2.48}$$

We analysed the A_{1g} mode in the range between 570 cm^{-1} and 750 cm^{-1} of the ZFO-C spectrum collected with the 638 nm source by performing a best-fitting procedure using two overlapping Lorentzian functions and one Gaussian function (Fig. 2.16a), centred out of the investigated range at about 530 cm^{-1}. The two Lorentz functions take into account the presence of two cationic vibration units in the tetrahedral site while the Gaussian peak empirically reproduces the phonon confinement induced by the nanometer dimension of the particles [142, 141]; the static disorder of cations, induced by the inversion, and of anions, due to oxygen vacancies [141]. As it is possible to observe from Fig. 2.16a, the peak is well reproduced by the sum of the three fitting functions. In particular, the first Lorentzian function, centred at 647.8 cm^{-1}, gives the main contribution, while the second one, centred at 691 cm^{-1}, results in a high energy shoulder. The obtained energy values are in good agreement with the ZnO_4 and FeO_4 unit vibrations reported

in literature [68]. The inversion degree was calculated by applying Eq. 2.48 and considering only the integrated intensities of the two Lorentzian functions. The obtained value demonstrates a slight inversion of the pure spinel: $x(Fe)_A = 0.12$.

The addition of dopants together with other elements (grain size, shape, *etc.*) could affect the Raman features. However, in our case with a dopant content of 10%, it seems reasonable to consider the A_{1g} Raman mode as determined by two different kind of vibrating units ZnO_4 and FeO_4, neglecting the other contributions. Indeed, the above-mentioned elements can be considered as perturbing agents in the shape and intensity of the Lorentzian oscillators. With this assumption we can also introduce empirical parameters for the evaluation of the inversion degree of the considered samples through a simplified approach. In particular, we evaluated the inversion degree by using the same formula (eq. 2.48), but instead of using the integrated intensity, we used the heights I_1 and I_2 where the two A_{1g} mode components fall. Since the absolute value of the inversion degree obtained with this procedure could be non-consistent with the value obtained for ZFO-C, we also evaluated the inversion degree of ZFO-C with the simplified procedure in order to normalize the obtained values. The normalization factor was used to rescale to the proper absolute values the inversion degrees of all the doped samples. From the reported data in Fig. 2.16b, it is possible to assert that the doping seems to affect the inversion, even at these low inversion degrees; in particular, the ZGFO sample results slightly less inverted, while the doping performed with the Mg ions induces more inversion in the structure if compared to the behaviour of ZFO-C. This could be consistent with the inverted spinel structure proper of the magnesium ferrite.

2.3.2.3 The inversion degree effect: Magnetic behaviour

The inversion strengthens the magnetic interaction due to the presence of Fe^{3+} on both sites. The value of the inversion degree suggests that our samples are characterized by a slight superparamagnetic behaviour. Nevertheless, it is possible to infer that the Mg doping aids the enhancing of the inversion and thus the superparamagnetic behaviour. Indeed, the EPR inspection highlights the superparamagnetic state of the MZFO sample already at room temperature (through its different $g-$value). The interpretations following the assessment of the inversion degree are supported by the magnetic results. Indeed, the hysteresis cycles recorded at room temperature for the three samples suggest room temperature superparamagnetism, since the following typical features of a superparamagnetic behaviour could be found (Fig. 2.17a): (i) negligible values of coercive field ($< 10\,\mathrm{G}$) and (ii) remanence magnetization without a full saturation even at the highest applied magnetic fields, typical for nanoparticles of this kind of materials.

All the samples show the S-type shape characteristic of a superparamagnetic behaviour. In particular, the MZFO is more pronounced compatibly with a higher

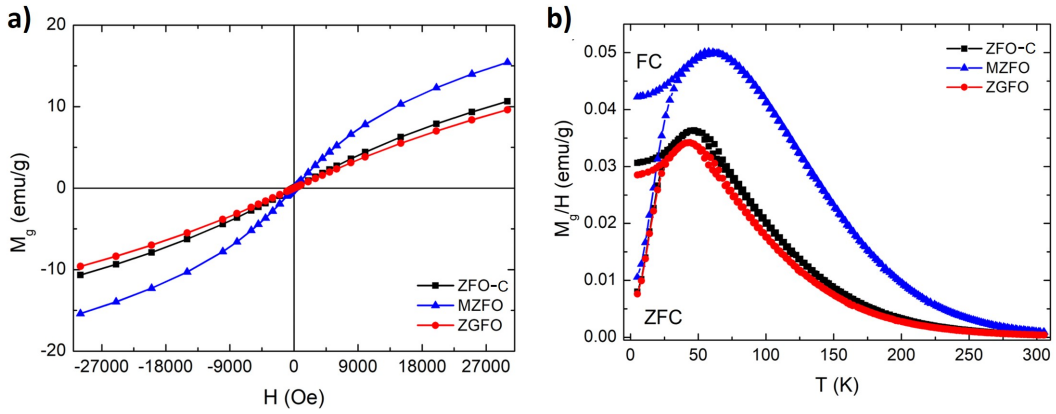

Figure 2.17: (a) Room temperature hysteresis cycles of ZFO-C, MZFO and ZGFO samples. (b) The relative ZFC and FC M vs T curves at 100 G (= 100 Oe). From *Albini et al.* [103].

inversion degree. Considering the obtained experimental evidence, we could state that the less marked S-type shape of the ZGFO hysteresis loop at room temperature could be ascribed to the effect of the performed doping. Indeed, the Ga ions substitute the Fe ones, consequently the sample has less magnetic iron centres, so the magnetic interactions could be interrupted by the presence of the dopant. Furthermore, Ga substitution tends to prevent the structural disorder of the spinel which is consistent with the lower inversion degree value estimated with Raman inspection. The temperature dependence of the magnetization (Fig. 2.17b) allows to validate even more the relationship between magnetic properties and the degree of inversion of the spinel structure. Indeed, the trend of the calculated inversion degree with the more simplified approach well matches the trend of the spin blocking temperatures T_B. To define the blocking temperature let's consider a nanoparticle with dimension d [158]. We can imagine the magnetization M of the nanoparticle as randomly oriented in absence of an external magnetic field. The interaction of a single particle with thermal energy can cause the flip of the direction of M in time. The average time for a magnetization flip is expressed with the relaxation time formula:

$$\tau = \tau_0 exp(\frac{\Delta E}{k_B T}) \tag{2.49}$$

where τ_0 is the characteristic of the probed material, ΔE is the energy barrier for the magnetization flip and $k_B T$ is the thermal energy. In real cases, we have to consider a magnetization measurement time τ_m typical of each experimental setup. Therefore, we find two extremal scenarios at play: (i) $\tau >> \tau_m$ or Blocked state and (ii) $\tau << \tau_m$ or Superparamagnetic state. If $\tau >> \tau_m$ the measurement is too

fast to observe a random flip. In this case we can consider M direction as fixed and the particles are considered as blocked. Instead, if $\tau << \tau_m$, M is continuously flipping during the measurement and the net magnetization will be zero. The two conditions can both be reached by acting on τ_m, for example, by using different setups or configurations or by fixing τ_m and acting on τ by decreasing the thermal energy *i.e.*, decreasing the temperature T. The temperature at which $\tau = \tau_m$ is T_B. It is detected as a maximum in the M value, and is theoretically expressed as:

$$T_B = \frac{\Delta E}{k_B ln(\frac{\tau_m}{\tau})} \tag{2.50}$$

The higher the inversion is, the higher the T_B value is, consistent with the fact that the cationic disorder within the two sublattices strengthens the magnetic interactions and, in turn, the transition to an ordered blocked state occurs at higher temperatures. This is in accordance with the observations in Fig. 2.17b which shows that T_B for the MZFO and ZGFO samples are respectively higher and lower than T_B of ZFO-C. The magnetic data corroborate the reasoning used to estimate the inversion degree of the spinel. Moreover, this correlation between the inversion degree and the blocking temperature has been also observed in the previously investigated samples, namely zinc ferrites characterized by Ca or Sr substitutions on the A site and Al or Gd on the B one. The results reported in *Gazzola et al.* [35], *Galinetto et al.* [68], and *Bini et al.* [34] shows this correlation except for the Sr doped sample which also presented a (Sr(NO3)2) impurity.

2.3.2.4 Photo-thermal stability of ZFO nanoparticles in different atmospheres.

From the analysis reported so far, $ZnFe_2O_4$ nanoparticles purity and properties were addressed in ambient atmosphere and at RT. However, the possible operative conditions arising in the applications may concern also different atmospheres in which the sample is applied. Therefore, we need to verify the chemical and structural stability at variance with the composition of the atmospheres and laser irradiation. The results of this study are reported in the following. Firstly, we studied the samples by performing thermal cycles in different areas of each sample in ambient atmosphere. These were performed by acquring the Raman signal with increasing incident power from 0.5 mW to 5 mW over an area of $4\,\mu m^2$. The ZFO-C and MZFO samples display the same characteristic Raman features of the zinc ferrite spinel before and after the thermal treatment, while the ZGFO one shows different response in two different investigated areas. In fact, Fig. 2.18b shows that a partial irreversible transition under thermal treatment occurs in some regions of the sample. We report the growth of four new peaks centred at $225\,cm^{-1}$, $299\,cm^{-1}$,

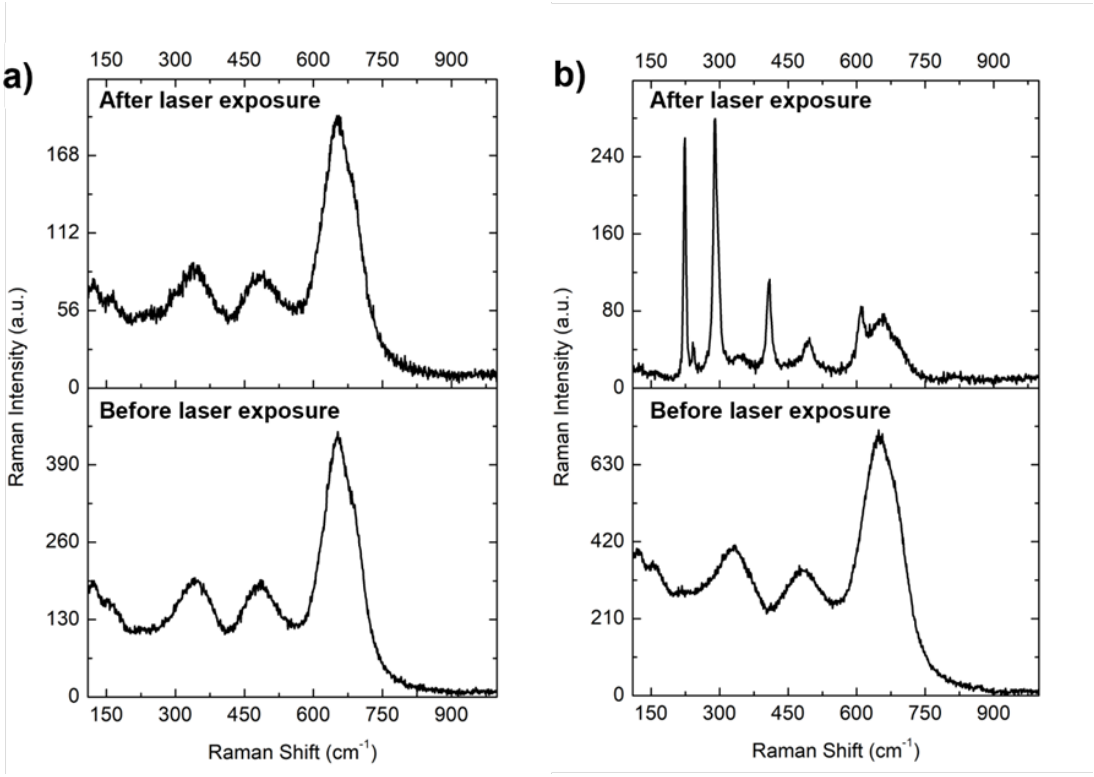

Figure 2.18: Laser induced thermal effect on Raman spectra of ZGFO sample. The reported room temperature Raman spectra were collected at the beginning (lower figures) and at the end (upper figures) of the thermal cycle with a 2.5×10^6 W/cm^2 incident power density, in two different regions of the sample displaying both (a) thermal stability and (b) a transition to hematite. From *Albini et al.* [103].

412 cm^{-1}, and 613 cm^{-1} characteristic of the hematite (α-Fe_2O_3) which displays trigonal symmetry in the $R3c$ space group and is the most stable iron oxide at normal ambient conditions [159, 160]. The growth of the α-Fe_2O_3 could have two possible sources, namely (i) the presence of maghemite or magnetite clusters [161] or (ii) the presence of a highly defective external shell in the ZFO nanoparticles surface [159].

To deepen the investigation on this last point *i.e.*, the chemical/structural composition gradient of the nanoparticles, we performed Raman measurements by varying the incident laser wavelength and, in turn, the penetration depth of the probe itself [102]. In Fig. 2.19a, the comparison between the Raman spectra of ZFO-C sample collected with 266 nm, 532 nm, 633 nm and 785 nm light is reported in the range between 100 cm^{-1} and 800 cm^{-1}, where the first order Raman signal of zinc ferrite nanoparticles can be observed. For the purposes of our investigation, we focused on the modifications occurring on the A_{1g} mode. Indeed,

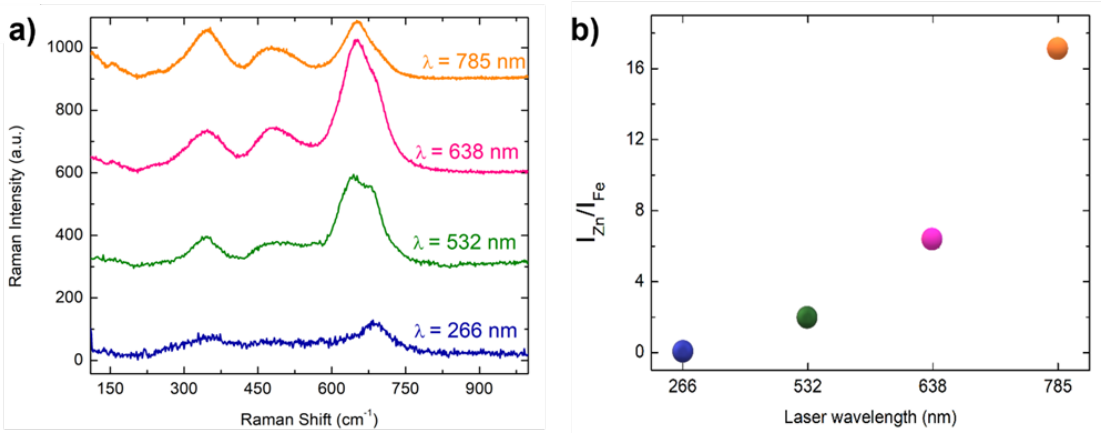

Figure 2.19: (a) Comparison between the ZFO-C Raman spectra collected with 266 nm, 532 nm, 633 nm and 785 nm laser wavelengths. (b) Ratio I_{Zn}/I_{Fe} of the integrated intensities of the two Lorentzian functions used to perform the fit on the A_{1g} mode as a function of the incident wavelengths. From *Albini et al.* [103].

despite the difference in the intensity yield caused by the different power density values and by the different scattering volumes, the latter is observed in each of the reported spectra. However, other differences can be noticed. For example, for 785 nm excitation wavelength, the two $F_{2g}(2)$ and $F_{2g}(3)$ modes have almost the same Raman yield, while in the UV Raman spectrum, these low frequency modes are hardly noticeable. We now focus on the A_{1g} mode. By decreasing the wavelength of the incident laser source, one can easily notice a progressive increase of the component pertinent to the FeO_4 vibration in the tetrahedral unit and a corresponding lowering of the ZnO_4 component till its complete disappearance in the UV Raman spectrum. This simple observation is corroborated by the results obtained from the best-fitting procedure performed on the investigated mode and from the integrated intensity ratio (I_{Zn}/I_{Fe}) of the two components reported in Fig. 2.19b.

For the UV Raman spectrum, a single Lorentzian curve fit was performed with peak at 687.2 cm^{-1}. This is because of the disappearance of the component pertinent to the ZnO_4 vibration. The fact that the Lorentzian curve peak is centred well below 700 cm^{-1}, namely where the maghemite mode should occur [161], could again support the hypothesis of a different cationic distribution from the stoichiometry ($Zn_xFe_{2-x}O_4$) in the external shell of the ZFO nanoparticles, characterized by a deficiency in Zn cations. This is consistent with the fact that, with the more energetic incident source (266 nm *i.e.*, 4.66 eV), we are sensitive to a very thin outer thickness of the ZFO nanoparticles [102]. However, a $Zn-$deficient shell is not the only possible mechanism for the UV Raman response observed. In fact,

266 nm (4.66 eV) radiation is resonant with an intersite charge transfer from O^{2-} $2p$ to Fe^{3+} $4s$ in the tetrahedral site [107]. Therefore, we should consider a resonant Raman scattering process in the presence of inversion which would lead to an increased $Fe-O$ vibrational response. Our interpretation does not exclude this phenomenon but finds stronger evidence for the presence of a $Zn-$deficient shell because: (i) the EPR inspection on the as synthesized particles ruled out the presence of magnetically ordered extrinsic iron oxides and (ii) we observed a transition to hematite consequent to the irradiation process.

After the stability evaluation in air atmosphere and ambient pressure, a study of the behavior of ZFO nanoparticles upon in-vacuum irradiation was performed. Fig. 2.20a shows the typical Raman spectrum of ZFO-SA sample recorded in air. The 340 cm^{-1}, 488 cm^{-1} and 644 cm^{-1} peaks are respectively assigned to $F_{2g}(2)$, $F_{2g}(3)$ and A_{1g} modes typical of ZFO and the two mode behaviour is detected in the A_{1g} mode. After the in-vacuum irradiation, a change in the Raman spectral features is observed (Fig. 2.20b). The best fit procedure indicates three main modes at 303 cm^{-1}, 532 cm^{-1} and 665 cm^{-1} which are typical of spinel Fe_3O_4(magnetite) and therefore are assigned to its E_g, F_{2g}, and A_{1g} modes, respectively [160]. The presence of iron oxide after the irradiation of $ZnFe_2O_4$ has been further evaluated by comparing the obtained Raman spectrum with several literature studies of magnetite both in nanoparticle and bulk form and also by comparison with spectra from the RRUFF database [109, 160, 162]. The in-vacuum irradiated sample has been irradiated again in air and another change of the spectral features has been observed, as reported in Fig. 2.20c. The signal shows 7 vibrational modes at 224 cm^{-1}, 242 cm^{-1}, 290 cm^{-1}, 407 cm^{-1}, 492 cm^{-1}, 609 cm^{-1} and 655 cm^{-1} all assigned to α-Fe_2O_3 (hematite) [159, 160]. It is important to underline that such kind of transformation is not observed when the ZFO-SA sample is simply irradiated in air. In this latter case, the ZFO Raman fingerprints are maintained without any appreciable change. This is valid for all the investigated samples, except for ZGFO, confirming good thermal stability, at least in the temperature range achievable by laser irradiation.

In Figs. 2.21a,b the comparison between the spectra of pure ZFO-SA and ZFO-C samples before and after in-vacuum irradiation at 5 mW is shown. The strong difference between the spectra suggests that most of the irradiated region has undergone a chemical transformation from $ZnFe_2O_4$ to Fe_3O_4, independently from the dimension of the powders and the synthesis. Instead, in Fig. 2.21c the Raman spectra before and after irradiation (30 min, 3×10^{-6} mbar, 5 mW) of the MZGFO sample are plotted. Only slight changes between the two spectra are observed with a weak redshift of the peak for the A_{1g} mode of the irradiated sample and even weaker changes for the low energy modes. Fig. 2.21d shows the signals of the ZFO-SA sample collected with a home-made optical chamber with vacuum level around

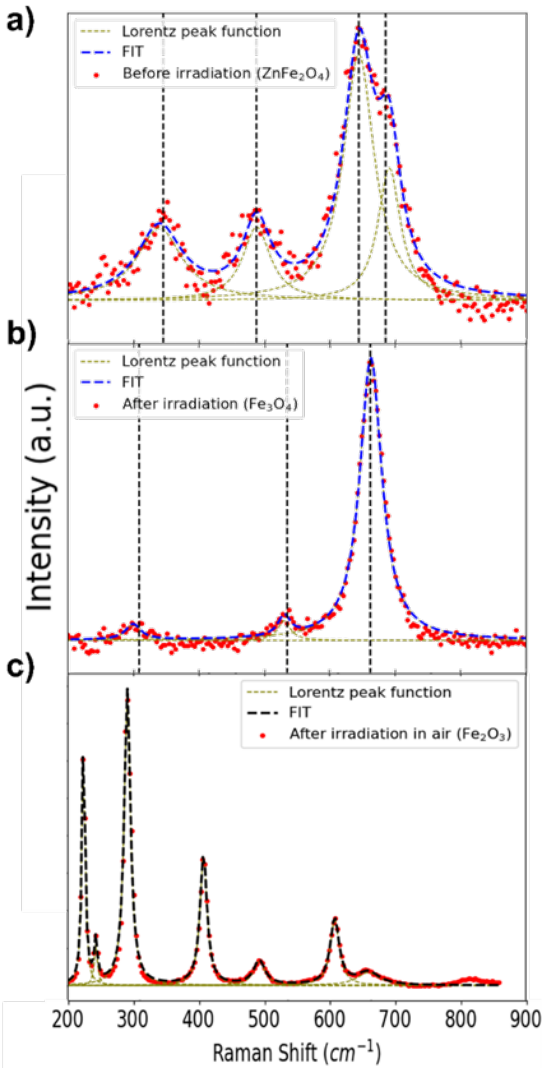

Figure 2.20: Raman mode analysis through Lorentzian fitting. Raman spectra collected in air of ZFO-SA sample a) before the irradiation, b) after irradiation in vacuum and c) after re-irradiation in air. The blue and green dashed lines correspond to the best fit functions and the Lorentzian components chosen for the fitting procedures in both cases, respectively. The black dashed lines correspond to the centroid of each peak and show strong differences between the samples before and after irradiation. In c) the black and green dashed lines correspond to the best fit function and the 7 Lorentzian components chosen for the fitting procedure. From *Restelli et al.* [33].

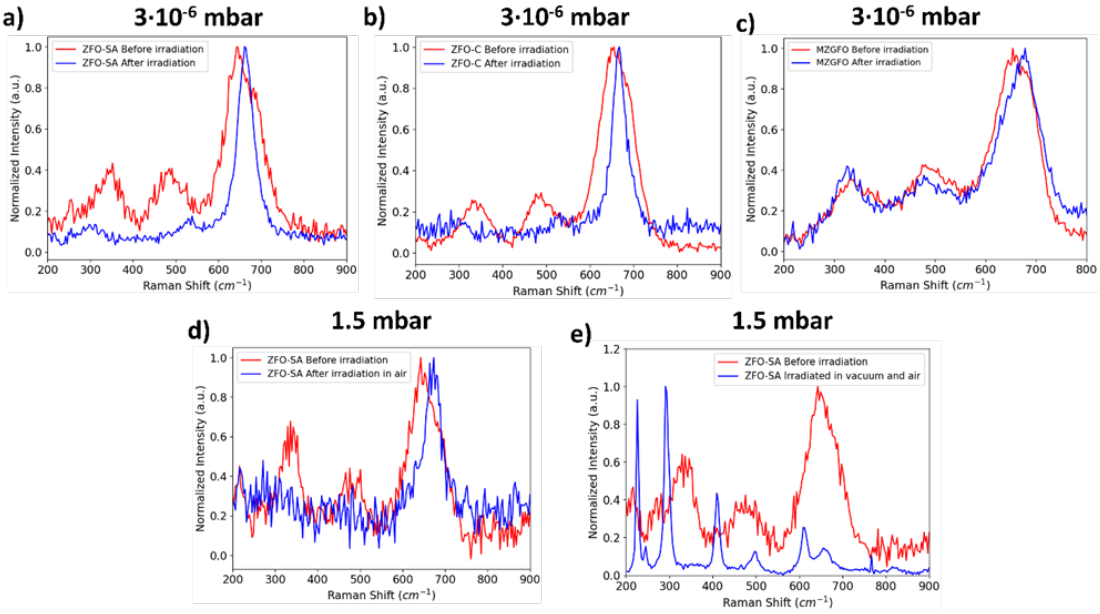

Figure 2.21: Raman spectra of different samples before and after in-vacuum irradiation. Comparison of Raman spectra of a) ZFO-SA and b) ZFO-C samples before and after irradiation at 3×10^{-6} mbar. (c) Comparison of Raman spectra of the MZGFO sample before and after irradiation at 3×10^{-6} mbar. (d) Comparison of Raman spectra of ZFO-SA before and after irradiation with a vacuum level of 1.5 mbar. (e) Comparison of Raman spectra of ZFO-SA before and after in-vacuum (1.5 mbar) and in-air irradiation at 5 mW. The spectra have been normalized for their maximum value to allow for visual comparison and an adjacent average of 3 points has been applied to decrease the noise level. From *Restelli et al.* [33].

1.5 mbar. The difference between the spectra of the sample before and after in-vacuum irradiation suggests that low vacuum levels are sufficient to obtain the Zn sublimation in the irradiated region. After the in-vacuum irradiation, the sample was also irradiated in the air with 5 mW laser power to trigger the transformation in hematite as shown in Fig. 2.21e.

Figs. 2.22a,b show the Raman spectra of MZGFO sample collected in air before and after the in-vacuum irradiation at 5 mW for 30 minutes fitted with 4 Lorentzian lineshapes. The A_{1g} peak areas for both $Zn-$ and $Fe-$cations are reported in Fig. 2.22c: a strong decrease of the ZnO_4 normal mode after the in-vacuum irradiation accompanied by the enhancement of the FeO_4 one is reported.

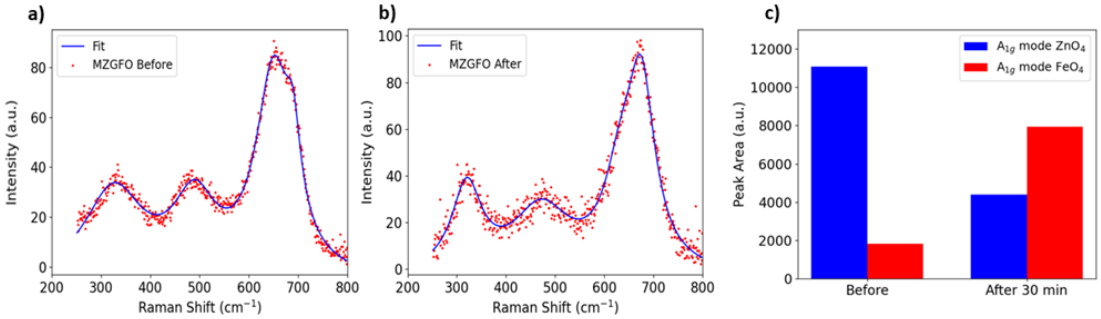

Figure 2.22: MZGFO Raman mode analysis. MZGFO Raman spectra collected in air a) before the irradiation and b) after the in-vacuum irradiation. The Lorentzian fit is reported in blue. c) The peak area of the components of the A_{1g} mode of the sample before and after the irradiation. From *Restelli et al.* [33].

2.3.2.5 Temperature calculation from Stokes and anti-Stokes measurements.

To give an estimation of the temperature reached in ZFO samples during the irradiation processes, we performed a Raman temperature analysis based on Boltzmann statistics on the ZFO-SA sample. The resulting spectrum taken in air is shown in Fig. 2.23. The ratio of the intensities between anti-Stokes and Stokes peaks of the Raman spectrum (see Fig. 2.23) is related to the temperature with the following formula:

$$\frac{I_{AS}}{I_S} = \left(\frac{E_R + E_S}{E_R - E_S}\right)^3 e^{-\frac{E_S}{K_B T}} \tag{2.51}$$

Where the AS, S and R subscripts indicate quantities associated with anti-Stokes, Stokes and Rayleigh peaks. I indicates the intensity of the mode while E is the energy expressed in in eV. K_B and T represent the Boltzmann's constant and Temperature, expressed respectively in eV/K and K. We used the F_{2g} Raman mode at around $330\,\mathrm{cm}^{-1}$ as the spectral band whose intensity in anti-Stokes and Stokes region allows the estimation of the temperature reached in the scattering volume, according to the eq. 2.51. The calculated temperature of the system irradiated with 3.2 mW laser power is $T \simeq 870\,\mathrm{K}$. The experiment was performed using a 532 nm (2.33 eV) excitation wavelength which is slightly above the bandgap reported in literature for nano- and micro-structured Zinc Ferrites ($E_g \simeq 2\,\mathrm{eV}$) but does not lie on a strong absorption region [110, 111]. Therefore, the estimated temperature represents an upper limit with respect to the aforementioned experiments performed using a 632.8 nm light as excitation.

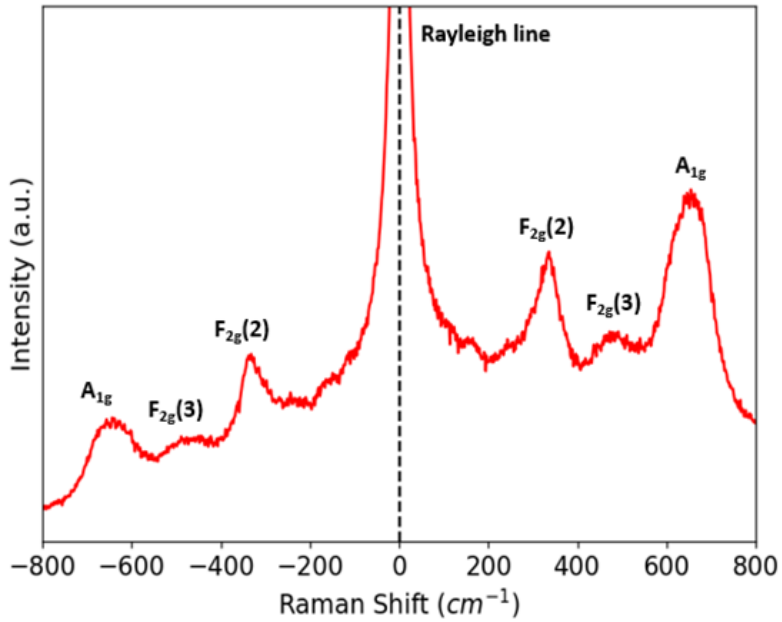

Figure 2.23: Stokes and anti-Stokes modes of ZFO-SA sample. The symmetries of each peak and the Rayleigh are indicated. From *Restelli et al.* [33].

2.3.2.6 Photo-degradation mechanism in ZFO pure and doped nanoparticles.

Focusing on the spectral changes induced in ZFO-SA and ZFO-C by the irradiation in vacuum, there is possible evidence that the 644 cm^{-1} peak disappears and the 690 cm^{-1} one shifts towards lower Raman shift values giving rise to magnetite Raman spectrum (Figs. 2.20a,b and Figs. 2.21a,b,d). Literature results for starting decomposition temperature obtained by *Kaneko et al.* [23] (1500 K) with a solar irradiation experiment in inert Ar atmosphere and by *Kuciakowski et al.* [30] (1273 K) in low vacuum (5 mbar) with nonstoichiometric ZFO samples suggest that the composition of the atmosphere and the pressure level reached in the irradiation or heating chamber play an extremely important role in the degradation of ZFO-SA and ZFO-C into Fe_3O_4. The degradation is compatible with the following chemical reaction [23, 30, 31]:

$$ZnFe_2O_4(s) + Thermal\,energy \rightarrow Fe_3O_4(s) + Zn(g) + O_2(g) \tag{2.52}$$

where (s) and (g) stand for "solid" and "gas" phases, respectively. A possible interpretation of our finding is: $Zn-$cations and a partial amount of $O-$anions undergo sublimation because of the local heating caused by the thermal energy transferred by the irradiation. The vacuum system carries the sublimated Zn and

O outside the chamber. Then, the irradiated powders chemically reorganize into magnetite with the tetrahedral and octahedral spinel sites occupied by Fe^{2+} and Fe^{3+} respectively. These transformations are completed (*i.e.*, only the magnetite Raman signals are detected) in a time period of the order of hundreds of seconds. In addition, the transformations seem to be independent, at least at these irradiation powers and vacuum conditions, from the grain size. This is because they happen in samples with both smaller (ZFO-C) and larger (ZFO-SA) dimensions. For ZFO-SA the Raman yield obtained in the magnetite is approximately equal to that observed in native zinc ferrite spinel structure while for ZFO-C it is about half. This is possibly due to the different starting grain sizes. The transformation is achieved with possibly a higher degree of disorder or amorphization when it is induced in smaller nanoparticles. When both samples are further irradiated in air at higher light intensities hematite *i.e.*, the most stable iron oxide, is easily established as expected.

Furthermore, from the analyses of the hematite linewidth of the A_{1g} mode at around $220\,cm^{-1}$ we obtain values for both samples of about $5\,cm^{-1}$ which is a typical value for particle sizes of the order of 100 nm [163]. This observation points out that the decomposition and subsequent magnetite polycrystalline formation happened with an appreciable increase in the starting grain size only for starting nanoparticles size of the order of 6 nm in agreement with what was reported by *Kuciakowski et al.* [30] based on XANES, EXAFS and Mossbauer data and obtained on different $Zn_xFe_{3-x}O_4$ samples having an average grain size around 3-6 nm. However, it is important to underline that we observed similar behavior by a photo-thermal treatment with a local temperature markedly lower with respect to the annealing temperature used in literature [23, 30]. Thus, it is plausible to suppose that a synergistic effect between temperature increase and a sizeable amount of photo-induced carriers is favoring the Zn depletion and ZFO transformation in accordance with *Ricci et al.* [164]. When pure ZFO is irradiated by red laser light with a power density of about $125\,mW/m^2$ ($12.5\,kW/cm^2$) the chemical decomposition takes place regardless of the grain size and even at low vacuum levels (1.5 mbar).

A completely different behavior has been observed substituting Mg for Zn and Ga for Fe, keeping the same grain size (MZGFO sample) [35]. The MZGFO sample was investigated because of the need to alter both A and B site occupancies and the possibility to do this with biocompatible ions like Mg and Ga, an important aspect in view of possible applications for photocatalysis and hyperthermia. The co-doping may alter fundamental properties. According to the literature for $Mg-$doped ZFO, a slight decrease in the bandgap of the material is expected [165]. Inverse behaviour is expected for Ga doped samples [166], therefore, we should expect negligible variation in the bandgap for the co-doped sample. Since the irradi-

ation at 632 nm (1.96 eV) is again around the bandgap, photoinduced degradation of the sample should not significantly vary. Instead, the spectra before and after vacuum irradiation (see Fig. 2.21d) are slightly varied without the indication of a net transformation to magnetite observed for ZFO-SA and ZFO-C. We can better appreciate the differences by interpolating the spectra by the usual superposition of Lorentzian curves (Figures 2.22a,b). Considering two-mode behavior on the A_{1g} mode it is possible to derive the relative weight for the two components [68]. The results (Fig. 2.21c) indicate an increased inversion degree after vacuum irradiation, but the whole zinc ferrite spinel structure is maintained. This marked stability versus laser irradiation in vacuum has been verified also for prolonged irradiation times (20 h). At this doping level (*i.e.* $\simeq 10\%$) and considering the nanometric regime *i.e.*, a partially inverted spinel structure, the substitution on both octahedral and tetrahedral sites could act as protecting agent for Zn depletion from the shell of the nanoparticles. This result could be also related to a non-homogenous distribution of Zn in the nanoparticle as already studied in [32, 159]. Because of the aforementioned mechanism, the lack of transformation should be a generic effect if the Zn ions are substituted in both tetrahedral and octahedral sites. Further studies are in progress to completely address this latter hypothesis. However, the obtained results are quite promising in highlighting the role of chemical doping of zinc ferrite to improve its chemical and structure stability, a crucial parameter for applications in different environments.

2.3.3 ZFO nanoparticles characterization: Conclusions

In this section, we used pure and $Ga/Mg/MgGa$ doped zinc ferrite nanoparticles synthesised by coprecipitation route and commercially available to highlight the potentiality of Raman spectroscopy as a fast and sensitive analytical tool in studying functional parameters in transition metal oxides. We focused particularly on the correlation between structural and magnetic properties and on the chemical transformations of $ZnFe_2O_4$ nanoparticles following irradiation in high (3×10^{-6} mbar) and low (1.5 mbar) vacuum environments at variance with dimension and doping. The Raman probe allowed us to evaluate the homogeneity of the samples at the micrometer scale. In this regard, we are likely to exclude the presence of extrinsic iron oxides in favour of a highly defective external shell of the nanoparticles. This hypothesis is corroborated by the measurements performed by varying the incident laser wavelength and thus by varying the probed investigated volume. Moreover, we applied a simplified approach to estimate the inversion degree that allowed us to predict the magnetic behaviour trend in the studied samples. Furthermore, we have found clear indications of the onset of magnetite following the in-vacuum irradiation as obtained from Raman mode analyses performed on pre- and post-irradiation spectra. Moreover, the subsequent trans-

formation to hematite of the magnetite product in air confirms the strong changes generated by the irradiation treatment. The results on the pure samples here shown could be interpreted through the sublimation of Zn inside the structure and the reorganization of the $Fe-$cations and $O-$anions in spinel iron oxide (magnetite) thanks to the presence of a highly reducing atmosphere. The re-irradiation in air of spinel iron oxides then produces Fe_2O_3 because, this latter, is the most stable iron oxide compound in normal conditions of temperature and pressure. Furthermore, we have found that the chemical transformation is partially suppressed by doping the structure substituting Zn^{2+} and Fe^{3+} with different metal cations such as Mg and Ga. This behavior is again interpreted with the effect of Mg and Ga co-doping which blocks the depletion of $Zn-$ions therefore maintaining a Spinel ferrite structure. The chemical degradation here reported allows for a better understanding of working conditions of $ZnFe_2O_4$ nanoparticles in different environments such as inert (*e.g.*, *Ar*-enriched) and Reactive (*e.g.*, N_2-enriched) atmospheres. All the Raman evidence on the sample characterization was supported and endorsed by the results obtained by XRPD, EPR and magnetic measurements. In view of the fulfilling results obtained in the presented study, the interesting functional properties of nanosized zinc ferrites as well as the intriguing overlapping between the RS characteristics and the properties of these compounds, we can investigate the functional response of ZFO on thin films deposited through RF magnetron sputtering as reported in the following.

2.4 Synthesis and characterization of $ZnFe_2O_4$ thin films from nanopowder precursors.

In this section, the synthesis and characterization of $ZnFe_2O_4$ thin films from nanoparticles is presented. Firstly, the synthesis parameters and post synthesis procedure are presented. Then the XRD, and Raman characterization of the films is carried out at variance with annealing temperature to assess their chemical composition and crystalline quality. The structural results are a starting point for the full optical and magnetic characterization that shall be shown in the final sections.

2.4.1 Synthesis parameters and thickness determination

The $ZnFe_2O_4$ thin films were synthesized through RF magnetron sputtering (see section 2.2.1.2 for details) using commercial ZFO nanopowders (Sigma Aldrich) as a target without any pre-treatment. This is possibly the first time that ZFO films are synthesized without any high-pressure or sintering treatment of the precursors.

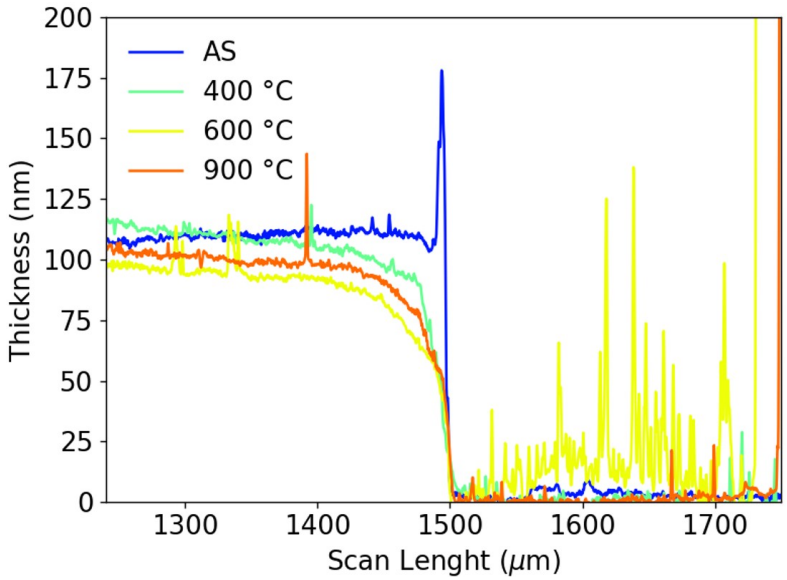

Figure 2.24: Profilometry thickness measurements of the ZFO samples for 4 selected annealing temperatures. A horizontal offset was added to the As synthesized profile to match the edge region of the other samples. A vertical offset was introduced to scale the profiles such that the scan length $> 1500\,\mu$m part is set to zero for simplicity in thickness determination.

The starting dimension of the powders is $d < 100\,$nm, 0.8 g of which were put in the cathode to be used as targets. Two sets of films were synthesized with an RF power of 50 W: (i) 4 hours sputtered and (ii) 2.5 hours sputtered. The starting atmosphere was about $1 \times 10^{-2}\,$mbar of pure Ar. Amorphous quartz (NanoQuartzWafer) was chosen as the substrate and it was fixed at 5 cm from the cathode on a rotating plate with a frequency of about 5 Hz. The sputtering plasma presented a white-violet color during the whole deposition time. Before the beginning of the deposition, a tape stripe was stuck on the substrate surface covering about 20% of the total sample area. Once the deposition procedure was over, the tape was removed to create a film-substrate edge which was used to determine the ZFO layer thickness through profilometry measurements. A post-synthesis annealing was performed. The 4 hours sputtered samples were annealed at 200 °C, 400 °C, 600 °C and 900 °C for 30 minutes. The 2.5 hours sputtered samples were annealed at 600 °C for 30 minutes and at 900 °C for 60 minutes. The complete set of investigated samples with related post-processing treatment is reported in Tab. 2.2.

The profilometry results are reported in Fig. 2.24 for the As Synthesized sample (AS, blue spectrum) and 400 °C (light green), 600 °C (yellow) and 900 °C (orange red) samples. The profiles are vertically shifted such that the substrate level (scan

Sample name	sputtering time	post-synthesis annealing
As Synthesised (AS)	4 h	no treatment
200 °C	4 h	200 °C - 30 min
400 °C	4 h	400 °C - 30 min
600 °C	4 h	600 °C - 30 min
900 °C	4 h	900 °C - 30 min
400-600-900 °C	4 h	400-600-900 °C - 30 min
2.5 h-AS	2.5 h	no treatment
2.5 h-600 °C	2.5 h	600 °C - 30 min
2.5 h-900 °C	2.5 h	900 °C - 60 min

Table 2.2: List of the samples employed in this work. The sputtering time and post-synthesis annealing are indicated

length > 1500 μm in Fig. 2.24) is set to zero for clarity in thickness measurements. The overall film thickness was estimated to be about 100-120 nm by computing the difference between the mean thickness value before 1500 μm scan length and 0. The thermal treatment has minor effects on the profile decreasing and smoothing the sample-substrate interface. In the 600 °C film, spurious components above 1500 μm scan length possibly due to dust or impurities are noticed.

2.4.2 Characterization of ZFO thin films

2.4.2.1 XRD

Fig. 2.25a shows the XRD patterns of the ZFO 200 °C, 400 °C, 900 °C, and 400-600-900 °C films compared with the ZFO Sigma Aldrich (SA) nanopowders. These patterns are obtained by subtracting the quartz and amorphous silicon background reported in Fig. 2.25b from the raw data and then applying a 6^{th}-grade polynomial (spline) subtraction to remove the features of other amorphous components. The sample patterns are compared with the nanopowder precursors (red curve). The lattice planes were assigned according to other literature studies [106, 167] and databases (*e.g.*, RRUFF ID: R070137.1) [162]. The AS sample (not shown) and similarly the 200 °C one (blue curve) do not show any diffraction peak in the considered range. By increasing the annealing temperature to 400 °C (cyan curve), the appearance of the (311) peak is noticed. If the annealing temperature is increased to 900 °C (yellow curve), the (200) and the (440) peaks appear along with the (311) one. In addition, the XRD pattern of the consecutively heated film at 400 °C, 600 °C and 900 °C (400-600-900 °C, orange curve) is reported. This sample shows again the three main (311), (200) and (440) features with increased peak intensities. The presence of two other spurious peaks (not shown) around

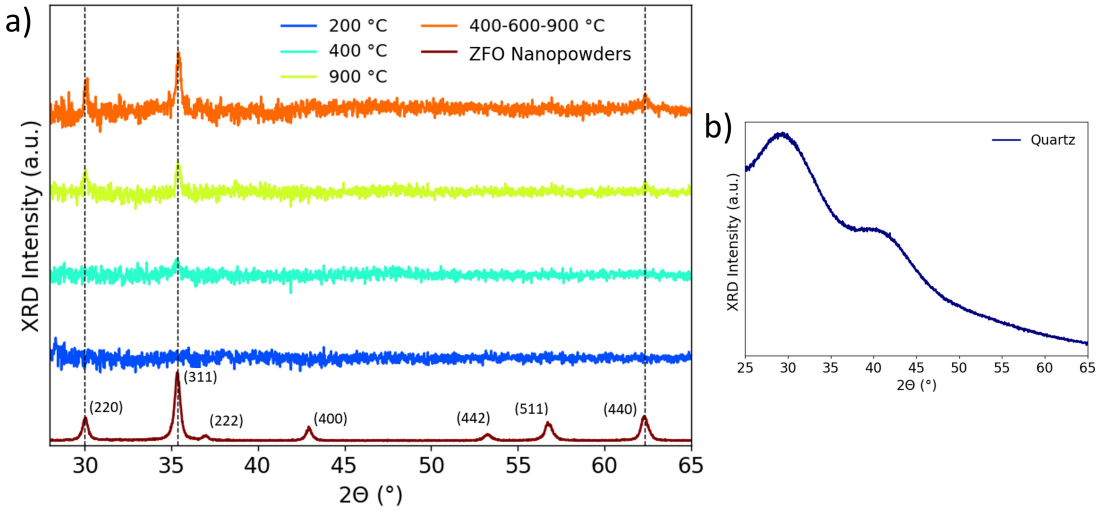

Figure 2.25: (a) XRD patterns of ZFO films annealed at different temperatures for 30 minutes. The patterns are compared to SA nanoparticles one (in red) reported along with the assignment of the lattice planes. The black dashed lines are used to allow for easy comparison between the SA nanopowders and the film patterns. (b) XRD pattern of the quartz substrate on the amorphous silicon background.

25.5° and 27° is also reported in the 900 °C and 400-600-900 °C films, respectively.

The XRD technique has limited sensitivity because it investigates the average response of the material. Therefore, the presence of isolated crystallite or ultrathin layers of ZFO cannot be excluded even for the AS and 200 °C samples. This reason justifies the need of a complementary microscopic probe that guarantees both the detection of crystalline (and chemical) properties expected for spinel ZFO and verifies the homogeneity of the sample giving more insights into the structure and composition at the micrometric level.

2.4.2.2 Raman spectroscopy

MicroRaman spectroscopy gets access to structural information from sample regions down to $4\,\mu m^2$ area and gives the possibility to evaluate the formation of ZFO, its amorphous/crystalline degree and the presence of other iron oxides. Fig. 2.26a shows the comparison between the Raman spectra of the 900 °C sample (orange) and the nanopowder precursors. Similar features at $350\,cm^{-1}$, $480\,cm^{-1}$, $630\,cm^{-1}$ and $690\,cm^{-1}$ are detected in both the two spectra and can be assigned to the $F_{2g}(2)$, $F_{2g}(3)$, and A_{1g} ZFO modes, respectively [34, 68, 102, 33] (see section 2.3.2.1). A similar comparison carried on the As Synthesized (AS) and other annealed (200 °C, 400 °C and 600 °C) films, gives again a good match of the Raman modes. In Fig. 2.26b, the homogeneity of each sample was verified through

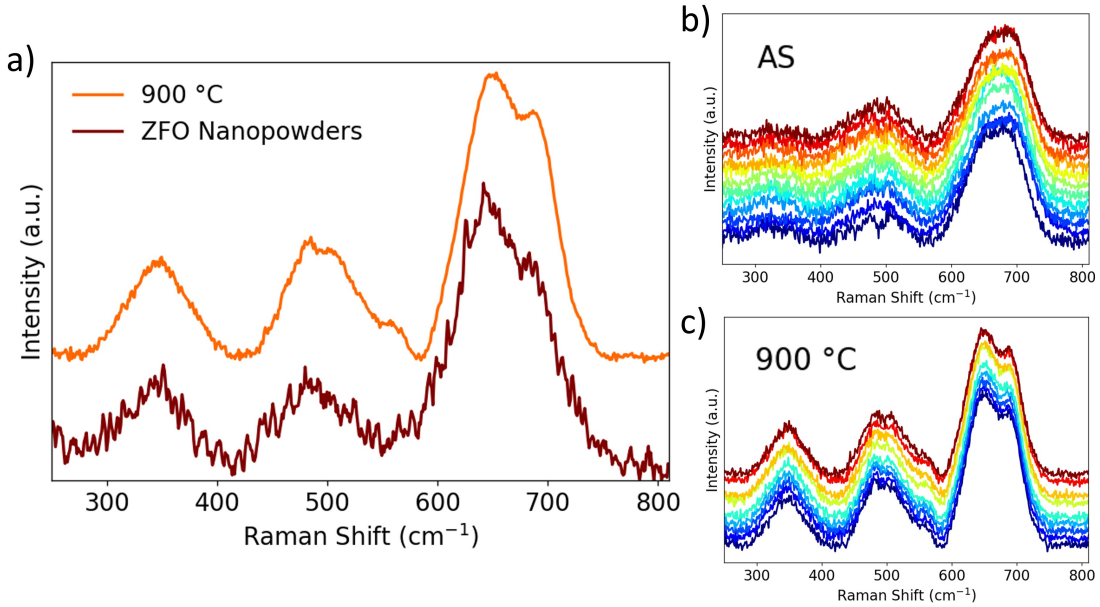

Figure 2.26: (a) Comparison between the Raman spectrum obtained from the ZFO nanopowder precursors and the 900 °C thin film. Homogeneity tests in different sample regions were performed on all the samples and are reported for the (b) AS sample and (c) 900 °C one.

mapping acquisitions in different points of each film. The results are shown for the AS and the 900 °C samples in Fig. 2.26b and 2.26c, respectively. The spectral features are invariant across all the maps with intensity differences due to loss of focus in the mapping acquisition.

Fig. 2.27a shows the comparison between samples annealed at different temperatures. The 350 cm^{-1}, 480 cm^{-1}, 630 cm^{-1}, and 690 cm^{-1} peaks are reported for all the considered samples. However, different responses in the AS and 400 °C samples with respect to the 600 °C and 900 °C ones are found in terms of signal intensity and shape. This is evidenced, in particular, in the A_{1g} mode assigned to the breathing of tetrahedral $Fe-$ and $Zn-$containing sites (see section 2.3 and section 2.1). Indeed, the portion of the peak associated with the vibration of the tetrahedral ZnO_4 cage ($\simeq$ 630 cm^{-1}) increases in intensity between 400 °C and 600 °C as shown in Fig. 2.27b. For instance, the intensities in the 400 °C sample are $I_{Zn} = 266$ and $I_{Fe} = 271.5$, while in the 600 °C sample $I_{Zn} = 325$ and $I_{Fe} = 263$.

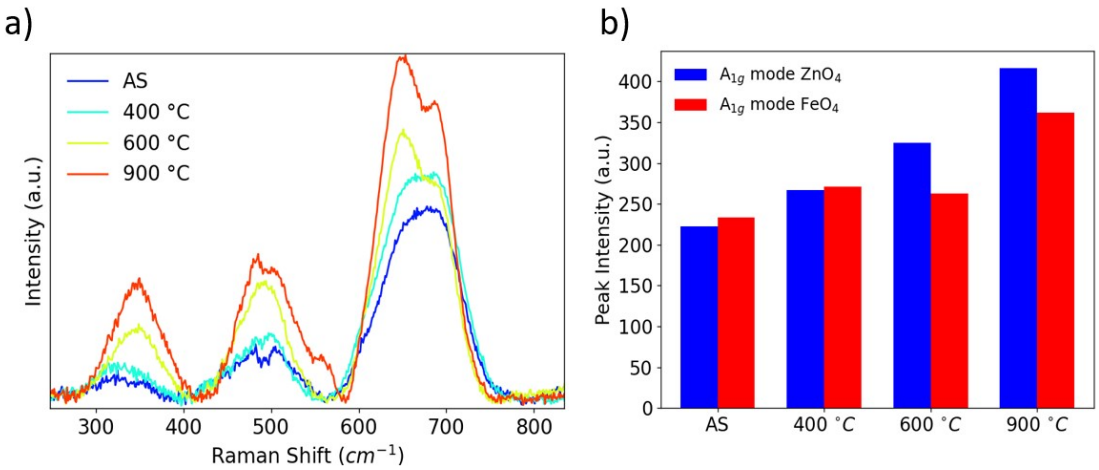

Figure 2.27: a) Raman spectra of the ZFO films annealed at different temperatures. The various spectra have been obtained by subtracting the quartz contribution and a 12^{th}-degree polynomial function from the raw data. b) Peak intensities of ZnO_4 and FeO_4 peaks composing the A_{1g} mode extracted from the Raman measurements.

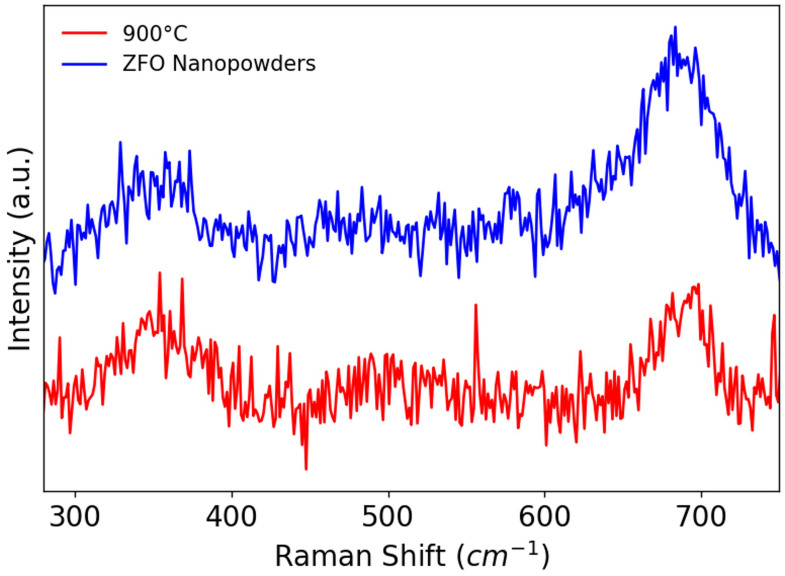

Figure 2.28: Comparison between the Raman UV spectra of ZFO thin film annealed at 900 °C (red spectrum) and ZFO Sigma Aldrich nanoparticles (blue spectrum) obtained with excitation wavelength $\lambda_{exc} = 266\,\text{nm}$. The thin film spectrum has been obtained from the raw data firstly by subtracting the quartz contribution. A 12^{th}-degree polynomial function is then used as baseline subtraction function to remove the quartz photoluminescence and other measurement artefacts.

2.4.2.3 UV Raman

The preliminary data from the UV Raman characterization of the films were obtained using an off-line setup at the Inelastic UV Scattering (IUVS) beamline station of Elettra sincrotrone in Trieste through the collaboration with Dr. F. D'Amico. Fig. 2.28 shows the comparison between the Raman UV spectra of 900 °C (red spectrum) and ZFO-SA nanoparticles (blue spectrum). The spectra were obtained with excitation wavelength $\lambda_{exc} = 266\,\text{nm}$ and both show two modes around $350\,\text{cm}^{-1}$ and $690\,\text{cm}^{-1}$ which are fully compatible with the ZFO UV Raman spectra presented in section 2.3.2.4. The low total Raman yield is due to the low scattering volume involved in the UV Raman process and weak source photon flux.

2.4.2.4 Optical Absorption

Fig. 2.29a shows the absorption coefficients of ZFO AS and annealed films after the subtraction of quartz substrate contribution. The reported absorption coefficients have been obtained normalizing by the average thickness of the films derived from profilometry measurements ($\simeq 110\,\text{nm}$). For all the samples, three different energy regions can be recognised: (i) a weak absorption shoulder around 1.5 eV; (ii) a higher absorption region above 5 eV; and (iii) an intermediate region in the 2.5-4.5 eV range. Assuming indirect bandgap [106, 168, 169], this last region can be used for the estimation of the optical bandgap energy by a Tauc plot using the simplified formula:

$$(\alpha h\nu) \propto (h\nu - E_g)^2 \tag{2.53}$$

According to eq. 2.53 the value of the bandgap (E_g) of the samples should correspond to the intercept of the linear region of $(\alpha h\nu)^{1/2}$ as a function of the photon energy [170, 171]. Fig. 2.29b shows the (E_g) calculation procedure in the example case of the as synthesized sample. The linear region of the spectrum is fitted (black line) extracting the intercept and slope parameters and calculating E_g. In order to visualize this in Fig. 2.29b, the black line energy range has been extended down to $(\alpha h\nu)^{1/2} = 0$. The estimated values of E_g are reported in Tab. 2.3 and in Fig. 2.29c for the AS, 400 °C, 600 °C, and 900 °C samples. The E_g values are all around 2.1 eV except for the 900 °C sample where $E_g \simeq 1.8\,\text{eV}$. This

Sample	AS	400 °C	600 °C	900 °C
E_g	2.099	2.148	2.086	1.869

Table 2.3: Bandgap values of the AS, 400 °C, 600 °C and 900 °C samples as extracted from the standard procedure described above and as reported in Figure 2.29c.

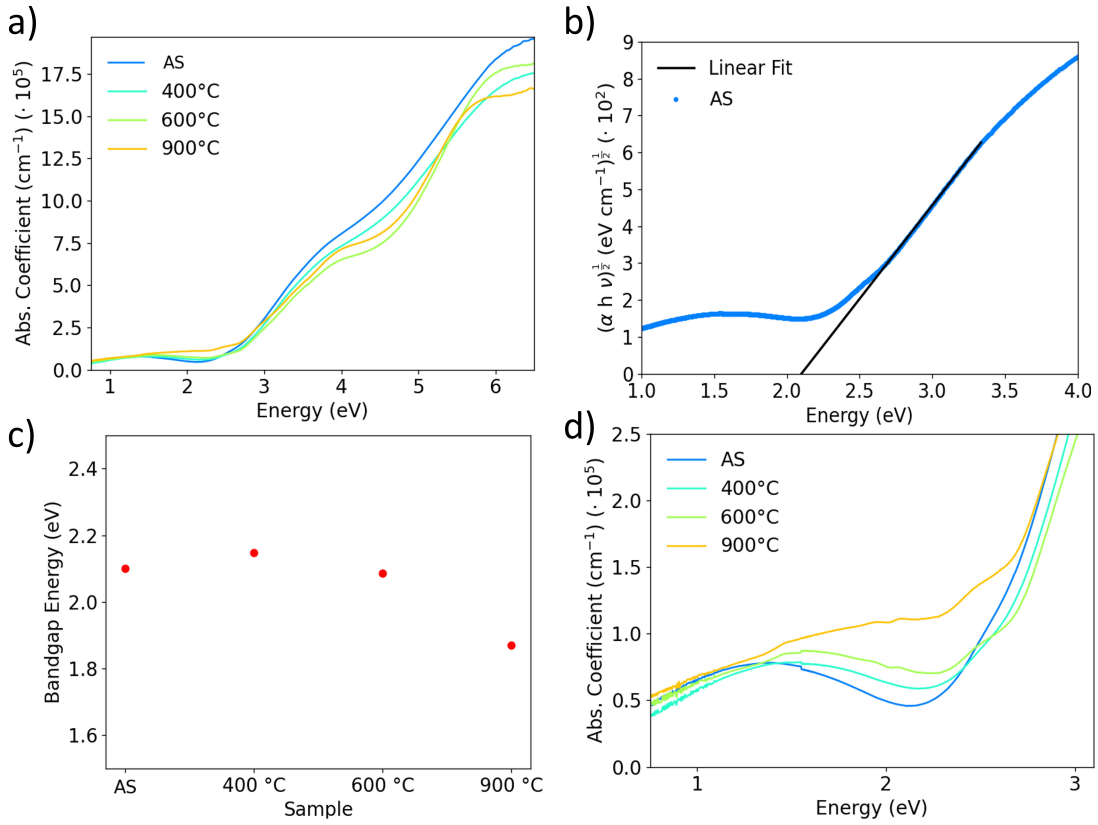

Figure 2.29: (a) Absorption coefficient of the ZFO films as a function of annealing temperature. (b) Bandgap calculation procedure on the AS sample. The linear fit is performed considering the region from 2.7 eV to 3.5 eV. The bandgap is quantitatively extrapolated by taking the ratio between slope and intercept. (c) Bandgap value of the samples as a function of the annealing temperature. (d) Inset in the 0.75-3.1 eV absorption region evidencing the behaviour of the weak absorption shoulder with annealing.

last evidence can possibly be rationalized by taking into account the blueshift of the first weak absorption region around 1.5 eV as the annealing progresses. This is shown in Fig. 2.29d which is an inset of Fig. 2.29a in the region between 0.75 eV and 3 eV. A peak around 1.5 eV is reported for the AS sample. This undergoes a gradual blueshift as the annealing temperature is increased. It is possible that the two separated regions (around 1.5 eV and in the 2.5-4.5 eV range) seen for the AS synthesized sample are merging at 900 °C affecting the E_g estimation.

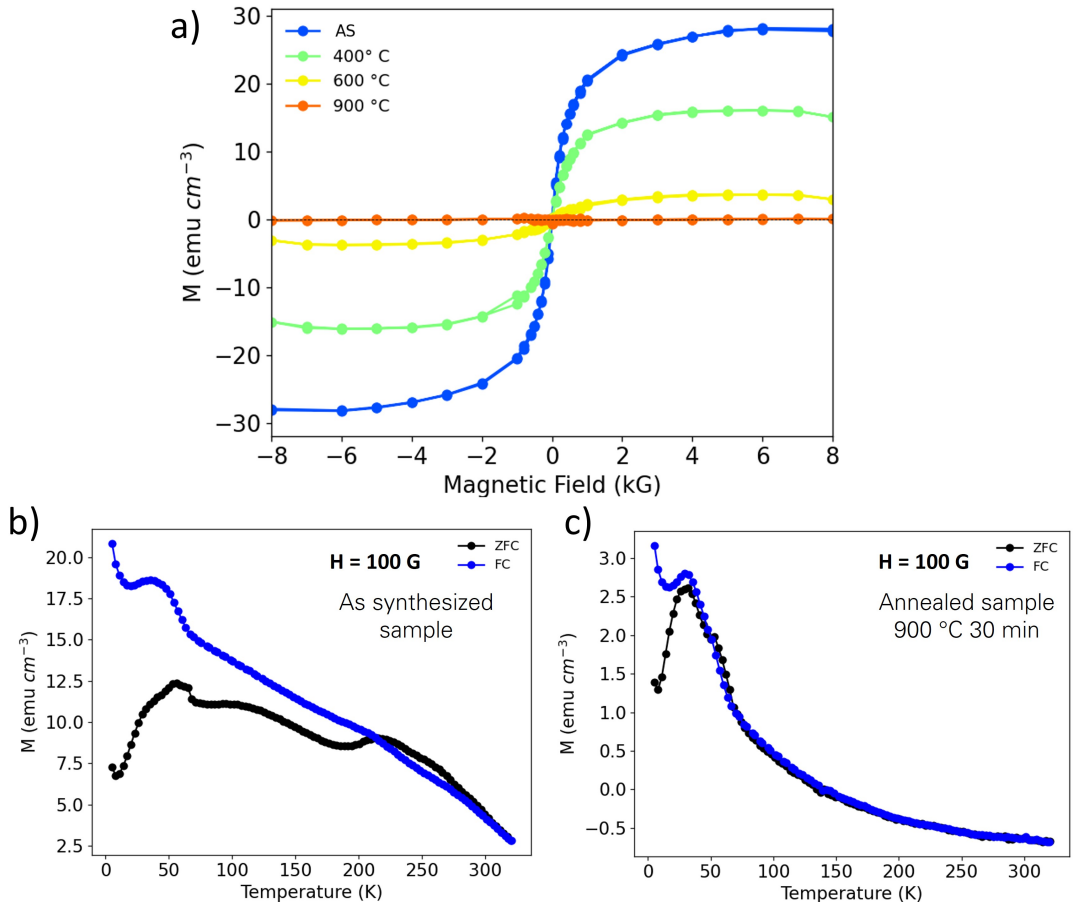

Figure 2.30: (a) RT Hysteresis cycles of the films annealed at different temperatures obtained by subtracting the quartz substrate diamagnetic contribution to the raw data. In (b) and (c) the Zero Field Cooled (black dots) and Field Cooled (Blue dots) curves of the as synthesized and the 900 °C samples are reported. The quartz diamagnetic contribution is kept thus obtaining negative values for the 900 °C sample in the 300—100 K temperature range.

2.4.2.5 SQUID magnetization results

In this section, the SQUID magnetometry results are presented for AS sample and annealed ones. As reported in section 2.2.4.2, the *M vs. H* responses were measured at RT with a magnetic field between 0 kG and ±8 kG, while the Zero-Field Cooled (ZFC) and Field Cooled (FC) measurements were taken in the 305-5 K temperature range at a fixed magnetic field of 100 G. Fig. 2.30a shows the RT hysteresis loops (*M vs. H*) of the films annealed at different temperatures obtained by subtracting the quartz substrate diamagnetic contribution to the raw data. All the samples except for 900 °C, show the typical superparamagnetic closed loop [172]. For the ZFO case, this behavior is known to arise in nanoparticles (see section 2.3.2.3) as well as in thin films obtained by both reactive (100% O_2 atmosphere) and non-reactive sputtering starting from a solid-state target [106, 173, 174, 175] with magnetization related to the inversion degree and oxygen content [72]. Quantitatively, the residual field H_{res} *i.e.*, the field at which M becomes 0, is around 10 G, around the experimental sensitivity. The saturation magnetization (M_{sat}) starts from a value of around 28 emu cm^{-3} in the AS film and goes towards zero as the annealing temperature is increased. Qualitative information on the homogeneity and magnetic ordering of the samples can be acquired from the Zero Field Cooled (ZFC) and Field Cooled (FC) curves. These are reported in Fig. 2.30b and c for the AS and 900 °C samples, respectively. Both in the ZFC and FC curves the substrate diamagnetic contribution was not removed. The ZFC curve in Fig. 2.30b shows three main peaks at 220 K, 110 K and 50-70 K. The latter is related to the paramagnetism of liquid Oxygen and is present in each measurement. Instead, the M response of the 900 °C sample (panel 2.30c) shows the following features: (i) it is negative in the 300-130 K temperature range because it is possibly dominated by quartz contribution; (ii) a peak around 50-40 K is detected corresponding with paramagnetism of liquid oxygen; and (iii) a separation between ZFC and FC curves is detected below 20 K.

2.4.2.6 Electron Paramagnetic Resonance

The EPR measurements were performed as indicated in section 2.2.3.2 at RT, with a frequency around 9.45 GHz, and a static magnetic field range between 200 G and 6000 G. The EPR response was investigated at variance with the angle between the samples and the cavity magnetic field in the 0-180 ° range. The results of this characterization are reported in Figs. 2.31a,b, which show the derivative EPR spectra and the calculated g values of the same sample as synthesized and after each treatment. The choice of performing this study on the same sample after each treatment (*e.g.*, 600 °C in Fig. 2.31a legend means that the sample has gone through annealing at 400 °C for 30 min and 600 °C for 30 min) is crucial because

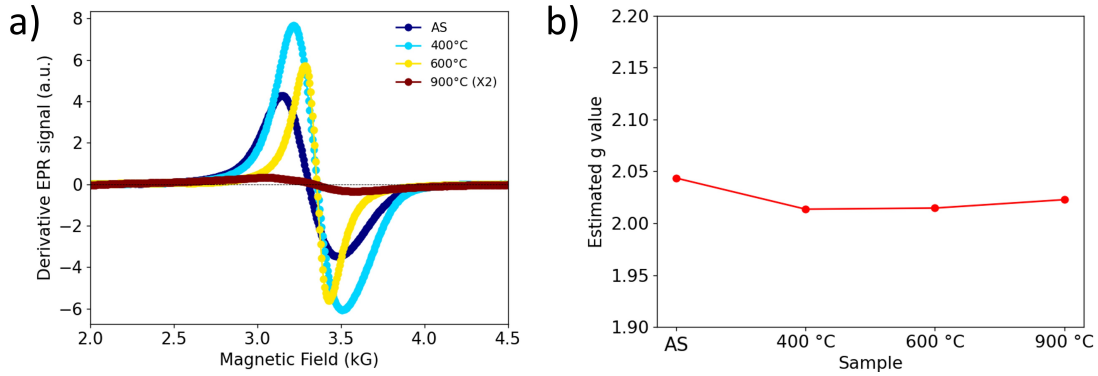

Figure 2.31: (a) Derivative EPR spectra of the same ZFO film annealed at different temperatures. (b) Estimated g value of the sample after each treatment. All the values calculated are compatible with the Fe^{3+} response in ZFO. The spectra and g values reported are obtained keeping an angle of 45 ° between the sample and the cavity magnetic field. This is the angle for which the signal is the most symmetric, making visual comparisons easier.

the area, thickness, mass and possibly film orientation shall be kept as fixed as possible. This is done with the aim of making quantitative comparisons between: (i) the signal symmetries, (ii) the resonance fields H_c to extract the g values, and (iii) the signal intensities. The symmetry of each signal is quantitatively estimated by taking the absolute value of the ratio between the maximum and the minimum points (p_S) in each derivative EPR signal. p_S values are reported in Tab. 2.4. Ideally, symmetric samples present $p_S = 1$. The greater the deviation from $p_S = 1$, the greater the asymmetry. The as synthesized sample presents a central field $H_c \simeq 3.30\,\text{kG}$ which increases to $H_c \simeq 3.35\,\text{kG}$ annealing at 400 °C and 600 °C. For the 900 °C annealing, the central field value is $H_c \simeq 3.34\,\text{kG}$. This signal is however contaminated by paramagnetic impurities contributions of the quartz substrate, which are non-negligible. The g values were estimated with the resonance condition shown in section 2.2.3.1:

$$\Delta E = h\nu = g_e \beta_B B_0$$

and are reported in Fig. 2.31b. At 45° ± 5°, the g values show a constant trend around 2.01-2.05 which is slightly greater than the free electron value ($g \simeq 2.0023$). Considering the signal intensity, Fig. 2.31a shows a first increase of the derivative signal from the as synthesized sample to the 400 °C one followed by a decrease between 400 °C and 600 °C and a huge drop from 600 °C to 900 °C annealing.

The EPR signal angular dependence results are now reported to understand the effects of demagnetizing fields and to investigate the presence of possible inhomo-

Sample	Symmetry parameter p_S
AS	1.23
400 °C	1.26
600 °C	1.02
900 °C	0.98

Table 2.4: Symmetry parameter of each sample obtained by taking the absolute value of the ratio between the maximum and minimum of the Derivative EPR signal at sample-field angle of 45°. An ideally symmetric signal has $p_S = 1$.

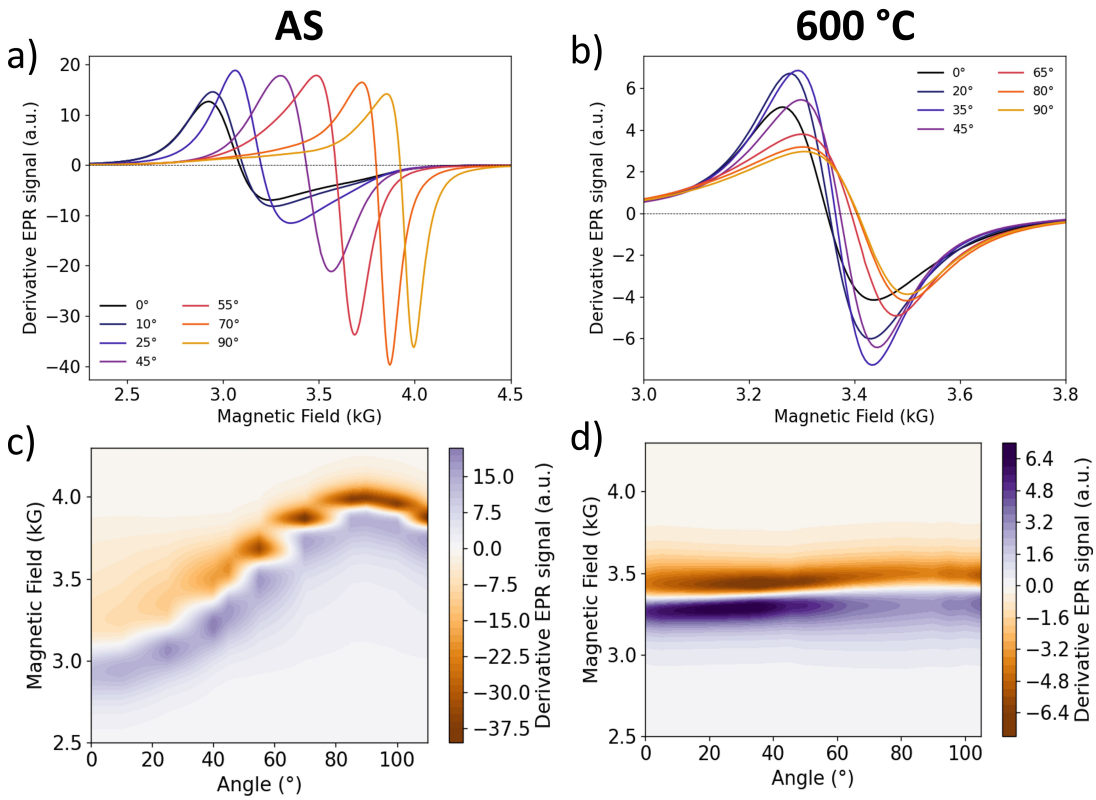

Figure 2.32: Derivative EPR spectra of the (a) as synthesized and (b) 600 °C - 30 min samples plotted as a function of the angle between the film surface and the static magnetic field vector inside the cavity. The shape asymmetry varies with the angle. The angular variation of the derivative EPR signal highlighting the change in the central field H_c is reported in the 2D maps of the (c) AS and (d) 600 °C samples. The central field of the resonance is a zero in the derivative spectrum and is color coded as a white line in the color map. The H_c variation in the as synthesized sample is about 1000 G while it is highly suppressed in the 600 °C sample.

Angle	g value AS	g value 600 °C	p_S AS	p_S 600 °C
0°	2.190	2.02	1.813	1.226
45°	1.968	2.004	0.839	0.846
55° - 65°	1.884 (@ 55°)	1.991 (@ 65°)	0.528 (@ 55°)	0.772 (@ 65°)
90°	1.722	1.984	0.391	0.763

Table 2.5: Angular variation of the estimated g values in some representative EPR spectra of as synthesized and 600 °C samples.

geneities or splittings. Fig. 2.32a shows the angular dependence of the derivative EPR spectrum of the AS sample. As the angle increases from 0° to 90° (*i.e.*, the sample goes towards becoming perpendicular to the magnetic field vector), g decreases from 2.19 to 1.72 (see Tab. 2.5 and Fig. 2.32c). The microwave frequency ν is only slightly varied in the 9.45-9.47 GHz region. Instead, the signal shape changes from asymmetric with a greater positive part at 0° to almost symmetric at 45° to asymmetric with greater negative part at 90°. Quantitatively, this is evidenced in the calculation of p_S which is shown in Tab. 2.5. The p_S value shows a variation from 1.813 at 0° which corresponds to a higher positive part, to 0.391 at 90°, corresponding to a greater negative part. As the sample goes through annealing at 600 °C, the g angular variation becomes less pronounced and is accompanied by a lower variation of the signal symmetry. Indeed, as reported in Tab 2.5, the g value goes from about 2.02 to 1.984 at 0° and 90°, respectively. In a similar extent, symmetry parameter p_S at 0° is 1.226 and decreases to 0.763 at 90° (Tab. 2.5), compatibly with a generally less pronounced positive-to-negative variation of the signal symmetry. This is evidenced in the almost straight zero line in the 2D map of Fig. 2.32d, where the angular variation of the derivative EPR signal is reported color coded such that the zeroes are depicted in white. Therefore, by looking at the white lines in both Fig. 2.32c and d, one can visually retrieve the differences in H_c (and therefore g, assuming almost constant ν) between as synthesized and annealed samples.

2.4.3 Discussion

In order to analyze and discuss the presented results the main objectives of this experimental work are briefly recalled: (i) feasibility of zinc ferrite thin films growth from ZFO nanoparticles precursors, (ii) characterization of crystalline quality of the obtained films depending on synthesis parameters, and (iii) characterization of the optical, electronic and magnetic responses of zinc ferrite thin films and their correlation with microscopic arrangement *i.e.*, cationic order/disorder and oxygen vacancies. Concerning the first point, ZFO thin film growth from nanoparticles precursors is feasible as demonstrated by the multitechnique analysis performed

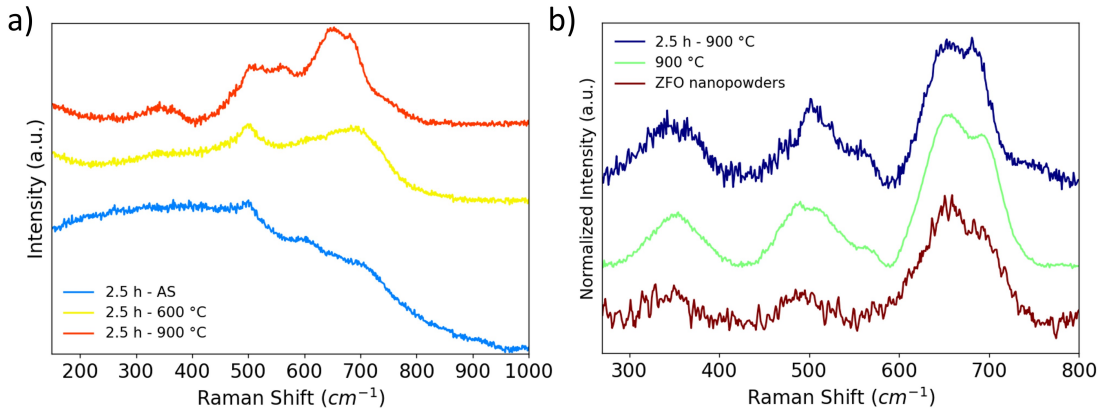

Figure 2.33: (a) Raman spectrum of the as synthesized sample with 2.5 h of sputtering time as a function of the annealing temperature. b) Comparison between the ZFO Raman spectra of the nanopowder precursor, the 4 h sputtered, 900 °C and 30 min (900 °C) annealed sample and the 2.5 h sputtered, 900 °C and 60 min (2.5 h-900 °C) annealed one. The spectra were normalized by their maximum value and vertical offset was added for clarity.

through: Raman (Fig. 2.27a), EPR (Fig. 2.31), XRD (Fig. 2.25) responses and bandgap calculation (Fig. 2.29c and Tab. 2.3). In the following, a detailed discussion of the behaviour of $ZnFe_2O_4$ thin films at different stages is provided. The XRD responses of the 400 °C and 900 °C samples show a match with some of the most intense features of the ZFO nanopowders XRD pattern (Fig. 2.25a). The data suggest that 400 °C and 900 °C samples possibly present a spinel structure compatible with Zinc Ferrite (Fig. 2.25a). Instead, the 200 °C sample in Fig. 2.25a does not show any characteristic peak in the considered range. The Raman response results in peaks at 350 cm^{-1}, 490 cm^{-1}, 630 cm^{-1}, and 690 cm^{-1} typical of crystalline spinel ZFO [68] (see Fig. 2.26). The increased intensity in the spectra upon annealing (Figs. 2.27a,b) corroborates the XRD results and suggests that crystalline spinel ZFO thin films are obtained upon annealing. In addition, the results reported in Figs. 2.26b,c suggest that the samples are homogeneous across all the investigated ranges. However, a seemingly crystalline structure can be detected also for the 4 h sputtered AS sample. This latter finding is further investigated considering recent Raman measurements on samples sputtered for 2.5 h.

Fig. 2.33a shows the spectra of the 2.5 h-AS, 2.5 h-600 °C and 2.5 h-900 °C samples without the contribution of the quartz substrate. A broad feature is present from 200 cm^{-1} to 800 cm^{-1} in the 2.5 h-AS sample (light blue spectrum). This is typical of amorphous samples and their absence of long-range structural order. The 2.5 h-600 °C sample (yellow spectrum) shows the appearance of a broad peak around 690-700 cm^{-1}, along with a tail going above 800 cm^{-1}. Instead, the

2.5 h-900 °C sample shows a spectrum similar to ZFO superimposed to a broad contribution in the 500-750 cm^{-1} region. The broad contribution in the 500-750 cm^{-1} region may be given by a combination of disorder and impurities and was removed by subtracting a 12^{th}-polynomial function with the purpose of performing spectra comparison with the precursors nanopowders and 900 °C, as shown in Fig. 2.33b. Similar features at 350 cm^{-1}, 480 cm^{-1}, 630 cm^{-1}, and 690 cm^{-1} compatible with $F_{2g}(2)$, $F_{2g}(3)$, and A_{1g} ZFO modes are detected for all the samples.

Moreover, the EPR investigation with the sample at 45 ° (Fig. 2.31) resulted in g values with a constant trend around 2.01-2.05. This is slightly greater than the free electron value ($g \simeq 2.0023$) and fully compatible with the ZFO values reported in the literature for nanoparticles and thin films [93, 32, 33]. Furthermore, the extracted E_g for all the samples (Fig. 2.29c and Tab. 2.3) are all around 1.8-2.2 eV compatibly with what is found in the literature for ZFO films by both experimental and theoretical studies [106, 165, 168, 169, 176, 177]. In this framework, it is reasonable to say that amorphous ZFO thin film samples are produced *via* sputtering and crystallize into the spinel structure as annealing is performed or through interaction with the sputtering plasma. The annealing time and annealing temperature both favour the crystallization of the sample.

It is also worth mentioning that, spurious peaks were detected in the XRD response around 25.5° and 27° on the 900 °C and 400-600-900 °C films (not shown). These do not match with crystal Fe, Fe_3O_4, Fe_2O_3 or ZnO patterns (from the RRUFF database [162]) and evidence of spurious compounds has not been retrieved with the other techniques presented. However, contributions such as the presence of crystalline impurities in the annealed substrate cannot be excluded.

Further comments on the correlation between microscopic arrangement and functional properties can be derived from the correlative analysis of vibrational, electronic and magnetic responses. For example, the possible cation inversion in the thin films can be estimated through the Raman response upon annealing and should also be responsible for the magnetic properties detected. The intensity differences in the A_{1g} mode as a function of annealing temperature (Fig. 2.27b) suggest an increase of the Zn content in the tetrahedral cage in the 600 °C and 900 °C samples. In nanoparticles, this increased Zn content is typical of ZFO with lower inversion and thus greater dimension [68, 102, 32, 178]. The same can be true in the film case: the change of the 630 cm^{-1} peak intensity between 400 °C and 600 °C annealing could be associated with an increase of the ZnO_4 unit vibration which, in turn, could be assigned to lower inversion and greater dimension of the grains in the thin film. To address the considerations mentioned above in a quantitative manner, the analysis of the sole A_{1g} mode was performed with a 2 Lorentz peak fit in accordance with section 2.3.2.1. The results of the fitting procedure are presented in Figs. 2.34a,b for the AS and 900 °C samples.

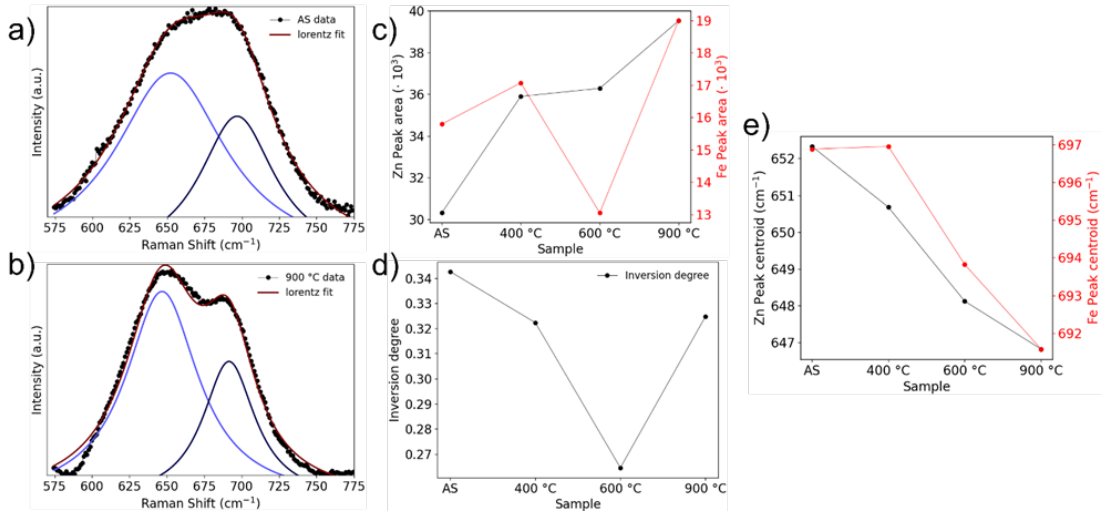

Figure 2.34: Best fit procedure with two Lorentz functions reported for (a) AS and (b) 900 °C samples. From the best fit procedure, the $Zn-$ and $Fe-$ peak areas (c) were extracted and the inversion degree (d) was calculated. The $Zn-$ and $Fe-$centroids (e) were also extracted and plotted for each sample.

The fitting procedure was performed after the subtraction of the quartz substrate and of a 12^{th}-degree polynomial. The differences between data and fit in the 900 °C sample are possibly due to this last procedure. Conversely, the AS sample data are well reproduced by the combination of two Lorentzians. From the best fitting procedures, the peak area of each component was extracted and reported in Fig. 2.34c. The behaviour of this last parameter associated with the ZnO_4 and FeO_4 vibrating units seems in contrast with what was reported in Fig. 2.27b looking at the pure intensities. This can be related to the use of the simplified model with two Lorentzians. Indeed, it is possible that the disorder induces Raman features displaying a Gaussian profile. Neglecting this component can alter the results of two lorentzians fitting procedure in terms of linewidth affecting, in turn, the peak area. Further analyses are in progress. Nevertheless, at this first stage a simplified model is preferred. A seemingly linear relationship is found between the Zn peak area and the annealing temperature with a fixed annealing time (30 minutes). Instead, the Fe related peak area does not show any apparent trend but has a strong minimum at 600 °C. These two behaviors are combined in the inversion degree between $Zn-$ and $Fe-$cations, calculated following the formula employed in section 2.3.2.2 (eq. 2.48), and reported in Fig. 2.34d. The inversion degree shows a negative decreasing trend up to 600 °C followed by another increase in 900 °C. In addition, a gradual redshift of both $Zn-$ and $Fe-$centroids is found and reported in Fig. 2.34e. Here, a negative seemingly linear relationship is found

between $Zn-$centroid and annealing temperature. This relationship can be also retrieved in the $Fe-$centroid from 400 °C onwards with a plateau-like behavior from AS to 400 °C.

The overall observations can possibly be interpreted considering the presence of a nanometric crystalline grains in the AS sample (Tab. 2.2). This would be compatible with the above reasoning and XRD-Raman results. Annealing would increase the dimension of the crystalline ZFO grains and reduce the cation inversion. The annealing temperature increase leads also to an increase of ZnO_4 cage vibration (Fig. 2.34c) and a slight decrease of the peak energy for both tetrahedral and octahedral sites (Fig. 2.34e). This can be explained as the result of different mechanisms happening with temperature: (i) the increase in the crystalline quality of the samples; (ii) the decrease in the inversion degree; and (iii) the decrease of oxygen vacancies. From Fig. 2.34, it seems that the 600 °C sample shows some singularities. This behavior could be rationalized considering the profilometry results reported in Fig. 2.24. There, a similarity in the estimated thicknesses was found, however, determining the real thickness of the 600 °C sample is difficult due to the spikes in the measured substrate profile. A lower 600 °C film thickness before the annealing could lead to a major crystallization with the same annealing temperature, partially explaining the singularities. Another possible motivation is given by a higher defect concentration in the other samples. Higher defect concentration hinders the possibility of good crystallization limiting the cation inversion. Thus, under the hypothesis of a lower defect concentration in the 600 °C sample, the results may be explained. In addition to the interpretation, the Raman response extended to the UV excitation (Fig. 2.28) gave similar results as the one presented in section 2.3.2.4 (Fig. 2.19). The two principal Raman modes are again associated with the vibration of the FeO_4 cage. Such Raman response could be detected in the presence of cation inversion between the sites and may be due to: (i) A highly defective nanoparticle's shell and/or (ii) a resonant Raman process with an intersite charge transfer from O^{2-} $2p$ to Fe^{3+} $4s$ states [107]. The results seem to possibly point towards a high Zn defective shell as in the case of nanoparticles. However, ZFO films are stable under in-air irradiation up to 25 GW/m^2 (or 2.5 MW/cm^2 *i.e.*, 100 mW laser power on 4 μm^2) at 638 nm. Therefore, to address this latter interpretation for ZFO thin films a higher incident laser power is required.

From the absorption spectrum the E_g extraction was carried out in Fig. 2.29. Additional information can be derived by trying to deconvolve the absorption spectra using the superposition of Gaussian components. Even if 3 different absorption regions are recognized, the best fitting procedure converges only using 4 components. The results of 4 Gaussian fit are used to comment on the main optical transitions even if the complete description of the optical behaviour of the sample would need to include additional components. Qualitatively, the presence of 4

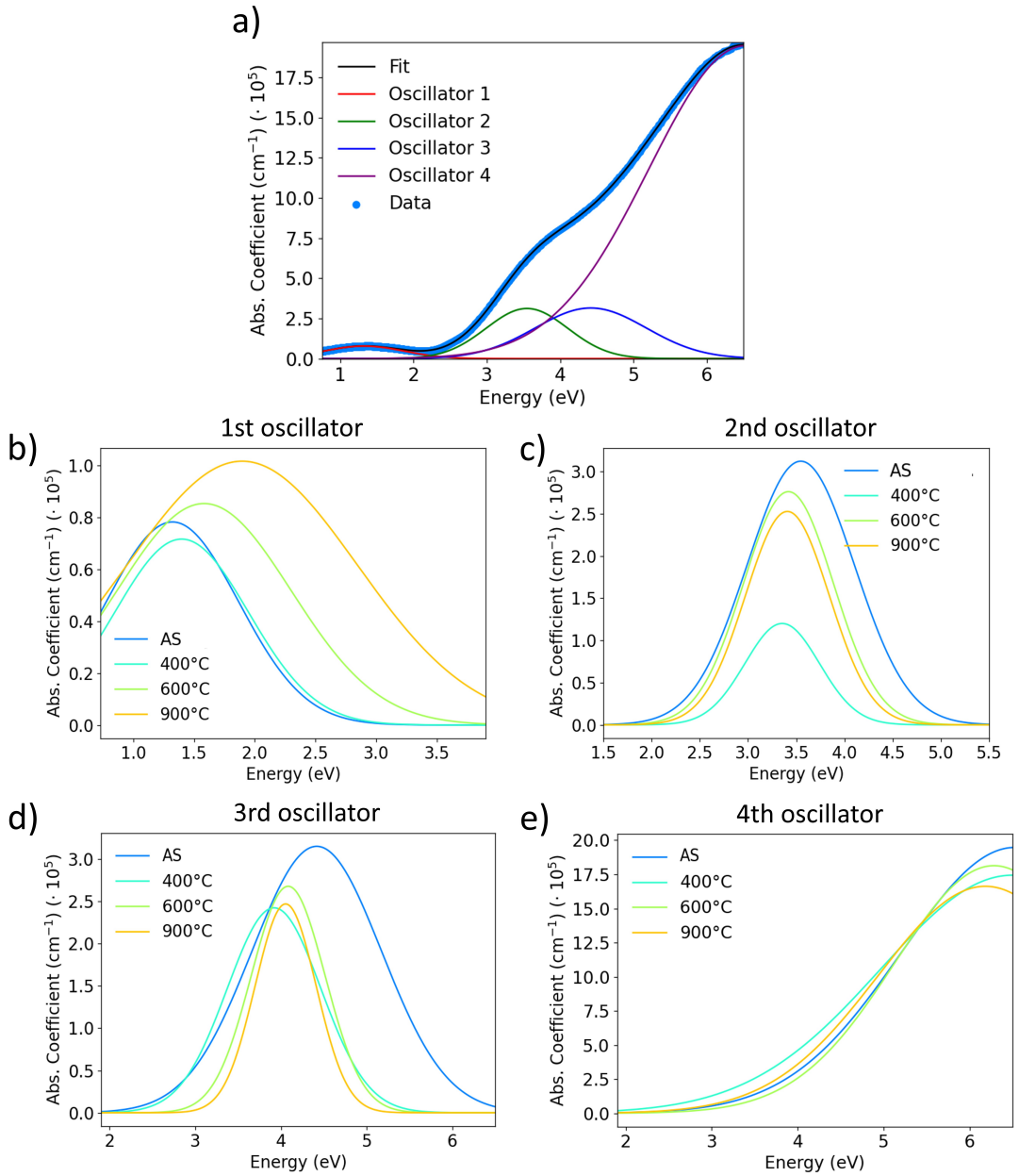

Figure 2.35: (a) Gaussian fit of the absorption coefficient of the ZFO as synthesized film. The variation of the extracted oscillators with the annealing temperature is indicated in (b), (c), (d) and (e).

main contributions centered at about 1.5 eV, 3.5 eV, 4-5 eV, and 6 eV is detected in all the investigated samples. The absorption coefficient measurements were fitted with 4 Gaussian peak functions as reported in Fig. 2.35a for the ZFO AS sample. However, 4 Gaussians are not enough to completely describe the plethora of optical transitions happening from 1 eV to 6 eV reported in literature [73, 179]. The tentative assignment of the transitions detected is presented in Tab. 2.6. The oscillators obtained from the fitting parameters are sorted by their central energy and graphically compared in figs. 2.35b,c,d and e while, Tab. 2.7 reports all the fitting parameters obtained for the as synthesized and annealed samples. Following the findings of *Zviagin et al.* [73, 179] for the ϵ_2, a possible assignment of the optical transitions involved in the absorption spectrum is given from direct comparison. The 1.5 eV transition is possibly ascribed to a mixture of intersite electron transfers (or Charge Transfer, CT) between $Fe^{2+}(Oh)$ – $Fe^{3+}(Oh)$ (from a_{1g} to t_{2g} or from a_{1g} to e_g states) that are typical in ZFO samples grown in low oxygen partial pressure. Indeed, the low oxygen pressure favors the formation of ligand vacancies during the deposition generating Fe^{2+} impurities which may cause the observed peak. The 3.5 eV peak may be ascribed to a mixture of $p-d$ Charge Transfer (CT) between O^{2-} $2p$ and Fe^{3+} t_{2g} and e_g states in the octahedral cage. Two other possible transitions are present in the 2.5-3.5 eV range which are an intersite $Fe^{3+}(Oh)$ $t_{2g} \rightarrow Fe^{3+}(Td)$ e CT and an onsite $3d-4s$ transition in Zn. The first transition would involve two d levels in presence of cation inversion, thus should show variations between AS (highest invertion, see Fig. 2.34c) and 600 °C (lowest inversion, see Fig. 2.34c) in partial contrast with what observed in Fig. 2.35c. Instead, the $3d-4s$ transition in Zn should span from 2-8 eV with a maximum around 3.5 eV [73]. Similarly, the 4.5 eV oscillator is possibly a mixture of $p-d$ CT between O^{2-} $2p$ and Fe^{3+} $4s$ states in both the octahedral and tetrahedral cages given by the cation inversion of nanostructured samples. The 6.5 eV oscillator is again an intersite $p-d$ CT in the tetrahedral cage between O^{2-} $2p$ and Zn^{2+} $4s$ states.

The results here shown can be compared with similar spinel systems such as magnetite (Fe_3O_4). The studies on optical conductivity (σ_1) and dielectric functions (ϵ_1 and ϵ_2) give assignments similar to the one reported for the 1.5 eV, 3.5 eV, and 4.5 eV oscillators [180, 181, 182, 179]. However, along with the $O\,2p \rightarrow$Fe $3d$ charge transfers in the 3.5-6 eV region, other transitions such as intersite $Fe^{3+}(Oh) \rightarrow Fe^{3+}(Td)$ CT, intersite $Fe^{2+}(Oh) \rightarrow Fe^{2+}(Td)$ CT, $Fe^{3+}(Td) \rightarrow Fe^{3+}(Oh)$ CT, and intersite $Fe^{3+}(Td) \rightarrow Fe^{2+}(Oh)$ CT were proposed, further complicating the possible electronic transition scenario even for inverted ZFO [181, 183, 184]. Instead, the 1.5 eV transition is in good agreement with the intersite $Fe^{2+}(Oh) \rightarrow Fe^{3+}(Oh)$ CTs reported also for ZFO. From the comparison between the parameters as a function of annealing temperature (Tab. 2.7) and from

Energy range	Literature assignment [73]
1.5 eV	Mixed:
	Intersite $d-d$ $Fe^{2+}(Oh)$ $a_{1g} \rightarrow Fe^{3+}(Oh)$ t_{2g} CT
	Intersite $d-d$ $Fe^{2+}(Oh)$ $a_{1g} \rightarrow Fe^{3+}(Oh)$ e_g CT
3.5 eV	Mixed:
	Intersite $p-d$ O^{2-} $2p \rightarrow Fe^{3+}_{Oh}$ t_{2g} CT
	Intersite $p-d$ O^{2-} $2p \rightarrow Fe^{3+}_{Oh}$ e_g CT
4.5 eV	Mixed:
	Intersite $p-d$ O^{2-} $2p \rightarrow Fe^{3+}_{Oh}$ $4s$ CT
	Intersite $p-d$ O^{2-} $2p \rightarrow Fe^{3+}_{Td}$ $4s$ CT
6.5 eV	Intersite $p-d$ O^{2-} $2p \rightarrow Zn^{2+}_{Td}$ $4s$

Table 2.6: Electronic transitions of $ZnFe_2O_4$ along with their assignment based on literature results [73]. The *Oh* and *Td* pedices stand for Octahedral and Tetrahedral sites, respectively.

Fig. 2.35b,c,d and e, a blueshift of the 1.5 eV oscillator central energy, increase in amplitude and FWHM are noticed accompanied by a decrease of 4-5 eV and 6 eV oscillators amplitudes. In addition, the feature at 3.5 eV of the 400 °C sample shows an intensity drop down to 1/3 of the AS value. This may be due to various reasons: (i) the samples employed in this study are different thus they could present impurities even if the sputtering should be, in principle, homogeneous; (ii) the absorption coefficients have been scaled by the same mean thickness based on profilometry results (Fig. 2.24) but morphological differences of 10-20 nm are still possible; and/or (iii) the fitting procedure led to a wrong balance between the gaussian components leading to a low value of amplitude for the 400 °C 3.5 eV oscillator.

The possible interpretation of the data shown so far allows one to have insights into the structural and functional optical properties of ZFO. Moreover, it is crucial for the understanding of the magnetic functional properties obtained through SQUID (Fig. 2.30) and EPR (Figs. 2.31 and 2.32) measurements. Firstly, the hysteresis loops in Fig. 2.30a show superparamagnetic behaviour of the AS, 400 °C, and 600 °C films. A superparamagnetic behaviour in ZFO is envisaged if a possible $Fe-O-Fe$ superexchange at $\theta_{int} \simeq 180\,^\circ$ in the sample is taken into account. This interaction may be given by both Fe^{3+} or spurious Fe^{2+} ions and should require a Fe ion in the tetrahedral sites. Therefore, inversion between Zn and Fe ions should be a necessary condition for superparamagnetism in this case. In the ZFO case, cation inversion is reached considering nanostructures, thus, it is possible to corroborate the interpretation of Raman and XRD results for which nanometric crystalline domains or a nanometric crystalline layer are present in the AS sample.

Sample	AS	400 °C	600 °C	900 °C
1st centroid (eV)	1.32	1.40	1.58	1.89
1st fwhm (eV)	1.09	1.10	1.43	1.89
1st amplitude	10690.6	9878.9	15339.5	24143.2
2nd centroid (eV)	3.55	3.35	3.42	3.41
2nd fwhm (eV)	1.11	0.77	0.93	0.87
2nd amplitude	43520.9	11612.4	32296.6	27514.2
3rd centroid (eV)	4.42	3.92	4.08	4.05
3rd fwhm (eV)	1.51	1.09	0.86	0.71
3rd amplitude	59750.6	33190.5	28899.6	22106.9
4th centroid (eV)	6.53	6.49	6.28	6.18
4th fwhm (eV)	2.63	3.06	2.31	2.49
4th amplitude	642345.9	668044.9	525282.6	519660.7

Table 2.7: Best fit parameters of the 4 gaussians model applied for the AS, 400 °C, 600 °C and 900 °C samples. The oscillators have been sorted by their central energy and are represented in Figure 2.35b-e.

Another possible evidence of this structure in the AS films comes from ZFC-FC curve in Fig. 2.30b. The presence of two peaks in the ZFC curve at 220 K and 110 K may be interpreted with the presence of two spin-blocking temperatures T_B. To understand the presence of blocking temperatures, one should first consider a thin film with magnetic domains of dimension d. Similar to the case of nanoparticles [158], the magnetization M of the domains is considered as randomly oriented in the absence of an external magnetic field. The T_B value can thus be defined similarly to what was done in section 2.3.2.3. Such temperature is also domain volume dependent by means of $\Delta E = KV$, where K is an anisotropy constant and V is the volume. Therefore, one should expect an increase in T_B increasing the domain dimension d. Nevertheless, for ZFO nanoparticles, the opposite behavior was found with T_B decreasing as d increases [185]. Another evidence comes from Mg doped core-shell ZFO-magnetite nanoparticles where the T_B dependence is not trivial [186]. These seemingly contrasting findings can be true also in the case of film domains and can explained again in terms of cation inversion between Fe and Zn at the nanostructure as considered in section 2.3.2.3. Indeed, it is reasonable to say that the higher the domain dimension is, the lower the inversion degree will be with an overall decrease of the Fe^{3+} -O^{2-}-Fe^{3+} 180° superexchange interaction. Thus, the lower the superexchange is, the lower the M is, possibly decreasing T_B. The presence of two maxima in the ZFC curve of Fig. 2.30b should imply the presence of two T_B, and thus, the presence of multiple domains with different dimensions. The domains with $T_{B1} \simeq 220$ K would give the highest contribution to the superparamagnetic behavior. The other domains with $T_{B2} \simeq 110$ K instead,

would show weaker M contribution and a lower inversion degree. Furthermore, the FWHM of the peaks should be correlated to the domains dimension dispersion. The higher the FWHM is, the higher the dimension dispersion will be. However, it is not possible to give a precise estimation on the dimension of the domains with the techniques employed. This latter is still a work in progress.

The superparamagnetism, magnetic anisotropy with different domains, and dimension dispersions may be changed or even suppressed by annealing the sample. Indeed, the superparamagnetic behaviour in Fig. 2.30a decreases with increased annealing. The limit is reached in the 900 °C sample where the M *vs.* H curve does not show any superparamagnetic behaviour. In addition, the ZFC and FC curves for 900 °C reported in Fig. 2.30c do not show any maxima ascribable to spin-blocking temperatures. Based on this data, it is reasonable to say that the crystallization induced by the annealing in air decreases the number of inverted unit cells and thus increases the dimension of the domains. Indeed, both ZFC and FC curves are coincident within the resolution of the experiment in the whole 320-40 K range. Below 40 K a contribution given by liquid Oxygen paramagnetism appears and is followed by the splitting of the curves at around 18-20 K. This last splitting is compatible with the appearance of AFM order given by the 90° Fe^{3+}-O^{2-}-Fe^{3+} superexchange in ZFO bulk [187] but also a non-negligible contribution of impurities.

The possible insights on ZFO thin films shown so far are useful for the interpretation of the EPR spectra. Considering the EPR spectra of the same sample for different annealing temperatures taken at 45 ° (Fig. 2.31), a possible interpretation for the intensity increase occurring from AS to 400 °C samples is given, considering the optical absorption measurements (Fig. 2.35). The absorption spectrum showed the presence of a 1.5 eV peak possibly interpreted as a mix of intersite $Fe^{2+} \rightarrow Fe^{3+}$ charge transfer processes between octahedral sites. These processes are related to the presence of oxygen vacancies that change the valences of EPR active Fe^{3+} ions into EPR inactive Fe^{2+}. The annealing at 400 °C would favour the incorporation of oxygen atoms in the structure with consequent oxidization of a partial amount of Fe^{2+} into Fe^{3+}. This would increase the EPR signal intensity. However, the crystalline domains of the sample would increase in size, reducing the cation inversion and decreasing the superparamagnetic contribution as observed in the hysteresis cycles in Fig. 2.30a. The further increase in annealing temperature and time would lead to a decrease in signal intensity for 600 °C annealing and a drop of the signal for 900 °C annealing. The mechanism here discussed may give also a possible explanation for the greater amplitude of the 1.5 eV oscillators for the 600 °C and 900 °C samples respect to the AS one (Fig. 2.35b). This is done by remarking that the 1.5 eV feature corresponds to a transition among octahedral sites. Therefore, if the two conditions: (i) the annealing favours crystallization and

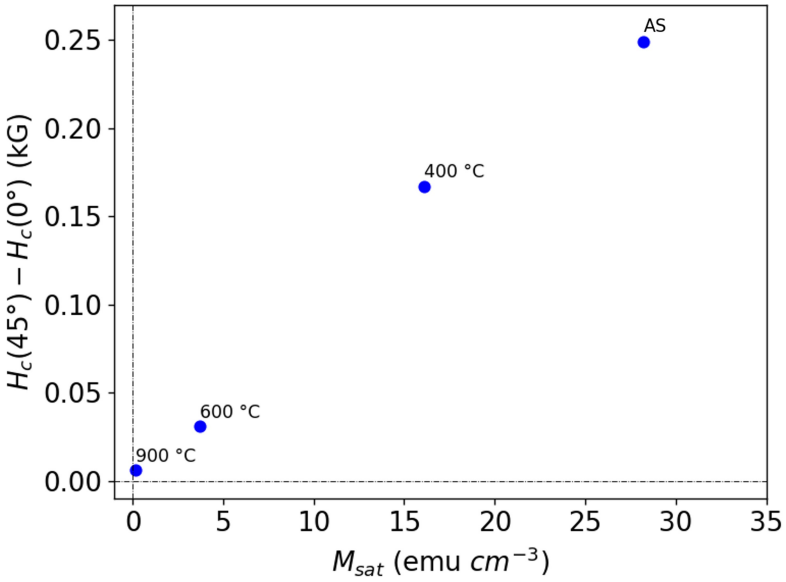

Figure 2.36: Correlation between the saturation magnetization of the samples obtained by SQUID measurements and the difference ΔH_c at 0 ° and 45 °.

decrease of the cation inversion and (ii) the Fe^{2+} ions are not fully oxidized into Fe^{3+} are satisfied, an increase of the amplitude of the 1.5 eV transition should be expected in the 600 °C and 900 °C samples.

The angular variation of the EPR signal (Fig. 2.32) is now analyzed taking into account demagnetizing fields. According to literature results [93], the signal shape change in EPR spectra of ZFO nanocrystalline thin films with angle is indicative of the presence of an uniaxial anisotropy in the film. This because the growth process of the film may be affected by internal stresses, preferential alignment of nanocrystalline grains or ions due to inter-atomic forces [94, 95]. Therefore, the findings are interpreted based on the following hypothesis: the signal shape change is due to the superposition of at least two signals with comparable intensity and with different angular variations. These signals can be assigned to a perpendicular and a parallel component of the solid-state sample magnetization with two different g values ($g_\perp = g_x = g_y$ and $g_z = g_\parallel$) as discussed in section 2.2.3 [143]. However, as reported in the literature for ZFO films [93], one should expect low or no angular variance of the in-plane resonance signal. Instead, the AS sample (Fig. 2.32a) shows an angular variation of both components. This phenomenon is possibly explained by taking into account the presence of two main competing structural phases in the sample as already suggested by Raman and XRD measurements: an amorphous and a spinel crystalline one. As the angle between the static magnetic field vector and the sample surface is varied, the Fe^{3+} signals in the amorphous and crystalline environments act with different demagnetizing

fields which shift the H_c proportionally to the magnetization of the sample. Indeed, the uniaxial anisotropy would be envisaged in a perfectly oriented crystal. Instead, in a mixture of amorphous and crystalline ZFO with different contributions of the Fe^{3+} ion, one should expect a change in both the components and a different demagnetization contribution hypothesizing that the two phases have different magnetizations. In general, the overall demagnetization contribution is suggested in the plot of Fig. 2.36 which shows the EPR signal central field variation between 0° and 45° as a function of the saturation magnetization retrieved in the hysteresis cycles (Fig. 2.30a). In this framework, the change in signal shape and angular variability of the 600 °C sample (Fig. 2.32b) would confirm the interpretation. Indeed, its lower M_{sat} and thus demagnetizing field contributions are compatible with a decrease of the amorphous layer with the annealing temperature and possibly a decreased number of crystalline domains. Again, the annealing of the films would increase the dimension of the crystalline part with a random orientation at the expense of the amorphous one, decreasing the inversion and thus the 180° favored Fe^{3+} - O^{2-} - Fe^{3+} superexchange. This would decrease the response to external magnetic fields giving a more symmetric derivative EPR signal with lower g angular variability.

2.5 Conclusion to this chapter

In this chapter, ZFO thin films were synthesized and characterized starting from unprocessed nanopowder precursors. In section 2.3, pure and $Ga/Mg/MgGa$ doped nanoparticles were used to highlight the potentiality of Raman spectroscopy as a fast and sensitive analytical tool in studying functional parameters in transition metal oxides. In particular, the focus was on the correlation between structural and magnetic properties and on the chemical transformations of $ZnFe_2O_4$ nanoparticles following irradiation in high (3×10^{-6} mbar) and low (1.5 mbar) vacuum environments at variance with dimension and doping. The overall framework was corroborated with EPR, XRD and SQUID results. After these preliminary evaluations, ZFO thin films were synthesized and their chemical, crystalline and multifunctional properties were characterized at variance with annealing temperature. This was possible through a complementary experimental approach based on XRD, Raman, Optical absorption and EPR measurements. In particular, annealing should favors crystallization but should decrease the superparamagnetic contribution because it decreases the inversion degree increasing the magnetic domains dimensions and suppressing magnetic inhomogeneity. In addition, the optical absorption and EPR measurements showed the possible presence of oxygen vacancies in the AS sample which are decreased but not suppressed with annealing. In this framework, the EPR signal shows g value and shape variability with

the angle between the sample and static magnetic field. This is compatible with uniaxial anisotropy of the samples and demagnetizing fields effect which give a greater EPR signal angular variability the greater the M_{sat}. However, these are not the only factors at play. Indeed, a competition between two different magnetic responses is hypothesized. This latter would be given by the amorphous and the crystalline layers of the sample. The overall study is crucial to industrial applications since it gives a route for low-cost production of ZFO thin films with tunable magnetic and photonic properties. Complementary studies with *e.g.*, X-Ray Photoemission Spectroscopy (XPS), grazing incidence XRD, Scanning Electron Microscopy (SEM), Transmission Electron Microscopy (TEM), and Density Functional Theory (DFT) calculations are expected in the next future to complete the interpretation on the composition, structure, morphology, and assignment of the electronic transitions detected, respectively.

Chapter 3

Characterization of Co_3O_4 thin films transient response

3.1 Introduction on Co_3O_4

Many of the potential technological applications of Transition Metal Oxides (TMOs) discussed in this thesis (*e.g.*, Photocatalysis, Photovoltaics, Magnetic Hyperthermia, and all-optical switching) rely on exploiting the photocarriers generated upon the above-band-gap excitation and the changes in the spin order within a magnetic phase. This necessitates a thorough investigation of the microscopic mechanisms governing the relaxation of charge carriers and the interactions between the coupled Degrees of Freedom (DOF) of the systems. This coupling strongly depends on internal properties such as cation geometry and valence state [3]. The complex internal structure primarily stems from the intermediate ionic character of the metal-oxide chemical bonds and the partially filled *d*-orbitals of the metal centres. Among TMO systems, Co_3O_4 benchmarks this complex behaviour. It is an excellent candidate for solar energy conversion, and water splitting applications, but also for gas sensing and cytotoxic-antibacterial devices [188, 189, 190]. The Room Temperature (RT) phase of Co_3O_4 follows the normal spinel structure, belonging to the O_h^7 - $Fd\bar{3}m$ space group. It comprises Co^{2+} and Co^{3+} centres in a 1:2 stoichiometric ratio, occupying tetrahedral and octahedral sites with O^{2-} vertices, respectively (Fig. 3.1). The lattice constant is a =8.0821 Å, and the oxygen parameter is u = 0.392 [192]. As reported in Fig. 3.1, the crystal field splitting results in a high-spin configuration for the Co^{2+} site with $e^4t_2^3$ ground state (S = 3/2, 4 paired e-electrons and 3 unpaired t_2-electrons) and low hybridization with the surrounding O^{2-} ions. The octahedral symmetry leads to a low-spin state for the Co^{3+} sites with t_{2g}^6 ground state (S = 0, 6 paired electrons, t_{2g} as lowest energy orbital),

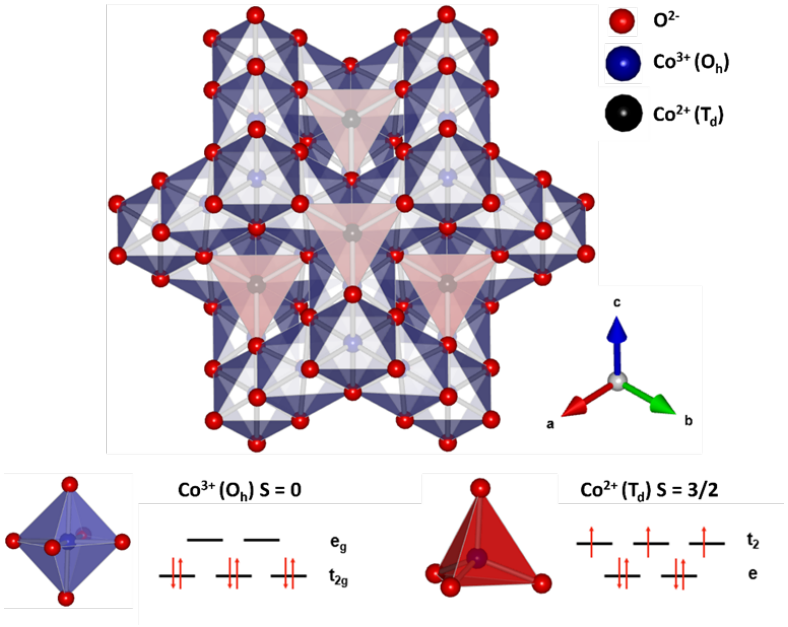

Figure 3.1: Co_3O_4 crystal structure viewed from the [111] direction (top). The tetrahedral and octahedral sites are shown in red and blue, respectively. d levels configuration due to crystal field splitting and the consequent total spin S number are reported (bottom). The images were made using the VESTA software [191].

due to the strong hybridization with the O^{2-} ligands [193, 61]. This lattice and electronic structures contribute to a rich optical absorption spectrum, featuring Mott-Hubbard and charge transfer gaps. This spectrum, shown in Fig.3.2, consists of four bands peaked at 0.82 eV, 0.94 eV, 1.66 eV and 2.81 eV [194]. Previous studies [195, 196, 194] attributed these optical features to specific electronic transitions: (i) the 2.81 eV band corresponds to intersite $p-d$ Charge Transfer (CT) transitions from O^{2-} to Co^{2+} and Co^{3+}; (ii) the 1.66 eV band primarily results from intersite $d-d$ CT transition between Co^{3+} and Co^{2+}; (iii) the 0.94 eV band involves an intersite $d-d$ CT between Co^{2+} and Co^{3+} sites; and (iv) the 0.82 eV band arises from an onsite $d-d$ transition localized in the Co^{2+} centre [194, 195, 196]. Additionally, a Near Infrared (NIR) absorption study identified a band centred at 0.55 eV at RT, attributed to dipole-allowed $d-d$ transitions of the Co^{2+} ion with a temperature dependent splitting due to spin-orbit coupling [197].

The spin arrangement in collinear tetrahedral sites is ferromagnetic (FM) but it is Antiferromagnetic (AFM) between non collinear sites [61]. Below $T_{Neel} = 30-40$ K, the system undergoes an AFM transition with Co^{2+} sites forming two Face-Centred-Cubic (FCC) sublattices with opposite magnetic moments. This behaviour stems from a relatively strong superexchange interaction, even in the

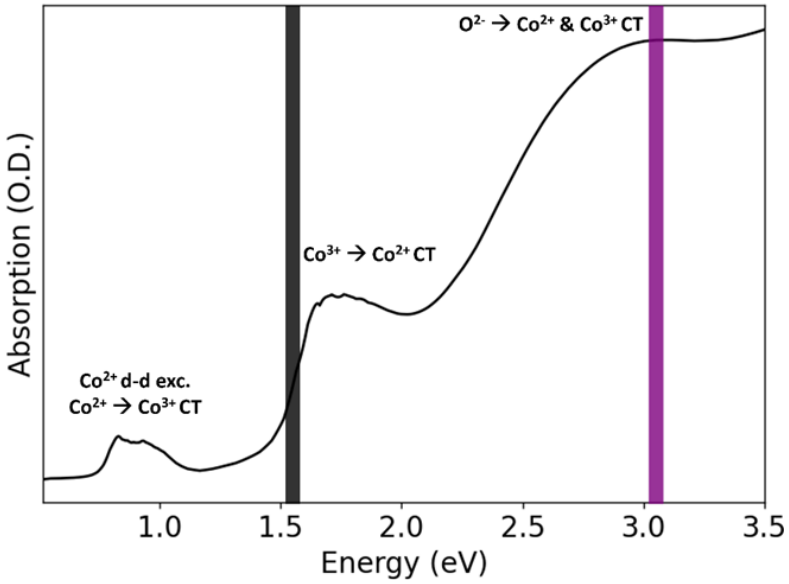

Figure 3.2: Spinel Co_3O_4 absorption spectrum at Room Temperature (RT). The main bands are labelled with the corresponding electronic transitions assigned in literature [194, 196, 201, 202].

presence of a significant distance (3.89 Å) between magnetic Co^{+2} ions [61, 198, 199] (see section 1.2.2). However, deviations from the paramagnetic behaviour were observed starting from 100 K, attributed to a possible spin-liquid phase [64]. Neutron diffraction and heat capacity studies showed that the AFM transition is accompanied by a symmetry change to the $T_d^2 - F\bar{4}3m$ space group due to the doubling of the unit cell, although no structural phase transition was detected [61, 198, 64, 200].

3.1.1 Open questions and state-of-the-art

Both from steady-state and time-resolved standpoints, numerous open questions persist, while conflicting findings emerged in the literature. A host of studies which employed optical spectroscopy, X-Ray scattering, and Density Functional Theory (DFT) calculations provided differing assignments of the optical transitions in the 0.5-1.6 eV range [193, 194, 203]. Some of these unresolved questions include: Which Cobalt centres are implicated in each electronic transition? How does the AFM transition impact the electronic properties observed *via* optical spectroscopy? What is the relaxation path of charge carriers upon excitation of a specific electronic transition? How does the AFM transition alter the relaxation pathways? What are, if any, the coherent modes preferentially activated upon intersite $d - d$ Charge Transfer (CT) or intersite $p - d$ CT?

Providing answers to these questions is crucial, given the aforementioned potential in applications. It would also facilitate a deeper understanding of the microscopic mechanisms governing TMOs. Furthermore, these questions are compounded by the fact that, to date, no studies have been dedicated to understanding the temperature and magnetic dependence of Co_3O_4 optical properties in the visible range using a time-resolved approach. In general, only a few time-resolved investigations were conducted to elucidate certain aspects of the photodynamics in Co_3O_4 under RT conditions [201, 202, 204], yielding to conflicting interpretations. Specifically, *Jiang et al.* [201] observed two hot carrier cooling phenomena occurring below 1 ps when pumping intersite $p-d$ CT excitations with 3.1 eV, 60 fs pulses and probing the system at cobalt $M_{2,3}$-edge. This resulted in the generation of Co^{2+} ions shortly after photoexcitation, partially contradicting the assignment of the optical transitions lying in the pump energy ranges identified by *Qiao et al.* [194], but aligning with the finding of *Kim et al.* [196]. *Jiang et al.* [201] also suggested two hot-carrier relaxation (cooling) phenomena with the following time scales: $\tau_1 = 190$ fs and $\tau_2 = 535$ fs. However, the assignment of the second timescale to hot-carrier cooling could be substantially different when accounting for an Intersystem Crossing (ISC) phenomenon bringing the carriers directly to the $d-d$ states. In another study, *Zhang et al.* [204] employed optical absorption and THz probes to examine the self-trapping of photogenerated free carriers and identified a self-trapping time of 0.5-1 ps. In addition, it is worth noting that the existing time-resolved data on Co_3O_4 were predominantly analysed and interpreted within a molecular framework rather than a solid-state perspective.

3.1.2 Goal of this thesis chapter

In this chapter, the microscopic mechanisms underlying the optical properties of Co_3O_4 are studied through a correlative approach combining steady-state and, critically, time-resolved spectroscopic techniques. In particular, the aim is to reach a comprehensive characterization of the photoinduced dynamics of the Co_3O_4 system upon 1.55 eV and 3.1 eV pumping. Such photon energies correspond to the selective pumping of intersite $d-d$ CT between Co^{3+} and Co^{2+} (black box in Fig. 3.2) and to a mix of two intersite $p-d$ CTs from O^{2-} to Co^{3+} and Co^{2+} (purple box in Fig. 3.2), respectively. Time-resolved techniques are envisaged in this case because they allow for the generation of charge carriers upon pumping of a specific electronic transition and to explore their relaxation channels. The most significant findings stem from broadband visible transient reflectivity measurements. This technique enables to capture the femtosecond-picosecond incoherent (charge) and coherent (phonon, magnon or electronic) dynamics of Co_3O_4 in the 1.63-2.7 eV probe energy range, following optical excitations across the AFM transition. To address the presented open questions, these measurements are complemented with

steady-state ellipsometry, Raman scattering, and Fourier Transform Infrared Spectroscopy (FTIR). The incoherent response of the sample offers insights into the dynamics of the photogenerated carriers and their interactions with the spins and lattice DOF on femtosecond to picosecond time scales. Such interactions are particularly relevant as they guide the charge carriers from the initially generated excited state to the long-lived $d-d$ states. Additionally, the coherent response sheds light on the impulsively generated lattice-, electronic-, and/or magnetic excitations within the system. Coherent response signifies that upon pump absorption, microscopic entities (ions, charge, spin, *etc.*) undergo a phase-locked motion over a macroscopic length scale manifested as an oscillatory signal in time [205]. This coherent response is particularly valuable for isolating the driving forces behind the formation of the ground state order. When detected by monitoring different DOFs (structural, electronic or magnetic) it provides information about the coupling between them [206]. Analysing the coherent response upon a 1.55 eV pump, the open questions about which structural modes are predominantly triggered by intersite and onsite $d-d$ transitions and the nature of these modes are addressed [207, 208]. The analysis would provide information regarding the electron-phonon coupling. Moreover, a remarkable observation occurs upon 3.1 eV pump (*i.e.*, pumping the two intersite $p-d$ CTs from O^{2-} to Co^{3+} and Co^{2+}). In fact, long-living electronic modes are induced in the sample and modulate all the electronic transitions in the probe region below the AFM transition. Similar electronic excitations were observed in the literature and were interpreted with mechanisms such as soft modes within a phase transition [39, 40, 41, 15], Polaron tunnelling (*e.g.*, as in the case of Fe_3O_4 [15]), *etc.* In this case, the observed oscillation is possibly interpreted as a purely electronic spin-orbital oscillation, which remains silent in the ground state but couples with structural (extended Jahn-Teller distortions) and possibly magnetic degrees of freedom, possibly generating a polaron. The observed responses shall be pivotal in gaining insight into the microscopic mechanisms of Co_3O_4, paving the way for a comprehensive understanding of the fundamental phenomena governing TMOs. Moreover, an oscillatory electronic response would give a possible route for the coherent control, relevant for subsequent applications in all-optical switching [21, 43, 45] or to steer chemical reactions in photocatalysis [36].

3.1.3 Sample preparation

The Co_3O_4 thin film samples were prepared by Dr. Natacha Ohannessian and Dr. Daniele Pergolesi in the Thin Films and Interfaces Group of the Paul Scherrer Institute (PSI). The synthesis is nontrivial because the formation of CoO by *e.g.*, in vacuum thermal treatment is reported in Co_3O_4 films deposited by R.F. reactive sputtering [209] and Chemical Vapour Deposition [210] with temperature T = 573 K. In fact, the thermodynamic data [211] of Co_3O_4 leads to the following

decomposition reaction in fixed oxygen partial pressures for the temperature range 1073-1173 K [212]:

$$Co_3O_4 \rightarrow 3\,CoO + \frac{1}{2}O_2 \tag{3.1}$$

The vacuum-annealing by evacuating air (O_2) accelerates the reduction of Co_3O_4 films and the formation of CoO. The sample is epitaxially grown along the [0001] direction on a sapphire (Al_2O_3) substrate by pulsed laser deposition [213, 214, 215]. The choice of sapphire substrate is due to the good matching of the unit cell dimensions and of the space group between Al_2O_3 and Co_3O_4, which favours ordered epitaxial growth along the [1111] direction. The sample crystallographic ordered growth facilitates the characterization with structural techniques and the identification of fingerprints not observed in literature even with optical spectroscopies. The samples prepared have thicknesses ranging from 27 nm to 200 nm. In Section 3.3.1, steady-state characterization will be carried on to evaluate the optimality of the 27 nm sample from different points of view *i.e.*, purity of the sample, crystallographic orientation, and optimal penetration depth matching between pump and probe in the techniques used to characterize the sample.

3.2 Methods

This section starts with a description of static optical characterization techniques employed: Ellipsometry and Fourier Transform Infrared spectroscopy (FTIR). Raman spectroscopy was also utilized and is detailed in section 2.2.2. Then, the description of the pump-probe technique and the techniques employed in this work *i.e.*, Time-Resolved Reflectivity (TRR), Time-Resolved X-Ray Emission Spectroscopy (TR-XES), and Time-Resolved X-Ray Diffraction (TR-XRD) is given. For each technique, the general principles, experimental implementations, and data analysis procedures are briefly presented.

3.2.1 At-equilibrium approaches

3.2.1.1 Spectroscopic visible ellipsometry

Optical spectroscopy ranging from near Infrared to Ultraviolet is a powerful tool to explore the key physical properties of correlated TMOs [216, 217]. In general, relevant optical quantities *e.g.*, optical conductivity σ are extracted from reflectivity or transmissivity through a Drude-Lorentz fitting or Kramers-Kronig transformations. Instead, the ellipsometry technique allows for the measurement of a pseudo-dielectric function and, from this, the relevant optical quantities are extracted without the need to apply fitting or Kramers-Kronig procedures. This

technique consists of measuring the complex r_p and r_s Fresnel coefficients which correspond to reflected light with parallel (p) and perpendicular (s = senkrecht) polarization with respect to the sample plane. For the material-air interface, the Fresnel coefficients are expressed as:

$$r_p = \frac{\widetilde{n_s}\cos\phi_0 - \widetilde{n_0}\cos\phi_s}{\widetilde{n_s}\cos\phi_0 + \widetilde{n_0}\cos\phi_s} \tag{3.2}$$

$$r_s = \frac{\widetilde{n_0}\cos\phi_0 - \widetilde{n_s}\cos\phi_s}{\widetilde{n_0}\cos\phi_0 + \widetilde{n_s}\cos\phi_s} \tag{3.3}$$

$$\tag{3.4}$$

where $\widetilde{n_s}$ is the complex refractive index of the sample, $\widetilde{n_0}$ is the air refractive index, ϕ_s and ϕ_0 are the angles resulting from Snell law ($\widetilde{n_0}\sin\phi_0 = \widetilde{n_0}\sin\phi_s$). By taking the ratio between the two coefficients, one can look at the polarization variation ρ. This is a complex number and thus can be decomposed in amplitude and phase:

$$\rho = \frac{r_p}{r_s} = \tan\Psi e^{i\Delta} \tag{3.5}$$

where Ψ and Δ are the ellipsometry angles related respectively to the amplitude and the phase changes. By combining this with a broadband source and a monochromator, energy-dependent information on the sample is obtained through the ellipsometry angles Ψ and Δ. The polarization variation ρ allows to retrieve the dielectric function ϵ. With the hypothesis of an isotropic material, the frequency (energy) dependent $\epsilon(\omega)$ as a function of ρ and the angle of incidence θ can be expressed as:

$$\epsilon(\omega) = \sin^2\theta\left[1 + \tan^2\theta\left(\frac{1+\rho(\omega)}{1-\rho(\omega)}\right)^2\right] \tag{3.6}$$

Considering a material within the hypothesis of linear response theory, *i.e.*, under small perturbative conditions, the optical response shall be given by the optical conductivity $\sigma_{\mu\nu}(\omega)$. $\sigma_{\mu\nu}(\omega)$ relates an applied electric field with a certain frequency ω to the measured current $\mathbf{J}(\omega)$ by:

$$J_\nu(\omega) = \sum^{\mu} \sigma_{\mu\nu}(\omega)E_\mu \tag{3.7}$$

where μ and ν are the components of the electric field $\mathbf{E}(\omega)$ and current $\mathbf{J}(\omega)$, respectively. $\sigma_{\mu\nu}(\omega)$ is generally a tensor and derives from the material's microscopic properties. In this theoretical framework, Kubo provided a formula to compute $\sigma_{\mu\nu}(\omega)$ components and express its momentum and frequency dependencies [218]:

$$\sigma_{\mu\nu}(q,\omega) = \frac{ie^2}{\omega}\left[\frac{1}{V}\chi^{jj}_{\mu\nu}(q, i\Omega_n \to \hbar\omega + i0^+) + \delta_{\mu\nu}\frac{\langle n\rangle}{m}\right] \tag{3.8}$$

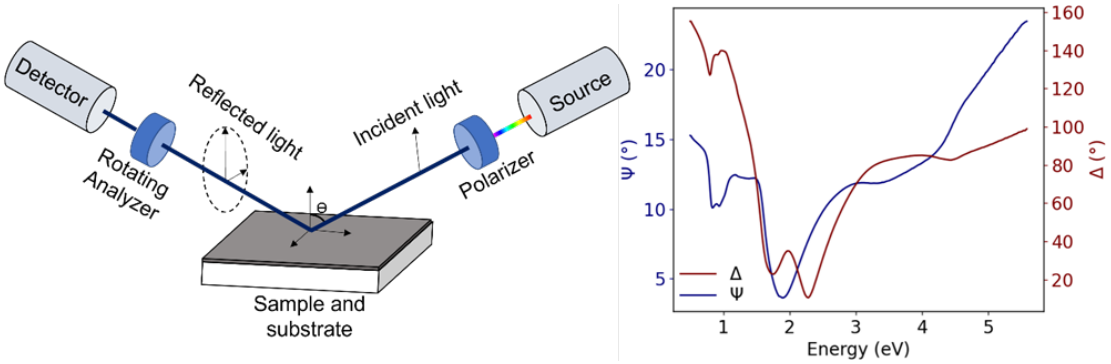

Figure 3.3: (a) Scheme of the ellipsometry setup with the main elements, as illustrated in the text. b) Example of a spectrum of the ellipsometry angles Ψ and Δ, measured on a Co_3O_4 sample at 300 K.

where e is the electron charge, ω the frequency, V is the system volume, $\langle n \rangle$ is the average free charges density, m is the charges mass, $\delta_{\mu\nu}$ is a Dirac Delta-function and $\chi^{jj}_{\mu\nu}(q, i\Omega_n)$ is the current-current susceptibility, which in imaginary time τ is defined as:

$$\chi^{jj}_{\mu\nu}(q,\tau) = -\langle T_\tau J^p_\mu(q,\tau) J^p_\nu(-q,0)\rangle \tag{3.9}$$

where J^p is the paramagnetic contribution to the current and T_τ the time ordering operator. The optical conductivity can be directly related to the dielectric function *via* the following equation:

$$\sigma(\omega) = \frac{i\omega}{\epsilon_0}(\epsilon(\omega) - 1) \tag{3.10}$$

With the Kubo formula, it is possible to compute $\sigma(\omega)$ from theoretical models and compare it to experimental data. Therefore, it is possible to connect a microscopic Hamiltonian description to the measured response and assign the proper transitions to the experimental response. Although in this thesis work there shall be no theoretical results on optical conductivity, it is important to highlight the Kubo formula since the real part of the optical conductivity σ_1 will be exploited in the results section. In fact, this is closely related to the absorption of Co_3O_4, therefore, the comparison with the dielectric function must be expressed.

A Woollam Vase ellipsometer with photon energy range from 0.5 to 5 eV was employed. The instrument was equipped with a mechanically-stabilized, Ultra High Vacuum (UHV) cryostat with the lowest temperature reachable ≈ 7 K. This provides the conditions for precise temperature dependent measurements and prevents condensation on the sample surface. The main components of the ellipsometer are sketched in Fig. 3.3. The incident fixed linear polarizer and the outgoing rotating one enable the reconstruction of the polarization ratio by measuring both

the reflection coefficients $r_{s,p}$ as a function of the angle between the two polarizers. The broadband source generates white light which is sent to a monochromator (not shown) and coupled with the first polarizer through an optical fiber. The linearly polarized light is then directed onto the sample and reflected by its surface. The reflected light is sent through a second polarizer (Analyzer) which rotates at a frequency of 20 Hz and detects the polarization state induced by the sample. A detector is then used to measure the intensity of the light as a function of the polarization angle. The employed detectors for this experiments are: strained InGaAs for the NIR (near infrared) energy range and Si detector for VIS-UV (visible-ultraviolet) frequency range. Setting the angle of incidence θ_p close to the Brewster angle allows for enhanced sensitivity of the measurements. Indeed, under the hypothesis of a non-absorbing sample, at the Brewster angle $r_p = 0$ (as will be shown in Fig. 3.9 for two energies). Since the analyser is rotating with a frequency ν, it modulates the intensity of the detected light as:

$$I = I_0(1 + \alpha\cos(\nu t) + \beta\sin(2\nu t)) \tag{3.11}$$

where the coefficients α and β can be extracted by performing a Fourier Transform of the intensity profile or fitting the time curve. The coefficients allow for Ψ and Δ retrieval thanks to the relations:

$$\alpha = \frac{\tan^2\Psi - \tan^2\theta_p}{\tan^2\Psi + \tan^2\theta_p} \qquad \beta = \frac{2\tan\Psi\cos|\Delta|\tan\theta_p}{\tan^2\Psi + \tan^2\theta_p} \tag{3.12}$$

That, expressing Ψ and Δ as a function of α and β, become:

$$\tan\Psi = \sqrt{\frac{1+\alpha}{1-\alpha}}|\tan\theta_p| \quad \text{and} \quad \cos\Delta = \frac{\beta}{\sqrt{1-\alpha^2}} \tag{3.13}$$

The temperature dependent measurements were performed with a cold finger cryostat, whose windows also show an ellipsometry signal. Therefore, it is crucial to remove this background contribution from the experimental data. This was done by comparing the spectra of the sample measured in air and inside the cryostat. The windows effect is then calculated with the following equations:

$$\begin{aligned} \tan\Psi_w &= \frac{\tan\Psi_{\text{cryo}}}{\tan\Psi_{\text{air}}} \\ \Delta_w &= \Delta_{\text{cryo}} - \Delta_{\text{air}} \end{aligned} \tag{3.14}$$

This correction was performed as a function of incident photon energy and it was assumed to be constant for every temperature. This is because the windows are considered as well insulated from the cold finger thanks to the vacuum pumped in

the cryostat. The following step is to extract the dielectric function from the windows corrected ellipsometry data. This was done using the RefFit software [219] with the employment of Variational Dielectric Functions (VDF). The RefFit software allows for thin film optical quantities retrieval by creating a model for each layer of the film (in this case substrate and film) considering the thickness, light incidence angle and light polarization. The optical quantities of Co_3O_4 on sapphire were extracted with the following steps: (i) fit of the substrate response given by its refractive index n_{sub} with a Drude-Lorentz model; (ii) simultaneous fit of the Co_3O_4 Ψ and Δ responses (whose spectrum for RT is shown in Fig. 3.3) with a Drude-Lorentz model; (iii) application of VDF to remove the discrepancies between the Drude-Lorentz model of Co_3O_4 and the real sample response keeping the Kramers-Kronig (KK) constraints and (iv) extraction of optical quantities through built-in conversion functions. The VDF method is described in detail in literature [219]. In the following, the fundamental aspects are highlighted. Consider a reflectivity (R) spectrum in the energy range [$\hbar\omega_{min}$, $\hbar\omega_{max}$] at a given incidence angle θ and polarization. A universal way to extract the dielectric function $\epsilon(\omega)$, is to fit $R(\omega)$ using some model function, which automatically satisfies the KK relation and uses the Fresnel relation between $\epsilon(\omega)$ and $R(\omega)$. Fresnel relation is crucial to properly account for particular experimental conditions such as the given θ, the substrate contribution, and so on. If the features of the reflection coefficient are matched, the model dielectric function shall resemble the true $\epsilon(\omega)$. In principle, no specific model can be assumed. Therefore one needs to take a trial function and give it a set of parameters to let it be "flexible enough" to effectively approximate the true dielectric function. In this particular case, a combination of Drude-Lorentz functions was used. These had fixed frequencies ω_i (i = 1, ..., N) and linewidths γ_i corresponding to the value of each point (or every two, three *etc.*) and the distances between adjacent points ($\gamma_i = \omega_{i+1} + \omega_{i-1}/2$), respectively. The only parameters that were left to change were the plasma frequencies ω_{pi} which determine the spectral weights of the oscillators. The idea is that each oscillator is "locally responsible" for the spectral weight near each ω_i. By choosing a frequency mesh that is fine enough, one can accurately fit every $R(\omega)$ spectrum and extract $\epsilon(\omega)$ keeping the KK relations satisfied. Then, from $\epsilon(\omega)$, one can retrieve interesting optical quantities such as transmission ($T(\omega)$), $\sigma(\omega)$ and so on in the [$\hbar\omega_{min}$, $\hbar\omega_{max}$] energy range.

3.2.1.2 Fourier Transform Infrared Spectroscopy

Here, the concept of Fourier Transform Infrared Spectroscopy is introduced and its experimental realization is described. The general principles and the setup description are based on the main literature reviews [220, 221, 222]. As stated in the Fourier Theorem, each signal $f(x)$ under certain conditions can be expressed

as a series expansion of sine and cosine waves:

$$f(x) = \frac{A_0}{2} + \sum_{n=1}^{\infty} \left(A_n \cos \frac{n\pi x}{L} + B_n \sin \frac{n\pi x}{L} + B_n \right) \tag{3.15}$$

where $A_0/2$ is the mean value of the signal f over an interval (-L,L):

$$\frac{A_0}{2} = \frac{1}{2L} \int_{-L}^{L} f(x) dx \tag{3.16}$$

and the coefficients A_n and B_n are expressed as:

$$\begin{aligned} A_n &= \frac{1}{L} \int_{-L}^{L} f(x) \cos \frac{n\pi x}{L} dx \\ B_n &= \frac{1}{L} \int_{-L}^{L} f(x) \sin \frac{n\pi x}{L} dx \end{aligned} \tag{3.17}$$

The expansion of $f(x)$ is known as the Fourier series and is periodic with period $2L$, while A_n and B_n are called Fourier coefficients. The extension of the Fourier series to include non-periodic functions or functions which are periodic in the interval $(-\infty,\infty)$ brings to Fourier integrals. With this extension one can find some functions $h(\nu)$ and $g(\delta)$ that are related as:

$$\begin{aligned} h(\nu) &= \int_{-\infty}^{\infty} g(\delta) e^{i2\pi\nu\delta} d\delta \\ g(\delta) &= \int_{-\infty}^{\infty} h(\nu) e^{-i2\pi\nu\delta} d\nu \end{aligned} \tag{3.18}$$

where

$$e^{\pm i2\pi\delta\nu} = \cos(2\pi\nu\delta) \pm i \sin(2\pi\nu\delta) \tag{3.19}$$

The $h(\nu)$ and $g(\delta)$ functions can be expressed in the following way:

$$\begin{aligned} h(\nu) &= F(\nu, \delta)[g(\delta)] \\ g(\delta) &= F^{-1}(\delta, \nu)[h(\nu)] \end{aligned} \tag{3.20}$$

where $F(\nu, \delta)$ and $F^{-1}(\delta, \nu)$ are called Fourier transform (FT) and Inverse Fourier Transform (IFT), respectively. $F(\tau, \delta)$ transforms a function $h(\nu)$ into the function $g(\delta)$, which is linear (*i.e.*, $g(ax + by) = ag(x) + bg(y)$ with a and b real numbers). By measuring $g(\delta)$, therefore, it is possible to recover $h(\nu)$ accurately.

The effect of F and F^{-1} is shown in Fig. 3.4 on two simple signals: a single frequency peak (Dirac Delta) and a broad peak represented with a single Lorentz function. If the input is a Dirac Delta *e.g.*, a monochromatic wave, the application

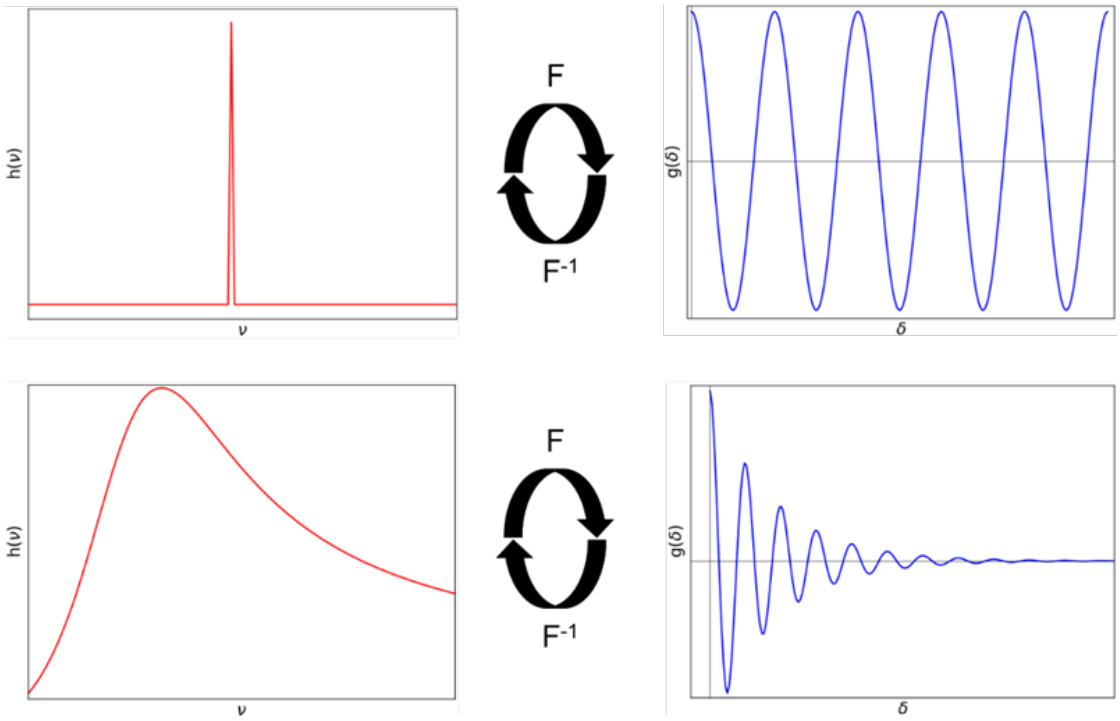

Figure 3.4: Fourier Transform applied to two main signals (upper spectra) Dirac Delta and its FT and (lower spectra) a broadband source and its FT showing a damped-cosine appearance.

of F results in a cosine function. Instead, if the input is a broadband source *e.g.*, the spectrum of a light source with some sample contributions, the output of the FT shall be maximum in 0 and shall have the form of a damped cosine-like function going to 0 as δ goes to infinity. If the source has more than one contribution *i.e.*, is represented by more than one oscillator, the FT output shall be a combination of damped cosine-like functions with different periods (not shown).

In this thesis work, FTIR was employed to look at the Infrared (IR) active vibrational modes of solid-state samples. For a nonlinear molecule with N atoms, there are $3N-6$ vibrational motions of the atoms. A vibrational mode is IR active (*i.e.*, it absorbs the incident infrared light) if the dipole moment of the molecule changes during the course of the vibration:

$$\langle \psi_i | qr | \psi_f \rangle = q \int \psi_i^* r \psi_f d^3r \neq 0 \tag{3.21}$$

where qr is the electrical dipole moment operator while ψ_i and ψ_f represent the initial and final vibrational states wavefunctions, respectively. Due to this, symmetric vibrations are usually not detected in the IR and in particular, in a centrosym-

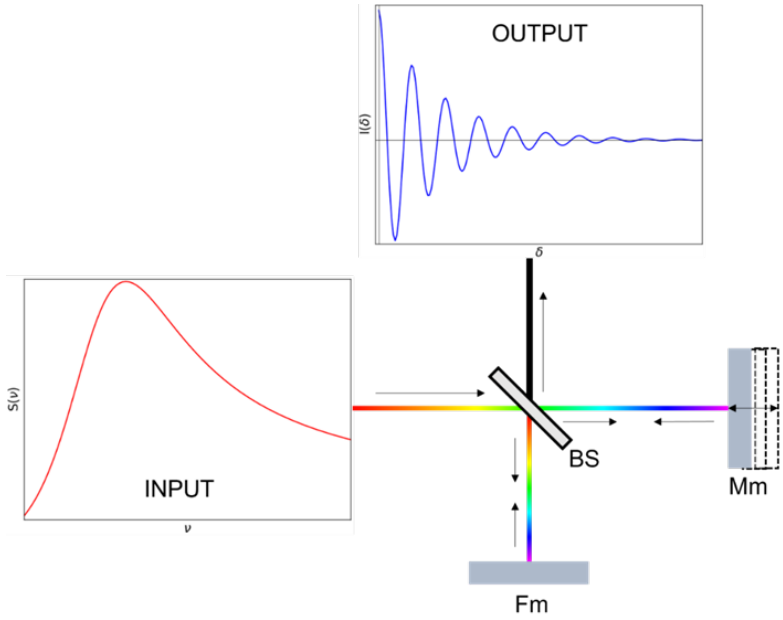

Figure 3.5: Sketch of the Michaelson interferometer configuration, the core element of FTIR setups. The input is a broadband spectrum taking into account the features of the source and of the sample. The output shall be an interferogram $I(\delta)$ (blue spectrum) as a function of the optical path difference δ created by the movable mirror Mm.

metric molecule, all vibrations which are symmetrical with respect to the centre are infrared inactive.

The FT spectrometer is characterized by two main optical components: (i) an input source which produces $g(\delta)$ over a range of values, and (ii) the system to perform all the mathematical operations to retrieve $h(\nu)$ *i.e.*, the spectrum in the frequency range. The principal component of such a spectrometer is a Michelson interferometer sketched in Fig. 3.5, with its main components: the source, the beam splitter (BS) with center O, the fixed mirror (Fm), the movable mirror (Mm) and the detector. In O the source beam is divided into two perpendicular components. One travels to Fm while the other travels to Mm and both are reflected back and recombined at the O position. If the the lengths $(\bar{O}\bar{M}\bar{m})$ and $(\bar{O}\bar{M}\bar{f})$ are equal $(\bar{O}\bar{M}\bar{m}) = (\bar{O}\bar{M}\bar{f})$, then the optical path difference (δ) introduced by Mm distance (L) from BS is $\delta = 2L$, since the ray travels along $(\bar{O}\bar{M}\bar{m})$ twice. If the input is monochromatic with wavelength λ the output shall be oscillatory (cosine-like) as already illustrated in Fig. 3.4. Moving Mm by $L = \lambda/4$, then $\delta = \lambda/2$ and the two beams interfere destructively at O, thus zero intensity is detected. Instead, moving Mm to $L = \lambda/2$, then $\delta = \lambda$ and the interference at O is constructive, thus maximum intensity is detected. This is the simplest

case but allows one to introduce the case of a polychromatic source which can be seen as an infinite series of monochromatic beams. With a polychromatic source, constructive interference (maximum intensity) is detected only at $\delta = 0$ while the rest of the output shall be composed by several maxima and minima in an oscillatory-like behaviour, approaching 0 as the δ goes to infinity. The intensity measured at the detector as a function of the optical path difference $I(\delta)$ shall be called interferogram. In real cases $I(\delta)$ has features caused by the source, the beam splitter and the sample responses. The spectrum $S(\nu)$ is related to $I(\delta)$ *via* the following formula:

$$S(\nu) = C \int_{-\infty}^{\infty} \left[I(\delta) \frac{1}{2} I(0) \right] e^{-i2\pi\nu\delta} d \tag{3.22}$$

where C is a constant $I(0)$ is the signal intensity at $\delta = 0$. Since Mm can move only for a finite distance in the interval (-L,L), the equation becomes:

$$S(\nu) = C \int_{-L}^{L} \left[I(\delta) \frac{1}{2} I(0) \right] e^{-i2\pi\nu\delta} d \tag{3.23}$$

resulting in a loss of spectral information in recovering $S(\nu)$. The more the mirror travels the better the $S(\nu)$ resolution is. The relation between the resolution $\Delta\nu$ and mirror displacement τ may be derived by considering an interferometer illuminated by two sources ν_1 and ν_2 with $\nu_2 - \nu_1 = \Delta\nu$. To completely resolve ν_1 and ν_2 the mirror Mm must be moved such that the two sources are out-of-phase. The theoretical resolution of a Michaelson interferometer is:

$$\Delta\nu = \frac{1}{\delta} = \frac{1}{2L} \tag{3.24}$$

For example, to resolve up to $1\,\mathrm{cm}^{-1}$ the mirror must move of 0.5 cm beyond $\tau = 0$, while, a resolution of $0.1\,\mathrm{cm}^{-1}$ is reached moving Mm of 5 cm.

3.2.2 Pump-probe approaches

The pump-probe technique is based on stroboscopic measurements on a repeatable dynamic. A pulsed laser is used as "clock" and divided into two branches *i.e.*, the pump and the probe. A delay is then introduced between the pump, which is devoted to the photoexcitation of the charge carriers and the probe, which takes snapshots either in the Fourier domain or in the real space acquiring the variation of a physical observable over time. To get access to the resulting output, spatio-temporal overlap on the sample is required. This is reached when both the pump and probe pulses are focused in the same sample area and impinge on the sample within the same time of flight (*i.e.*, the two branches have equal length). Then, one

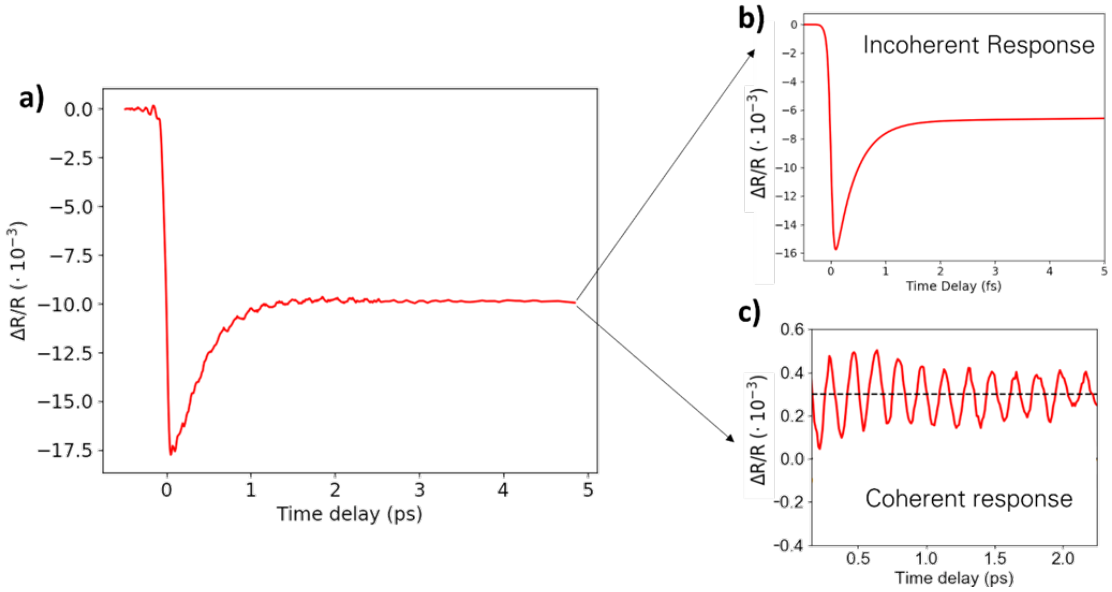

Figure 3.6: (a) An example of ΔR/R trace *vs.* time delay in ps as detected by the TR experiment. The trace is decomposed on the right into its incoherent (b) and coherent (c) responses.

of the branches' length is increased or decreased to introduce the delay and look at the response as a function of time. This method can be implemented in various regimes such as optical (UV-Vis-Nir), hard and soft x-rays, THz and electrons. In this work, the focus is on Time-Resolved Reflectivity (TRR), Time-Resolved X-Ray Emission (TR-XES), and Time-Resolved X-Ray Diffraction (TR-XRD), which will be described in the following.

3.2.2.1 Time-resolved reflectivity (TRR)

Time-resolved Reflectivity is a pump-probe technique sensitive to the photoinduced variation of the sample optical properties as a result of the changes in its dielectric function $\epsilon(\omega)$. Assuming a linear response and using a simple first-order perturbation, one can explicit the pump-induced modifications of charge carriers density n_e, electronic temperature T_e and lattice coordinates Q_n in the transient reflectivity signal, through the dielectric function [208, 223]:

$$\frac{\Delta R}{R} = \frac{\partial ln(R)}{\partial \epsilon} \cdot \frac{\partial \epsilon}{\partial n_e} \cdot \Delta n_e + \frac{\partial ln(R)}{\partial \epsilon} \cdot \frac{\partial \epsilon}{\partial T_e} \cdot \Delta T_e + \frac{\partial ln(R)}{\partial \epsilon} \cdot \frac{\partial \epsilon}{\partial Q_n} \cdot \Delta Q_n + ... \tag{3.25}$$

The first and second terms in the sum ($\frac{\partial ln(R)}{\partial \epsilon} \cdot \frac{\partial \epsilon}{\partial n_e} \cdot \Delta n_e$ and $\frac{\partial ln(R)}{\partial \epsilon} \cdot \frac{\partial \epsilon}{\partial T_e} \cdot \Delta T_e$)

show the dependence of ϵ from the charge carriers density n_e and the electronic temperature T_e, indicating the electron dynamics. The third term ($\frac{\partial ln(R)}{\partial \epsilon} \cdot \frac{\partial \epsilon}{\partial Q_n} \cdot \Delta Q_n$), shows the dependence of ϵ from the lattice coordinates Q_n and explicits the lattice dynamics. Eq. 3.25 can be generalized by adding terms which explicitly account for the charge-lattice and spin-lattice couplings [223, 224, 225, 226, 227, 228]. A $\Delta R/R$ trace as a function of (from now on indicated also as "*vs.*") time delay in ps is reported in Fig. 3.6a. The photoinduced response of the sample can be divided into two components, namely, an incoherent and a coherent response (Fig. 3.6b and c).

The above band gap excitation of a material and the subsequent relaxation of the charge carriers affects the dielectric function of the system and thus its reflectivity giving the incoherent response. On sub-100 fs time scales, the photoexcited nonequilibrium charge density, described as a Fermi-Dirac distribution characterized by an electronic temperature T_e, thermalizes *via* electron-electron scattering. Later, on sub-ps time scales, the relaxation is mediated by electron-phonon scattering which leads to the equilibration between carrier and lattice temperatures $T_e = T_L$ [229]. Eventually, the photocarriers recombine *via* radiative and/or non-radiative Auger recombination processes, the latter being dominant at high carrier densities [230]. The relaxation pathways of the material and their characteristic time scales can be extrapolated from the incoherent response through a multiexponential fitting procedure as shall be shown later in this chapter.

Furthermore, when an ultrafast pump pulse has a duration shorter than the period of a collective excitation be that electronic, structural or magnetic, a coherent response can be observed (see section 3.1.2). The phase-locked oscillation of the collective excitation (*e.g.* coherent phonons) introduces a periodic modulation of the dielectric function seen as an oscillation in the $\Delta R/R$ trace *vs.* time delay (Fig. 3.6c) [231]. In the example case of coherent phonon generation, the two principal mechanisms are represented by Impulsive Stimulated Raman Scattering (ISRS) and Displacive Excitation of Coherent Phonons (DECP). A scheme of the two processes is shown in Figure 3.7. In ISRS (3.7a), if the dielectric function is dependent on the lattice displacement of the phonons *i.e.*, $\frac{\partial \epsilon}{\partial Q_n} \neq 0$, the pump laser may trigger a coherent vibrational motion in the electronic ground state potential. The coherently excited phonon must be Raman active for the condition imposed on the dielectric function [207, 232]. Instead, the DECP process (Fig. 3.7b) is configured as an impulsive shift of the excited state potential energy surface triggered by the pump pulse. This is due to the electron-phonon interaction between the photocarriers and the lattice crystal [208]. The first theoretical treatment of this mechanism hypothesized linear dependence of the lattice shift from the charge carrier density, thus describing the generation of one or more totally-symmetric (*e.g.*, A_{1g}) modes upon excitation [208]. However, if the appropriate symmetry

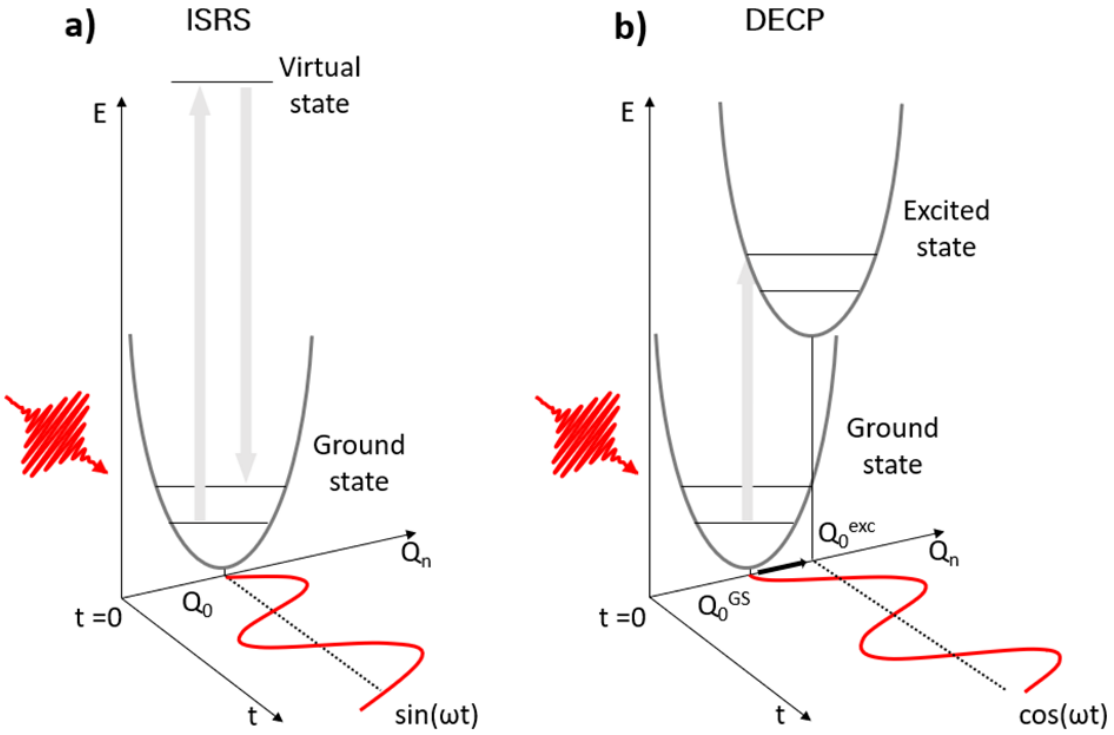

Figure 3.7: Schematic layout of the generation mechanisms and the expected $\Delta R/R$ signal *vs.* time of ISRS (a) and DECP (b). In ISRS, the coherent dynamics occurs in the ground state electronic potential and its outcome is a sin-like wave. Instead, the DECP coherent response is in the excited state potential energy surface and is seen as a cosine-like wave on the $\Delta R/R$ *vs.* time.

components of the carrier density are taken into account, the DECP theory can be extended to phonons with lower symmetry. Despite both mechanisms manifesting as coherent modulation of the optical properties of a system, they can be distinguished by looking at the relative phase of the oscillatory response. ISRS phonons are expected to follow a sine-like behaviour as a function of time since they start from the equilibrium position of the ground state (Fig. 3.7a). DECP phonons follow a cosine-like behaviour with time caused by the generation due to impulsive shift of the excited electronic potential energy surface(Fig. 3.7b).

In the following, the femtosecond broadband visible set-up is presented. It operates either in absorption or reflection geometry. The measurements were performed in the Laboratory for Ultrafast Spectroscopy (LSU, LACUS) of Prof. M. Chergui at the École Polytéchnique Fédérale de Lausanne (EPFL) with the collaboration of Dr. Oliviero Cannelli. A sketch view of the system is shown in Fig. 3.8. A Ti:sapphire oscillator (Halcyon, KMLabs), pumped by a continuous wave Nd:YVO4 laser (VERDI, Coherent), delivers sub-50 fs pulses centred at

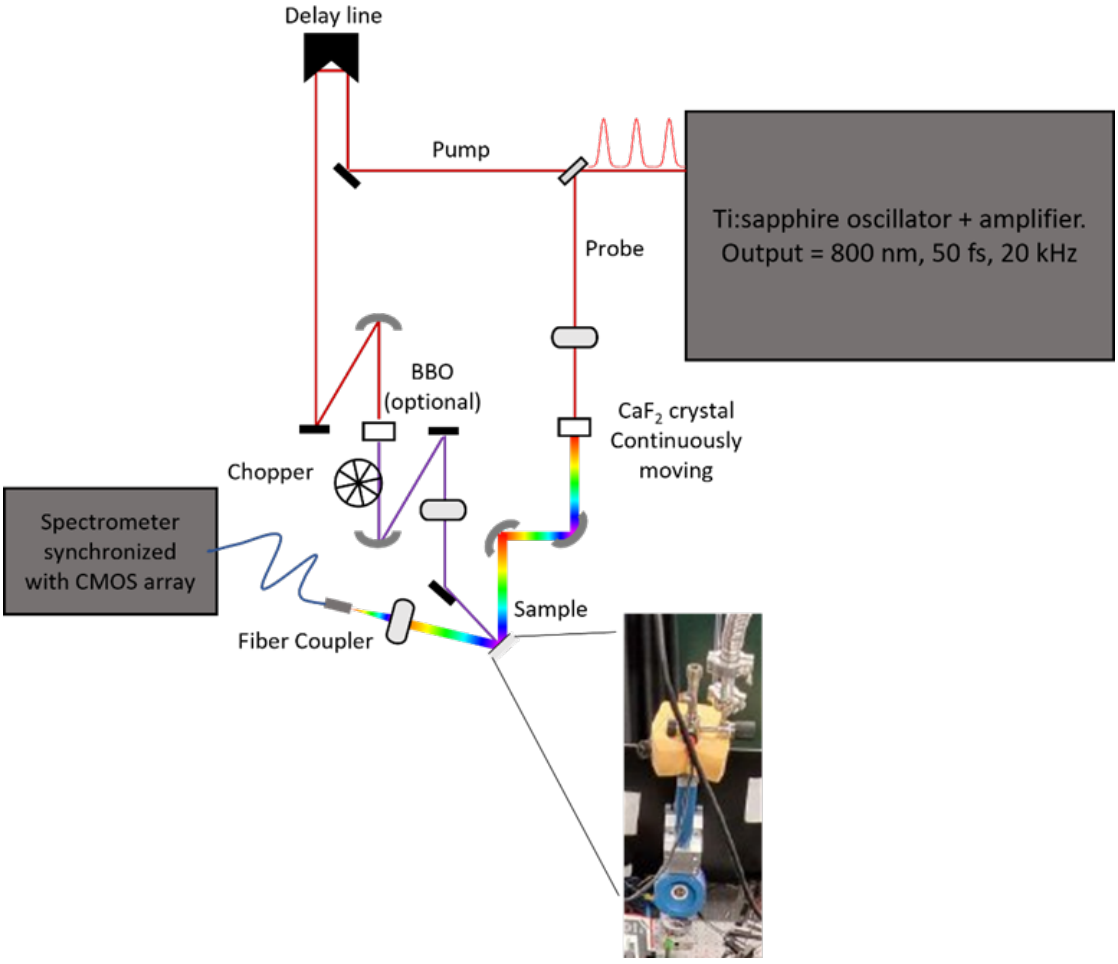

Figure 3.8: Diagram of the 20 kHz laser system and transient reflectivity visible set-up.

1.55 eV with a repetition rate of 80 MHz, and is used as a seed for a cryogenically cooled regenerative amplifier (Wyvern500, KMLabs). This latter is pumped by three Q-switched Nd:YVO4 pump lasers (Photonics Industries) and is set to operate at 20 kHz. The output of the amplifier consists in 60 fs pulses of 6 mJ centred at 1.55 eV with a shot-to-shot energy fluctuation below 0.1% rms [233]. The time-resolved broadband visible experiment takes about 10 μJ of the resulting output with p-polarization selected through a thin polarizer and splits it into pump and probe branches with an 80% - 20% ratio by an ultrafast beam splitter. The pump pulse is delayed in time with respect to probe through a motorized delay line and can be optimally focused with a 20 cm spherical mirror into a 0.5 mm-thick type I β-BaB_2O_4 (BBO) crystal to generate 3.1 eV pulses. A 100-blade mechanical chopper is placed close to the focus position and is set to operate at 10 kHz,

phase-locked to the laser repetition rate (20 kHz). The beam is then collimated and, if the pump is frequency doubled, the residual 1.55 eV intensity is removed with 4 harmonic separators. The beam is focused into the sample in normal incidence when working in transmission mode or at 22° incidence angle when working in reflection. In the probe branch, a supercontinuum white light is generated by focusing the fundamental into a 2 mm-thick CaF_2 crystal. To increase the quality of the spectrum and prevent damaging of the CaF_2 the following steps were implemented. Firstly, the 1.55 eV fundamental is filtered down to 0.5 μJ by means of a Neutral Density (ND) filter. Secondly, the quality of the white light is optimized *via* an iris positioned before the 15 cm focusing lens and by translating the CaF_2 position along the beam focus with a micrometric manual stage. During the operations, the crystal is continuously moved at 10 kHz along the vertical direction and scanned along the horizontal direction with a motorized stage to prevent respectively short and long-term photoinduced degradation. A pair of 90° off-axis parabolic mirrors is used to collimate and focus the probe on the sample and the residual 1.55 eV is filtered by a long-pass glass filter. Typical sizes of the pump and probe beams as spatio-temporally overlapped on the sample are $150 \times 150\,\mu m^2$ and $90 \times 80\,\mu m^2$, respectively. If the reflection geometry is chosen, the sample is tilted by 22° with respect to the probe beam and the probe output is delivered by a 45° tilted, 2 m long multi-mode optical fibre into a spectrograph where the broadband pulse is dispersed by a 150 gr/mm holographic grating. The resulting spectrally-resolved, pumped and unpumped signal intensities are measured in a shot-to-shot detection mode with a Complementary Metal-Oxide Semiconductor (CMOS) array detector (Hamamatsu S11105, 512 pixels, $12.5 \times 250\,\mu m^2$ pixel size) synchronized to a lock-in data acquisition system. The shot-to-shot acquisition is possible because the maximum readout rate *per* spectrum is almost 100 kHz (each pixel has a readout up to 50 MHz) [233]. A gated signal is delivered by a triggering card which synchronizes the laser amplifier signal (20 kHz) with the 11 MHz master clock of the 16-bit analog-to-digital converter (ACD) and triggers the CMOS readout operation. A replica of this gated trigger is halved and used to phase-lock the chopper at 10 kHz to the laser amplifier outputs [234]. For each time delay, 20000 consecutive shots are recorded, sorted into pumped and unpumped and averaged. If the reflectivity mode is employed, the $\Delta R/R$ signal is computed as:

$$\frac{\Delta R(\omega,t)}{R} = \frac{R_p(\omega,t) - R_u(\omega,t)}{R_u(\omega,t)} \tag{3.26}$$

Where the p and u subscripts respectively stand for *pumped* and *unpumped*, while ω and t correspond to the spectrally-resolved frequency of the probe and the time delay between the pump and the probe at which the pumped and unpumped signals were collected. The transient reflectivity datasets thus obtained were acquired consecutively for c.a. 20 times to increase the Signal-to-Noise Ratio (SNR) in post-

processing. The frequency calibration was performed measuring the absorption of a Holmium solution and the corresponding pure solvent (Hellma). Since the supercontinuum probe is not dispersion (chirp) compensated, the TR maps should be compensated in post-processing. To define the parameters for Group Velocity Dispersion (GVD) correction, pump-probe measurements on the sample substrate (pure sapphire in the case of Co_3O_4) must be performed. The substrate should not absorb light in the pump and probe energy ranges employed. If these conditions are met, the substrate pump-probe measurements shall show a coherent artefact signal only at time delays when the pump and probe pulses overlap in time. The analysis of this measurement allows to determine the frequency-dependent time zero position and the Instrument Response Function (IRF), defined as the cross-correlation width of the pump and probe pulses. An optical cryostat (Optistat, Oxford instruments) with a lower limit below 4.2 K was implemented in the setup to carry out the measurements as a function of temperature. The cryostat is equipped with a Copper cold finger sample holder, a heating resistance and a thermocouple connected to an external temperature controller (Oxford instruments). The vacuum system consists of a turbomolecular pump (Pfeiffer) with minimum reachable pressure of 10^{-6} mbar equipped with a backup scroll pump. The helium flux was regulated through a membrane pump (Pfeiffer) and a gas flowmeter (Oxford instruments) and the gaseous outlet was sent to the laboratory recovery line.

The data analysis was carried out through a combination of Python scripts developed on Jupyter notebooks and other literature-available software such as OPTIMUS [235]. Firstly, the raw TRR datasets from consecutive scans were calibrated with the holmium reference and were averaged together. The substrate and sample processed data were then imported in the OPTIMUS software [235]. The substrate measurements were used to define the precise white light chirp through a second-order polynomial function fitting of the coherent artefact signals. The TRR sample maps were analysed through Global Lifetime Analysis (GLA) approach. The GLA consists in the simultaneous fit of the pump-probe time traces at each frequency ($S_\omega(t)$) of the 2D map with a sum of exponential functions convoluted with a gaussian IRF function [235, 236]:

$$S_\omega(t) = \sum_{i=1}^{n} A_i(\tau_i, \omega) \cdot e^{-\frac{t}{\tau_i}} * IRF(t) \tag{3.27}$$

where $A_i(\tau_i, \omega)$ is the frequency-dependent amplitude of the exponential decay characterized by the τ_i time constant and $*IRF(t)$ indicates the convolution of each component with a Gaussian function. The GLA is a powerful method since it allows fast simultaneous fitting of all the probe energies employed in the experiment and returns the global time constants of the systems. However, it does not take into account the presence of a coherent response that can be excited in the

system in the form of oscillations and may not necessarily give all the information on the behaviour of the electronic transitions in the probe region. Therefore, other Jupyter script routines were developed with the aim of analysing the chirp-corrected 2D maps extrapolating the coherent responses and the behaviour of the electronic transitions as a function of time. The coherent response was analyzed by applying a Fast Fourier Transform (FT) to the residuals thanks to a built-in library. To increase the Signal-to-Noise Ratio (SNR) of the FT traces, multi-energy binning, zero-padding method and Kaiser-Bessel windowing were also applied [237, 238]. The FT and oscillation traces were respectively fitted with Lorentz and sinusoidal functions through Origin Pro 8.5 extrapolating the energy, amplitude, Full Width at Half Maximum (FWHM), phase, and damping-time of each coherent oscillation. The effect of the TRR response on the oscillators (*i.e.*, the electronic transitions) in the probe energy region was analysed by extracting the photon energy-dependent effective R (R_{eff}) at a given time delay t (or fluence F in the case of fluence dependence) from $\Delta R/R$ signal *via* the following formula:

$$R_{eff}(E,t) = (\frac{\Delta R}{R} + 1)R_{static}(E) \tag{3.28}$$

where E represents the photon energy while R_{static} represents the steady-state R measured through ellipsometry. The R_{eff} response was fitted for each time delay starting from the R_{static} Lorentz fit *via* a home-built RefFit macro [219] and the variations as a function of time (or fluence) of oscillators position, amplitude (area) and FWHM were extracted.

3.2.2.2 Time Resolved X-Ray Emission Spectroscopy & Time Resolved X-Ray Diffraction

In this section, the Time Resolved X-Ray Emission (TR-XES) and Time Resolved X-Ray Diffraction (TR-XRD) experiments at the Free Electron Laser (FEL) EXFEL facility shall be discussed in detail addressing the key aspects of: grazing incidence experimental geometry, general principles, and experimental implementation. To measure the TR-XES and TR-XRD response on Co_3O_4 three main requests must be, firstly, satisfied: (i) spatio-temporal overlap in the volume of the sample, (ii) minimization of thermal load and (iii) separation of the sample signal from the substrate one. To satisfy these requirements, a grazing incidence configuration is envisaged. The optical pump reflectivity is retrieved following Fresnel's law. As shown in Fig. 3.9, the pump spot-size in grazing incidence implies a significant reduction of the excitation fluence at constant pump energy since the Reflectivity of the sample grows rapidly to 1. The penetration depth of optical pump changes following Snell's law but, for incidence angles less than 5-10° it is close to the normal incidence ones, respectively 137 nm and 27 nm for 1.55 eV

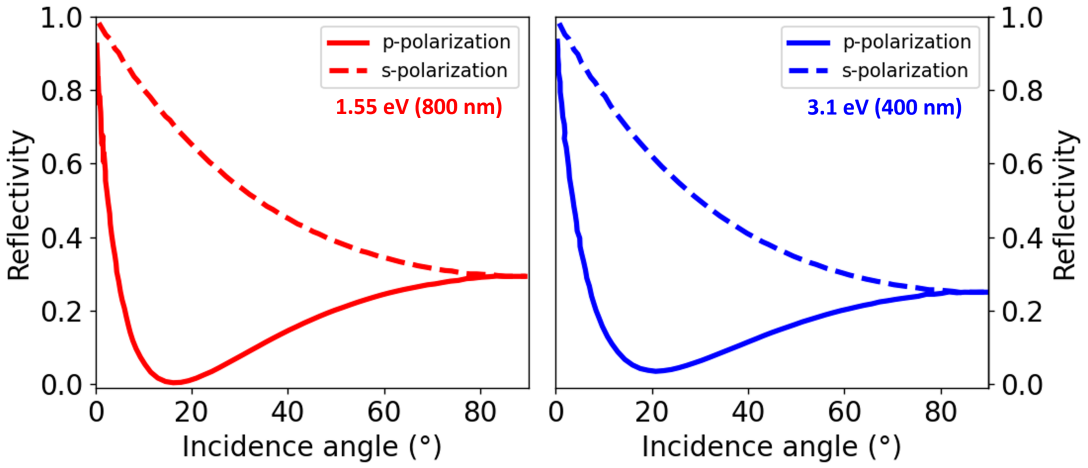

Figure 3.9: Reflectivity for s (dashed) and p (full) polarized light as a function of incidence angle at fixed energy 1.55 eV (red curve, left plot) and 3.1 eV (blue curve, right plot).

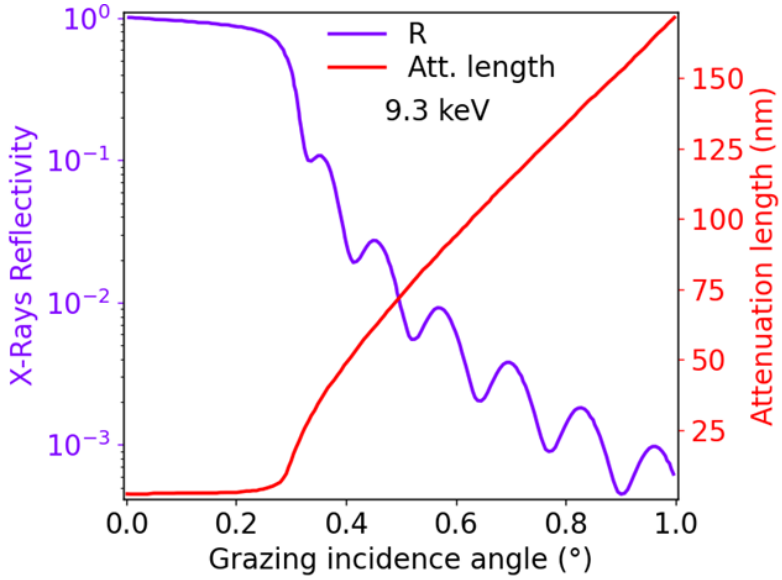

Figure 3.10: Reflectivity (blue, left axis) plotted in $\log_{10}$ scale and attenuation length (red, right axis) in nm plotted as a function of the grazing incidence angle of a 9.3 keV X-Ray. The data are based on CXRO predictions for a 27 nm Co_3O_4 thin film with density 6 g/cm^3 on top of a sapphire (Al_2O_3) substrate with density 3.98 g/cm^3.

(800 nm) and 3.1 eV (400 nm). The probe attenuation length as a function of grazing incidence was instead obtained following CXRO predictions (Figure 3.10, red curve). A strong dependence on the incidence angle is seen above 0.3° with a variation of 50 nm in the 0.3-0.4° region. Therefore, the two conditions of minimization of X-Rays thermal load and matching of pump and probe penetration lengths are achieved for angles between 0.3° and 1°. The sample reflectivity also significantly changes. Above 0.3°, it is kept below 10% and does not affect the experimental conditions (Fig. 3.10, blue curve).

TR-XES X-ray Emission Spectroscopy (XES) is an element-selective technique which is sensitive to the electronic, spin and local structural configuration of the probed site. Among the multiple implementations of this method, the focus shall be on the non-resonant XES applied to Co_3O_4. The reviews made by Bergmann and Glatzel [239] and Van Bokhoven and Lamberti [240] give further information on the other implementations such as Resonant XES, the complementarities between XES and X-Ray Absorption Spectroscopy and other important aspects. A sketch of the XES process and typical spectra obtained for the Co_3O_4 are reported in Fig. 3.11. An inner-shell (core) electron of an element is excited to the continuum following X-Ray absorption (Fig. 3.11a). The process leaves the system in an excited state with a core hole that is immediately filled by an outer-shell electron. The resulting excess energy is released *via* competing Auger or fluorescence decay processes *i.e.*, with the emission of an electron or a X-Ray photon that have lower energies with respect to the exciting photon (Fig. 3.11b). If the removed electron belongs to the K shell ($1s$ orbital) the resulting XES peak shall be referred to as K-line, if instead it is removed from the L shell ($2s$ or $2p$ orbital) the peak shall be L-line and so on. The emission lines shall be also labelled first with α, β, *etc.* symbols and then sub-divided with "1" and "2" depending on their intensities. For example, the K_α line refers to the most intense κ-line given by the filling of a hole in the $1s$ orbital with an electron from the $2p$ orbital. This is sub-divided into $K_{\alpha 1}$ and $K_{\alpha 2}$ depending on whether the starting orbital is $2p_{3/2}$ or $2p_{1/2}$. In the following, Cobalt K_α and K_β lines are considered and their static spectrum is reported in Fig. 3.11c. Even though these processes involve electronic transitions between inner orbitals, both K_α and K_β spectra are indirectly sensitive to the valence electrons of the probed site, which in the case of transition metal atoms correspond to $3d$ orbitals. The valence electrons' sensitivity reflects in the fine structure of the lines through two major effects. (i) the interaction of the electron spin with its own orbital momentum known as Spin-Orbit coupling, especially strong for the K_α lines (≈ 10 eV). (ii) electron-electron interactions that occur within the valence shell or between a core electron (*i.e.*, $2p$, $3p$) and the valence electrons (*e.g.*, $3d$). Therefore, information on valence electronic configuration is obtained

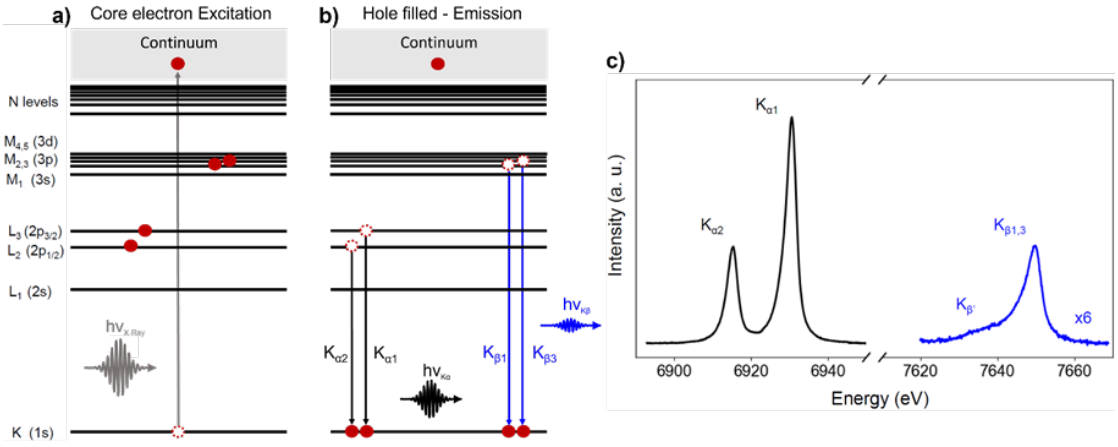

Figure 3.11: Energy level diagrams showing (a) the non-resonant X-Ray photon absorption and (b) recombination and emission of X-Rays that build up the K_α and K_β peaks. (c) Co_3O_4 emission lines at the Cobalt K_α and K_β energies.

by analysing the interaction between the $3d$ occupied orbitals and the $2p$ or $3p$ hole left in the system upon fluorescence decay. Such interaction scales with the overlap between the inner orbitals and the $3d$ wave functions, thus it is stronger for the $3p$ orbitals [241]. Consequently, K_β lines are more sensitive markers of the electronic configuration of the system compared to K_α. More specifically, the position of K_β peaks scales linearly with the number of unpaired $3d$ electrons, provided that the oxidation state and the local environment of the metal site remain constant [239]. Also, K_β divides into $K_{\beta 1,3}$ and $K_{\beta'}$ as a consequence of the $3p-3d$ exchange coupling. This makes the $K_{\beta 1,3}$ and $K_{\beta'}$ sensitive to the spin since their energies move towards each other upon spin decrease. A different relationship is found between the spin states and K_α lines. In this case, the FWHM of the emission lines scale linearly with the effective spin configuration due to the $2d-3d$ exchange interaction [239]. When an optical transition is pumped, charge carriers are moved from the valence to the conduction band. This causes a redistribution of the charges which is reflected in the changes of K_α and K_β spectra. The sensitivity to the valence orbitals makes the time-resolved implementation of XES (TR-XES) suitable to probe photoinduced spin and electronic changes in the transition metal ion's surroundings as a function of time [242, 243, 244, 245].

TR-XRD Atoms have diameters of the order of Ångströms ($1\,\text{Å} = 10^{-10}\,\text{m}$), thus unit cells have dimensions of several Å. This implies that crystals with sizes of microns or larger consist of several unit cells, which repeat periodically in the three dimensions *i.e.*, they possess long-range order. When such periodic structures are irradiated with a wavelength comparable with the periodicity of the material,

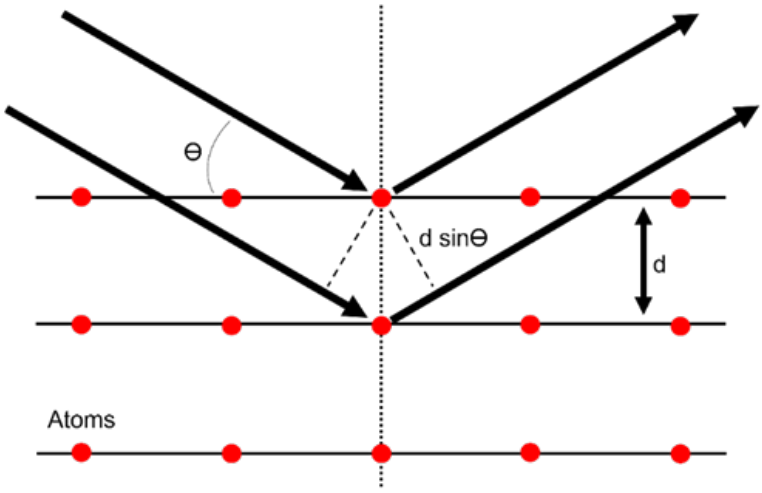

Figure 3.12: Sketch of X-Ray diffraction mechanism in crystalline sites. The relevant parameters such as distance between planes (d) and incidence angle (θ) are indicated.

diffraction effects are produced. To do this, sources that match the unit cell dimensions of a crystal are required. These are represented by X-Rays. The electric field of such waves interacts with an atom which then emits an almost spherical wave with the same wavelength as the incident radiation. The amplitude of this outgoing wave is described by the so-called atom form factor f and is proportional to the number of electrons in the atom. f depends also on the incidence angle θ because of the interference in-between individual atoms (Fig. 3.12). Figure 3.12 illustrates the situation in which constructive interference is obtained *i.e.* when the path of the wave in the lower of the two planes is longer than that of the wave in the upper plane by an integer number of wavelengths λ. In this case, the diffracted beam follows Bragg's equation:

$$n\lambda = 2d\sin(\theta) \tag{3.29}$$

where n is an integer number, θ is the incidence angle and d is the distance between two lattice planes. The positions of the diffraction peaks give precise identification of the sample in Fourier space. Therefore, pumping an electronic transition induces structural changes reflected in the diffraction pattern through changes of: (i) position, (ii) Full Width at Half Maximum (FWHM), and (iii) intensity of the peaks. The peak position change reflects the lattice expansion in a homogeneous way. The FWHM reflects the loss or recovery of the long-range crystalline order through peak broadening or peak narrowing, respectively. Intensity change is related to the atomic displacement due to temperature (Debye-Waller factor) [246]. These aspects are crucial to understanding the lattice dynamics following for example an intersite electron transfer and may be also able to retrieve information

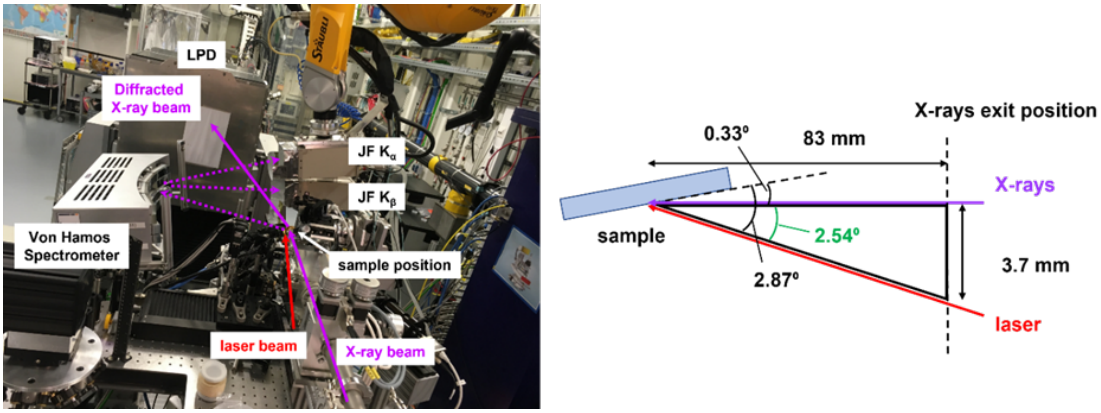

Figure 3.13: (left picture) Back view of the setup utilized for the simultaneous TR-XES and TR-XRD experiments on Co_3O_4 thin film at the FEX instrument at EXFEL. The components are indicated in white boxes. The pump laser is indicated with a red line while the probe X-Ray beam path is traced with both solid (incident, XRD) and dashed (XES) violet arrows. A Von Hamos spectrometer is placed at 90° with respect to the X-rays and is equipped with 6 Si(531) and 10 Ge(111) crystals. The Jungfrau 1M detector (JF k_α) is mounted on a motorized robot arm to collect Cobalt K_α lines while a Jungfrau 500k detector (JF k_β) is mounted on pillars and collects the K_β lines. The LPD detector used for collecting the (311) XRD peak, is placed behind the optical table and can be moved back and forth through a rail. (right) Sketch of the grazing incidence geometry used for the experiment.

on optical-acoustic phonons or other electronic/magnetic excitations launched in the sample after the photoinduced transfer.

In this thesis, the implementation of both TR-XES and TR-XRD techniques shall be carried on in the Femtosecond X-ray Experiments (FXE) beamline of European X Free Electron Laser (EXFEL) in Hamburg [247, 248]. The FXE beamline is equipped with a specially designed burst-mode femtosecond laser system [249]. This system generates broadband 1.55 eV pulses amplified in a multi-stage non-collinear optical parametric amplifier (NOPA) and compressed to 15 fs pulse durations and can be operated at variable repetition rate. In the experiments, the laser fundamental (1.55 eV) or its second harmonic (3.1 eV) were employed at 5 Hz repetition rate and with a spot size of 300x150 μm^2 in normal incidence conditions. An X-Ray pink beam centred at 9.3 keV energy was generated *via* a self-amplified spontaneous emission (SASE) process [250] and was used as a probe for off-resonance XES and XRD measurements. 9.3 keV energy was chosen because it is the optimum intensity and stability trade-off for a pink beam, which is suitable for the experiment, provided by SASE1, which is the EXFEL beamline branch of FXE. Its pulse duration was less than 100 fs, and the laser was impinging on the sample at 10 Hz repetition rate with a maximum average energy of 2.5 mJ

and a spot size of $20 \times 20\,\mu m^2$ FWHM at normal incidence. The total X-Ray transmission was from 4.8% to 1.5% determined as the product of the fixed FEL transmission (30%) and the FXE beamline transmission (16-5%), varied through the insertion of metal filters with different thicknesses. The choice of single-pulse mode, 10 Hz repetition rate and attenuation of the FEL transmission was based on sample damaging tests conducted on-site. Indeed, such a low repetition rate was beneficial in reducing the thermal load on the thin film, representing the most important source of sample degradation. The timing jitter between the laser pump and the FEL probe makes the effective time resolution of pump-probe experiments at the FXE beamline of about 115 fs FWHM [251].

The sample was mounted on a Huber stage on top of a motorized sample manipulator in grazing incidence geometry with an angle of 0.33° with respect to the incoming X-rays and 2.87° with respect to the pump as shown in Fig. 3.13 right panel. A side view camera and a microscope were employed to determine the centre of rotation of the stage using a metallic pin. The pump and probe spot sizes in this geometry were $6\,mm \times 150\,\mu m$ and $3.5\,mm \times 20\,\mu m$, respectively. With these parameters the pump fluences employed were calculated as $7\,mJ/cm^2$ and $5\,mJ/cm^2$ for the 1.55 eV and 3.1 eV beams, respectively. The XES signal was collected using a high-energy resolution Von Hamos spectrometer. This was equipped with 6 Si(531) and 10 Ge(111) crystals to disperse respectively Cobalt K_α and K_β lines. The K_α and K_β emission lines were separately detected using two single module Jungfrau 1M and Jungfrau 500k detectors, respectively. The Jungfrau 1M contains two Jungfrau 500k modules, which have an active area of about $38 \times 76\,cm^2$. The Jungfrau 1M was mounted on a vibrationally stabilized inverted robot arm while the Jungfrau 500k was mounted on fixed pillars [252]. An LPD detector, used to measure the sample (311) XRD peak, was mounted behind the optical table equipped with a rail to adjust its position in the FEL beam direction. A Helium bag and a helium chamber (not shown) were installed to reduce the air scattering of the dispersed X-ray signals at the Von Hamos spectrometer and at the sample position, respectively. During the data acquisition, the time delay between the optical pump and the X-Ray probe pulses was varied using an optical delay line. However, the nominal time delay between the two pulses is affected by the timing jitter of the SASE FEL and electron bunch drifts.

All FEL shots and detector signals are labelled with a so-called "trainID", which enables performing an *a posteriori* sorting of the pump-probe time delays based on machine parameters. In the experiment, the actual time difference between the pump and probe beams was computed accounting for the changes in the "Beam Arrival Monitor" (BAM), a machine feedback which measures the arrival time of the electron bunches on a shot-to-shot basis. During the TR-XRD data analysis, the LPD images were sorted according to the actual time delay and the pump-

probe signal was obtained, for each time delay, with the following procedure: (i) a small ROI of 50×50 pixels was defined, considering only the pixels adjacent to the (311) XRD peak, significantly reducing the data size with respect to the original image of 16 million pixels; (ii) the images were sorted as pumped or unpumped based on the presence of an optical signal measured by a feedback photodiode collecting a small leak of the pump pulse before the sample; (iii) pumped and unpumped images were averaged together and the difference signal was computed; (iv) a figure of merit (FOM) was obtained by taking the absolute value of the full vertical and horizontal binning of the difference signal. For what concerns TR-XES analysis, the traces were obtained by collecting multiple FEL shots at fixed nominal time delays. Due to the low intensity level of the single-shot XES signal, for each image a photon counting correction was applied, harnessing the photon energy sensitivity of the Jungfrau detectors. This procedure enabled a strong suppression of the elastic scattering signal, which is about two orders of magnitude stronger than the XES signal, and to distinguish single-, double-, and multi-photon XES events. Following a procedure similar to the one described for TR-XRD, the actual time delay of the Jungfrau images was computed *a posteriori* accounting for the BAM correction. For each time delay, the images were sorted as pumped or unpumped, averaged, vertically binned, and normalized by their underlying areas. The pump-probe signal was obtained as the difference between the pumped and the unpumped spectra.

3.3 Results & Discussion

3.3.1 Co_3O_4 steady state characterization

In this section, Co_3O_4 main experimental results obtained both through steady-state and time-resolved spectroscopies are presented. Firstly, the chemical and crystalline quality of the sample is assessed through static X-Ray Absorption Spectroscopy (XAS), XRD and electron diffraction experiments and the optical properties in the NIR-Vis-UV ranges are described through ellipsometry. Secondly, an extensive transient reflectivity study is provided showing the main results obtained by looking at the incoherent and coherent responses. Among these, a 10.2 meV oscillation not present in the steady-state is detected. In the attempt to assign the mechanisms related to the origin of such a mode, static Raman and FTIR experimental results are provided, corroborated by DFT calculations. A possible phonon, magnon, bi-magnon origin is discussed. In addition, a possible coupling of the mode with the spin degree of freedom and its effect on the electronic transitions is considered. The results and related observations are ultimately corroborated by presenting TR-XES and TR-XRD preliminary results.

3.3.1.1 Static XAS characterization

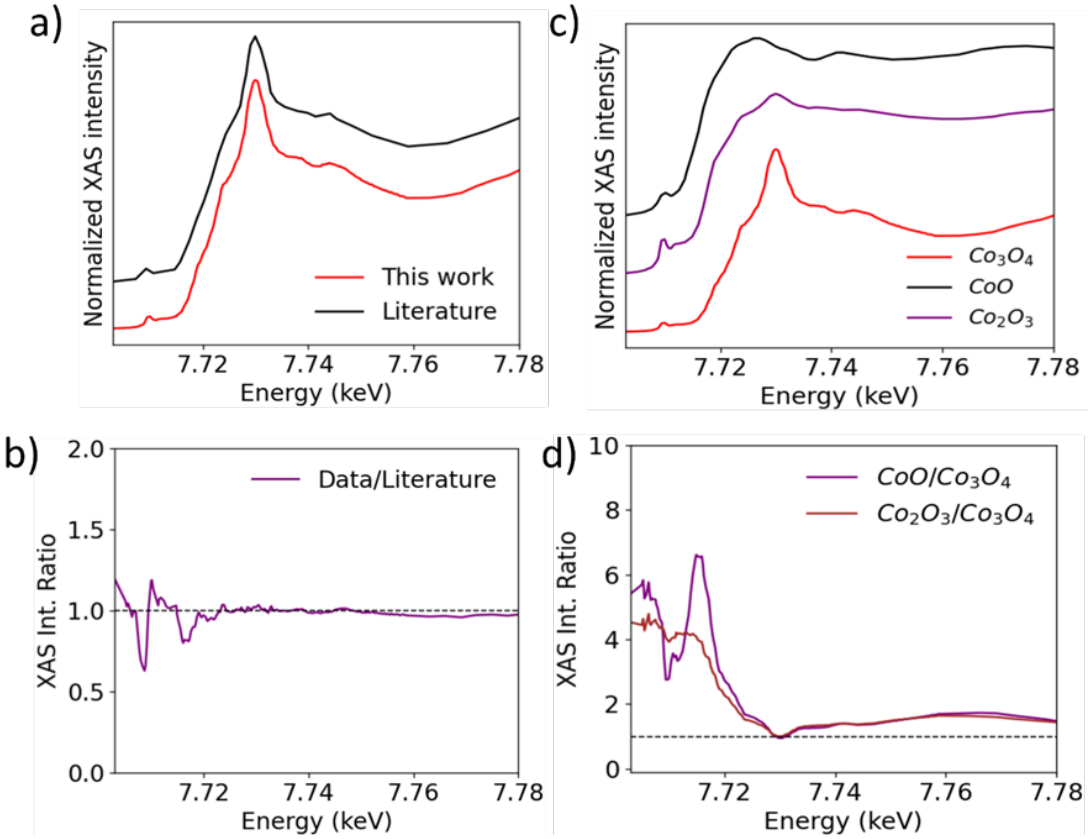

Figure 3.14: (a) XAS spectrum of the Co_3O_4 film (red line) compared with literature measurements (black line) from *Bordage et al.* [253]. (b) Ratio between experimental measurements and literature spectra. c) XAS spectra of Co_3O_4 (blue line) and reference standards: CoO (red line), and Co_2O_3 (black line) which possess exclusively Co^{2+} and Co^{3+} ions, respectively. d) Ratio between the Co_3O_4 XAS spectrum and the reference samples spectra. The spectra in (a) and (c) are normalized by their maximum of intensity and shifted by an arbitrary offset along the vertical axis.

Steady-state X-Ray Absorption Spectroscopy (XAS) characterization was performed at the MicroXAS beamline at the Swiss Light Source (SLS). This study is important to exclude the presence in the sample of Cobalt oxides with stoichiometries different from the Co_3O_4 and is linked to the sample preparation performed to avoid the presence of other oxides with spurious signal (see Section 3.3.1 for details). A fluorescence geometry was employed by putting the sample and detector respectively at 45° and 90° with respect to the incoming X-rays. The Cobalt K absorption edge (7.700-7.780 keV) was probed using a Ketek detector with a

resolution of about 150 eV and a Si (311) crystal monochromator. Such resolution was needed to exclude the elastic scattering signal and isolate Co fluorescence lines. The intensity was corrected by the incoming X-Ray flux while the energy was calibrated using a Cobalt foil. The detected signal is proportional to the XAS absorption coefficient considering the conditions of thin-sample limit [254] which well applies to the sample. The resulting spectrum is reported in Fig. 3.14a and is compared with literature XAS experiments on Co_3O_4 [253]. The spectra are normalized by their maximum intensity and shifted by an arbitrary offset along the vertical axis for clarity. Good correspondence is found between the two spectra in both pre-, main- and post-edge regions suggesting a good quality of the thin film. This conclusion can also be evidenced by plotting the ratio between the two spectra (Fig. 3.14b) showing an almost constant line close to unity. Moreover, the presence of other Cobalt Oxide crystalline compounds is possibly excluded by measuring the spectra of two Cobalt oxide compounds: CoO (red line in Fig. 3.14c), and Co_2O_3 (black line in Fig. 3.14c) which possess exclusively Co^{2+} and Co^{3+} ions, respectively. The difference between Co_3O_4 and the other reference samples is evidenced by the shifted K-edges and, most importantly, by the narrow peak at 7730 eV and broad deep at 7760 eV which are not found in any of the reference sample spectra as shown also by taking the ratio between CoO and Co_2O_3 XAS spectra with respect to the Co_3O_4 one (Fig. 3.14d).

3.3.1.2 Static XRD characterization

Static XRD at the Surface Diffraction end station of the Material Science beamline of Swiss Light Source (SLS) was performed. This study is needed to optimize the experimental geometry in view of the TR-XES and TR-XRD experiments at EXFEL. The aims of this study were: (i) to retrieve the in-plane and out-of-plane vectors; (ii) to define the orientation matrix which relates the reciprocal axes of the crystal with the Cartesian coordinate system of the beamline; (iii) to detect the most intense Co_3O_4 diffraction peaks in the tridimensional space compatible with the experimental geometry of the FEL experiment shown in Section 3.2.2.2 and (iv) to disentangle the peaks of the sample from the substrate ones. The synchrotron setup is shown in Fig. 3.15a. The sample was mounted on a hexapod stage and oriented vertically with respect to the floor. The experimental grazing incidence geometry with an angle of 0.33° and X-Ray beam energy at 9.3 keV were chosen (see section 3.2.2.2). In addition to what discussed in section 3.2.2.2, the 9.3 keV beam energy avoids the collection of fluorescence background since it excites above the Cobalt absorption edge (see Fig. 3.14). The diffracted signal was collected with a Pilatus 100k detector.

The experimental procedure starts with a preliminary assumption on the sample orientation and knowledge of its lattice parameters given by the $Fd\bar{3}m$ struc-

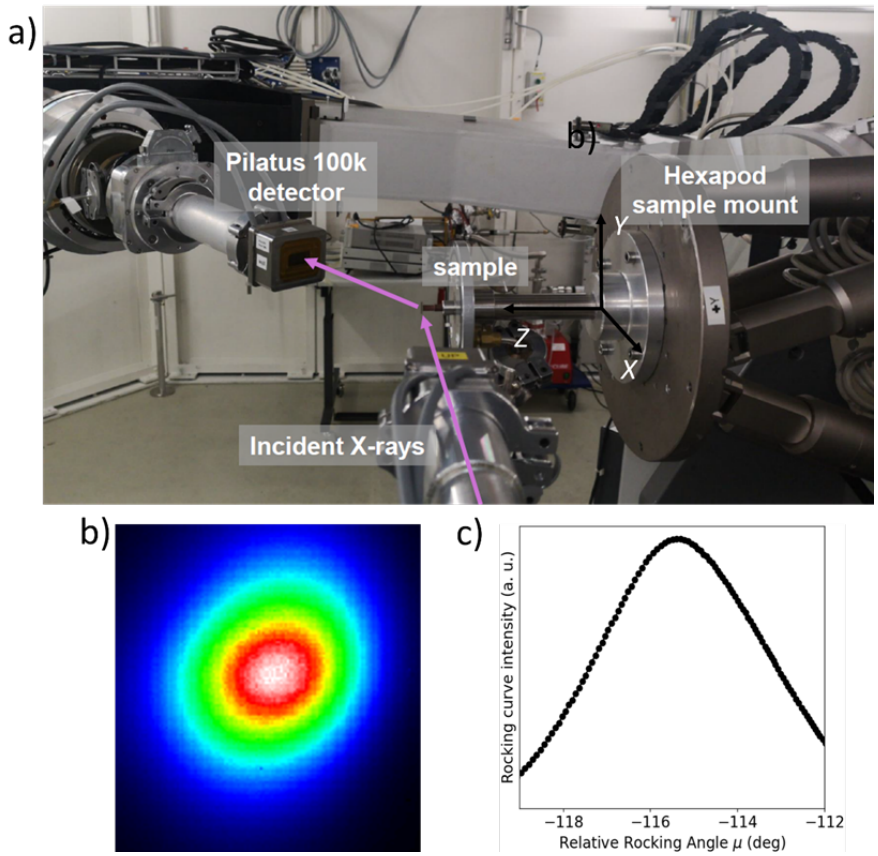

Figure 3.15: a) XRD experimental layout of the Material Science beamline at SLS. The sample is vertically oriented in grazing incidence geometry with respect to the incoming X-Rays. The Pilatus 100k detector is set in the geometry corresponding to the (311) diffraction peak. b) (311) diffraction peak image. c) Rocking curve of the (311) peak.

ture: $a = b = c = 8.151\,85\,\text{Å}$ and $\alpha = \beta = \gamma = 90°$. Once the sample is set in position, the orientation matrix must be defined through the determination of Co_3O_4 in-plane and out-of-plane vectors. These are respectively [111] given by the epitaxial growth direction and $[\bar{1}10]$ (where $\bar{1} = -1$). Such an orientation matrix allows for the prediction of Bragg reflections composing the Ewald sphere in the 3D space. After that, the diffraction peaks of both film and substrate are identified and disentangled and Miller's (h, k, l) indexes are assigned. As shown in Fig. 3.15b for the Co_3O_4 (311) diffraction, the peaks presented a circular shape typical of good quality samples [255, 256] and covered about 28×30 pixels. The pixel size of the peak in the Pilatus 100k was $172 \times 172\,\mu\text{m}^2$ and was compared to the performances of the LPD detector employed in the FEL experiment. The LPD detector has a pixel size of about $500 \times 500\,\mu\text{m}^2$. Therefore, the diffraction peaks

should occupy an area of about 9 pixels, allowing for the detection of photoinduced intensity, position, and FWHM variations during the TR-XRD experiment. Starting from the determined diffraction peaks, the orientation matrix can be fitted and in-plane sample rotation ("Rocking curves") scans can be performed to maximize the diffraction intensity (Fig. 3.15c). During the full procedure, care must be taken to ensure that the Bragg peaks do not shift in the 3D space as the sample is rotated. The procedure is concluded by choosing the peaks to be detected in the FEL experiment, specifying their Miller indexes.

3.3.1.3 Electron diffraction

To conclude the crystalline and chemical quality characterization, Reflection High-Energy Electron Diffraction (RHEED) was performed thanks to the collaboration with Dr. Francesco Pennacchio. The technique allowed to have a full characterization of the surface crystallinity and homogeneity of the sample. Indeed, a non-homogeneous sample surface would change the diffraction peak position if the sample position is changed during TR-XRD measurements. The setup is available in the group of Prof. F. Carbone at EPFL and the details of the experimental implementation are described in *G.F. Mancini et al.* [257]. Firstly, we assigned the diffraction spot in Fig. 3.16a starting from a lattice parameter of both a =8.151 85 Å considered in grazing incidence XRD and a =8.0821 Å reported in literature [258]. We also considered a CCD of 1340 × 1300 pixels with an active area of 25 mm, thus, a pixel size of $\phi = 21\,\mu$m. During the entire process, we must account for the FCC crystal symmetry selection rule which states that the detected diffraction peaks must have all even or all odd Miller's indexes (h, k, l). Starting from Fig. 3.16a, we assumed the central peak to be the (004) one. This is confirmed by the following crystallographic considerations. We estimated the spacing of the correspondent planes by using the following formula:

$$d_{hkl} = \frac{a}{\sqrt{h^2 + k^2 + l^2}} \tag{3.30}$$

which, for the 004 family, gives:

$$d_{004} = \frac{8.15185}{\sqrt{4^2}} = 2.04\,\text{Å} \quad \text{or} \quad d_{004} = \frac{8.0821}{\sqrt{4^2}} = 2.02\,\text{Å} \tag{3.31}$$

From the Bragg condition we determined the angle correspondent to the aforementioned reflection:

$$\theta = \arcsin(\frac{\lambda}{2d}) \simeq 0.98^\circ \text{ or } 0.99^\circ \tag{3.32}$$

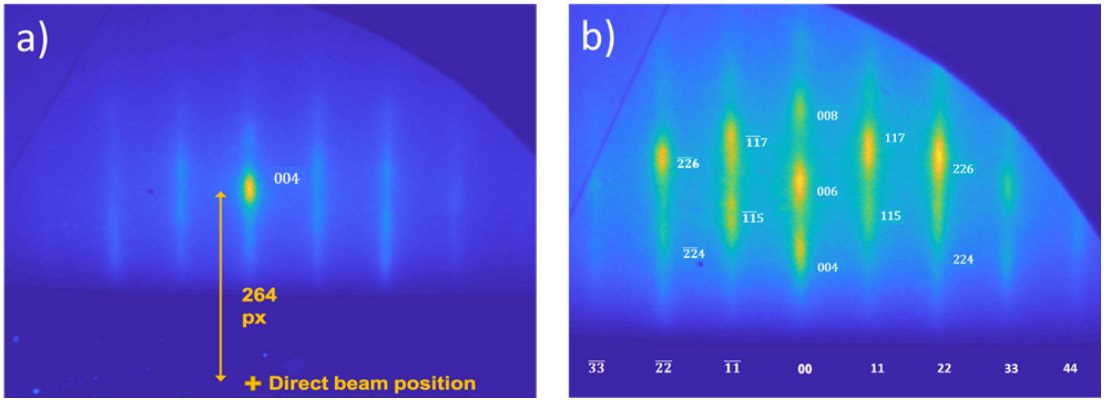

Figure 3.16: Electron diffraction patterns. a) (004) peak assigned by calculating its expected position with the sample-camera distance. b) Full Co_3O_4 diffraction pattern. We indexed the diffraction peaks based on XRD results *i.e.*, knowing that the sample surface is [111] oriented by epitaxial growth with $[\bar{1}10]$ in-plane vector and through a simulation of the single crystal pattern in the Single Crystal 4 software.

and calculated *a priori* the (004) peak expected position knowing the sample-camera distance L = 160 mm:

$$r = L\tan(\theta) \simeq 5.4752\,\text{mm or } 5.530\,\text{mm} \tag{3.33}$$

We can now compare the *a priori* estimation of the (004) peak position with the experimental values obtained by Fig. 3.16a, knowing the distance in pixel from the direct beam position $\Delta_{px} = 264$ pixels:

$$r = \phi\Delta_{px} \simeq 5.544\,\text{mm} \tag{3.34}$$

which suggests the goodness of the assumption on the (004) diffraction peak for both the lattice parameters. We can also calculate the correct sample-camera distance from experimental values as:

$$L = \frac{\phi\Delta_{px}}{\tan(2\theta)} \simeq 162\,\text{mm or } 160.41\,\text{mm} \tag{3.35}$$

corroborating our assumptions. From this starting point we consider the full electron diffraction pattern in Fig. 3.16b. We can see 11 most intense peaks which present a streaked shape. We indexed the peaks starting from the (004) one suggested from the aforementioned calculations and considering the $[\bar{1}10]$ in-plane vector. The indexing was performed by comparison with the simulated Co_3O_4 electron diffraction pattern obtained through the Single Crystal 4 software from CrystalMaker Software Ltd. The peaks present a streaked shape. This generally

appears when a multi-domain surface is observed. We interpret the presence of these streaked patterns as possibly given by the creation of rotational domains with a dimension inferior to 1 mm along the growth axis. As reported in literature [259], the presence of a streaked pattern is indicative of a flat surface with small domains within a high crystalline matrix. Satellites, modulated or inclined streaks were not observed. Therefore, our observations suggest that the Co_3O_4 thin film is characterized by a high level of epitaxial crystallinity and a flat surface characterized by small rotational domains. Furthermore, a possible presence of crystalline CoO ($Fm\bar{3}m$) would generate satellite-like spurious peaks which have the same assignment as the ones reported but have different distance from the (000) peak *i.e.*, the zero-order peak. Therefore, the data also suggest that no spurious CoO components were detected in the sample.

3.3.1.4 Optical transitions assignment

Before diving into the TRR results on Co_3O_4, ellipsometry measurements were carried out as a function of temperature. This was done to assign the electronic transitions in Co_3O_4 and to understand what are the main transitions involved in the pump-probe experiments. Fig. 3.17a shows the real (absorptive) part of the optical conductivity σ_1 of Co_3O_4 plotted as a function of the photon energy in the UV-Vis-NIR range for 4 selected temperatures (300 K, 70 K, 35 K and 7 K) across the antiferromagnetic transition ($T_N \approx 30 - 40$ K). The optical conductivity was extracted from ellipsometry measurements as described in Section 3.2.1.1. The σ_1 spectra were fitted as a function of temperature with 9 Gaussian peak functions and the obtained results are reported for the 7 K spectrum in Fig. 3.17b. The choice of a Gaussian fit is due to two main factors: (i) the Drude-Lorentz model does not fit well or produces unphysical results and (ii) the same fitting procedure on absorption coefficient and ellipsometric (ϵ_2) quantities was applied in literature in *e.g.*, Co_3O_4 and $ZnFe_2O_4$ thin films, respectively [194, 260]. The electronic transitions extrapolated from Gaussian deconvolution were assigned based on the comparison with available literature optical, RIXS experiments and DFT calculations [193, 194]. The comparison between a zero-momentum experiment such as ellipsometry and RIXS experiments is possible considering only the $d-$bands which are in general almost dispersionless. However, electronic structure calculations to verify the completeness of the interpretation are work in progress. It must be stressed that it is difficult to give a precise assignment of the transitions found since the different measurements and DFT calculations reported in the literature are seemingly in disagreement [193, 194, 195, 203]. At 300 K, a tail at 0.74 eV and features at 0.82 eV, 0.92 eV, 1.3 eV, 1.6-1.9 eV and 2.5-4 eV are observed, in agreement with the literature measurements (Fig. 3.17a) [194, 196, 261]. Based on the approach used by *Qiao et al.* [194], the feature at 0.82 eV is assigned to onsite $d-d$

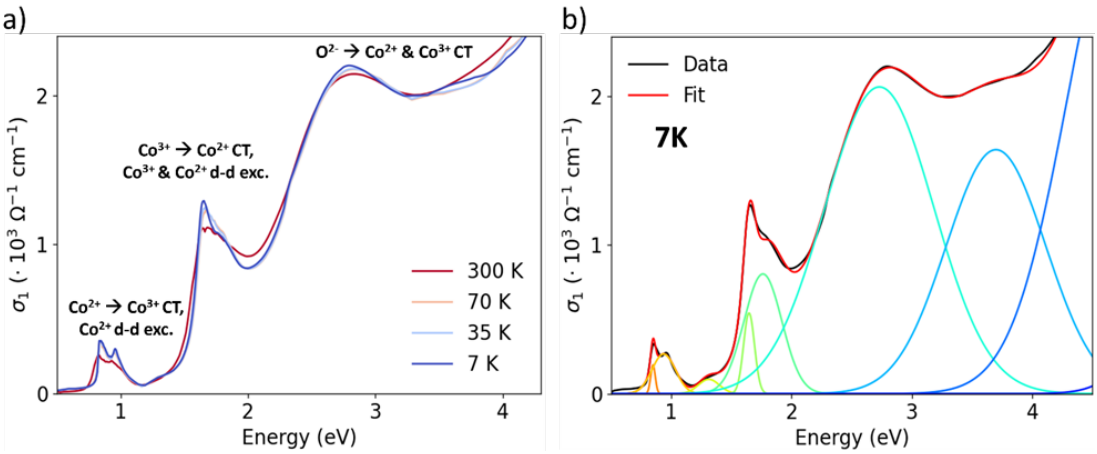

Figure 3.17: a) Real (absorptive) part of the optical conductivity σ_1 of Co_3O_4 plotted as a function of photon energy at 300 K, 70 K, 35 K, and 7 K *i.e.*, across the antiferromagnetic transition ($T_N \approx 30 - 40$ K). The spectra are colour coded from red (RT, 300 K) to deep blue (7 K). (b) 7 K static optical conductivity of Co_3O_4 sample extracted from ellipsometry measurements. The data are indicated in black and the fit is indicated in red. The Gaussian deconvolution is reported with colours ranging from red to blue as the energy increases.

transitions in the Co^{2+} cations (indicated as Co^{2+} $d-d$ exc. in Fig. 3.17a). The comparison with Resonant Inelastic X-ray Scattering (RIXS) measurements [193] suggests that the reached state has a $^4T_1$ configuration. The 0.92 eV and 1.3 eV transitions can be ascribed to two Intersite $d-d$ CTs involving the t_2 and e orbitals of Co^{2+} and the e orbitals of Co^{3+} sites ($Co^{2+} \rightarrow Co^{3+}$ CT in Fig. 3.17a). The overall effect is an exchange of the cation valences in their respective sites (Co^{2+} occupation in octahedral sites and a partial Co^{3+} occupation in the tetrahedral ones) [195]. Another possible assignment for the 1.3 eV feature can be a $d-d$ transition in the Co^{3+} site to the $^3T_{2g}$ state since it matches with a similar transition measured through RIXS [193]. The 1.63 eV feature was mainly attributed to an intersite electron transfer between Co^{3+} t_{2g} and Co^{2+} t_2 sites, producing a Co^{4+} ion in the octahedral site and a Co^{1+} ion in the tetrahedral one ($Co^{3+} \rightarrow Co^{2+}$ CT in Fig. 3.17a) [194, 195]. The oscillator at 1.76 eV corresponds to a mixture of two onsite $d-d$ transitions: (i) electron transfer from t_{2g} to e orbitals in Co^{3+} ($^1T_{1g}$) and (ii) an excitation of an e electron in Co^{2+} reaching the $^2E_1$ electronic state (Co^{3+} & Co^{2+} $d-d$ exc. in Fig. 3.17a). Moreover, the 2.5-4 eV transitions correspond to two intersite $p-d$ CTs processes ($O^{2-} \rightarrow Co^{2+}$ & Co^{3+} CT in Fig. 3.17a). The low energy side of the band centred at 2.71 eV is assigned to an electron transfer between a O^{2-} $2p$ and Co^{2+} t_2 level. The high energy side is instead centred at 3.63 eV and is ascribed to the electron transfer between a O^{2-}

300 K energies (eV)	7 K energies (eV)	Literature 300 K (Abs + RIXS) [193, 194]	Optical transitions assignment
5.74	5.78	5.8	Intersite $p-d$ CT $O^{2-}2p \rightarrow Co^{3+}$ e_g
4.68	4.76	4.69	Intersite $p-d$ CT $O^{2-}2p \rightarrow Co^{2+}$ t_2
3.63	**3.70**	**3.66**	**Intersite $p-d$ CT $O^{2-}2p \rightarrow Co^{3+}$ e_g**
2.71	**2.73**	**2.62**	**Intersite $p-d$ CT $O^{2-}2p \rightarrow Co^{2+}$ t_2**
1.76	**1.76**	**1.84**	**Mixed:**
			Onsite Co^{3+} $d-d$ $t_{2g} \rightarrow e_g$ ($^1T_{1g}$)
			Onsite Co^{2+} $d-d$ ($^2E_1$)
1.63	**1.65**	**1.64**	**Intersite $d-d$ CT Co^{3+} $t_{2g} \rightarrow Co^{2+}$ t_2**
1.27	1.31	1.3 (RIXS)	Intersite $d-d$ CT Co^{2+} $t_2 \rightarrow Co^{3+}$ e_g
0.92	0.94	0.94	Intersite $d-d$ CT Co^{2+} e $\rightarrow Co^{3+}$ e_g
0.82	0.85	0.83	Onsite Co^{2+} $d-d$ e $\rightarrow$ t_2 ($^4T_1$)

Table 3.1: Oscillator central energies extracted from fit and gaussian deconvolution of the static optical conductivity at 300 K (RT) and 7 K compared to the oscillators found in literature [193, 194]. The assignment of each optical transition is indicated in the last column. The black coloured bold transitions are the ones triggered by the 1.55 eV pump. The purple bold transitions are the ones triggered by the 3.1 eV pump. The shaded gold region comprises the transitions investigated by the white light probe of the TRR experiment.

$2p$ and Co^{3+} e states [193, 194]. Other studies reported similar interpretations but found the energies of the intersite $p-d$ CT to be lower (2.4 and 2.8 eV) than the ones reported here [196].

As the temperature lowers, a rearrangement of spectral weights is observed. In particular, the first strong absorption edge is blueshifted to around 0.8 eV and is followed by two sharp peaks at 0.85 eV and 0.94 eV and the 1.3 eV feature. In the 1.6-1.9 eV band the two features at 1.65 eV and 1.76 eV are now clearly visible due to decreased FWHM of the oscillators. In addition, a strong blueshift of the 1.65 eV oscillator between RT and 70 K followed by a slight gradual redshift from 70 K to 7 K was observed. The data suggest that the Gaussian-like behaviour of the transitions can possibly be ascribed to the broadening due to phonons or impurities [262] which change the shapes of typical Drude-Lorentz oscillators to the ones observed. From Fig. 3.17a it is possible to observe that the spectral features at 0.8 eV and 1.63 eV are more affected by temperature changes. Both the first, assigned as a $d-d$ transition in the Co^{2+} site and the second, assigned to the $Co^{3+} \rightarrow Co^{2+}$ intersite $d-d$ CT strongly decrease in FWHM compatible with a possible decrease in the phonon contributions as temperature lowers but also with a possible change in the exchange interactions or in the charge transport mechanisms. In fact, the results indicate that the two affected features are the ones in which an Co^{2+} excited state is reached suggesting a strong change in both electronic (exchange)

and structural (Jahn-Teller distortions) interactions. These observations agree

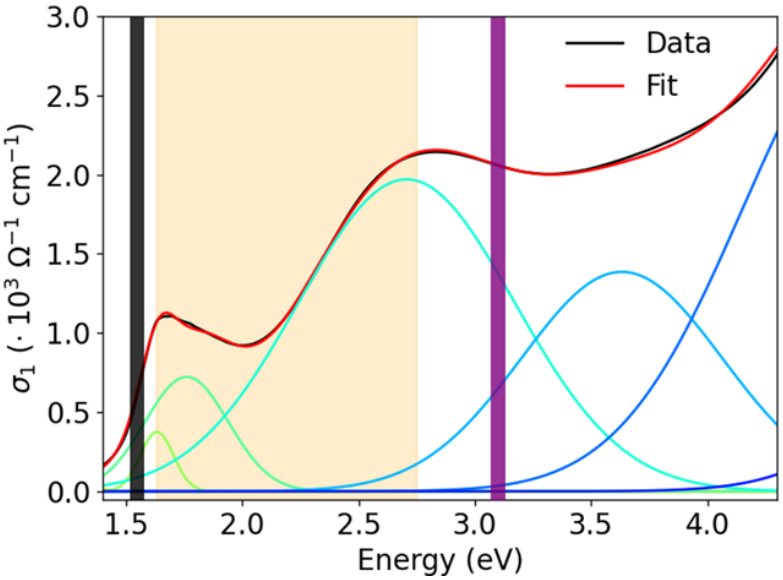

Figure 3.18: Real (absorptive) part of the optical conductivity σ_1 of Co_3O_4 at RT with the pump and probe energy ranges involved in the Transient Reflectivity experiments. The Gaussian deconvolution is reported along with the 3.1 eV (purple shaded box), 1.55 eV (black shaded box) pumps and 1.63-2.75 eV eV probe (orange shaded box) energies. The bands are colour coded with Tab. 3.1.

well with the interpretation of two electronic transitions from Co^{3+} t_{2g} to Co^{2+} t_2 and from Co^{2+} e to Co^{2+} t_2. The intersite $p-d$ CT band remains similar to the 300 K measurement with a slight decrease of FWHM. The oscillator energies compared with literature optical absorption and RIXS measurements are reported in Tab. 3.1 [193, 194] along with their relative optical transitions assignments. In addition, electrical conductivity measurements on Co_3O_4 chemical vapour deposited films found out that, below $T \approx 220$ K the conductivity mechanism changes from polaronic hopping between the two Co sites to variable range hopping [210]. This physical process change could also affect the optical conductivity with a change in the shape of the transition that, coupled with the change in exchange interaction and phonon contributions, could decrease the FWHM. Moreover, the change in the oscillator positions with an overall blueshift of the bandgap from RT to 7 K is typical in AFM systems and can be due to several phenomena such as magnetoelastic coupling or, again, modifications of the exchange interactions [263, 264]. This latter mechanism is reported in *Blazey and Rohrer* [263] for $NaCrS_2$ and is based on the extra AFM or FM components to the exchange (or superexchange) interaction given by holes or electrons in the excited state. An AFM component would give a blueshift of the bandgap while an FM one would give a redshift. If

a competition is found between these two components, it would be possible to observe a first blueshift accompanied by a small redshift as in this case where the exchange coupling in each sublattice is of the FM type, while among sublattices the coupling is of the AFM one.

In Fig. 3.18 the starting conditions of Transient Reflectivity experiments are highlighted on the real part of the optical conductivity at RT and color coded with Tab 3.1. Table 3.1 is colour coded such that the transitions pumped at 1.55 eV are represented in bold black, the transitions pumped at 3.1 eV are represented in bold purple, while the transitions probed in the 1.63-2.7 eV energy range are highlighted in gold. Upon pumping at 1.55 eV (solid black box in Fig. 3.18) two main transitions are triggered: (i) the intersite $d-d$ CT that brings an electron from Co^{3+} to Co^{2+} giving rise to Co^{4+} and Co^{1+} states and (ii) the mixture of onsite $d-d$ transitions in Co^{3+} and Co^{2+} sites. Upon pumping at 3.1 eV (purple box in Fig. 3.18), the two intersite $p-d$ CT transferring an electron from an O^{2-} ion to (i) the t_2 state of Co^{2+} or (ii) to the e_g state of Co^{3+} are excited. Within the 1.63-2.7 eV probe energy range one probes the $Co^{3+} \rightarrow Co^{2+}$ intersite $d-d$ electron transfer (1.64 eV oscillator), the Co^{3+} $d-d$ transition into ${}^1T_{1g}$ state, the Co^{2+} $d-d$ transition into the ${}^2E$ state (1.76 eV oscillator), and the $O^{2-} \rightarrow Co^{2+}$ intersite $p-d$ CT (2.7 eV oscillator). The AFM transition changes the FWHM and positions of the oscillators indeed causing a change in the transient signal as shown later in this chapter. The results and assignments clarify the state-of-the-art presented in the introduction (Section 3.1.1) and clarify the framework of the TRR results which shall be presented in the following.

3.3.2 Transient Reflectivity (TRR) incoherent responses

3.3.2.1 Room Temperature relaxation pathways

As the first step, the RT fluence dependence of the sample is reported. This study must be carried out to ensure the repeatability of the observed physical processes across multiple laser pulses *i.e.*, avoid sample damage and multiphoton absorption processes by laying in a linear response regime. The fluence dependence is calculated considering the incident fluence F, which is an instrumental parameter corresponding to the energy of the laser pulse in mJ impinging on a sample area in cm^2. F is then normalized by the energy of the photons $h\nu$ and their penetration depth d. The angle dependent reflectivity of the sample is then considered with the term $(1-R(\theta))$ obtaining the excitation density of the sample n_e as:

$$n_e[\mathrm{cm}^{-3}] = \frac{F[\frac{\mathrm{mJ}}{\mathrm{cm}^2}]}{h\nu[\mathrm{mJ}]d[\mathrm{cm}]}(1-R(\theta)) \tag{3.36}$$

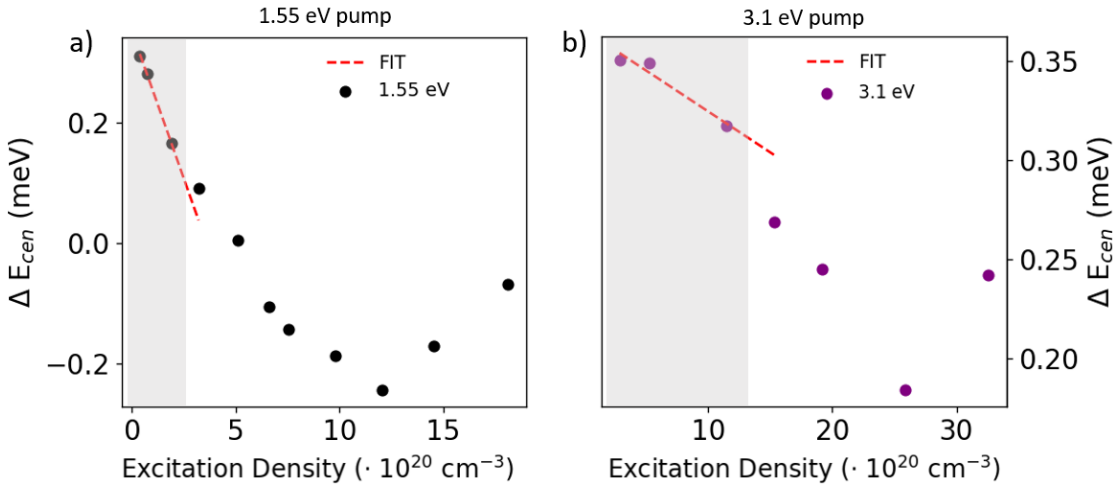

Figure 3.19: Co_3O_4 RT fluence dependence of the 2.7 eV oscillator centroid (ΔE_{cen}) taken at 1.7 ps for (a) 1.55 eV and (b) 3.1 eV pump energies, respectively. The linear fit of the fluence dependence is indicated as a red dashed line, while the region considered for the measurements is highlighted in a shaded gray box.

	1.55 eV pump	3.1 eV pump
Incident fluences (mJ/cm^2)	0.2 – 1	0.6 – 2.4
Excitation densities (cm^{-3})	3.7×10^{19} - 1.9×10^{20}	2.9×10^{20} - 1.4×10^{21}

Table 3.2: Linearity ranges of the incident fluences and excitation densities employed in the TRR experiments at Room Temperature.

n_e corresponds to the density of carriers excited *per* unit volume and was calculated considering the 22° reflection angle between the probe and the sample given by experimental geometry. A fluence dependence both for 1.55 eV and 3.1 eV pump was performed on the centroid position (ΔE_{cen}), amplitude and FWHM of the three oscillators comprised in the probe energy range (see Tab. 3.1 and Section 3.2.2.1 for details) for a total of 9 fluence dependences. For simplicity, the behaviour of the 2.7 eV (intersite $p-d$ CT) oscillator centroid is reported in Fig. 3.19. This is the parameter with the highest nonlinearity among the 9 analysed. Figs. 3.19a,b show the ΔE_{cen} fluence dependence at 1.7 ps for 1.55 eV pump with excitation densities from 3.7×10^{19} cm^{-3} to 1.8×10^{21} cm^{-3} and for 3.1 eV pump with excitation densities from 2.9×10^{20} cm^{-3} to 3.2×10^{21} cm^{-3}. These correspond to the incident fluence ranges from 0.2 mJ/cm^2 to 9.6 mJ/cm^2 for 1.55 eV pump and from 0.6 mJ/cm^2 to 6.8 mJ/cm^2 for 3.1 eV pump. In both Figs. 3.19a,b the linearity ranges, indicated from a linear fit reported in red dashed lines, correspond to the excitation density and incident fluence ranges reported in Tab. 3.2. For 1.55 eV pump the linearity range is between an incident fluence value

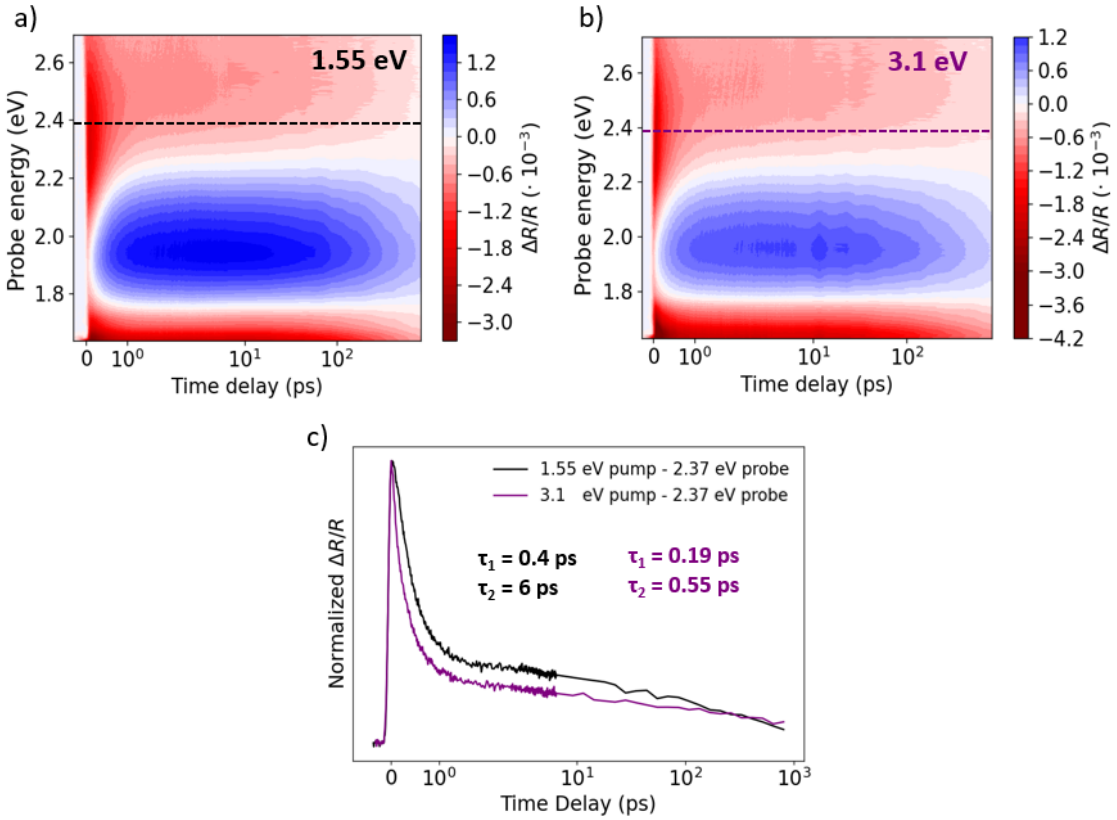

Figure 3.20: RT TRR 2D maps obtained by pumping the Co_3O_4 at 1.55 eV ($1.5 \times 10^{20}\,cm^{-3}$) and at 3.1 eV ($5.3 \times 10^{20}\,cm^{-3}$) pump energies (excitation densities), respectively. The TRR response is plotted as a function of the probe photon energy in eV and time delays are in ps. c) Comparison between time traces obtained with 2.37 eV probe and 1.55 eV (black) and 3.1 eV (purple) pumps, respectively. The first two time constants are reported colour coded with the corresponding trace. In all the plots, the time delay scales are linear up to 2.5 ps and logarithmic from 2.5 ps to 800 ps.

of $0.2\,mJ/cm^2$ and $1\,mJ/cm^2$ which corresponds to a range from $3.7 \times 10^{19}\,cm^{-3}$ to $1.9 \times 10^{20}\,cm^{-3}$ in excitation densities. For 3.1 eV pump the linearity range reported is from $0.6\,mJ/cm^2$ to $2.4\,mJ/cm^2$ incident fluences which corresponds to the range from $2.9 \times 10^{20}\,cm^{-3}$ to $1.4 \times 10^{21}\,cm^{-3}$ excitation densities. The Room Temperature TRR experiments are performed by pumping in these regimes highlighted with a shaded gray box in Figs. 3.19a,b.

The TRR datasets taken at RT with 1.55 eV, $1.5 \times 10^{20}\,cm^{-3}$ and 3.1 eV $5.3 \times 10^{20}\,cm^{-3}$ pump energies and excitation densities are respectively shown in Figs. 3.20a,b. The maps are reported after the Global Lifetime Analysis (GLA) and chirp correction procedure performed with OPTIMUS [235] as explained in Section 3.2.2.1. In the 2D maps of Figs. 3.20a,b three main regions are distin-

guished: (i) 1.63 – 1.77 eV with negative TRR signal, (ii) 1.77 – 2.25 eV with positive TRR signal and (iii) 2.25 – 2.75 eV with negative TRR signal. The behaviour of the TRR signals as a function of time delay for both 1.55 eV and 3.1 eV pumps are qualitatively similar. Indeed, both the negative regions in Figs. 3.20a,b are characterized by a global negative minimum in the first hundreds of fs followed by a long tail reaching zero for time scales longer than the experimental range. Moreover, the positive regions are characterized by a negative signal in the first 100 fs and a global positive maximum in the 1-10 ps regions followed by a tail that again brings the signal to zero outside the time range of the experiment. However, at a closer look, significant differences are observed in the relaxation time scales of the system upon 1.55 eV and 3.1 eV excitation. Fig. 3.20c shows the normalized time traces for 2.37 eV probe energy as extracted from the 2D TRR maps (black and purple lines in Figs. 3.20a,b) after the GLA fit within the OPTIMUS software framework [235] (see Section 3.2.1). The first two time scales (τ_1 and τ_2) from GLA are reported colour coded with the selected traces. The other time scales (τ_3, τ_4, and τ_5) obtained are reported in Tab. 3.3.

Dataset	τ_1 (ps)	τ_2 (ps)	τ_3 (ps)	τ_4 (ps)	τ_5 (ps)
1.55 eV pump, RT	0.41	5.9	204	Offset	–
3.1 eV pump, RT	0.19	0.55	8.00	229	Offset

Table 3.3: Time constants retrieved from GLA on RT datasets with 1.55 eV and 3.1 eV pumps. The offsets have a fixed value of 3 ns and were employed to account for the fact that the dynamics does not end in the 800 ps range considered in the experiment.

From the data presented, differences in the time scales in the first few picoseconds are found. In fact, by pumping the system at 1.55 eV, a first rapid decay with $\tau_1^{1.5\,\mathrm{eV}} = 0.4$ ps followed by two other exponential decay processes with $\tau_2^{1.5\,\mathrm{eV}} = 4.9$ ps and $\tau_3^{1.5\,\mathrm{eV}} = 204$ ps time constants are observed. Instead, by pumping the system at 3.1 eV, two ultrafast decays at $\tau_1^{3.1\,\mathrm{eV}} = 0.19$ ps and $\tau_2^{3.1\,\mathrm{eV}} = 0.55$ ps followed by two exponential decays with characteristic times of $\tau_3^{3.1\,\mathrm{eV}} = 8$ ps and $\tau_4^{3.1\,\mathrm{eV}} = 229$ ps are observed. A $\tau_{4,5}$ time constant was considered as an offset since the dynamic processes do not end in the 800 ps range used in the experiments. The data and analysis here presented seem in contrast with the following hypothesis: pumping charge carriers at 3.1 eV brings them in a higher energy state, thus the decay process should be slower with respect to 1.55 eV pumping one. It is also instructive to look at the Co_3O_4 response from the standpoint of the oscillators. The oscillators analysis was performed following the approach reported in Section 3.2.2.1. The variations as a function of the time delay of the 1.64 eV (Intersite $d-d$ CT), 1.76 eV (onsite $d-d$ transition), and 2.7 eV (intersite $p-d$ CT) oscillators centroid position (ΔE_{cen}), amplitude

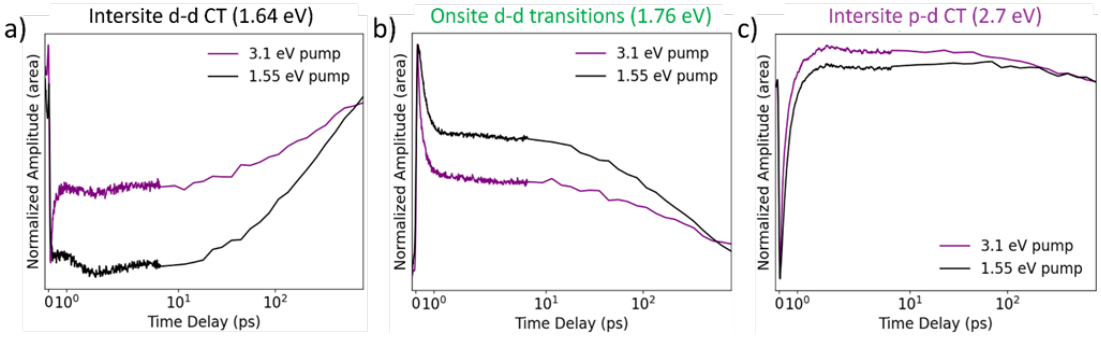

Figure 3.21: Comparison between the oscillator amplitudes responses upon 1.55 eV and 3.1 eV pumping for the (a) 1.64 eV (Intersite $d-d$ CT), (b) 1.76 eV (onsite $d-d$ transition), and (c) 2.7 eV (intersite $p-d$ CT) oscillators. The time axis is shown in linear-$\log_{10}$ scale (linear up to 6 ps and $\log_{10}$ scale from 6 ps to 800 ps). Excitation fluences of $1.5 \times 10^{20}\,\mathrm{cm}^{-3}$ and $5.3 \times 10^{20}\,\mathrm{cm}^{-3}$ were used respectively for the 1.55 eV and 3.1 eV pumps. The traces were processed by computing their absolute value and normalized by the first maximum after the rise.

and FWHM were considered for a total of 9 time traces for each pumping energy. Only the amplitude will be considered for simplicity. Figs. 3.21a,b and c show the comparison between the amplitudes (areas) of the 1.64 eV (panel 3.21a), 1.76 eV (panel 3.21b), and 2.7 eV (panel 3.21c) oscillators upon 1.55 eV and 3.1 eV pumping. The traces were processed by computing their absolute value and normalized by the first maximum after the rise. The overall data trend corroborates what was reported in Fig. 3.20c and Global Lifetime Analysis *i.e.*, the relaxation processes at 3.1 eV pump show a faster decay respect to the ones obtained by pumping at 1.55 eV. For example, the 1.64 eV oscillator amplitude in Fig. 3.21a shows, upon 1.55 eV pump, a fast decrease after the photoexcitation followed by a relaxation with $\tau_1^{1.5\,\mathrm{eV}}(1.64\,\mathrm{eV}) = 1.7\,\mathrm{ps}$ to an almost constant value for the first 10 ps, then decays with a timescale $\tau_2^{1.5\,\mathrm{eV}}(1.64\,\mathrm{eV}) = 266\,\mathrm{ps}$. The same oscillator pumped at 3.1 eV shows an ultrafast relaxation with $\tau_1^{3.1\,\mathrm{eV}}(1.64\,\mathrm{eV}) = 155\,\mathrm{fs}$ followed by another ultrafast timescale $\tau_2^{3.1\,\mathrm{eV}}(1.64\,\mathrm{eV}) = 518\,\mathrm{fs}$, a ps relaxation with $\tau_3^{3.1\,\mathrm{eV}}(1.64\,\mathrm{eV}) = 7\,\mathrm{ps}$, and a final recombination with $\tau_4^{3.1\,\mathrm{eV}}(1.64\,\mathrm{eV}) = 256\,\mathrm{ps}$.

3.3.2.2 TRR response across the AFM transition

Fig. 3.22 shows the 4.2 K fluence dependence of the 2.7 eV oscillator centroid (ΔE_{cen}) taken at 1.7 ps for 1.55 eV (Fig. 3.22a) and 3.1 eV (Fig. 3.22b) pump energies, respectively. The calculation of the excitation density from the incident fluence followed the same procedure reported in Section 3.3.2.1. The fluence dependence at 1.55 eV pump was performed in the range from $3.8 \times 10^{19}\,\mathrm{cm}^{-3}$ to

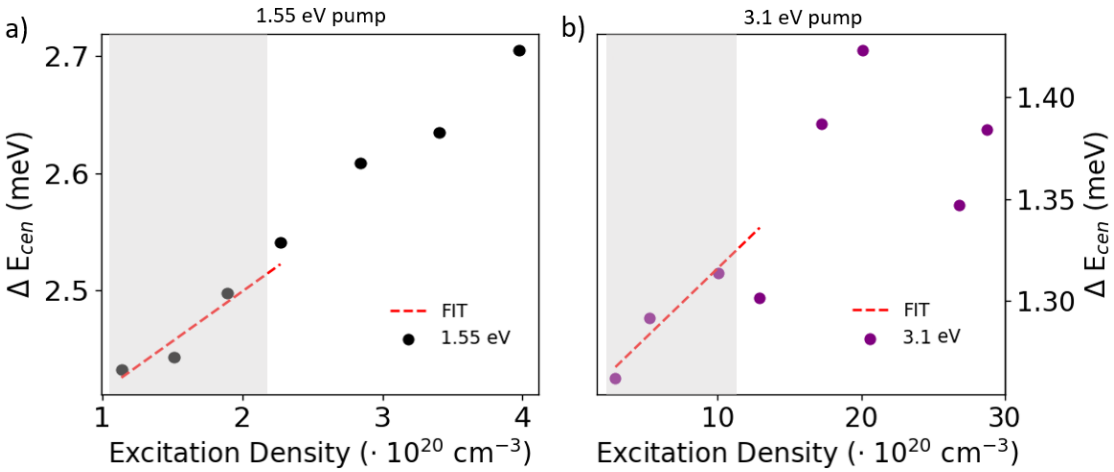

Figure 3.22: 4.2 K fluence dependence of the 2.7 eV oscillator centroid of Co_3O_4 taken at 1.7 ps for (a) 1.55 eV and (b) 3.1 eV pump energies, respectively. The linear fit of the fluence dependence is indicated as a red dashed line, while the region considered for the measurements is highlighted in a shaded gray box.

	1.55 eV pump	3.1 eV pump
Incident fluences (mJ/cm^2)	0.2 – 0.77	0.6 – 3
Excitation densities (cm^{-3})	3.8×10^{19} - 1.4×10^{20}	2.9×10^{20} - 1.4×10^{21}

Table 3.4: Linearity ranges of the incident fluences and excitation densities at 4.2K.

3.8×10^{20} cm^{-3} which corresponds to an incident fluence range from 0.2 mJ/cm^2 to 6 mJ/cm^2. The fluence dependence at 3.1 eV pump was performed in the range from 2.9×10^{20} cm^{-3} to 2.9×10^{21} cm^{-3} which corresponds to an incident fluence range from 0.6 mJ/cm^2 to 6 mJ/cm^2. In both Figs. 3.22a,b the linearity ranges, indicated from a linear fit reported in red dashed lines, correspond to the excitation density and incident fluence ranges reported in Tab. 3.4. For 1.55 eV pump the linearity range (gray box) is between an incident fluence value of 0.2 mJ/cm^2 and 0.77 mJ/cm^2 which corresponds to a range from 3.8×10^{19} cm^{-3} to 1.4×10^{20} cm^{-3} in excitation densities. For 3.1 eV pump, the linearity range (gray box) reported is from 0.7 mJ/cm^2 to 3 mJ/cm^2 incident fluences which corresponds to the range from 2.9×10^{20} cm^{-3} to 1.4×10^{21} cm^{-3} in excitation densities.

The measurements performed varying the temperature are reported with fixed excitation densities of 1.5×10^{20} cm^{-3} for 1.55 eV pumping and of 5.3×10^{20} cm^{-3} for 3.1 eV pumping, within the linearity range of both RT and 4.2 K fluence dependences. The selected temperatures for this study are 300 K (RT), 150 K, 70 K, 40 K, 32 K, 27 K, 22 K, and 4.2 K taking care in collecting a fine grid of temperatures with 5-8 K steps in the 40-20 K range to better resolve the signal change

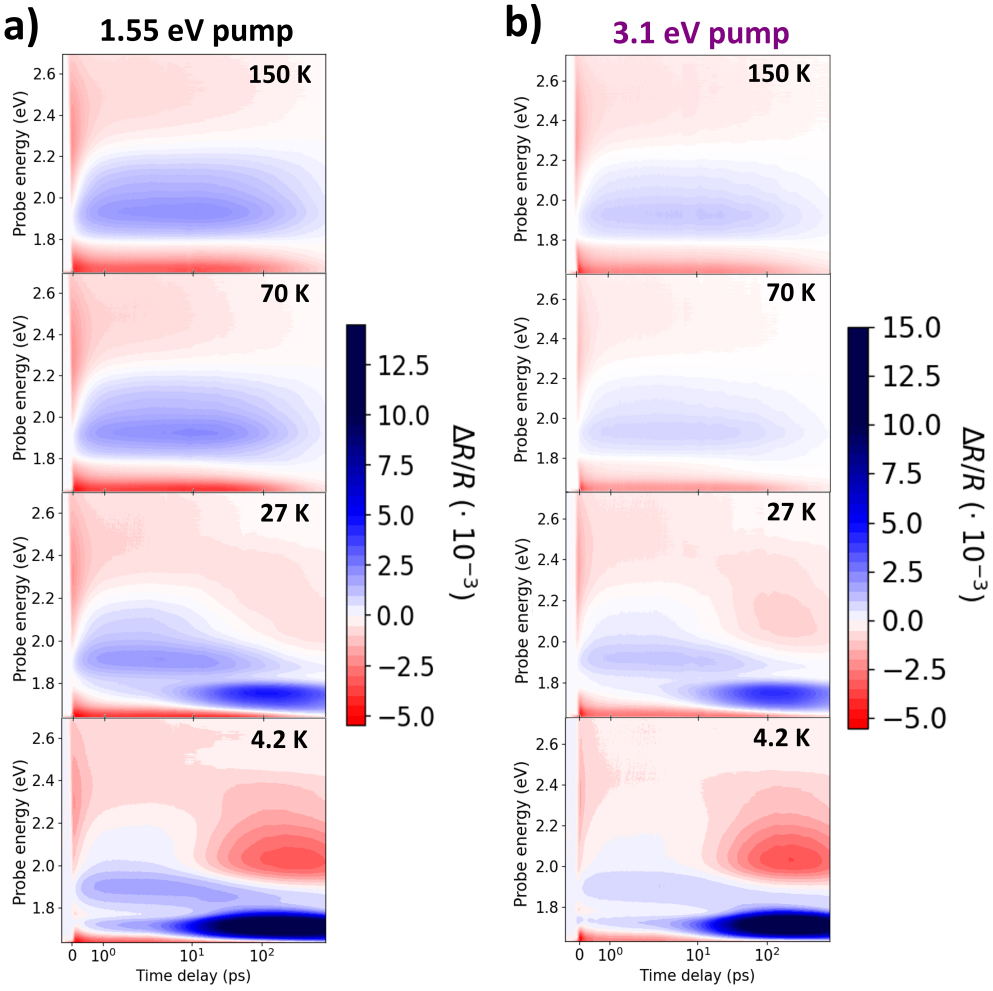

Figure 3.23: Broadband transient reflectivity maps of Co_3O_4 as a function of the temperature, obtained by pumping at (a) 1.55 eV and (b) 3.1 eV. For each pump energy, the maps are displayed from 150 K (top) to 4.2 K (bottom). The time axis is shown in linear-$\log_{10}$ scale (linear up to 2.5 ps and $\log_{10}$ scale from 2.5 ps to 800 ps). Excitation fluences of $1.5 \times 10^{20}\,\mathrm{cm}^{-3}$ and $5.3 \times 10^{20}\,\mathrm{cm}^{-3}$ were used respectively for the 1.55 eV and 3.1 eV pumps.

T (K)	τ_1 (ps)	τ_2 (ps)	τ_3 (ps)	τ_4 (ps)	τ_5 (ps)	τ_6 (ps)
1.55 eV pump						
70	0.38	6.4	151	Off		
40	0.39	5.7	40	236	Off	
4.2	0.38	6.7	18	145	Off	
3.1 eV pump						
70	0.18	0.55	16	178	Off	
40	0.2	0.64	11	58	167	Off
4.2	0.17	0.53	6.5	40	710	Off

Table 3.5: Time constants retrieved from the GLA method for the transient reflectivity maps at 70 K, 40 K and 4.2 K upon 1.55 eV and 3.1 eV excitations.

across the AFM transition, as illustrated in the following. TRR 2D maps as a function of the temperature are reported in Fig. 3.23 for 4 selected temperatures: 150 K, 70 K, 27 K and 4.2 K. At 150 K, upon 1.55 eV pump (1.5×10^{20} cm^{-3}, Fig. 3.23a), three main regions are identified: 1.63-1.77 eV, 1.77-2.25 eV and 2.25-2.7 eV. Similarly to the RT measurements, the 1.63-1.77 eV and 2.25-2.7 eV regions show a broad negative signal increasing in amplitude within the IRF and strongly decaying in the first 2 ps. After 2 ps, the decay continues at a slower rate. The 1.77-2.25 eV region shows a negative signal in the first few hundreds of fs, changing sign and reaching its maximum after 1.5 ps, and then decreasing over time. At 70 K, transient signals similar to RT and 150 K are observed, except for the positive feature which changes in time evolution in the 1.77-1.91 eV range increasing up to 200 ps and then decaying beyond 800 ps, the time limit of the experiment. At 27 K an additional $\Delta R/R$ feature appears on sub-ps time scales red shifting up to 1.72 eV and undergoing a strong rise up to 100 ps. In addition, another negative band appears between 1.97 eV and 2.48 eV, in the time range between 80 ps and 800 ps. At 4.2 K the positive feature appears in the 1.65-1.8 eV probe energy range immediately after the excitation, partially overlapping with the negative band at 1.65-1.71 eV, while the appearance and decay of the negative band at 1.97-2.48 eV remains confined to the 10-800 ps time range. Qualitatively, a similar behaviour is observed upon pumping the intersite $p-d$ CT transitions at 3.1 eV (5.3×10^{20} cm^{-3}, Fig. 3.23b), but quantitative differences are retrieved in the relaxation time scales. The 2D maps were analysed through GLA model [235], retrieving the time scales reported in Tab. 3.5 for 1.55 eV and 3.1 eV pumps at selected temperatures across the AFM transition, namely 70 K, 40 K (T_{Neel}) and 4.2 K. By pumping the $d-d$ transitions at 1.55 eV (Fig. 3.23a) at 70 K a total of three exponential components and an offset is considered, with only one sub-ps constant at $\tau_1^{1.55\,\mathrm{eV}}(70\,\mathrm{K}) = 0.38$ ps and two other components $\tau_2^{1.55\,\mathrm{eV}}(70\,\mathrm{K}) = 6.4$ ps and

$\tau_3^{1.55\,\mathrm{eV}}(70\,\mathrm{K}) = 151\,\mathrm{ps}$. Instead, below 40 K, the emergence of a new exponential component is reported at $\tau_3^{1.55\,\mathrm{eV}}(40\,\mathrm{K}) = 40\,\mathrm{ps}$. At 4.2 K the following results are retrieved: $\tau_1^{1.55\,\mathrm{eV}}(4.2\,\mathrm{K}) = 0.38\,\mathrm{ps}$, $\tau_2^{1.55\,\mathrm{eV}}(4.2\,\mathrm{K}) = 6.7\,\mathrm{ps}$, $\tau_3^{1.55\,\mathrm{eV}}(4.2\,\mathrm{K}) = 18\,\mathrm{ps}$, $\tau_4^{1.55\,\mathrm{eV}}(4.2\,\mathrm{K}) = 145\,\mathrm{ps}$ and an offset. The additional component decreases from $\tau_3^{1.55\,\mathrm{eV}}(40\,\mathrm{K}) = 40\,\mathrm{ps}$ to $\tau_3^{1.55\,\mathrm{eV}}(4.2\,\mathrm{K}) = 18\,\mathrm{ps}$, while the other time constants remain in the same fs, ps and 100 ps ranges. Differently, upon 3.1 eV pump (Fig. 3.23b) at 70 K, four time components and an offset are obtained, two on sub-ps time scales, $\tau_1^{3.1\,\mathrm{eV}}(70\,\mathrm{K}) = 0.18\,\mathrm{ps}$ and $\tau_2^{3.1\,\mathrm{eV}}(70\,\mathrm{K}) = 0.55\,\mathrm{ps}$, and two at longer time delays, $\tau_3^{3.1\,\mathrm{eV}}(70\,\mathrm{K}) = 16\,\mathrm{ps}$, $\tau_4^{3.1\,\mathrm{eV}}(70\,\mathrm{K}) = 178\,\mathrm{ps}$. By lowering the temperature to $T = T_{Neel} \simeq 40\,\mathrm{K}$, a new component appears at $\tau_4^{3.1\,\mathrm{eV}}(40\,\mathrm{K}) = 58\,\mathrm{ps}$. At 4.2 K the first two components remain substantially unchanged $\tau_1^{3.1\,\mathrm{eV}}(4.2\,\mathrm{K}) = 0.17\,\mathrm{ps}$ and $\tau_2^{3.1\,\mathrm{eV}}(4.2\,\mathrm{K}) = 0.53\,\mathrm{ps}$, the third and fourth components decrease to $\tau_3^{3.1\,\mathrm{eV}}(4.2\,\mathrm{K}) = 6.5\,\mathrm{ps}$ $\tau_4^{3.1\,\mathrm{eV}}(4.2\,\mathrm{K}) = 40\,\mathrm{ps}$, respectively, and the longest component increases up to $\tau_5^{3.1\,\mathrm{eV}}(4.2\,\mathrm{K}) = 710\,\mathrm{ps}$.

For both 1.55 eV and 3.1 eV excitations, the data suggest that the presence of an additional time component can be traced back to the influence of the AFM order on the photodynamic of the charge carriers. As reported for RT measurements, it is important to look at the behaviour of the oscillators as a function of time. The main focus will be on the variation of the amplitude (area) of each oscillator at 300 K comparing them with the ones at 40 K and at 4.2 K, as shown in Figs. 3.24a,b for 1.55 eV and 3.1 eV pumps, respectively. In the traces at 40 K and 4.2 K an additional time component is arising in the 10-100 ps region with respect to RT. At 40 K a faster rising respect to the time scales retrieved with GLA ($\tau_3^{1.55\,\mathrm{eV}}(40\,\mathrm{K}) = 40\,\mathrm{ps}$ and $\tau_4^{3.1\,\mathrm{eV}}(40\,\mathrm{K}) = 58\,\mathrm{ps}$) is detected. In fact, the extracted time scales τ_3 at 40 K and 1.55 eV pumping are: $\tau_3^{1.55\,\mathrm{eV}}(1.64\,\mathrm{eV}, 40\,\mathrm{K}) = 18\,\mathrm{ps}$, $\tau_3^{1.55\,\mathrm{eV}}(1.76\,\mathrm{eV}, 40\,\mathrm{K}) = 19\,\mathrm{ps}$, and $\tau_3^{1.55\,\mathrm{eV}}(2.7\,\mathrm{eV}, 40\,\mathrm{K}) = 22\,\mathrm{ps}$. The extracted time scales τ_4 at 40 K and 3.1 eV pumping are: $\tau_4^{3.1\,\mathrm{eV}}(1.64\,\mathrm{eV}, 40\,\mathrm{K}) = 16\,\mathrm{ps}$, $\tau_4^{3.1\,\mathrm{eV}}(1.76\,\mathrm{eV}, 40\,\mathrm{K}) = 18\,\mathrm{ps}$, and $\tau_4^{3.1\,\mathrm{eV}}(2.7\,\mathrm{eV}, 40\,\mathrm{K}) = 25\,\mathrm{ps}$. The new component increases its contribution as the temperature is lowered, suggesting the possibility of a thermal effect driven by the lattice response. At 4.2 K and for both the 1.55 eV and 3.1 eV pumps, the amplitude of the 1.64 eV oscillator (intersite $d - d$ CT) shows a first strong decrease right after time zero. This is accompanied by a rise with a local maximum in the 10 ps range and again a huge drop with a minimum at 100 ps. The 1.76 eV oscillator shows a strong rise and a global maximum in the 10-100 ps region. This maximum is centred at about 100 ps. The 2.7 eV oscillator shows again a minimum right above time-zero with a first ultrafast decay and a strong decrease starting below 10 ps and with a global minimum above the 100 ps, shifted respect to the other two datasets. The extracted time scales τ_3 at 4.2 K and 1.55 eV pumping are: $\tau_3^{1.55\,\mathrm{eV}}(1.64\,\mathrm{eV}, 4.2\,\mathrm{K}) = 25\,\mathrm{ps}$, $\tau_3^{1.55\,\mathrm{eV}}(1.76\,\mathrm{eV}, 4.2\,\mathrm{K}) = 29\,\mathrm{ps}$, and $\tau_3^{1.55\,\mathrm{eV}}(2.7\,\mathrm{eV}, 4.2\,\mathrm{K}) = 21\,\mathrm{ps}$. The extracted

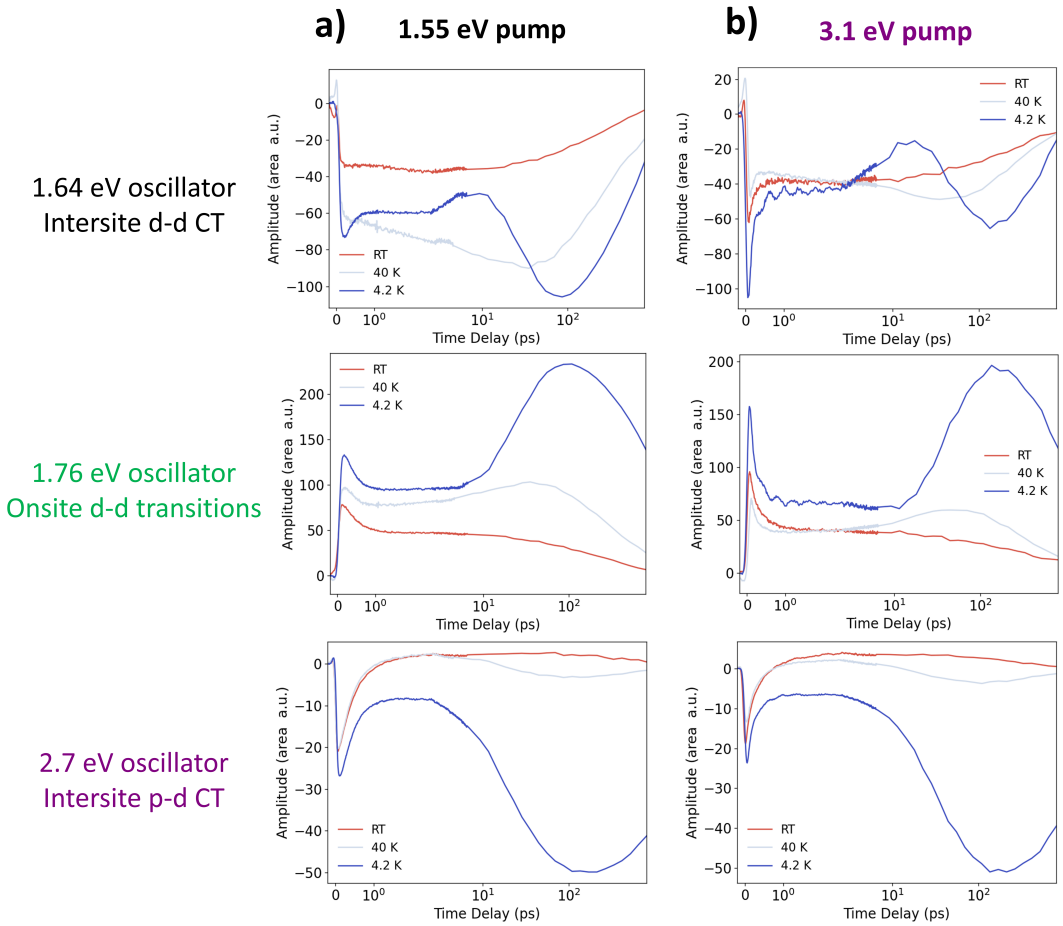

Figure 3.24: Comparison between the 300 K, 40 K and 4.2 K extracted amplitude variations of 1.64 eV, 1.76 eV and 2.7 eV oscillators obtained by pumping at (a) 1.55 eV and (b) 3.1 eV. The time axis is shown in linear-$\log_{10}$ scale (linear up to 6 ps and log_{10} scale from 6 ps to 800 ps). Excitation fluences of $1.5 \times 10^{20}\,\mathrm{cm}^{-3}$ and $5.3 \times 10^{20}\,\mathrm{cm}^{-3}$ were used respectively for the 1.55 eV and 3.1 eV pumps.

time scales τ_4 at 4.2 K and 3.1 eV pumping are: $\tau_4^{3.1\,\mathrm{eV}}(1.64\,\mathrm{eV}, 4.2\,\mathrm{K}) = 55\,\mathrm{ps}$, $\tau_4^{3.1\,\mathrm{eV}}(1.76\,\mathrm{eV}, 4.2\,\mathrm{K}) = 43\,\mathrm{ps}$, and $\tau_4^{3.1\,\mathrm{eV}}(2.7\,\mathrm{eV}, 4.2\,\mathrm{K}) = 37\,\mathrm{ps}$.

3.3.2.3 Suggested interpretation for the incoherent response

As suggested by the RT data, pumping the system at 3.1 eV leads to a faster decay with respect to 1.55 eV pumping. In particular, this was seen both, when comparing single traces (Fig. 3.20c), in the Global Lifetime Analysis, and in the single oscillator amplitude analysis. The first two time scales obtained through GLA are: $\tau_1^{3.1\,\mathrm{eV}} = 0.19\,\mathrm{ps}$ and $\tau_2^{3.1\,\mathrm{eV}} = 0.55\,\mathrm{ps}$ upon 3.1 eV pumping and $\tau_1^{1.55\,\mathrm{eV}} = 0.4\,\mathrm{ps}$ and $\tau_2^{1.55\,\mathrm{eV}} = 5.9\,\mathrm{ps}$ upon 1.55 eV pumping. These results suggest that the states involved in the relaxation upon 3.1 eV pump are possibly different with respect to the ones involved in the relaxation upon 1.55 eV pump. In fact, if the relaxation cascades were the same, upon 3.1 eV pumping one should observe a first ultrafast relaxation $\tau_1^{3.1\,\mathrm{eV}} = 0.19\,\mathrm{ps}$ and then the same relaxation time scales as the 1.55 eV dataset $\tau_1^{1.55\,\mathrm{eV}} = 0.4\,\mathrm{ps}$ and $\tau_2^{1.55\,\mathrm{eV}} = 5.9\,\mathrm{ps}$.

A possible relaxation mechanism is proposed. After the photoexcitation, the first electron-electron scattering relaxation happens in the excited state ($p-d$ CT or $d-d$ CT). This is followed by an electron-phonon scattering which brings the photoexcited carriers in a $d-d$ band; the carriers then recombine. The states reached by pumping at 3.1 eV and 1.55 eV are different and, upon 3.1 eV pumping, the $d-d$ band should be reached faster. The overall interpretation is in accordance with several literature studies which focused on transient optical measurements pumping both the $p-d$ CTs (at 3.1 eV) and the intersite and onsite $d-d$ transitions (at 1.55 eV) on Co_3O_4, probing in the NIR region [202, 204]. These found a negative-to-positive signal behaviour with zero-crossing in the 100 fs-1 ps range when the probe energy is set in the 0.94 eV - 0.83 eV band. This fact corroborates the possible interpretation for which $d-d$ states are progressively filled during the charge carrier's relaxation. In addition, an RT femtosecond visible pump/XUV probe study of the intersite $p-d$ CTs photoinduced relaxation dynamics assigned both the first and second time scales to hot-carrier cooling, but did not exclude the possibility of an ultrafast relaxation to $d-d$ band [201]. However, the TRR technique is not able to give a precise indication on what are the real d states reached during the relaxation process. Therefore, an electronic state selective technique is envisaged to corroborate the interpretation.

Below the AFM transition (*e.g.*, 4.2 K), the signal shape change with a new positive band (Figs. 3.23) can partially be associated to the decrease in FWHM of both the intersite $d-d$ CT and onsite $d-d$ excitations peaks and the shift in position of the oscillators in the static spectra as the temperature lowers. Indeed, considering the static oscillators at 300 K and 7 K, the intersite $d-d$ CT oscillator shifts from 1.632 eV to 1.646 eV (about 14 meV) decreasing its FWHM from

143 meV to 91 meV (50 meV). Instead, the onsite $d-d$ Co^{3+} and Co^{2+} excitation oscillator is only slightly blueshifting (from 1.76 eV to 1.7616 eV, about 1.6 meV) while its FWHM decreases from 0.359 eV to 0.316 eV (about 43 meV).

The first two time scales are similar with respect to RT, 150 K or 70 K (see Tab. 3.5), and this behaviour is independent of the pumped process (1.55 eV, intersite and onsite $d-d$ transitions or 3.1 eV, intersite $p-d$ CTs). This means that the mechanisms of the hot-carrier relaxation *via* electron-electron scattering and the relaxation to the $d-d$ band are not influenced by the AFM order or by the temperature of the system. However, for both pump photon energies, one extra time constant is found below 40 K in the 10-100 ps range. A similar phenomenon was observed in other Transition Metal Oxide systems such as $TbMnO_3$ [265] and was interpreted as lattice-mediated AFM magnetic order melting. As suggested by the data, a similar mechanism can be at play in Co_3O_4. Following the interpretation of $TbMnO_3$ [265] response, the lattice-mediated AFM melting should work as follows: the charge localization in a long-lived self-trapped state would hinder spin-flip mechanisms and the generation of magnons, causing the energy transfer from the charge to the spin system to be mediated by the lattice. The aforementioned picture would be in accordance with other RT time-resolved spectroscopic and THz measurements performed on Co_3O_4 by *Zhang et al.* [204]. According to the authors, after the intersite $p-d$ CTs excitation the photoexcited charge carriers relax in few ps into a self-trapped state which lasts up to the recombination process occurring above 1 ns. Although the time scales found in this work do not fully agree with the values obtained by *Zhang et al.* [204], the formation of a self-trapped state is compatible with the observations. The increase in the amplitude of the new exponential component with decreasing temperature can be thus justified as a consequence of the same aforementioned mechanism. Indeed, at 40 K the spin-flips are not only caused by the photoexcitation but also by the random lattice-spin interactions due to finite temperature. As the sample temperature is decreased the thermal lattice contributions in the ground state become less intense. Therefore, the majority of the spin-flip mechanisms can be due to the photoinduced lattice-mediated magnetic order melting.

3.3.3 TRR coherent responses

The coherent response upon 1.55 eV and 3.1 eV pumping shall now be presented. The coherent response gives insights on the phonon, magnon or even electronic modes impulsively excited in the system. With these insights, one can study what are the modes preferentially triggered by intersite and onsite $d-d$ excitations or by the intersite $p-d$ CTs through the selective 1.55 eV (transitions between d levels of Co ions) and 3.1 eV (transition between p levels of O ligands and d levels of Co iond) pumping, respectively. For example, a coherent lattice response

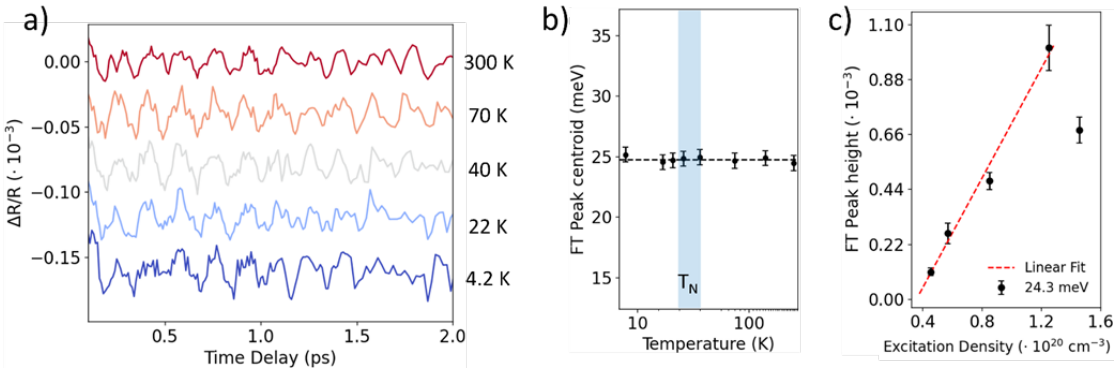

Figure 3.25: Coherent response upon 1.55 eV. a) Coherent response plotted as a function of the time delay at different temperatures (300 K, 70 K, 40 K, 22 K, 4.2 K) and constant excitation density $1.5 \times 10^{20}\,\mathrm{cm}^{-3}$ ($0.8\,\mathrm{mJ/cm}^2$ incident fluence). For each temperature, the traces were obtained firstly by subtracting the GLA multiexponential fitting function from the data to remove the incoherent response. Secondly, a binning in the 1.73-1.88 eV region was performed to increase the SNR and a polynomial function was subtracted to remove other contributions due to overdamped acoustic phonons. b) Oscillation frequency as a function of temperature in linear scale up to 50 K and $\log_{10}$ scale up to 300 K. The Neel temperature (T_N) range is highlighted with a shaded light blue box [61, 64]. The error bars are equal to the resolution of the FFT algorithm employed $\simeq 0.6$ meV. c) Height of the FT peak as a function of the fluence. A linear fit is shown as red dashed line and highlights nonlinear scaling of the signal above $1.42 \times 10^{20}\,\mathrm{cm}^{-3}$ ($0.75\,\mathrm{mJ/cm}^2$ incident fluence) compatibly with the fluence dependence. The error bars are equal to the standard error on the parameters obtained through the Lorentz peak fit.

would give insights into the electron-phonon coupling. The measurements as a function of temperature were taken at: 300 K, 150 K, 70 K, 40 K, 32 K, 27 K, 22 K, and 4.2 K. The measurements as a function of fluence instead were taken at fixed 4.2 K temperature and at the following excitation density values: $4.5 \times 10^{19}\,\mathrm{cm}^{-3}$, $5.7 \times 10^{19}\,\mathrm{cm}^{-3}$, $8.5 \times 10^{19}\,\mathrm{cm}^{-3}$, $1.2 \times 10^{20}\,\mathrm{cm}^{-3}$ and $1.5 \times 10^{20}\,\mathrm{cm}^{-3}$ for 1.55 eV pump and at $3.3 \times 10^{20}\,\mathrm{cm}^{-3}$, $6.2 \times 10^{20}\,\mathrm{cm}^{-3}$, $9.6 \times 10^{20}\,\mathrm{cm}^{-3}$, $1.4 \times 10^{21}\,\mathrm{cm}^{-3}$, $2.3 \times 10^{21}\,\mathrm{cm}^{-3}$ for 3.1 eV pump.

3.3.3.1 Transient Reflectivity coherent response: 1.55 eV pump

Fig. 3.25 shows the temperature dependence of the coherent response obtained with 1.55 eV pump. All the oscillatory time traces shown in the upcoming section were obtained firstly by subtracting the Global Lifetime Analysis (GLA) multiexponential fitting function from the data to remove the incoherent response; secondly, a binning in different probe energy regions (1.65-1.75 eV for 1.55 eV pump and

2.2-2.5 eV for 3.1 eV pump) was performed to improve the Signal-to-Noise Ratio (SNR). A polynomial function was subtracted to remove other contributions due to overdamped acoustic phonons and coherent artefacts. The Fourier Transform traces were obtained through the Python FFT library with the application of a zero-padding method with padding parameter $p = 2$ and Kaiser-Bessel windowing with $\beta = 1$ ($p = 5$ and $\beta = 3$ for the 2D FT maps) [237, 238]. The considered FT peaks both as a function of fluence and as a function of temperature were fitted with Lorentz peak functions and the center energy and height parameters were extracted. The coherent response upon 1.55 eV excitation has a period $T \approx 170$ fs, which correspond to $E \approx 24.3$ meV. As shown in Fig. 3.25a, the oscillations are present in the 300-4.2 K range of temperatures with constant frequency (Fig. 3.25b) and dephasing before complete damping in a time $t_D > 2$ ps. Furthermore, no other oscillation is detected both in the time traces and in the FT spectra. The fluence dependence of the FT peak amplitude is shown in Fig. 3.25c. Its linearity range hints to an impulsive generation mechanism [207, 232, 208]. The range of excitation densities spanned from 0.45×10^{20} cm^{-3} to 1.55×10^{20} cm^{-3}, within the TRR linearity response regime (see Fig. 3.22).

3.3.3.2 Transient Reflectivity coherent response: 3.1 eV pump

Fig. 3.26 shows the temperature and probe energy dependence of the coherent response obtained upon 3.1 eV excitation. The coherent response consequent to the O^{2-} to Co^{3+} and Co^{2+} electron transfer is in the form of oscillations with period $T \approx 400$ fs which correspond to $E \approx 10.2$ meV. As shown in Fig. 3.26a, the oscillations are present in the 300 - 4.2 K range of temperatures with constant frequency (Fig. 3.26b) and are completely damped in a time $t_D > 2$ ps. Furthermore, the oscillation is present in the 1.65-2.6 eV probe energy range without any clear dispersion with the photon energy, as shown in the example case of the 2D FT map (Fig. 3.26c) taken at 4.2 K and 2.5×10^{21} cm^{-3} (4.7 mJ/cm^2). Other contributions to the coherent response are not detected since the oscillations in Fig. 3.26a do not present beats. In Fig. 3.27 the fluence dependence of the 10.2 meV oscillations in the 2.2-2.5 eV probe energy region at 4.2 K is reported. As shown in the residual traces plotted in Fig. 3.27a, the oscillation increases in amplitude as the fluence is increased. The better SNR in the highest fluence measurement (2.5×10^{21} cm^{-3}, 4.7 mJ/cm^2) confirms the fact that the complete damping of the oscillations is reached well above 2 ps and that no other beating effects are present. Therefore, no other oscillation should be detected in the FT process. The frequency of the mode remains constant for every fluence as seen in Fig. 3.27b, where the FT amplitude of the time traces is plotted as a function of frequency of the modes. The height of each peak (Fig. 3.27c), obtained through a Lorentzian fitting, has a linear behaviour up to 9.6×10^{20} cm^{-3} (2 mJ/cm^2 incident fluence) compatibly with the

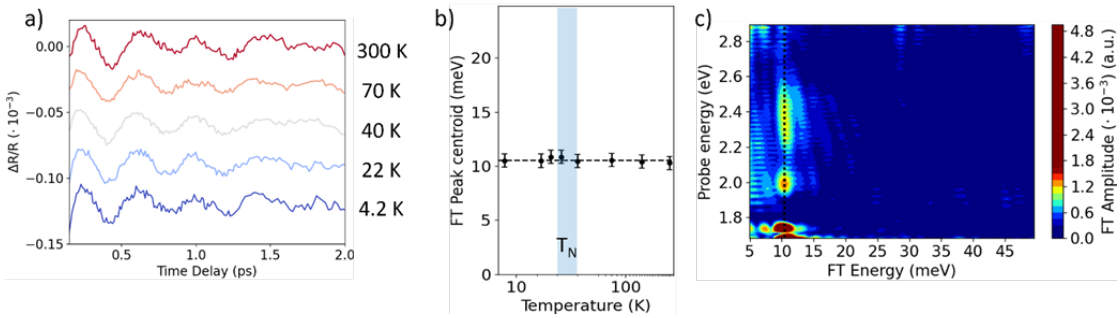

Figure 3.26: Coherent response upon 3.1 eV excitation. a) Coherent response plotted as a function of the time delay at different temperatures (300 K, 70 K, 40 K, 22 K, 4.2 K) and constant excitation density $5.3 \times 10^{20}\,\mathrm{cm}^{-3}$ ($1.1\,\mathrm{mJ/cm}^2$ incident fluence). For each temperature, the traces were obtained firstly by subtracting the GLA multiexponential fitting function from the data to remove the incoherent response. Secondly, a binning in the 2.2-2.5 eV region was performed to increase the signal-to-noise ratio and a polynomial function was subtracted to remove other contributions due to overdamped acoustic phonons. b) Oscillation frequency as a function of temperature in linear scale up to 50 K and $\log_{10}$ scale up to 300 K. The Neel temperature (T_N) range is highlighted with a shaded light blue box [61, 64] The error bars are equal to the resolution of the FFT algorithm employed $\simeq 0.6$ meV. c) Fourier Transform 2D map at 4.2 K, $2.5 \times 10^{21}\,\mathrm{cm}^{-3}$ ($4.7\,\mathrm{mJ/cm}^2$ incident fluence). The FT peak is shown as a function of the probe energy highlighting its presence across all the probe spectrum with constant frequency (evidenced by the black dotted line). The FT map was obtained through the python FFT library with a zero-padding method with padding parameter $p = 5$ and Kaiser-Bessel windowing with $\beta = 3$ [237, 238].

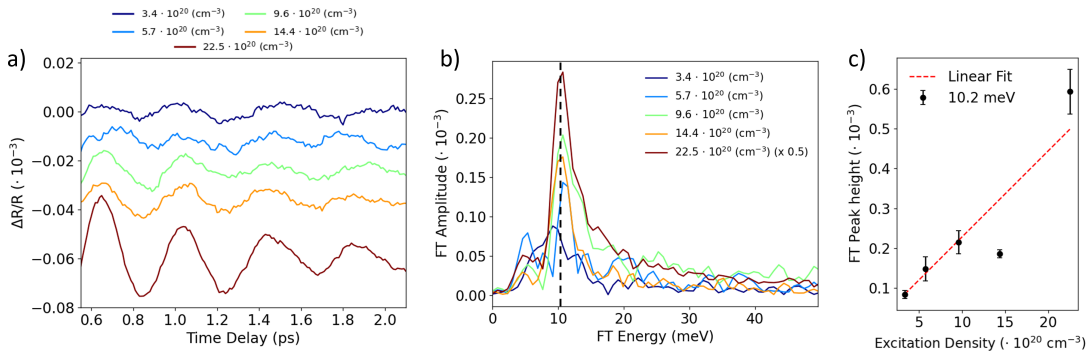

Figure 3.27: Fluence dependence of the coherent response upon 3.1 eV excitation. a) Coherent response plotted as a function of the time delay at different excitation densities at 4.2 K. For each fluence, the traces were obtained firstly by subtracting the GLA multiexponential fitting function from the data to remove the incoherent response. Secondly, a binning in the 2.2-2.5 eV region was performed to increase the signal-to-noise ratio and a polynomial function was subtracted to remove other contributions due to overdamped acoustic phonons. b) Fourier transform of the oscillations as a function of fluence. A black dashed line is used to highlight the constant frequency within the FT resolution (0.6 meV) of the oscillations across all the fluence ranges. The FT traces were obtained through the Python FFT library and a zero-padding method with padding parameter p = 2 and Kaiser-Bessel windowing with $\beta = 1$. The 4.7 mJ/cm^2 trace is rescaled for better comparison c) Height of the FT peak as a function of the fluence. A linear fit is shown as a red dashed line and highlights nonlinear scaling of the signal above 2 mJ/cm^2, compatibly with the fluence dependence. The error bars are equal to the standard error on the parameters obtained through the Lorentz peak fit.

fluence dependence reported in Fig. 3.22b.

3.3.4 Discussion on coherent response

In the following, an in-depth discussion for the possible interpretation of the mechanism underlying the coherent response detected at 24.3 meV and 10.2 meV shall be provided using steady-state characterization techniques and Density Functional Theory (DFT) calculations.

3.3.4.1 Optical phonons

This section starts with a steady-state characterization of optical phonons in Co_3O_4 by Fourier Transform IR (FTIR) and Raman spectroscopies (see sections 2.2.2 and 3.2.1.2). Co_3O_4 unit cell contains 8 sites with a total of 56 atoms, while the Bravais cell contains 2 formula units for a total of 14 atoms, thus giving

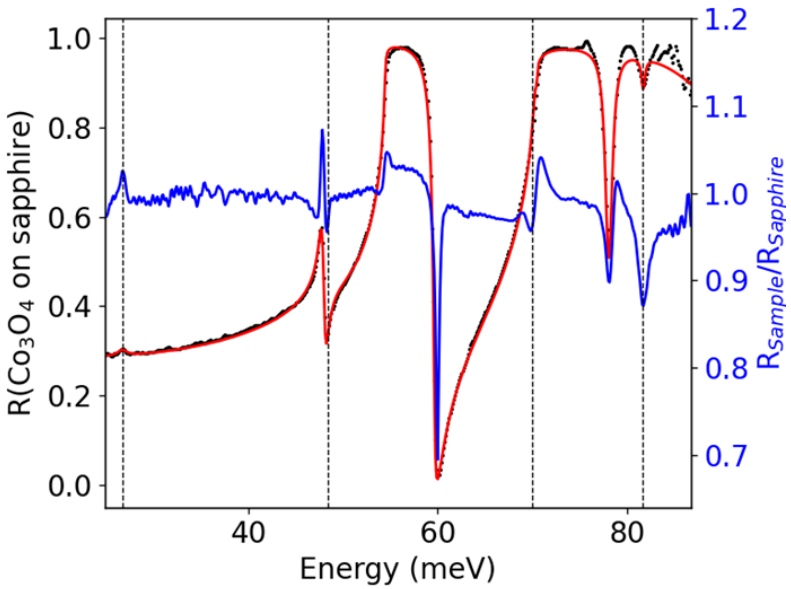

Figure 3.28: Reflectivity of Co_3O_4 on sapphire substrate in the Far Infrared (FIR) (black dots) fitted through a Drude-Lorentz model (red line). The blue line is the ratio between the reflectivity of Co_3O_4 on sapphire and the pure sapphire substrate to evidence the Co_3O_4 IR active phonons indicated with black dashed lines. Other spurious features come from the difference between the sapphire used as a reference and the real sapphire substrate.

42 modes (3 acoustic and 39 optical) [50]. The reduction of the 42-dimensional representation into irreducible representations of the O_h^7 factor group gives $\Gamma = A_{1g} + E_g + 3F_{2g} + 4F_{1u} + 2A_{2u} + 2E_u + 2F_{2u} + F_{1u} + F_{1g}$ as stated by *White and DeAngelis* [50]. Among these, 4 are IR active with F_{1u} symmetry [266, 267] and 5 are Raman active with symmetries $3F_{2g}$, E_g and A_{1g} [268]. The symbol A (B) means that the mode is single degenerate and symmetric (antisymmetric) with respect to a C_n rotation (with angle expressed in $2\pi/n$) while E and F stand for doubly and triply degenerate, respectively. The subscripts "g" (*gerade*) and "u" (*ungerade*) stand for symmetric and antisymmetric with respect to the inversion operation, respectively. The Raman and FTIR measurements were performed in collaboration with the Earth and Planetary Science Laboratory of the École Polytechnique Fédérale de Lausanne and with Dr. F. Barantani, Dr. J. Teyssier and Dr. V. Multian of the Quantum Materials Group of the University of Geneva.

Fig. 3.28 shows the Far infrared (FIR) reflectivity spectrum of Co_3O_4 on sapphire (black dots) normalized by a gold film standard (perfect mirror $R = 1$ across the energy range), fitted with a Drude-Lorentz model (red line). We detected and retrieved all the IR active modes of the $Fd\bar{3}m$ structure of Co_3O_4 with F_{1u} symmetry at the following energies (black dashed lines): 26.6 meV, 48.9 meV, 70.5 meV,

Energy in meV Fit	Energy in meV DFT GGA+U	HREELS spectrum Literature [267]	IR spectra Literature [266]	Symmetry
26.6	26.9	26.8	26.8	F_{1u}
48.9	47.8	47.5	48.6	F_{1u}
70.5	68.4	71.0	70.0	F_{1u}
81.7	82.6	84.7	81.5	F_{1u}

Table 3.6: IR active modes detected and their comparison with our DFT simulations and literature. The symmetry of each mode is indicated in the fourth column and is based on HREELS and IR spectra found in literature [267, 266] and on the normal mode analysis of the spinel structure [50, 268]

and 81.7 meV. Their comparison with Density Functional Theory (DFT) calculations and literature HREELS [267] and FIR [266] measurements along with their symmetries is reported in Tab. 3.6. We underline the fact that the sample features are hidden by strong sapphire substrate response because of the long penetration depth of Far- and Mid-Infrared radiations. Therefore, we validated the fit and phonon energies retrieval by taking the ratio between the Co_3O_4 on sapphire and reference sapphire reflectivity spectra. The latter is shown in the blue curve of Fig. 3.28 highlighting all the Co_3O_4 IR active phonons. The strong features observed at 61 meV and 75 meV can possibly be assigned to the discrepancies between the thin film substrate and the reference sapphires, which are not the same sample. Spurious contributions may arise by a different normalization with the gold standard, impurities, unpolished surfaces, and by the silver paste used to glue the sample into the sample holder. In addition, we also mention that the presence of spurious effects does not allow the detection of other IR active modes in the region below 12.4 meV, be they of electronic or structural origin but, based on literature results, we should not expect any other IR active contribution down to 6.2 meV [266].

The Raman response of Co_3O_4 was investigated in literature in several studies [268, 269, 270]. These used excitation energies resonant with the intersite $p-d$ CT between O^{2-} and Co^{2+} (2.33 eV). In addition, the lower limit of these measurements was set at 12.4 meV. We investigated the Raman spectra resonant with both intersite $d-d$ CT, onsite $d-d$ excitations, and intersite $p-d$ CTs optical transitions (see Fig. 3.29a). In Fig. 3.29b we report the resonance Raman spectra in the 9.5-95 meV shift region, exciting the sample with 2.33 eV and 1.58 eV photons at RT and with 3.06 eV photons at 77 K. We detected all Raman active modes with A_{1g}, E_g and $3F_{2g}$ symmetries, consistently with the factor group analysis [50]. These are highlighted by black dashed lines in Fig. 3.29b and reported in Tab. 3.7 along with their energy calculated through DFT calculations and their symmetry assignment based on polarization dependent measurements [268]: 24.3 meV

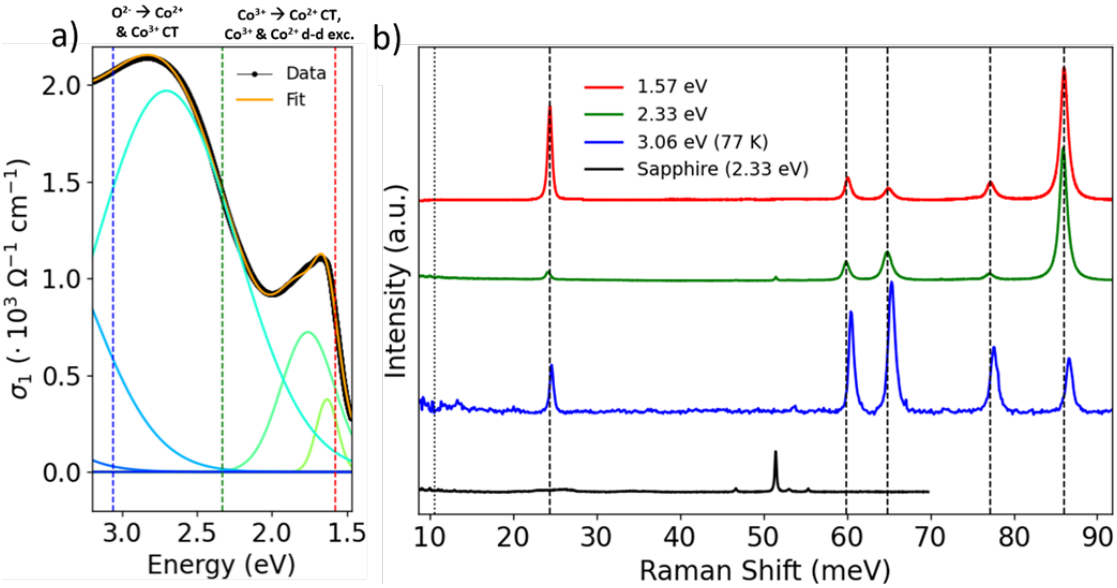

Figure 3.29: a) Inset in the optical conductivity spectrum with the Raman excitation lines indicated with green (2.33 eV), red (1.57 eV) and blue (3.06 eV) dashed lines. b) Raman spectrum of the Co_3O_4 thin film and sapphire substrate obtained with a 100x magnifying objective. An arbitrary offset was introduced along the vertical axis for clarity. Each Co_3O_4 spectrum was normalized by its most intense peak. The pure sapphire substrate ($E_{exc} = 2.33$ eV) is shown in black and is scaled by an arbitrary factor to highlight the presence of a peak at 51.4 meV visible also in the 2.33 eV spectrum of the Co_3O_4 film. The dashed black lines mark the Raman shift position of the modes having energies and symmetries: 24.3 meV F_{2g}, 59.9 meV E_g, 64.8 meV F_{2g}, 77.1 meV meV F_{2g}, and 85.9 meV A_{1g}. The dotted line highlights the absence of any Raman feature at 10.2 meV.

F_{2g}, 59.9 meV E_g, 64.8 meV F_{2g}, 77.1 meV F_{2g}, and 85.9 meV A_{1g}. We observed a faint feature in the 2.33 eV excitation measurements at 51.4 meV which is ascribed to the sapphire substrate as confirmed by a separate measurement of the pure substrate (Fig. 3.29b, black spectrum). Instead, no sign of a 10.2 meV Raman active mode is detected (dotted line in Fig. 3.29b). The Co_3O_4 spectra, normalized to the A_{1g} 85.9 meV feature for 2.33 eV and 1.58 eV excitation and to the E_g 65 meV one for 3.06 eV, show strong dependence of the mode intensities from the excitation energy. We notice that the most affected feature is the F_{2g} 24.3 meV mode, which decreases significantly when the excitation is switched from 1.58 eV to 2.33 eV and increases again when the excitation is at 3.06 eV. In particular, the Raman spectrum with excitation at 3.06 eV shows blueshifted peaks given by the phonon hardening expected at lower temperatures accompanied by a different arrangement of the intensities. Indeed, the most intense mode becomes the 65 meV

Energy in meV Fit	Energy in meV DFT GGA+U	Raman spectrum Literature [268]	Symmetry
24.2	25.1	24.1	F_{2g}
59.9	58.9	59.8	E_g
64.8	66.3	64.7	F_{2g}
77.1	77.9	76.7	F_{2g}
85.9	87.9	85.7	A_{1g}

Table 3.7: Raman modes detected and their comparison with DFT calculations and literature. The symmetry of each mode is indicated in the fourth column and is based on polarization dependent measurements [268]

accompanied by a strong decrease of the 86 meV A_{1g} one.

In Fig. 3.30, the results of Density Functional Theory (DFT) calculation are reported. These were carried out in collaboration with Prof. Przemysław Piekarz and Dr. Andrzej Ptok of the Polish Academy of Science. The crystal and electronic structures of spinel Co_3O_4 were optimized using the projector augmented-wave method [271] within the Generalized Gradient Approximation (GGA) [272] implemented in the VASP program [273]. The full relaxation of the lattice parameters and atomic positions was performed in the crystallographic cell of the $Fd\bar{3}m$ structure containing 256 atoms. The phonon dispersion curves were obtained using the direct method [274] implemented in the PHONON software [275]. Through this calculation, we retrieved the IR, Raman and inactive phonon modes. In particular, the IR and Raman active modes are in agreement with the experimental ones as presented in Tab. 3.6 and 3.7, respectively. In addition, we retrieved the $2A_{2u}$, $2E_u$, $2F_{2u}$, F_{1u}, and F_{1g} inactive phonon modes as reported in Tab. 3.8 along with their energies at the Γ point. The energies are reported both for the structure with optimized cell parameters and with the cell parameters taken from literature [276]. The lowest inactive mode at the Γ point has an energy of 28.7 meV and symmetry F_{2u}. Furthermore, no other feature is detected below 24 meV with the first phonon being the 24.3 meV Raman active one. The acoustic branches allow also for the extraction of the sound velocities along the principal crystallographic directions of the sample. The extracted value is around 6 km/s in agreement with literature studies on Bulk and Young's moduli [277, 278].

From the Raman experimental evidence and DFT calculations a possible interpretation of the mechanism of generation of the 24.3 meV oscillation observed upon 1.55 eV pumping can be provided. Indeed, the frequency of the oscillation is in optimal agreement with the 24.3 meV mode detected in steady-state Raman experiment reported in this section (Fig. 3.29b), DFT calculations, and literature data [268, 269, 270]. In addition, in Fig. 3.29b one can observe that, upon 1.58 eV excitation, the 24.3 meV peak shows a strong enhancement in amplitude possibly

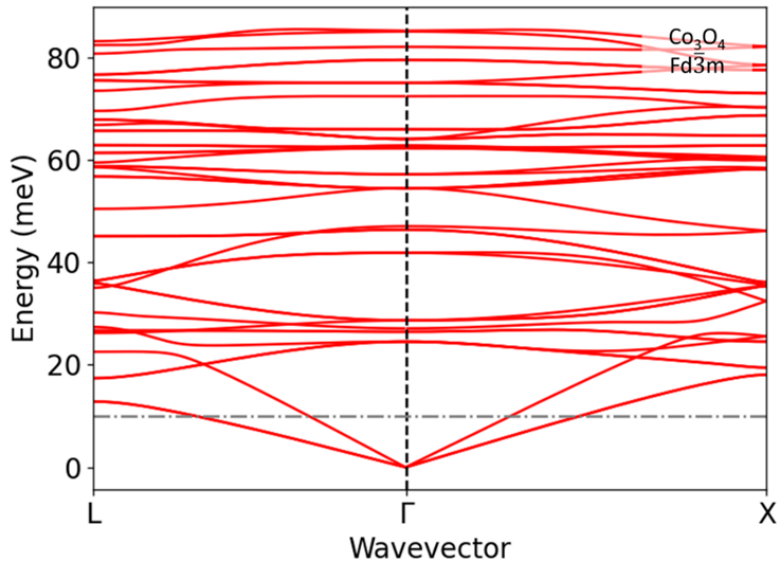

Figure 3.30: Phonon dispersion in the Brillouin zone of Co_3O_4 with $Fd\bar{3}m$ structure obtained through DFT calculations.

indicating that the mode is resonant with the intersite $d-d$ CT and onsite $d-d$ electronic transitions. Therefore, the data suggest that the coherent oscillation obtained upon 1.55 eV pumping can be ascribed to an impulsively excited coherent phonon with F_{2g} symmetry. To clarify the possible mechanism of generation (ISRS or DECP), the oscillations were fitted with a damped cosine function as shown in Figure 3.31 for the 70 K trace, extracting precise indications on the damping time *i.e.*, the time needed for the oscillation amplitude to be decreased by $1/e$ and, most importantly, about the phase of the oscillation. A damping constant $t_D \approx 4$ ps and a phase $\phi \approx 0$ were obtained. Therefore, the analysis suggests that the generation mechanism is possibly a DECP process [208].

Moreover, DFT calculations [269] ascribed the F_{2g} Raman mode to a specific lattice distortion involving the Co^{2+} tetragonal sites displacement along the [111] direction. This displacement induces changes in the lattice structure which, in turn, change the XRD pattern. The consequence of a model distortion similar to the F_{2g} Raman mode is sketched in Figs. 3.32a,b. Here, a single rhombohedral Co_3O_4 primitive cell is considered in steady-state conditions (a) and with an exemplary model distortion of the Co^{2+} ion (b). The arrow indicates the direction of the distortion induced by the 24.3 meV phonon and the surface of the sample is sketched as a grey [111] plane. A possible estimation of the 24.3 meV phonon-sensitive Bragg peaks is done by computing the XRD signal intensities with the help of VESTA [197]. These are reported in Fig. 3.32c computed for the two cases. Based on this simple analysis, one can select the brightest peaks for which

Energy in meV DFT GGA+U (opt)	Energy in meV DFT GGA+U	Symmetry
28.7	28.7	F_{2u}
41.9	42.9	E_u
54.4	56.2	F_{1g}
54.5	56.3	A_{2u}
62.3	64.8	F_{2u}
62.8	64.9	E_u
82.1	85.0	A_{2u}

Table 3.8: Inactive phonon mode energies reported at the Γ point both with optimized cell parameters and with literature cell parameters [276]. The symmetry of each mode is reported in the third column.

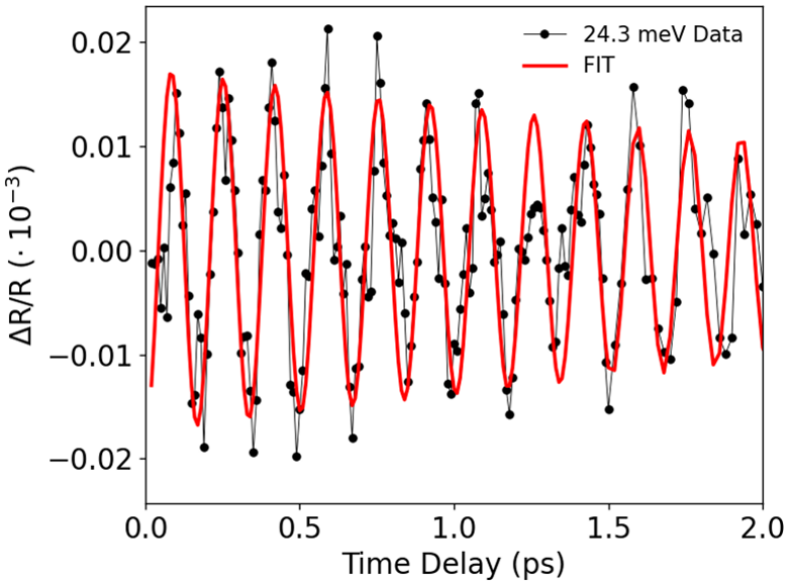

Figure 3.31: 70 K residual time trace showing the 24.3 meV oscillation fitted with a damped cosine function. The data are reported with black dots connected by a black line while the fit is reported with a red line.

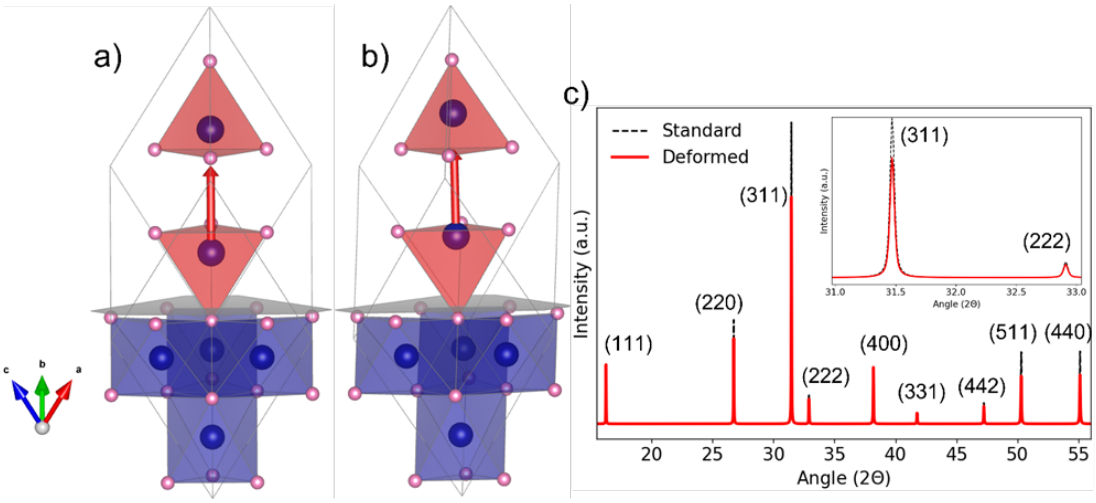

Figure 3.32: Effect of the Co^{2+} tetrahedral atomic displacement induced by the F_{2g} 24.3 meV phonon in the primitive rhombohedral unit cell. a) Standard rhombohedral Co_3O_4 unit cell b) Co_3O_4 unit cell with an exemplary model distortion acting solely on Co^{2+} ions. The red arrow points along the distortion direction orthogonal to the [111] plane which is reported in grey and corresponds to the out-of-plane orientation of the Co_3O_4 sample. c) XRD patterns of the standard and distorted unit cells in an unoriented sample (*e.g.* powder) calculated with VESTA [197] (inset) zoom on the region of the (311) and (222) peaks.

the intensity is strongly modified and compatibly with the experimental geometry of XRD. This selection is crucial for the combined FEL TR-XES and TR-XRD analysis experiments (see characterization section 3.3.1.2 and FEL setup section 3.2.2.2). The chosen peak is the three-fold degenerate (311) (Figure 3.32c, inset) because it is the most sensitive, thus, gives the highest SNR.

In this last section, the characterization of the Raman active, IR active, and inactive modes of Co_3O_4 was shown accompanied by DFT calculations. This characterization helped in providing an interpretation mechanism for the 24.3 meV oscillation found as coherent response pumping at 1.55 eV. Instead, no 10.2 meV mode was detected either in the steady-state characterization and in the DFT calculations. To give an interpretation for this latter mode it is necessary to consider optical phonon modes not related to Co_3O_4 but to another stoichiometry of the Cobalt oxide, CoO or to the sapphire substrate.

3.3.4.2 CoO phonons

First of all, it is essential to exclude that the 10.2 meV oscillation stems from Cobalt oxide in other stoichiometries *e.g.*, CoO which phonon dispersion is reported in

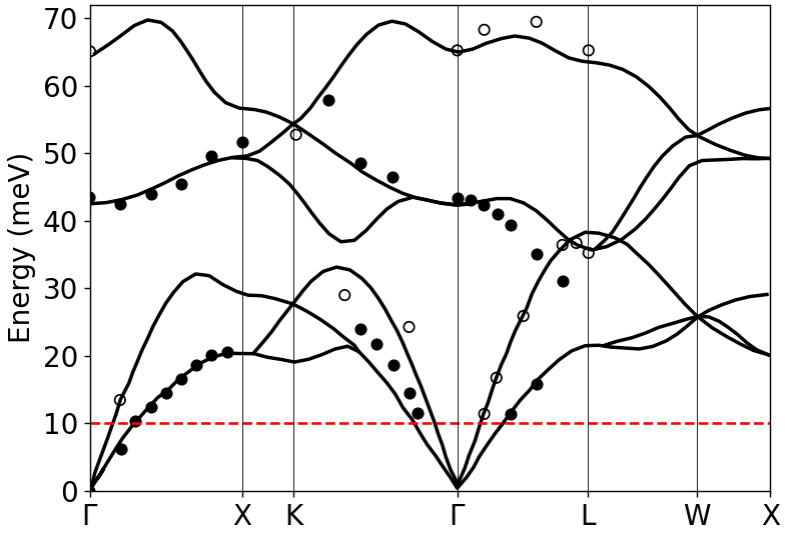

Figure 3.33: Phonon dispersion curves for CoO obtained through *ab initio* calculation (solid line) and through inelastic neutron scattering experiments at 110 K (dots). Solid and open symbols indicate transverse and longitudinal modes, respectively. The high-symmetry points are labelled according to the FCC Brillouin zone. A red dashed line is used to highlight the absence of optical modes at 10.2 meV (2.46 THz). Picture adapted from *Wdowik et al.* (copyright 2007 The American Physical Society) [279] with data from *Sakurai et al.* [280].

Fig. 3.33 [279, 280]. The phonon dispersion curves are obtained through *ab initio* calculations (solid lines) and inelastic neutron scattering at 110 K. CoO has a rocksalt structure within the $Fm\bar{3}m$ space group and has only one phonon at the Γ point that is IR active with F_{1u} symmetry. Since CoO can be regarded as a wide-gap insulator ($E_{gap} \approx 2.8$ eV), it is required to consider the coupling between atomic displacements and the long-range macroscopic electric field. This field splits the F_{1u} optical mode to transverse (TO, open dots in Fig. 3.33) and longitudinal (LO, solid dots in Fig. 3.33) components, the so-called LO-TO splitting. The IR internal vibrations have TO and LO modes absorbing at different frequencies with the LO frequency being greater than the TO frequency. This happens because the local electric field causes polarization of the surrounding atoms in the opposite direction for the LO mode but in the same direction for the TO mode. Therefore, two modes are observed in the phonon dispersion. Their energies are reported in Tab. 3.9. The absence of a mode at 10.2 meV is highlighted with a red dashed line which does not intersect the optical phonon dispersion curve. Indeed, the lowest optical phonon at the Brillouin zone centre (F_{1u} TO at the Γ point) has energy $E \approx 43$ meV (10 THz). This comparison suggests that the 10.2 meV oscillation it is hardly ascribable to an optical phonon of CoO impurities in the sample.

Mode	Calculated energy in meV [279]	Exp energy in meV Neutron diffraction [280]	Exp energy in meV IR spectroscopy [281]
TO	42.4	43.4	42.6
LO	65.1	65.2	67.4

Table 3.9: Longitudinal and Transverse frequencies of the F_{1u} optical phonon in CoO. The second column shows the phonons calculated in *Wdowik et al.* [279] compared with the experimental ones obtained by neutron scattering (third column) from *Sakurai et al.* [280] and IR spectroscopy (fourth column) from *Gielisse et al.* [281].

3.3.4.3 Sapphire phonons

The other system that needs to be considered for the possible assignment of the 10.2 meV oscillation is sapphire (Al_2O_3). The motivations behind this reside in the fact that a [1111]-oriented sapphire was employed as substrate for the film synthesis. Therefore, it is crucial to understand if the 10.2 meV oscillation comes from the phonon modes of the substrate detected in the TRR experiment. Sapphire (α-Al_2O_3) crystalizes in a trigonal structure with point group $\bar{3}m(D_{3d})$ and space group $R\bar{3}c(D^6_{3d})$. Group theory predicts 18 phonon modes reported by *Kappus* [282] at the Γ point with the following decomposition:

$$\Gamma = 2A_{1g} + 2A_{1u} + 3A_{2g} + 3A_{2u} + 5E_g + 5E_u \tag{3.37}$$

The two A_{1g} and the five E_g phonons are Raman active; two out of three of the A_{2u} phonons and four out of five of the E_u phonons are IR active, the other two left are acoustic modes. A_{1u} and A_{2g} modes are inactive. The phonon dispersion curves are reported in Fig. 3.34 where the open and solid black dots represent the IR and Raman active phonons at the Γ point, respectively. The phonons frequencies of the active and inactive modes are reported in Tab. 3.10 along with their symmetries, reported in several literature studies [282, 283, 284, 285, 286]. Again, a red dashed line indicates the total absence of a mode at 10.2 meV since it does not intersect with any optical phonon dispersion curve at the Γ point. This is corroborated by the lowest optical phonon available in Tab. 3.10 which is inactive, has energy $E \approx 37.3$ meV and A_{2g} symmetry. It is stressed that all the modes predicted for the trigonal α-Al_2O_3 at the Γ point were found.

Further confirmation of the absence of 10.2 meV feature can be found in TRR measurements on the sapphire substrate. The results are reported in Fig. 3.35. In particular, Fig. 3.35a shows the 2D map of the $\Delta R/R$ response plotted as a function of the probe energy and the time delay. It is noticed that no clear signature of oscillation can be extracted from the bare data and no other incoherent response was detected since the bandgap of α-Al_2O_3 with corundum structure was determined to be $E_g \approx 8.8$ eV from optical measurements and *ab initio* simulations [287, 288, 289]. In addition, in Fig. 3.35b two traces are obtained by removing

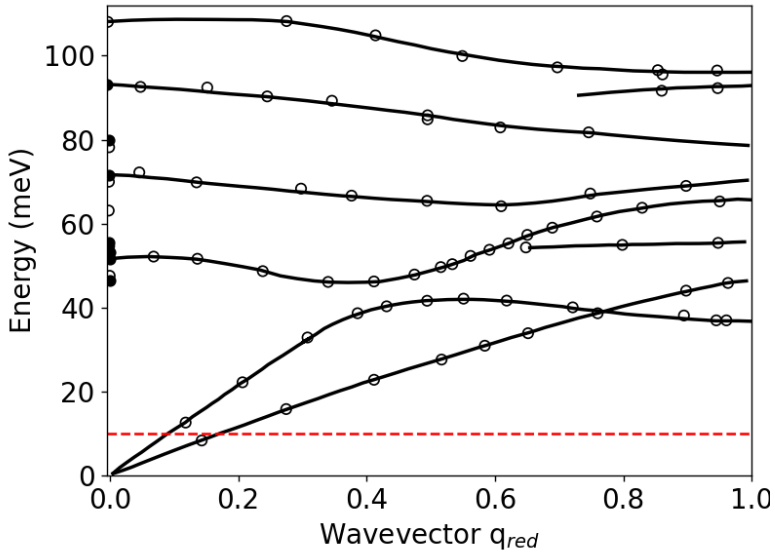

Figure 3.34: Phonon dispersion curves measured through inelastic neutron scattering. At the Γ point ($q_{red} = 0$) the open and solid black dots represent the IR and Raman active phonons, respectively. A red dashed line is used to highlight the absence of optical modes at 10.2 meV (2.46 THz). Adapted from *Bialas and Stolz* [283].

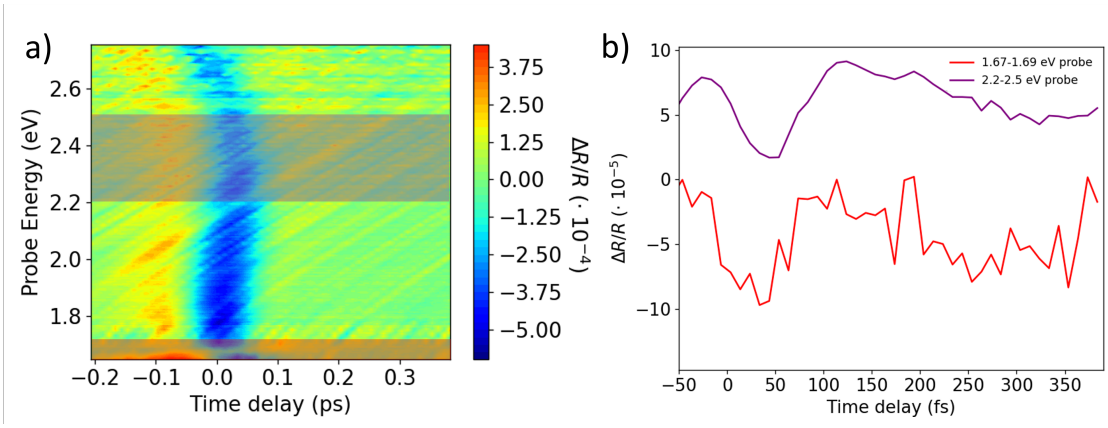

Figure 3.35: Transient reflectivity response of Sapphire upon 3.1 eV pump, plotted in the first 0.5 ps. a) 2D TRR map as a function of probe energy and time delay the highlighted regions represent the probe energies considered for the binning. b) Residual time traces obtained by binning in the 1.67-1.69 eV and 2.2-2.5 eV probe energy regions. No clear sign of the beginning of the 10.2 meV oscillation is detected

Energy in meV	Raman, IR, Inactive mode	Symmetry
37.3	N	A_{2g}
46.9	R	E_g
48.0	I	E_u
49.6	I	A_{2u}
51.8	R	A_{1g}
53.6	R	E_g
55.1	I	E_u
55.9	R	E_g
66.5	N	A_{2g}
70.7	I	E_u
71.7	R	E_g
72.4	I	A_{2u}
73.7	N	A_{1u}
79.0	I	E_u
80.0	R	A_{1g}
85.3	N	A_{1u}
92.8	N	A_{2g}
93.1	R	E_g

Table 3.10: Shappire Raman, IR and Inactive phonon mode energies obtained from literature Raman [284] and IR [285] experiments and calculations [282] In the second column the phonons are labelled as Raman active (R), IR active (I) or Inactive (N). The symmetry of each mode is instead reported is in the third column.

the coherent artefact and performing a probe energy binning in the main regions where the 10.2 meV oscillation was found *i.e.*, 1.67-1.69 eV and 2.2-2.5 eV. All the reasons discussed in this paragraph suggest that it is not possible that the mode belongs to the sapphire substrate be it an optical or acoustic phonon or of other origin.

3.3.4.4 Acoustic phonons

A separate discussion is needed in the case of the acoustic phonons. Indeed, in the previous dispersion curves presented in Figs. 3.30, 3.33, 3.34 a phonon with 10.2 meV energy is possible. It must be acoustic and could be found between the Γ and the L points of the Brillouin zone. Therefore, an acoustic phonon scenario for the 10.2 meV oscillation should be considered. Such a scenario can be excluded for two reasons: (i) the frequency of the mode should have a linear dispersion with probe energy due to Brillouin scattering [290] and (ii) the calculated sound velocity for the mode should match the typical sound velocity (v_s) of Co_3O_4. Instead,

no probe energy dependence of the frequency can be observed in Fig.3.26c. In addition, if the 10.2 meV oscillation was an acoustic phonon the sound velocity associated with the mode could be calculated *via* the following formula [291]:

$$v_s = \frac{4d}{\tau_0} \tag{3.38}$$

where d is the thickness of the film and τ_0 is the period of the oscillation. Taking the values $d \approx 27 \times 10^{-9}$ m and $\tau_0 \approx 407 \times 10^{-15}$ s, $v_s \approx 265$ km/s which is almost two orders of magnitude higher than the calculated v_s in bulk Co_3O_4, $v_s \approx 6$ km/s from DFT calculations and experimental measurements [277, 278]. Moreover, Young's modulus can be also calculated starting from the estimated v_s through the following formula:

$$v_s = \sqrt{\frac{Y}{\rho}} \tag{3.39}$$

which, by solving for Y, becomes:

$$Y = v_s^2 \rho \tag{3.40}$$

By putting in the values of v_s and ρ (6 g/cm^3), $Y \approx 4 \times 10^5$ GPa which is two orders of magnitude the one of diamond (1050 GPa). These calculations and the absence of frequency variation with the probe energy in Fig. 3.26c suggest that the 10.2 meV oscillation is not an acoustic phonon.

3.3.4.5 Magnons and Bi-Magnons

Magnons and Bi-magnons may modulate the TRR response in an oscillatory way compatible with the 10.2 meV oscillation. Magnons can be explored only below the magnetic ordering temperature T_N because they are bound to long-range correlations [292]. The data suggest that a magnon picture is likely to be excluded. In fact, the oscillation is present well above T_N (30-40 K) with no significative FT energy and intensity temperature dependence (Figs. 3.26a,b).

Instead, bi-magnons are linked to short-range magnetic correlations in one or two unit cells and thus may survive well above T_N [293, 294, 295, 296]. However, they were detected in Raman experiments on different systems, *e.g.* superconducting $YBa_2Cu_3O_7$ (YBCO) [296] or α-MnTe [295]. Therefore, they should be Raman active modes. In the case of YBCO and other systems presented in *Sugai et al.* [296] the Raman shift produced by bi-magnons is around 0.1-0.2 eV with FWHM around 0.2 eV at RT. The effective lifetime can be calculated from the width of the Raman resonance through the simple formula $FWHM(THz) = 1/\tau(ps)$ obtaining about 20 fs [297]. Therefore, they should be seen as overdamped oscillations in

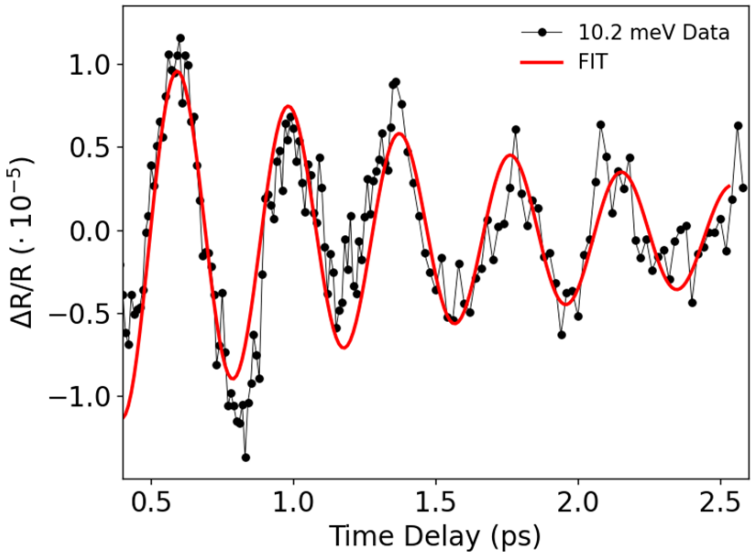

Figure 3.36: 150 K residual time trace showing the 10.2 meV oscillation fitted with a damped cosine function. The data are reported with black dots connected by a black line while the fit is reported with a red line.

the time traces. In another case, α-MnTe, bi-magnons are found at about 33 meV and are subjected to an energy shift of about 0.7 meV, a 40% drop in intensity, and a broadening of the linewidth as the temperature is increased [293, 294, 295]. Due to the aforementioned considerations, it seems reasonable to exclude even the bi-magnon picture since no Raman signal is detected at 10.2 meV. Moreover, the damping of the 10.2 meV oscillation can be analyzed, preferentially above T_N. This was done for the oscillation at 150 K as reported in Fig. 3.36. The data were fitted with a damped cosine function and the damping time *i.e.*, the time needed for the oscillation amplitude to be decreased by $1/e$ and the phase of the oscillation were extracted obtaining $t_D \approx 1.6$ ps and $\phi \approx 0$, respectively. The results corroborate the exclusion of the bi-magnon picture since the complete damping of the mode is reached above 2.5 ps (Fig. 3.36 and Fig. 3.26a). In addition, it is less favourable to have a detection of magnons or bi-magnons by a TRR channel but rather by optical Kerr effect [295, 298, 299] (*e.g.*, Time Resolved Magneto Optical Kerr Effect) or Faraday rotation [300] experiments.

3.3.4.6 Hidden-order phase transition modes

More in general, the 10.2 meV oscillation can be associated with excitation of modes within a phase transition (*e.g.*, Charge Density Waves) with critical temperature between RT and 4.2 K or to impulsively stimulated phase transitions. In

the first case, the elementary excitations might be able to modulate the $\Delta R/R$ response. Some examples of transient response modulation related to phase transitions are found in CDW detected in $TiSe_2$ [301], superconductors like $BaFe_2As_2$ [302] and tritellurides [303] soft modes linked to the trimeton network in Fe_3O_4 [15] under the Verwey transition and possibly even optical phonons in WTe_2 [304]. A crucial point regarding these excitations based on the aforementioned systems is that a softening of the oscillatory response is expected as the critical temperature is approached or as the fluence is increased. This softening may appear both on the frequency and on the amplitude of the response and present a quenching when the fluence is above a critical value [15, 301, 304]. In the TRR data (see Fig. 3.26 and 3.27), no amplitude or frequency softening and quenching of the 10.2 meV oscillation is observed as a function of fluence or temperature. This happens even for fluences out of the linearity range as reported in Fig. 3.29c. Therefore, it is reasonable to say that the mode cannot be associated to elementary excitations corresponding to a phase transition in Co_3O_4 at least in the considered temperature and fluence ranges.

3.3.4.7 Pump-induced structural transition exclusion

A further mechanism that might induce TRR oscillatory modulation is related to pump-induced structural phase transitions. Following this approach, the pump would lead to an ultrafast structural change generating Co_3O_4 with other crystalline arrangements. Then, during the decay, the same fingerprints of spinel $Fd\bar{3}m$ Co_3O_4 would be observed with an oscillatory modulation given by an impulsively stimulated optical phonon of the other excited structural phase. This phenomenon was studied in a CoFe Prussian blue analogue where the system was excited with a 2.3 eV pulse to study the charge transfer processes with XAS and TR-absorption with an overall time resolution of 25 fs and 80 fs, respectively [305]. A 6.8 meV oscillation was detected and ascribed to the coupling of the spin transitions with lattice bending in the Co site.

The scenario here presented can possibly be excluded by looking at the phonons of the other common structures of Co_3O_4 through DFT calculation. These were performed through collaboration with Prof. Przemysław Piekarz and Dr. Andrzej Ptok of the Polish Academy of Science as described in section 3.3.4.1. At ambient pressure and temperature, Co_3O_4 is found in the sole $Fd\bar{3}m$ structure and no structural phase transition is reported to lower the temperature. The only structural phase transitions that can be found for this system are obtained by increasing the pressure [306, 307, 308]. A first transition from the $Fd\bar{3}m$ structure to the orthorhombic $Fddd$ one was found at 23 GPa followed by other two transitions towards monoclinic $C2/m$ and $P2_1/c$ at 45 GPa and 52 GPa, respectively. In this framework, *Golosova et al.* [309] found a coexistence between long-range AFM

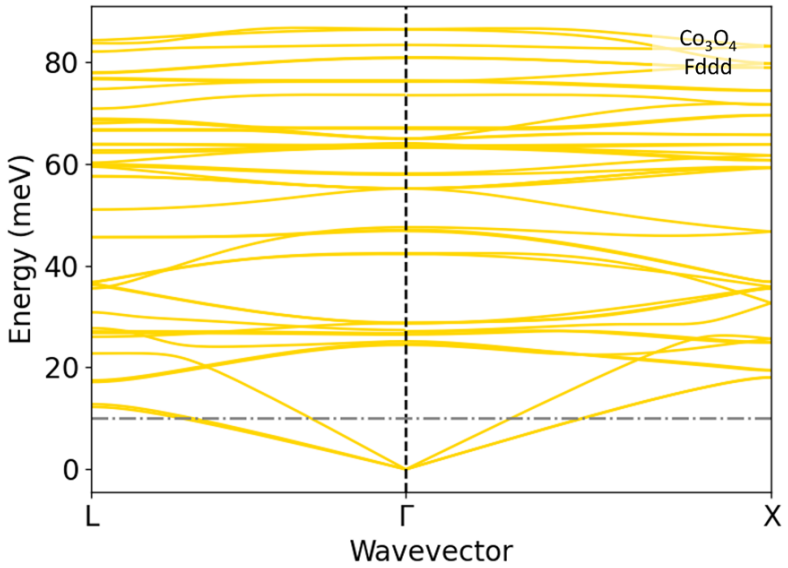

Figure 3.37: Phonon dispersion in the orthorhombic $Fddd$ structure of Co_3O_4 calculated through DFT. A red dashed line is used to highlight the absence of optical modes at 10.2 meV.

ordered and short-range disordered phases below the AFM transition at ambient pressure. The latter phase disappears as the pressure is increased above 2 GPa with an increase of the Neel temperature up to 50 K.

Within this framework, in Fig. 3.37 we report the phonon dispersion of the $Fddd$ phase of Co_3O_4 obtained through DFT. The presence of 39 phonons was found at the Γ point. Their energies, Raman (R) and Infrared (I) activity or their Inactivity (N) are indicated along with their symmetry in Tab. 3.11. As highlighted by the red dashed line and by the lowest phonon energy around 24 meV, no 10.2 meV optical phonon is detected in the $Fddd$ structure. From this standpoint, literature studies stop only to the lowest 24.3 meV mode which was explored, for example, through Raman spectroscopy as a function of the pressure in *Cova et al.* [306].

In Fig. 3.38a, we report a sketch of the transition from the $Fd\bar{3}m$ structure to the monoclinic $P2_1/c$ one taken from *Kaewmaraya et al.* [276]. The monoclinic phase reached contains two classes of octahedra, namely Co(II)O_6 and Co(III)O_6 interconnected to each other by sharing edges with open structure layered along the [001] direction. This is a direct consequence of the increased coordination number of Co(II) from 4 in $Fd\bar{3}m$ to 6 in $P2_1/c$ structure. As a result, the cation–cation bond distances become nearly the same; Co^{2+}-Co^{2+} = 2.73 Å, Co^{2+}–Co^{3+} =2.68 Å and Co^{3+}–Co^{3+} =2.73 Å in a different way from those in the cubic structure where Co^{2+}–Co^{2+} > Co^{2+}–Co^{3+} > Co^{3+}–Co^{3+}. Further-

Energy in meV	Raman, IR, Inactive mode	Symmetry
24.4	R	B_{3g}
24.7	R	B_{2g}
25.1	R	B_{1g}
26.4	I	B_{3u}
26.5	I	B_{2u}
27.0	I	B_{1u}
28.7	I	B_{3u}
28.7	I	B_{2u}
28.8	I	B_{1u}
42.3	N	A_u
42.4	N	A_u
46.8	I	B_{2u}
46.9	I	B_{3u}
47.0	I	B_{1u}
55.1	R	B_{1g}
55.1	N	A_u
55.2	R	B_{2g}
55.2	R	B_{3g}
57.9	R	A_g
58.1	R	A_g
63.2	I	B_{3u}
63.2	I	B_{2u}
63.5	N	A_u
63.5	I	B_{1u}
64.0	N	A_u
64.9	R	B_{1g}
65.0	R	B_{3g}
65.0	R	B_{2g}
66.8	I	B_{1u}
67.1	I	B_{3u}
67.1	I	B_{2u}
76.1	R	B_{3g}
76.2	R	B_{1g}
76.3	R	B_{2g}
80.7	I	B_{3u}
80.8	I	B_{2u}
80.9	I	B_{1u}
83.3	N	A_u
86.4	R	A_g

Table 3.11: *Fddd* structured Co_3O_4 Raman, IR and Inactive phonon mode energies obtained from DFT calculations. In the second column, the phonons are labelled as Raman active (R), IR active (I) or Inactive (N). The symmetry of each mode is instead reported in the third column.

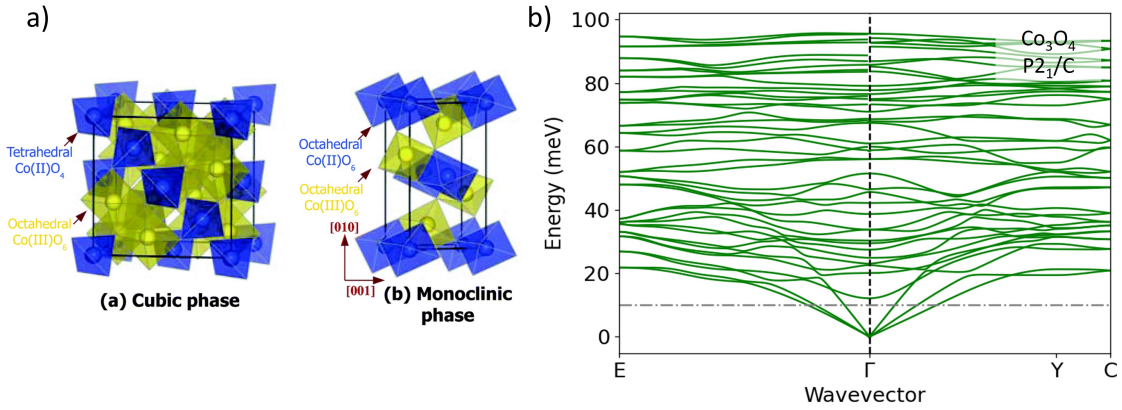

Figure 3.38: a) Sketch of the Cubic and Monoclinic $P2_1/c$ phase of Co_3O_4 adapted from *Kaewmaraya et al.* [276] b) Phonon dispersion in the monoclinic structure of Co_3O_4 calculated through DFT. A red dashed line is used to highlight the absence of optical modes at 10.2 meV.

more, the Co(II)O_6 and Co(III)O_6 octahedra are highly distorted with the average Co^{2+}–O^{2-} and Co^{3+}–O^{2-} bond distances of 1.89 Å and 1.92 Å, respectively. The phonon dispersion of the $P2_1/c$ phase of Co_3O_4 obtained through DFT is reported in Fig. 3.38b. The energies of each phonon at the Γ point, their Raman (R) and Infrared (I) activity or their Inactivity (N) is indicated along with their symmetry in Tab. 3.12. Again, as sketched by the red dashed line and indicated by the lowest optical phonon energy at the Γ point being around 12 meV, the presence of an optical phonon with 10.2 meV energy is likely to be excluded.

It is important to stress that DFT calculations on the phonon dispersion of the other monoclinic $C2/m$ structure were not performed because of the lack of parameters describing completely this phase and the difficulty in the convergence of the DFT algorithms. Furthermore, this last structure lasts only in a small range of pressures as mentioned above. The result shown above suggests that the pump-induced structural phase transition mechanism is unlikely to happen in Co_3O_4. In fact, the calculations show that no optical phonon mode of the other Co_3O_4 structural phases, *i.e.* orthorhombic $Fddd$ and monoclinic $P2_1/c$, has frequency matching with the results obtained upon 3.1 eV pumping [276]. Furthermore, it is unlikely to have a pump-induced structural phase transition exciting a coherent phonon in the sample with 3.1 eV photons. This is rather possible with photon energies comparable with the phonon modes induced in the sample which, in turn, are obtained through THz sources.

Energy in meV	Raman, IR, Inactive mode	Symmetry
12.1	I	A_u
20.1	I	A_u
22.6	R	A_g
23.0	I	B_u
24.9	R	A_g
27.5	R	B_g
29.4	I	B_u
30.3	I	A_u
33.8	I	A_u
33.8	I	B_u
38.7	R	B_g
42.2	R	B_g
45.6	R	A_g
46.4	I	B_u
51.5	I	A_u
56.0	R	B_g
56.0	R	A_g
58.5	I	B_u
58.8	I	A_u
61.0	R	A_g
67.4	R	B_g
67.8	I	B_u
68.6	I	A_u
71.0	R	A_g
72.1	I	B_u
73.3	I	A_u
75.0	R	B_g
76.6	R	B_g
77.8	R	A_g
79.1	I	A_u
79.6	I	B_u
83.7	I	A_u
85.9	R	A_g
86.0	I	B_u
87.0	R	B_g
91.5	I	B_u
92.8	R	A_g
94.2	I	A_u
95.6	R	B_g

Table 3.12: $P2_1/c$ structured Co_3O_4 Raman, IR and Inactive phonon mode energies obtained from DFT calculations. In the second column, the phonons are labelled as Raman active (R), IR active (I) or Inactive (N). The symmetry of each mode is instead reported in the third column.

3.3.5 Suggested interpretation of the 10.2 meV mode

In the last sections, the possibility of the 10.2 meV mode to be an acoustic or optical phonon, a magnon, a bi-magnon or a phonon induced by pump-induced structural transition was excluded based on experimental data and literature review. All the results shown so far involve only the 2.2-2.6 eV probe energy region which corresponds to the inflection point of the intersite $p-d$ $O^{2-} \rightarrow Co^{2+}$ CT transition. Therefore, it is reasonable to state that this transition is modulated at all temperatures by the mode with a damping time above 2.5 ps. However, the effect of the 10.2 meV oscillation in the 1.65-1.8 eV probe region must also be considered.

Figure 3.39 shows the 2D FT amplitude (Fig. 3.39a) and phase (Fig. 3.39b) maps plotted as a function of the probe energy in the 1.65-1.77 eV region and of the FT energy for two selected temperatures above (70 K) and below the AFM transition (4.2 K). At 70 K *i.e.*, above T_N a peak centred at 10.2 meV is found with an extracted phase of 0 across the 1.65-1.72 eV probe energy region. Below the AFM transition at 4.2 K two distinct regions of maximum of the oscillation are found: 1.65-1.70 eV and 1.72-1.74 eV. These two regions are in antiphase with each other as shown in the phase 2D map at 4.2 K(Fig. 3.39b) and can be seen by overlapping two residual time traces (*i.e.*, with GLA fit subtracted from raw data) in the 1.65-1.70 eV and 1.72-1.74 eV ranges as shown in Fig. 3.39c for the 4.2 K dataset. By looking at the static R spectra restricted to the 1.5-1.9 eV region (Fig. 3.39d), it is possible to see that the two peaks retrieved in the 4.2 K 2D FT map correspond to the maximum slope points of the onsite Co^{3+} and Co^{2+} $d-d$ transitions (gold shaded box) and of the intersite $d-d$ $Co^{3+} \rightarrow Co^{2+}$ CT (black shaded box). Therefore, by pumping the intersite $p-d$ O^{2-} to Co^{2+} and O^{2-} to Co^{2+} CTs below the AFM transition, the oscillation is possibly modulating all the transitions in the probe energy region being them intersite CT involving $p-d$ or $d-d$ states or onsite $d-d$ excitations. Furthermore, as reported in literature for systems such as rare earth tritellurides (RTe_3), $BaFe_2As_2$ and α-MnTe [295, 302, 303, 310] the detection of antiphase oscillations is indicative of the modulation of an electronic transition position and amplitude with the coherently excited mode frequency. In this case, the antiphase behaviour between the intersite $d-d$ CT and onsite $d-d$ excitation suggests that this 10.2 meV mode is affecting the probability of the $d-d$ transitions in the 1.65-1.8 eV range. Above the T_{Neel}, the peak is mostly concentrated in the 1.66-1.68 eV region hinting to a modulation of the sole onsite $d-d$ excitations which adds to the modulation of the intersite $p-d$ CT discussed above (thus the intersite $d-d$ CT is not modulated). This is a suggestion that the switching of the spin degree of freedom by the magnetic ordering is causing the switching of the modulation of the intersite $d-d$ electron transfer between Co^{3+} and Co^{2+} sites. The modulation is complementary to the

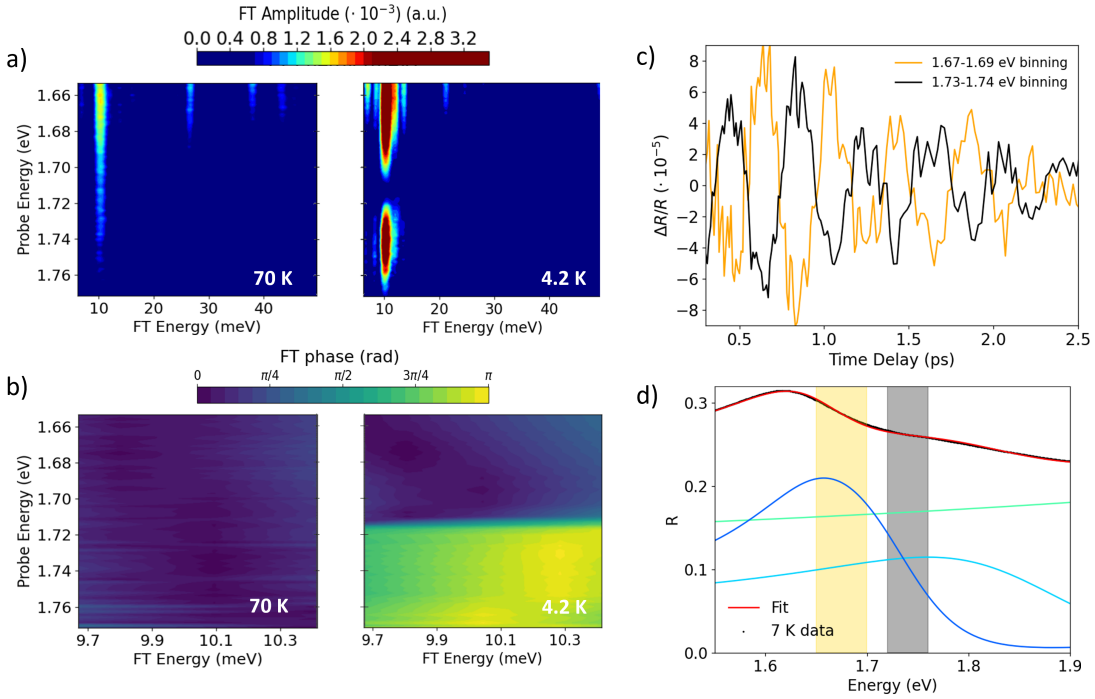

Figure 3.39: a) FT 2D amplitude and b) FT 2D phase maps of the residuals above (70 K) and below (4.2 K) the AFM transition plotted as a function of the probe energy and FT energy in the 1.65-1.77 eV probe energy range for 3.1 eV pump. The FT energy range is 6-50 meV for the amplitude map while it is restricted to 9.7-10.4 meV (peaks region) for the phase map. c) 4.2 K TRR residual time traces extracted from two different probe energy regions showing the antiphase behaviour of the 10.2 meV oscillation: 1.67-1.69 eV (gold) and 1.73-1.74 eV (black). d) Co_3O_4 static R spectrum in the 1.5-1.9 eV region fitted with a Drude-Lorentz model. The relevant oscillators are plotted below the data and fit curves. The gold and black shaded regions indicate the probe energies where the antiphase oscillations were detected, colour coded in accordance with the timetraces.

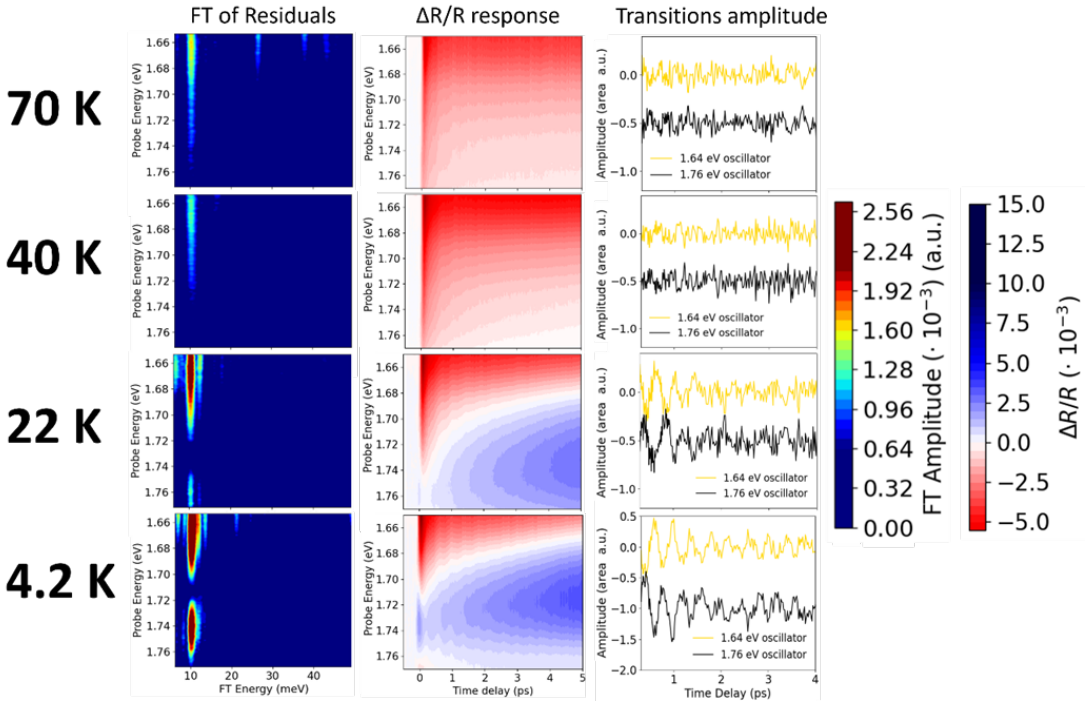

Figure 3.40: Correlation between the FT of the 10.2 meV oscillation (left), the change in the raw ΔR/R response (centre), and the residuals of the amplitude variation of the 1.64 eV and 1.76 eV transitions (right) as a function of temperature in the 1.65-1.77 eV probe energy region. The amplitude variations' residuals were obtained starting from the amplitude traces and subtracting a multiexponential fit and a 10th-degree polynomial function to eliminate the incoherent response and the acoustic phonons and coherent artefact contributions, respectively.

onsite $d-d$ transitions one so that, if the probability (amplitude) of the onsite $d-d$ excitation is increased, the probability of the intersite $d-d$ CT is decreased and *vice versa*. The latter scenario is suggested in Fig. 3.40 where the correlation as a function of the temperature between the FT of the 10.2 meV oscillation (left), the change in the $\Delta R/R$ response (centre) and the residuals of the amplitude variation of the 1.64 eV and 1.76 eV oscillators (right) is reported. It is reminded that the 1.64 eV transition is associated to the intersite $d-d$ CT from a Co^{3+} ion to the Co^{2+} one while, the 1.76 eV transition is a mix of onsite $d-d$ transitions in the Co^{3+} and Co^{2+} ions. Details on the process followed to obtain the variation of the amplitude as a function of time delay are shown in section 3.2.2.1. As the temperature is lowered below T_{Neel} (30-40 K), the 1.65-1.75 eV region shows a splitting of the FT 2D map which is correlated with the appearance of a positive $\Delta R/R$ response from the first fs in the 1.72-1.76 eV energy region accompanied

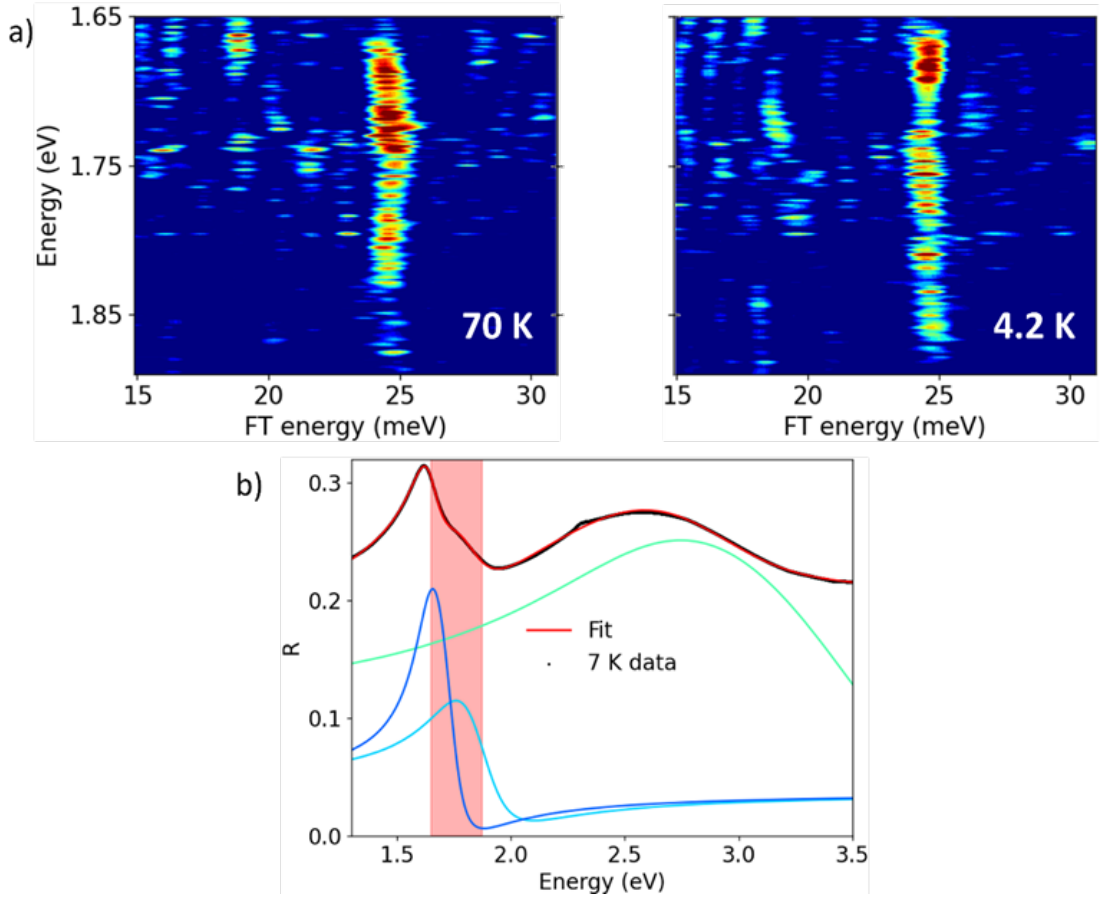

Figure 3.41: a) 2D FT amplitude maps obtained by pumping the $d-d$ transitions at 1.55 eV above (70 K) and below (4.2 K) the AFM transition plotted as a function of the probe energy and FT energy in the 1.65-1.77 eV probe energy range. b) Co_3O_4 static R spectrum in the 1.45-3.5 eV region fitted with a Drude-Lorentz model. The relevant oscillators are plotted below the data and fit curves. The red-shaded region indicates the probe energies where the 24.3 meV F_{2g} phonon was detected.

by a visible antiphase behaviour in the raw data. This correlation is retrieved also in the amplitude (and thus the probability) of the oscillators involved in the probe region which show the characteristic antiphase oscillations below T_{Neel}. This means that, if the probability of the 1.64 eV is increased, the probability of the 1.76 eV is decreased by an equal amount. Instead, above T_{Neel} no sign of coherent oscillations are retrieved in both the transition amplitudes. In addition, the data show that this antiphase amplitude and $\Delta R/R$ response is starting in between 32 K and 22 K which is near the estimations of T_{Neel} (30-40 K) [61, 64, 311].

Instead, the 1.55 eV pump acts directly on the $d-d$ transitions (intersite and onsite) triggering a lattice response which is not dependent on the spin degree of freedom and acts only in the 1.65-1.8 eV region. Therefore, it modulates only the intersite $d-d$ Co^{3+} to Co^{2+} CT. This is shown in Fig. 3.41 where the 2D FT map amplitude is reported at RT and 4.2 K for 1.55 eV pump along with the deconvoluted static R response in the 1.45-3.5 eV region.

The provided framework, suggests that the 10.2 meV mode excited through 3.1 eV pump is likely a purely electronic mode which can be coupled to the other degrees of freedom (lattice and spin). A possible assignment of the generation mechanism is the following: by pumping at 3.1 eV pump *i.e.*, exciting the intersite $p-d$ CT of the system, the Spin-Orbit coupling changes. This may cause a splitting of the energy bands generating a coherent electronic mode during the relaxation. The mode may be accompanied by a long-standing structural distortion through extended Jahn-Teller phenomena generating a Spin-Orbit polaron. Such polaron would not be seen when pumping the intersite $d-d$ CT at 1.55 eV as shown in section 3.3.3.1 and would have a long-standing character since it is completely damped after 2.5 ps. In addition, this mode is possibly collective as it modulates all the sites in the system and is possibly intertwined with the spin degree of freedom (Figs. 3.39 and 3.40). A possible mechanism for the antiphase modulation below the AFM transition is the following: the electronic coherent mode would modulate the probability and energy of the $d-d$ transitions in the 1.65-1.8 eV range thanks to warping of the band structure induced by a change in the exchange interaction which is traceable to the strong decrease in FWHM and position shifting of the intersite $d-d$ CT oscillator seen in 7 K optical conductivity measurements [302]. However, this picture must be compatible with the difference between two spin-orbit levels of, for example, Jahn-Teller distorted Co^{3+} site in Co_3O_4 [203]. Therefore, the final completion of the framework and the possible interpretation of the 10.2 meV mode would be reached only with electronic multiplet calculations including Spin-Orbit coupling. These shall be completed in the next months thanks to the collaboration with Dr. S. Chaudhary and Prof. G. Fiete from Northeastern University in the USA.

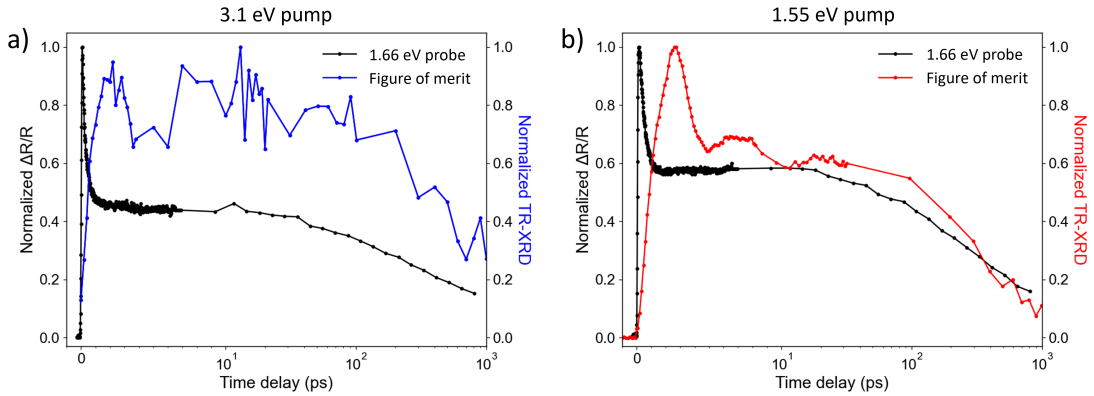

Figure 3.42: Comparison between the TRR and TR-XRD time traces obtained for a) 3.1 eV (blue) and b) 1.55 eV (red) pumps respectively. The TR-XRD traces were obtained with a 9.3 keV X-Ray pink beam considering the variation of the (311) XRD peak. The TRR traces are represented in black and are both extracted at 1.66 eV probe energy. The data were normalized to their maximum intensity for clarity.

3.3.6 TR-XRD and TR-XES preliminary results

TR-XRD and TR-XES preliminary results are shown in Figs. 3.42 and 3.43. These were obtained by probing the sample with an X-Ray pink beam centred at 9.3 keV, in the framework of the combined TR-XRD and TR-XES experiment carried on at EXFEL that was described in section 3.2.2.2

Figs. 3.42a,b show the comparison between the TRR and TR-XRD traces for 3.1 eV and 1.55 eV pumps, respectively. The XRD traces were obtained by detecting the variation in time of the (311) XRD peak. The choice of this peak was done considering the variation of the static XRD response to a deformation induced by the F_{2g} phonon at 24.3 meV (section 3.3.4.1). For both 3.1 eV and 1.55 eV pumping, the TR-XRD transient reaches a maximum within a few ps and, after an intensity modulation, it stabilizes around a plateau value at about 10-100 ps, further decaying in the 100-1000 ps time scale. The overall behaviour resembles the TRR signal, with notable differences limited to the first few ps, where the optical transients are characterized by steep growth and ultrafast decay. From the preliminary analysis of the traces, one can see that the XRD time trace at 3.1 eV pump has possibly a faster response with respect to the 1.55 eV pump one. By fitting with a multiexponential function both the traces the following time scales were found: $\tau_1^{3.1\,\mathrm{eV}} = 200$ fs and $\tau_2^{3.1\,\mathrm{eV}} = 3.3$ ps for 3.1 eV pump and $\tau_1^{1.55\,\mathrm{eV}} = 730$ fs and $\tau_2^{1.55\,\mathrm{eV}} = 3.6$ ps for 1.55 eV pumping. This pairs with what was seen in the optical TRR response. Therefore, it is reasonable to say that the lattice response should be faster if the intersite $p-d$ CTs are pumped. The correlation between the TRR

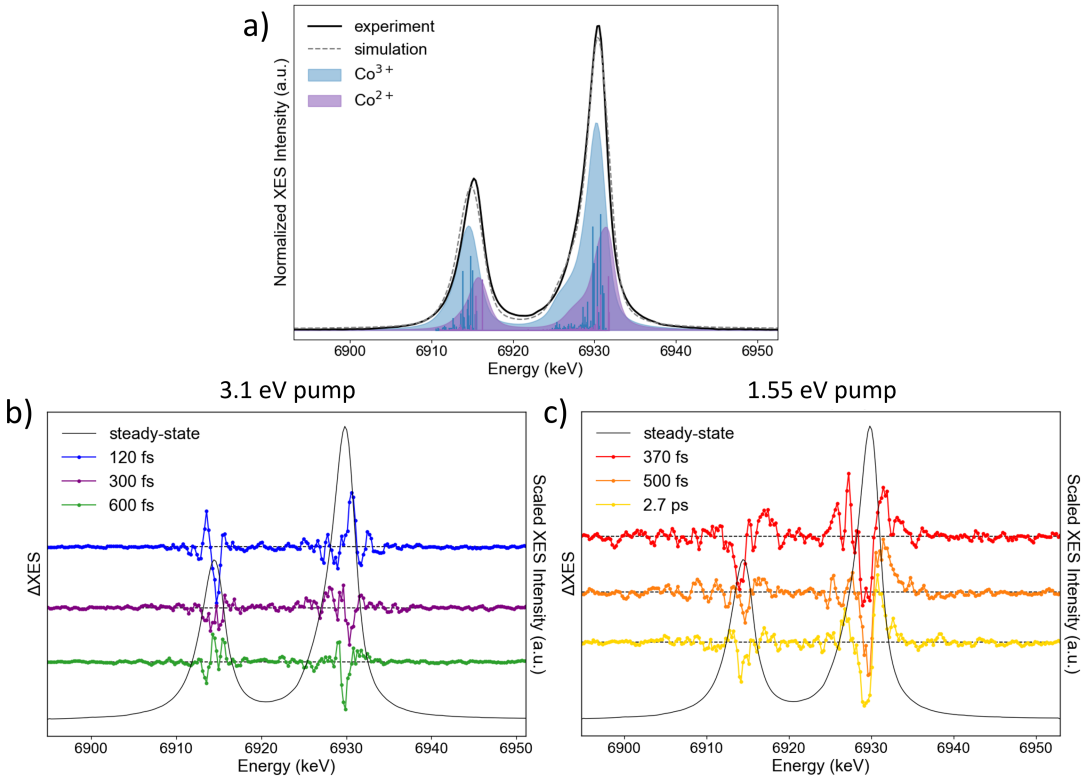

Figure 3.43: a) Steady-state XES K_α spectrum (solid line) of Co_3O_4 thin film compared with the electronic levels simulations (dashed spectrum). The Co^{3+} and Co^{2+} contributions are indicated in light blue and blue, respectively. The intensity of the XES spectrum and simulation are normalized for clarity. The histograms superimposed to the contributions indicate the possible final states involved in the XES spectrum. TR-XES traces at different time delays for b) 3.1 eV and c) 1.55 eV pumps. The steady-state trace is superimposed to the TR-XES ones as a black solid line.

decay and the TR-XRD rise suggests that the ultrafast process following both excitation photon energies involves electron-phonon scattering occurring after hot carrier relaxation through electron-electron interaction. Furthermore, the decay of both TRR and TR-XRD signals on ps-ns time scales shows a correlation between light-induced structural distortions and charge carriers recombination, suggesting the presence of polaronic distortions in the system.

Other possible hints of the correctness of the interpretation of the incoherent dynamics in spinel Co_3O_4 come from the preliminary TR-XES data and steady-state XES spectra simulations. Fig. 3.43a shows the steady-state XES K_α spectrum of the Co_3O_4 thin film (solid lines) compared to the crystal field multiplet calculations (dashed lines) performed using the BlueprintXAS software [312] in

collaboration with Prof. M. U. Delgado-Jaime from the Universidad de Guadalajara in Mexico. The plot shows two peaks centred around 6915 eV and 6930 eV, which correspond to the Cobalt transitions of an electron from the $2p$ shell to the unoccupied $1s$ shell. The two peaks are defined as $K_{\alpha 1}$ (from $2p_{3/2}$ shell to $1s$ shell) at 6930 eV and $K_{\alpha 2}$ (from $2p_{1/2}$ shell to $1s$ shell) at 6915 eV emissions, respectively. A match between the calculation and data is noticed with little discrepancies confined in the $K_{\alpha 2}$ part of the spectrum. The shaded light blue and purple areas correspond to the calculated Co^{3+} and Co^{2+} calculated contributions to the spectra, with the former consistently lying at lower emission energies with respect to the latter. The histograms superimposed on the contributions indicate the possible final states involved in the XES spectrum. The assignment of the precise states involved is still a work in progress.

Figs. 3.43b,c show the TR-XES traces for 3.1 eV and 1.55 eV pumps, respectively superimposed to the steady-state spectrum. The traces were obtained following the procedure described in section 3.2.2.2. The transients in Fig. 3.43b,c show a remarkable difference for the two pump photon energies. The spectra in panel 3.43b are characterized by a drastic change on ultrafast time scales, with a sign flip of the main transient feature at 6930 eV between 120 fs and 300 fs. The simulations in panel 3.43a suggest that these changes involve an initial, transient increase of the number of Co^{2+} centres consistently with *Jiang et al.* [201], followed by a decrease with respect to the ground state. A correlated modulation is observed at the $K_{\alpha 2}$ line, where the transient changes from a derivative-like shape to a less pronounced pump-probe signal. At longer time scales, between 300 fs and 600 fs, only minor modifications occur, mostly limited to the low-energy side of the $K_{\alpha 1}$ line. The transients reported in panel 3.43c show a more pronounced modulation of the K_{α} signal for both emission lines. At 370 fs, the $K_{\alpha 1}$ line is characterized by an increase of the spectral intensity at both lower and higher energies with respect to the main peak, which instead has a negative amplitude. These changes suggest a transient decrease in the number of Co^{3+} sites and their conversion into Co^{2+}. However, due to the overlapping contribution of the two Cobalt sites, a more detailed analysis is required based on simulations. In this respect, the XES computation for the excited state Cobalt electronic configurations of the system is currently in progress. The consistency of the spectral line shapes across the investigated time scales (370 fs, 500 fs, 2.7 ps), confirms that after a charge carrier relaxation occurs in about 400 fs, the system does not undergo further changes in the local Cobalt electronic configuration, in tentative agreement with the population of long-lived onsite $d-d$ excited states [202]. The pronounced differences between the TR-XES spectra and their evolution over time corroborate the findings based on the TRR response analysis, where a faster response of the system upon 3.11 eV excitation with respect to the 1.55 eV one was observed.

Therefore, they corroborate the possible interpretation for which Co_3O_4 does not undergo a cascade relaxation process.

3.4 Conclusion to this chapter

In this chapter, the complex interplay between the electronic, lattice and spin degrees of freedom of a 27 nm Co_3O_4 thin film was investigated. Firstly, the sample composition and crystalline quality were verified through XAS, XRD and electron diffraction. The steady-state optical response of the film was then characterized assigning the main optical transitions. This assignment is crucial to distinguish the pumped and probed transitions and their behaviour with temperature. After the first steady-state characterization, the time resolved response of Co_3O_4 under 1.55 eV and 3.1 eV pumps was shown starting from the incoherent response as a function of temperature. A qualitatively similar broadband incoherent response is detected for both pump energies. However, the time scales retrieved by Global Lifetime Analysis (GLA), showed a faster decay when the system is pumped at 3.1 eV with respect to 1.55 eV pumping. This behaviour is corroborated by the comparison of the oscillators' amplitudes and is in contrast with the reasoning for which pumping charge carriers at 3.1 eV bring them in a higher energy state, thus the decay process should be slower with respect to 1.55 eV pump. The incoherent response across the AFM transition shows a change in the broadband signal shape with the appearance of a new positive band in the 1.77-1.91 eV probe energy range and the appearance of a new timescale in the 10-100 ps range for both the pumping energies below $T_N = 40$ K. This latter result is confirmed by both GLA and the amplitude of the oscillators. The amplitude of the new exponential decay detected below T_N is temperature dependent hinting to a possible interplay between lattice and spin degrees of freedom. A possible interpretation for the faster response upon 3.1 eV pumping is that the states involved in the relaxation are different with respect to the ones followed after 1.55 eV excitation. In fact, if the relaxation cascades were the same, upon 3.1 eV pumping one should observe a first ultrafast relaxation $\tau_1^{3.1\,\mathrm{eV}} = 0.19$ ps and then the same relaxation time scales as the 1.55 eV dataset. The change in the signal shape as the temperature lowers is possibly interpreted based on the changes in central energy and FWHM of the intersite $d - d$ CT oscillator as a function of temperature. The mechanism for the new timescale arising below T_N is possibly lattice-mediated magnetic order melting which was investigated in other Transition Metal Oxides such as $TbMnO_3$ [265]. The mechanism should work as follows: the charge localization in a long-lived self-trapped state would hinder spin-flip mechanisms and the emission of magnons, causing the energy transfer from the charge to the spin system to be mediated by the lattice.

The 1.55 eV pump coherent response is in the form of oscillations with energy 24.3 meV. These oscillations are given by an optical phonon of symmetry F_{2g} concerning the Co^{2+} site and modulate the intersite and onsite $d-d$ CT transitions. The phonon is impulsively generated through DECP as retrieved by the phase of the oscillation. By pumping the intersite $p-d$ CT transitions from O^{2-} to Co^{2+} and Co^{3+} at 3.1 eV an oscillation at 10.2 meV was found. This is not present in the steady-state Raman and FTIR responses. The possible origin of this oscillation was discussed taking into account different other phenomena which can give a coherent response in the form of oscillations, namely: acoustic or inactive phonons, magnons, bi-magnons, spurious phases in the sample, or pump-induced structural phase transitions. Such phenomena were possibly excluded through the data analysis, DFT calculations and comparison with literature. Moreover, the mode possibly couples with the spin degree of freedom and modulates all the oscillators below the AFM transition temperature. In this framework, the modulations of the intersite $Co^{3+} \rightarrow Co^{2+}$ CT and the onsite Co^{3+} and Co^{2+} excitations are in antiphase. The results suggest that an elementary excitation with the above-mentioned signatures is possibly a purely electronic one. In particular, the possible mechanism of generation of such mode is through a purely electronic oscillation within two Spin-Orbit levels split by the 3.1 eV pump. Furthermore, this mode can possibly be coupled with structural distortions induced by extended Jahn-Teller phenomena, generating a Spin-Orbit polaron. However, electronic structure calculations are needed to completely address this latter scenario.

In conclusion, preliminary TR-XRD and TR-XES results were shown. These corroborated the interpretation of the incoherent dynamics in the sample. Indeed, TR-XRD preliminary analysis of the traces, showed that the XRD time trace at 3.1 eV pump has possibly a faster response respect to the 1.55 eV pump one. Therefore, it is reasonable to say that the lattice response is faster if the intersite $p-d$ CTs are pumped. In addition, the correlation between the TRR decay and the TR-XRD rise suggests that the ultrafast process following both excitation photon energies involves electron-phonon scattering. Furthermore, the decay of both TRR and TR-XRD signals on ps-ns time scales shows a correlation between light-induced structural distortions and charge carriers recombination, suggesting the presence of polaronic distortions in the system. The TR-XES results showed different responses in the $K_{\alpha 2}$ signals at 3.1 eV and at 1.55 eV pump. Moreover, the 1.55 eV pump $K_{\alpha 1}$ TR-XES response showed an increase in the positive shoulder at 6931 eV which is not retrieved in any of the the 3.1 eV pump signals. The results suggest that the underlying relaxation mechanisms may be different, corroborating the TRR results. In addition, the results corroborate the interpretation for which also the states reached during the relaxation processes are possibly different.

The results here shown provide a framework for the understanding, the disen-

tanglement and the possible control of the electronic, structural and spin responses in Co_3O_4. In particular, the presence of a purely electronic oscillation coupled with both lattice and spin degrees of freedom would be at the forefront of the possible preparation, engineering, and manipulation of the quantum states in Co_3O_4. This could be used *e.g.*, to steer photochemical reactions into a pre-defined target channel and for all-optical switching [36, 37, 38, 21]. Moreover, it might give a possible understanding of intimate phenomena concerning the charge, lattice and spins in TMOs.

Chapter 4

Conclusions & Perspectives of this work

4.1 Conclusions

Functional materials are defined as compounds with *ad hoc* tailored responses to external triggers such as light, thermal, chemical, magnetic, *etc.* My PhD work has been devoted to advancing the understanding of the fundamental and applicative aspects of a particular class of functional materials, spinel transition metal oxides. Spinel structured oxides belong to the $O_h^7 - Fd\bar{3}m$ space group (FCC structure) and present stoichiometric formula AB_2O_4. They are characterized by tetrahedrons (A) and octahedrons (B) with O^{2-} ions vertices and divalent and trivalent metal cations occupying A and B-sites interstices, respectively. The two non-equivalent centres can be occupied by either different elements (*e.g.*, Zn, Fe, Co) or the same element with different oxidation states (*e.g.*, Co^{2+} and Co^{3+}). The spin configuration changes with the type of element populating the A and B-sites, and/or their oxidation state, thus changing the spinel TMOs structure-property relations. Because of this complexity, spinel TMOs are characterized by correlated interactions of multiple degrees of freedom which need to be disentangled. In my thesis work, I focused on two key benchmark cases, namely: Zinc Ferrites (ZFO) and Co_3O_4. ZFOs are relevant for their magnetic and photocatalytic properties. The objective of this study was the synthesis and characterization of the multifunctional behaviour of ZFO thin films starting from nanoparticle precursors with a step-by-step approach. Co_3O_4 shows applicative relevance for photovoltaics and photocatalysis. The objective of the study was the understand the Co^{2+} and Co^{3+} involvement in the electronic, structural, and magnetic dynamics upon photoexcitation. The steady-state techniques and data analysis protocols from the ZFO project were harnessed to understand Co_3O_4 ground-state properties. Conversely, the unique knowledge gathered with the time-resolved methods on Co_3O_4 shall

be applied to ZFO thin films after the synthesis and characterization protocol is validated. The aim of my PhD thesis work is to take ownership of innovative correlative methods that can be harnessed to study complementary systems (Fe_3O_4, $MgAl_2O_4$, *etc.*) and for realistic applications.

In the second chapter, the focus was firstly on the characterization of pure and $Ga/Mg/MgGa$ doped zinc ferrite nanoparticles synthesised by coprecipitation route and commercially available. This was done in preparation for thin film production and to highlight the potentiality of Raman spectroscopy as a fast and sensitive analytical tool in studying functional parameters in transition metal oxide nanoparticles. The focus was initially moved to the correlation between structural and magnetic properties and on the chemical transformations of $ZnFe_2O_4$ nanoparticles following irradiation in high (3×10^{-6} mbar) and low (1.5 mbar) vacuum environments varying dimension and doping. The homogeneity of the samples was evaluated at the micrometer scale excluding the presence of extrinsic iron oxides in favor of a highly defective external shell of the nanoparticles. In addition, a simplified approach was applied to estimate the inversion degree that allowed to predict the magnetic behavior of the employed samples. Moreover, fingerprints of the onset of the magnetite phase were found following the in-vacuum irradiation and hematite after in-air irradiation as obtained from Raman mode analyses performed on pre- and post-irradiation spectra. These latter results on the pure samples can be interpreted through the sublimation of Zn inside the structure and the reorganization of the $Fe-$ cations and $O-$ ions in spinel iron oxide (magnetite) thanks to the presence of a highly reducing atmosphere. Furthermore, it is possible that the chemical transformation is partially suppressed by doping the structure substituting Zn^{2+} and Fe^{3+} with different metal cations such as Mg and Ga. This behavior is again interpreted with the effect of Mg and Ga co-doping which blocks the depletion of $Zn-$ions therefore maintaining a Spinel ferrite structure.

After this study, commercially available Sigma Aldrich ZFO nanoparticles were employed as a target to produce thin films via RF magnetron sputtering. These thin films have been extensively studied to assess their crystal and chemical quality as well as to understand their functional properties. The studies were conducted at variance with annealing temperature. The profilometry results indicated that the thickness of the sample remains around 100-120 nm and is only slightly affected by thermal treatment. Only the 600 °C annealed film showed spurious components above 1500 μm scan length possibly due to dust or impurities. With XRD as a function of annealing temperature, the appearance of the (311) peak at 400 °C and of the (200) and the (440) ones at 900 °C was found. These three peaks are compatible with the most intense features retrieved in the XRD pattern of the ZFO nanopowders and give a first suggestion of the presence of the Zinc Ferrite spinel structure. After this step, the sample homogeneity and composition

were characterized by Raman spectroscopy as a function of annealing temperature. The spectra are typical of ZFO as compared to the nanopowder precursors and are similar across all the investigated areas of the samples. Compatibly with XRD results as the annealing temperature is increased, the film may tend towards higher crystallinity. Additionally, it was found that: (i) the As synthesized sample shows ZFO typical Raman features, thus it is possible that nanocrystalline ZFO is formed during the 4 h sputtering and (ii) above 600 °C the spectra should show a decreased inversion. This latter fact is not completely true for the 900 °C sample where the inversion degree estimation through Lorentz fitting fails possibly because of artefacts created by the Quartz response subtraction. Similar ZFO spectral features were retrieved on other thin films obtained by reducing the sputtering time from 4 h to 2.5 h in the 900 °C annealed samples possibly confirming the robustness of the synthesis and characterization methods so far. After the profilometry, XRD, and Raman investigation, the optical absorption of the samples was analyzed. Firstly, the bandgap values were calculated considering an indirect ZFO gap. Values around 2-2.1 eV were obtained except for the 900 °C annealed sample which had a gap of 1.87 eV. All the values are compatible with ZFO reported gaps. After the E_g extraction, the main optical transitions of the samples were determined through a 4 Gaussian fit. The 1.5 eV transition is possibly ascribed to a mixture of intersite electron transfers (or Charge Transfer, CT) between $Fe^{2+}(Oh)$ – $Fe^{3+}(Oh)$ (from a_{1g} to t_{2g} or from a_{1g} to e_g states) that are typical in ZFO samples grown in low oxygen partial pressure. Indeed, the low oxygen pressure favors the formation of ligand vacancies during the deposition generating Fe^{2+} impurities which may cause the observed peak. The 3.5 eV peak may be ascribed to a mixture of $p-d$ Charge Transfer (CT) between O^{2-} $2p$ and Fe^{3+} t_{2g} and e_g states in the octahedral cage. Two other possible transitions are present in the 2.5-3.5 eV range which are an intersite $Fe^{3+}(Oh)$ $t_{2g} \rightarrow Fe^{3+}(Td)$ e CT and an onsite $3d-4s$ transition in Zn. The first transition would involve two d levels in the presence of cation inversion, thus should show variations between AS and 600 °C in partial contrast with what is observed. Instead, the $3d-4s$ transition in Zn should span from 2-8 eV with a maximum around 3.5 eV. Similarly, the 4.5 eV oscillator is possibly a mixture of $p-d$ CT between O^{2-} $2p$ and Fe^{3+} $4s$ states in both the octahedral and tetrahedral cages given by the cation inversion of nanostructured samples. The 6.5 eV oscillator is again an intersite $p-d$ CT in the tetrahedral cage between O^{2-} $2p$ and Zn^{2+} $4s$ states. From the magnetic standpoint, the AS samples show a superparamagnetic hysteresis cycle which is progressively decreased as the annealing temperature is increased. At 900 °C annealing the film does not show any contribution typical of superparamagnetic samples. The Zero-Field cooled and Field cooled curves indicated the presence of two main domains with huge dimension variability in the AS films one

of which is the most responsible for the superparamagnetic behaviour. Annealing should increase the size and merge these domains giving, in the end, a ZFC and FC curve for the 900 °C sample similar to the bulk response. The Antiferromagnetic (AFM) transition is evidenced in both samples at around 10-20 K. The magnetic and optical characterization corroborated the EPR findings. g values are compatible with Fe^{3+} in ZFO matrix. However, huge variability of the EPR signal central field and shape is reported as a function of the angle between the static magnetic field and the AS sample compatible with the uniaxial anisotropy of the sample. The annealing reduces this angular variability and gives more symmetric signals. In the end, the 900 °C annealed sample shows only a weak EPR response. All the magnetic characterization was possibly interpreted on the basis of two hypotheses: (i) the presence of oxygen vacancies generates Fe^{2+} sites, as corroborated by the optical absorption findings and (ii) two main competing amorphous and crystalline phases are present in the sample. The As synthesized sample may be composed of domains with both Fe^{3+} and Fe^{2+} sites giving a superparamagnetic response retrieved in both SQUID and the peculiar EPR behaviour upon annealing. Furthermore, the angular variation of the EPR signals can be attributed to the demagnetizing fields in the samples which scale with the saturation magnetization. Annealing the samples favours crystallization compatibly with XRD and Raman but does not remove the oxygen vacancies eventually fixing Fe^{2+} sites in a generally paramagnetic matrix. By annealing the samples, even the angular variability of the shape is suppressed. This can be interpreted with the second hypothesis of two competing phases which generate two superimposed EPR signals. As the annealing temperature is increased, the amorphous layer becomes crystalline and the signal becomes more symmetrical.

In the third chapter, the ultrafast transient response of a 27 nm thick, [1111] epitaxially grown Co_3O_4 thin film was investigated. Initially, a comprehensive characterization of the film's crystalline and chemical quality was conducted utilizing X-Ray Absorption Spectroscopy and grazing incidence X-Ray and Electron diffraction techniques. These analyses confirmed the presence of a pure Co_3O_4 spinel crystal with rotational domains, while no spurious compounds such as CoO were detected. Next, the possible optical transitions occurring both above and below the AFM transition temperature were assigned. To accomplish this, ellipsometry measurements were analyzed. The results provided a detailed description of the parameters involved in the Time-Resolved Reflectivity (TRR) experiments. Specifically, the experimental setup involved pumping at 1.55 eV, which triggered two significant transitions: (i) intersite $d-d$ Charge Transfer (CT), resulting in electron transfer from Co^{3+} to Co^{2+}, leading to the formation of Co^{4+} and Co^{1+} states, and (ii) a mixture of $d-d$ transitions in Co^{3+} and Co^{2+} states. Additionally, pumping at 3.1 eV induced two intersite $p-d$ CT processes, transferring an

electron from an O^{2-} ion to either (i) the t_2 state of a Co^{2+} cation or (ii) to the e_g state of Co^{3+}. A white light probe was utilized within the 1.63-2.7 eV photon energy range. This range allowed to probe several processes: (i) the $Co^{3+} \rightarrow Co^{2+}$ electron transfer, (ii) the Co^{3+} $d-d$ transition into $^1T_{1g}$ state and, (iii) the $O^{2-} \rightarrow Co^{2+}$ intersite $p-d$ CT. Analyzing the incoherent dynamics, faster responses were observed when the pumping at 3.1 eV compared to 1.55 eV. At room temperature (RT) conditions, the first timescales ($\tau_1^{1.55eV} = 0.4$ ps and $\tau_1^{3.1eV} = 0.19$ ps) were attributed to a possible hot carrier cooling via electron-electron scattering, followed by a possible relaxation into $d-d$ states ($\tau_2^{1.55eV} = 5.9$ ps and $\tau_2^{3.1eV} = 0.55$ ps) via electron-phonon scattering. The later timescales found ($\tau_3^{1.55eV} = 204$ ps, $\tau_3^{3.1eV} =$ 8 ps and $\tau_4^{3.1eV} = 229$ ps) could be attributed either to relaxation within the $d-d$ states or to heat transfer, with additional consideration for carrier recombination in the nanosecond range. Based on the results, it is likely that the two relaxation processes obtained by pumping at 3.1 eV and 1.55 eV involve different electronic states. If this was not the case, by pumping at 3.1 eV one should observe the same timescales as 1.55 eV pumping after a first ultrafast relaxation. Approaching the AFM transition temperature, a new timescale emerged (*e.g.*, $\tau_3^{1.55eV}(4.2K) = 18$ ps, $\tau_4^{3.11eV}(4.2K) = 40$ ps) within the entire pump-probe response. This timescale could possibly be ascribed to lattice-mediated magnetic order melting which is based on the formation of small polarons following the photoexcitation of $d-d$ or $p-d$ intersite CTs. Polarons are states in which phonon and electrons degrees of freedom are strongly entangled and the presence of an electron is associated with a finite lattice distortion. The formation of small-polarons prevents ultrafast spin flip mechanisms, thus, the demagnetization process may primarily occur by the heat transfer between electrons and lattice and then between lattice and spin degrees of freedom.

The coherent response of Co_3O_4 provides valuable insights into the impulsively generated phonon and electronic excitations within the system. By pumping the intersite $d-d$ CT (1.55 eV pump), an oscillation in the response with an energy of 24.3 meV (196 cm^{-1}) is induced. This oscillation corresponds to a F_{2g} Raman-active phonon mode, present in the ground-state Raman spectrum. Notably, a linear dependence of the mode's intensity on the pump fluence was also observed with temperature-independent behaviour. This phonon mode helps answer the question of which structural modes are preferentially triggered by the intersite $d-d$ CT and provides insights into the nature of these modes. An even more intriguing result emerged upon 3.1 eV pump. In this case, an oscillation at 10.2 meV appeared in TRR data. The mode is present at Room Temperature possibly modulating the $O^{2-} \rightarrow Co^{2+}$ intersite $p-d$ CT. In the region of the $O^{2-} \rightarrow Co^{2+}$ intersite $p-d$ CT oscillator is temperature independent and scales linearly with the fluence. Around and below the AFM transition, the data suggest that the mode

is modulating also the intersite $d-d$ CT and onsite $d-d$ excitation oscillators with no dispersion in frequency. Several potential origins for this mode were possibly excluded. Specifically, the optical phonon scenario was excluded because this mode was not found in the Raman and IR spectra. Moreover, it was not retrieved in Density Functional Theory (DFT) calculations. The possibility of this mode being an acoustic phonon was also excluded, as calculations of its presumed sound velocity (200 km/s) significantly deviate from the measured value (6 km/s) by two orders of magnitude. Furthermore, the magnon or bi-magnon at the Brillouin zone edges origin was excluded because this mode exists far above the T_{Neel} and again it is not in the Raman spectrum or has temperature or fluence dependence similar to Brillouin Zone edge modes should be. Ultimately, the possibility of it being related to CoO or sapphire phonons was ruled out through comparisons with experimental data and theoretically calculated modes found in the literature. The emergence of a pump-induced structural phase transition phonon mode was also excluded through DFT calculations. Therefore, in the light of experimental evidence and the above considerations, the observed oscillation can be ascribed to a purely electronic oscillation of spin-orbital character which is silent in the ground state. Upon photoexcitation of the intersite $p-d$ CT band, the coupling between structural polaronic distortion and the electronic/spin degrees of freedom leads to the appearance of this purely electronic excitation in the excited state. Multiplet simulations are ongoing to completely confirm this hypothesis. The possibility to trigger and control purely electronic excitations represents the forefront of ultrafast solid-state physics with profound implications in controlling the quantum-mechanical properties of Co_3O_4 guiding the system from the ground-state to a predefined target state and perspective intriguing applications in all-optical switching.

4.2 Proposal for further development

In Chapter 1 it was highlighted that one of the main aspects of this work is a correlative approach in order to have a complete and comprehensive study of all the properties of TMOs. The complete steady-state characterization of ZFO nanoparticles and films and the results of a time-resolved spectroscopic study in spinel Co_3O_4 thin film were shown. The ZFO characterization should be completed by proposing a time-resolved reflectivity on thin films. Fig. 4.1 shows the optical absorption spectrum of RF sputtered ZFO thin film annealed at 900 °C along with its Gaussian deconvolution. The assignment of each oscillator is reported in section 2.4.3. In Chapter 2 the presence of oxygen vacations in the ZFO thin film matrix was analyzed highlighting their contribution in both the magnetic and optical responses. The following time-resolved experiments are proposed: the pump excites either mixed $Fe^{2+} \rightarrow Fe^{3+}$ intersite CTs at 1.55 eV or mainly $O^{2-} \rightarrow Fe^{3+}$

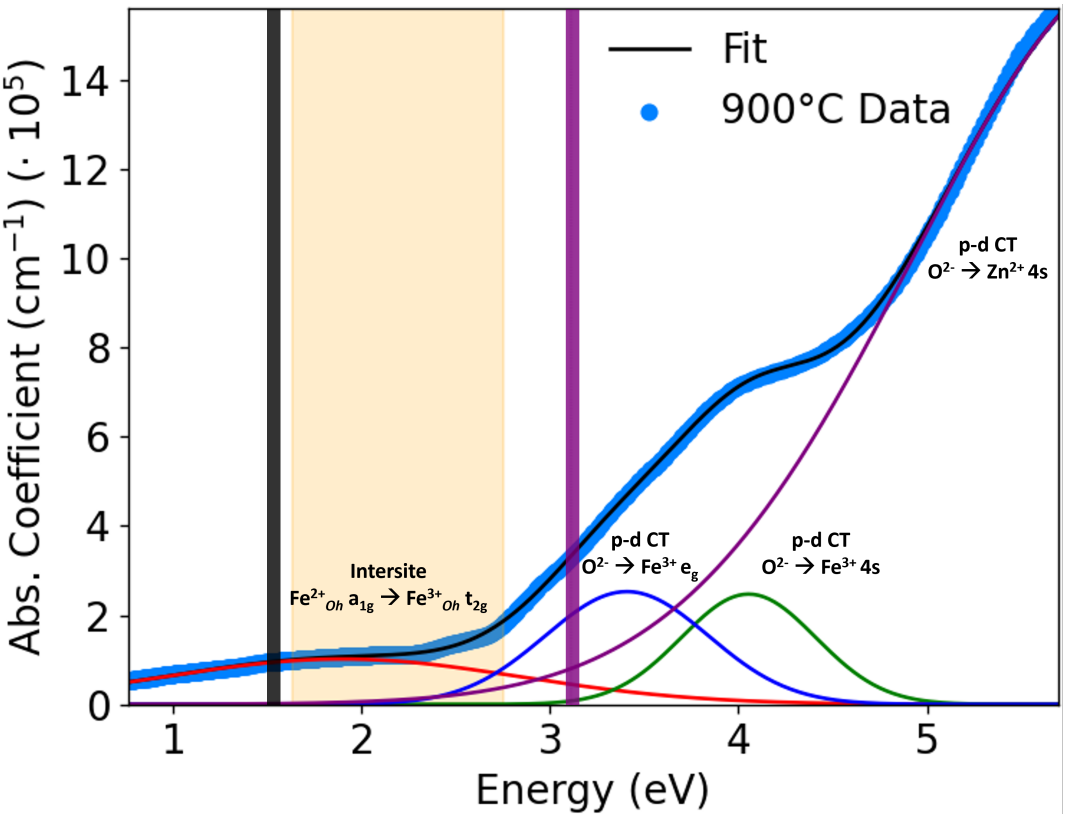

Figure 4.1: Absorption spectrum of ZFO thin films annealed at 900 °C for 30 minutes. The Gaussian deconvolution is reported along with the assignment of each oscillator. A sketch of the proposed experimental parameters is indicated: a 1.55 eV (black vertical line) or 3.1 eV pump (purple vertical line) excites the intersite Fe^{2+} $a_{1g} \rightarrow Fe^{3+}$ e_g or $O^{2-} \rightarrow Fe^{3+}$ e_g $p-d$ CT transitions respectively; meanwhile the white light visible probe region between 1.6 eV and 2.7 eV (orange shaded box) probes the variation of the intersite Fe^{2+} $a_{1g} \rightarrow Fe^{3+}$ e_g and $O^{2-} \rightarrow Fe^{3+}$ e_g $p-d$ CT transitions as a function of the time delay.

e_g $p-d$ CT at 3.1 eV while a white light probe from 1.6 eV to 2.7 eV looks at the variation of both the two oscillators as a function of time. As discussed in section 2.4.3, $Fe^{2+} \rightarrow Fe^{3+}$ intersite CT is envisaged when oxygen vacancies are statistically relevant in the sample. Therefore, by pumping the intersite CT at 1.55 eV an indirect insight into the behaviour of oxygen vacancies and spurious Fe^{2+} valences in the sample could be detected. These latter cations participate in the magnetic response without being EPR active since their spin is an integer number. Therefore, a strong correlation between the electronic and spin degrees of freedom is expected upon photoexcitation with possible changes in the superexchange interaction. The excitation of mainly $O^{2-} \rightarrow Fe^{3+}$ e_g $p-d$ CT at 3.1 eV would also excite the perfect octahedrally coordinated sites. By assuming this, one would in principle be able to disentangle the oxygen vacancies dynamics from the pure octahedrally coordinated system. In addition, one would be also able to look at the system response below the AFM transition at 10 K investigating the effect of long-range magnetic order. Furthermore, by keeping the temporal pulse duration around 40 fs one would be able to see the contribution of all the Raman active phonons of ZFO, getting possible insights on the Zn and Fe cation inversion or on possible pure electronic or polaronic modes silent in the ground state but photoexcited in the sample upon electron transfer.

4.3 Applicative challenges: Is it possible to transfer the characterization approach used for thin films on the nanoparticles?

Another possible improvement and perspective of this work is in extending the complete characterization of general TMO nanoparticles. In this work, it was shown that reliable results and conclusions on both the thin films and nanoparticle samples are obtained only through the use of a multitechnique approach. This is because a multitechnique approach provides different responses which guide the overall understanding of the macro- and microscopic behaviours of the samples analysed. From an applicative industrial standpoint, it is easier to produce nanoparticle samples but the use of only one characterization technique is not enough to provide their stability parameters and their purity in crystalline and chemical qualities. Furthermore, it was shown that ZFO thin films could be sputtered starting from unprocessed nanoparticles. Therefore, it is possible to extend this research to produce thin film samples from other industrially available nanoparticles. If the work provided so far for ZFO and Co_3O_4 is transferred to nanoparticles, it can pave the way to Research and Development industrial applications with a higher fidelity on the final product quality and employability. In

addition, the possibility of thin film production starting from nanoparticles should be also beneficial for R&D industrial purposes.

List of Figures

List of Tables

Bibliography

[1] Structural materials. `https://www.nature.com/subjects/structural-materials`. Accessed: 2023-09-18.

[2] G. Pacchioni. Nuovi materiali funzionali, 2010. Accessed: 2023-09-18.

[3] D. Khomskii. *Transition metal compounds*. Cambridge University Press, 2014.

[4] Z. S. Lim, H. Jani, T. Venkatesan, and A. Ariando. Skyrmionics in correlated oxides. *MRS Bulletin*, 46(11):1053–1062, 2021.

[5] L. Wang, Q. Feng, Y. Kim, R. Kim, K. H. Lee, S. D. Pollard, Y. J. Shin, H. Zhou, W. Peng, D. Lee, et al. Ferroelectrically tunable magnetic skyrmions in ultrathin oxide heterostructures. *Nature materials*, 17(12):1087–1094, 2018.

[6] Z. Li, R. Laskowski, T. Iitaka, and T. Tohyama. First-principles calculation of helical spin order in iron perovskite srfeo 3 and bafeo 3. *Physical Review B*, 85(13):134419, 2012.

[7] Y. Tokura and S. Seki. Multiferroics with spiral spin orders. *Advanced materials*, 22(14):1554–1565, 2010.

[8] A. Gabovich and A. Voitenko. Superconductors with charge-and spin-density waves: theory and experiment. *Low Temperature Physics*, 26(5):305–330, 2000.

[9] A. Gabovich, A. Voitenko, T. Ekino, M. S. Li, H. Szymczak, and M. Pękała. Competition of superconductivity and charge density waves in cuprates: recent evidence and interpretation. *Advances in Condensed Matter Physics*, 2010, 2010.

[10] A. Gabovich, A. Voitenko, J. Annett, and M. Ausloos. Charge-and spin-density-wave superconductors. *Superconductor Science and Technology*, 14(4):R1, 2001.

[11] E. J. W. Verwey. Electronic conduction of magnetite (fe3o4) and its transition point at low temperatures. *Nature*, 144:327–328, 1939.

[12] M. S. Senn, J. P. Wright, and J. P. Attfield. Charge order and three-site distortions in the verwey structure of magnetite. *Nature*, 481:173–176, 2012.

[13] M. S. Senn, I. Loa, J. P. Wright, and J. P. Attfield. Electronic orders in the verwey structure of magnetite. *Phys. Rev. B*, 85, 2012.

[14] P. Piekarz et al. Trimeron-phonon coupling in magnetite. *Phys. Rev. B*, 103, 2021.

[15] E. Baldini et al. Discovery of the soft electronic modes of the trimeron order in magnetite. *Nat. Phys.*, 16:541–545, 2020.

[16] L. Pawlowski and P. Blanchart. *Industrial chemistry of oxides for emerging applications*. Wiley, 2018.

[17] J. Védrine. Heterogeneous catalysis on metal oxides. *Catalysts*, 7, 2017.

[18] Z. Hedayatnasab, F. Abnisa, and W. M. A. W. Daud. Review on magnetic nanoparticles for magnetic nanofluid hyperthermia application. *Mater. Des.*, 123:174–196, 2017.

[19] F. Rossella, P. Galinetto, M. C. Mozzati, L. Malavasi, Y. Diaz Fernandez, G. Drera, and L. Sangaletti. Tio2 thin films for spintronics application: a raman study. *Journal of Raman Spectroscopy: An International Journal for Original Work in all Aspects of Raman Spectroscopy, Including Higher Order Processes, and also Brillouin and Rayleigh Scattering*, 41(5):558–565, 2010.

[20] M. Bibes and A. Barthelemy. Oxide spintronics. *IEEE Trans. Electron Devices*, 54:1003–1023, 2007.

[21] S. Saha, B. T. Diroll, M. G. Ozlu, S. N. Chowdhury, S. Peana, Z. Kudyshev, R. D. Schaller, Z. Jacob, V. M. Shalaev, A. V. Kildishev, et al. Engineering the temporal dynamics of all-optical switching with fast and slow materials. *Nature Communications*, 14(1):5877, 2023.

[22] S. E. Braslavsky. Glossary of terms used in photochemistry, 3rd edition (iupac recommendations 2006). *Pure Appl. Chem.*, 79:293–465, 2007.

[23] H. Kaneko et al. Decomposition of zn-ferrite for o2 generation by concentrated solar radiation. *Sol. Energy*, 76:317–322, 2004.

[24] Y. Tamaura and H. Kaneko. Oxygen-releasing step of znfe2o4/(zno+fe3o4)-system in air using concentrated solar energy for solar hydrogen production. *Sol. Energy*, 78:616–622, 2005.

[25] A. G. Hufnagel et al. Zinc ferrite photoanode nanomorphologies with favorable kinetics for water-splitting. *Adv. Funct. Mater.*, 26:4435–4443, 2016.

[26] H. Kaneko et al. Reaction mechanism of h2 generation for h2o/zn/fe3o4 system. *Int. J. Hydrog. Energy*, 27:1023–1028, 2002.

[27] C. P. Bean and J. D. Livingston. Superparamagnetism. *J. Appl. Phys.*, 30:S120–S129, 1959.

[28] E. A. Périgo et al. Fundamentals and advances in magnetic hyperthermia. *Appl. Phys. Rev.*, 2, 2015.

[29] A. B. Salunkhe, V. M. Khot, and S. H. Pawar. Magnetic hyperthermia with magnetic nanoparticles: a status review. *Curr. Top. Med. Chem.*, 14:572–594, 2014.

[30] J. Kuciakowski et al. Thermal decomposition pathways of zn $_{x}$ fe $_{3-x}$ o $_{4}$ nanoparticles in different atmospheres. *Ind. Eng. Chem. Res.*, 61(34):12532–12544, August 31, 2022. DOI: 10.1021/acs.iecr.2c01572.

[31] A. Kmita et al. Effect of thermal treatment at inert atmosphere on structural and magnetic properties of non-stoichiometric zinc ferrite nanoparticles. *Metall. Mater. Trans. A*, 52:1632–1648, 2021.

[32] B. Albini et al. Raman spectroscopy in pure and doped zinc ferrites nanoparticles. *J. Mater. Sci. Mater. Electron.*, 34, 2023.

[33] S. Restelli et al. Raman study of the laser-induced decomposition of znfe2o4 nanoparticles. *Mater. Today Commun.*, 2023.

[34] M. Bini et al. Superparamagnetic znfe2o4 nanoparticles: the effect of ca and gd doping. *Mater. Chem. Phys.*, 204:72–82, 2018.

[35] G. Gazzola et al. Tuning the superparamagnetic effect in znfe2o4 nanoparticles with mg, ga doping. *Mater. Chem. Phys.*, 273, 2021.

[36] M. Wollenhaupt and T. Baumert. Ultrafast laser control of electron dynamics in atoms, molecules and solids. *Faraday discussions*, 153:9–26, 2011.

[37] A. I. Kuleff and L. S. Cederbaum. Ultrafast correlation-driven electron dynamics. *Journal of Physics B: Atomic, Molecular and Optical Physics*, 47(12):124002, 2014.

[38] C. Heide, T. Eckstein, T. Boolakee, C. Gerner, H. B. Weber, I. Franco, and P. Hommelhoff. Electronic coherence and coherent dephasing in the optical control of electrons in graphene. *Nano Letters*, 21(22):9403–9409, 2021.

[39] H. M. Bretscher, P. Andrich, P. Telang, A. Singh, L. Harnagea, A. K. Sood, and A. Rao. Ultrafast melting and recovery of collective order in the excitonic insulator ta2nise5. *Nature communications*, 12(1):1699, 2021.

[40] R. Yusupov, T. Mertelj, V. V. Kabanov, S. Brazovskii, P. Kusar, J.-H. Chu, I. R. Fisher, and D. Mihailovic. Coherent dynamics of macroscopic electronic order through a symmetry breaking transition. *Nature Physics*, 6(9):681–684, 2010.

[41] D. H. Torchinsky, F. Mahmood, A. T. Bollinger, I. Božović, and N. Gedik. Fluctuating charge-density waves in a cuprate superconductor. *Nature materials*, 12(5):387–391, 2013.

[42] D. Mihailovic, D. Dvorsek, V. Kabanov, J. Demsar, L. Forro, and H. Berger. Femtosecond data storage, processing, and search using collective excitations of a macroscopic quantum state. *Applied physics letters*, 80(5):871–873, 2002.

[43] P. Colman, P. Lunnemann, Y. Yu, and J. Mørk. Ultrafast coherent dynamics of a photonic crystal all-optical switch. *Physical Review Letters*, 117(23):233901, 2016.

[44] L. Stojchevska, I. Vaskivskyi, T. Mertelj, P. Kusar, D. Svetin, S. Brazovskii, and D. Mihailovic. Ultrafast switching to a stable hidden quantum state in an electronic crystal. *Science*, 344(6180):177–180, 2014.

[45] Z. Chai, X. Hu, F. Wang, X. Niu, J. Xie, and Q. Gong. Ultrafast all-optical switching. *Advanced Optical Materials*, 5(7):1600665, 2017.

[46] F. Raineri, C. Cojocaru, P. Monnier, A. Levenson, R. Raj, C. Seassal, X. Letartre, and P. Viktorovitch. Ultrafast dynamics of the third-order nonlinear response in a two-dimensional inp-based photonic crystal. *Applied physics letters*, 85(11):1880–1882, 2004.

[47] Z. Sun, X. Yang, Y. Huang, L. Ding, L. Qin, and Z. Wang. π-electron density dependence of third-order optical nonlinearities in poly (1, 4-phenylene vinylene) derivatives. *Optics communications*, 160(4-6):289–291, 1999.

[48] N. Kinsey, C. DeVault, J. Kim, M. Ferrera, V. Shalaev, and A. Boltasseva. Epsilon-near-zero al-doped zno for ultrafast switching at telecom wavelengths. *Optica*, 2(7):616–622, 2015.

[49] M. Clerici, N. Kinsey, C. DeVault, J. Kim, E. G. Carnemolla, L. Caspani, A. Shaltout, D. Faccio, V. Shalaev, A. Boltasseva, et al. Controlling hybrid nonlinearities in transparent conducting oxides via two-colour excitation. *Nature communications*, 8(1):15829, 2017.

[50] W. B. White and B. A. DeAngelis. Interpretation of the vibrational spectra of spinels. *Spectrochim. Acta Part Mol. Spectrosc.*, 23:985–995, 1967.

[51] H. A. Kramers. L'interaction entre les atomes magnétogènes dans un cristal paramagnétique. *Physica*, 1:182–192, 1934.

[52] P. W. Anderson. Antiferromagnetism. theory of superexchange interaction. *Phys. Rev.*, 79:350–356, 1950.

[53] P. W. Anderson. New approach to the theory of superexchange interactions. *Phys. Rev.*, 115:2–13, 1959.

[54] C. G. Shull and J. S. Smart. Detection of antiferromagnetism by neutron diffraction. *Phys. Rev.*, 76:1256–1257, 1949.

[55] G. Shirane, S. J. Pickart, and Y. Ishikawa. Neutron diffraction study of antiferromagnetic mntio 3 and nitio 3. *J. Phys. Soc. Jpn.*, 14:1352–1360, 1959.

[56] C. G. Shull, W. A. Strauser, and E. O. Wollan. Neutron diffraction by paramagnetic and antiferromagnetic substances. *Phys. Rev.*, 83:333–345, 1951.

[57] J. Van Den Brink, P. Horsch, F. Mack, and A. M. Oleś. Orbital dynamics in ferromagnetic transition-metal oxides. *Phys. Rev. B*, 59:6795–6805, 1999.

[58] A. Moskvin, N. Ovanesyan, and V. Trukhtanov. Angular dependence of the superexchange interaction fe 3+-o 2–cr 3+. *Hyperfine Interactions*, 1:265–281, 1975.

[59] B. H. Kim, H. Choi, and B. I. Min. Superexchange interaction revisited: the role of the a -site cations in a cuo 3 (a =se, te). *New J. Phys.*, 12, 2010.

[60] J. Hastings and L. Corliss. An antiferromagnetic transition in zinc ferrite. *Physical Review*, 102(6):1460, 1956.

[61] W. L. Roth. The magnetic structure of co3o4. *J. Phys. Chem. Solids*, 25:1–10, 1964.

[62] P. Cossee. Magnetic properties of cobalt in oxide lattices. *Journal of Inorganic and Nuclear Chemistry*, 8:483–488, 1958.

[63] J. Van Vleck. Magnetism and quantum mechanics the theory of electric and magnetic su. sceptibilities. *Nature*, 1932.

[64] O. Zaharko, A. Cervellino, V. Tsurkan, N. B. Christensen, and A. Loidl. Evolution of magnetic states in frustrated diamond lattice antiferromagnetic co (al1-xcox)2o4 spinels. *Phys. Rev. B*, 81:064416, 2010.

[65] C. Meier et al. Silicon nanoparticles: absorption, emission, and the nature of the electronic bandgap. *J. Appl. Phys.*, 101, 2007.

[66] X. Huang and M. A. El-Sayed. Gold nanoparticles: optical properties and implementations in cancer diagnosis and photothermal therapy. *J. Adv. Res.*, 1:13–28, 2010.

[67] S. V. Koniakhin et al. Raman spectra of crystalline nanoparticles: replacement for the phonon confinement model. *J. Phys. Chem. C*, 122:19219–19229, 2018.

[68] P. Galinetto, B. Albini, M. Bini, and M. C. Mozzati. Raman spectroscopy in zinc ferrites nanoparticles. In G. M. d. Nascimento, editor, *Raman Spectroscopy*. 2018. DOI: 10.5772/intechopen.72864.

[69] K. Heydaryan et al. Reaction time-induced improvement in hyperthermia properties of cobalt ferrite nanoparticles with different sizes. *Mater. Chem. Phys.*, 303, 2023.

[70] B. Jyothish and J. Jacob. Synthesis and characterization of ni2+ and al3+ doped zinc ferrite nanoparticles for antibacterial, antioxidant, and anticancer (mcf-7) analysis. *Chem. Phys. Impact*, 6, 2023.

[71] C. R. Kalaiselvan et al. Manganese ferrite (mnfe2o4) nanostructures for cancer theranostics. *Coord. Chem. Rev.*, 473, 2022.

[72] J. G. Monsalve, C. Ostos, E. Ramos, J. G. Ramírez, and O. Arnache. Insight into magnetic properties in zinc ferrite thin films by tuning oxygen content. *Current Applied Physics*, 22:77–83, 2021. DOI: 10.1016/j.cap.2021.01.002.

[73] V. Zviagin, C. Sturm, P. D. Esquinazi, M. Grundmann, and R. Schmidt-Grund. Control of magnetic properties in spinel znfe 2 o 4 thin films through intrinsic defect manipulation. *J. Appl. Phys.*, 128:165702, 2020.

[74] C. R. Torres, G. A. Pasquevich, P. M. Zélis, F. Golmar, S. Heluani, S. K. Nayak, W. A. Adeagbo, W. Hergert, M. Hoffmann, A. Ernst, et al. Oxygen-vacancy-induced local ferromagnetism as a driving mechanism in enhancing the magnetic response of ferrites. *Physical Review B*, 89(10):104411, 2014.

[75] Q. Chen et al. Synthesis of superparamagnetic MgFe2O4 nanoparticles by coprecipitation. *J. Magn. Magn. Mater.*, 194(1):1–7, April 1999. DOI: 10.1016/S0304-8853(98)00585-X.

[76] C. T. Yavuz et al. Low-field magnetic separation of monodisperse fe 3 o 4 nanocrystals. *Science*, 314:964–967, 2006.

[77] Y. Jun et al. Nanoscale size effect of magnetic nanocrystals and their utilization for cancer diagnosis via magnetic resonance imaging. *J. Am. Chem. Soc.*, 127:5732–5733, 2005.

[78] F. Ozel and H. Kockar. Growth and characterizations of magnetic nanoparticles under hydrothermal conditions: reaction time and temperature. *J. Magn. Magn. Mater.*, 373:213–216, 2015.

[79] R. F. Butler and S. K. Banerjee. Theoretical single-domain grain size range in magnetite and titanomagnetite. *J. Geophys. Res.*, 80:4049–4058, 1975.

[80] D. L. Leslie-Pelecky and R. D. Rieke. Magnetic properties of nanostructured materials. *Chem. Mater.*, 8:1770–1783, 1996.

[81] Q. Li et al. Correlation between particle size/domain structure and magnetic properties of highly crystalline fe3o4 nanoparticles. *Sci. Rep.*, 7:9894, 2017.

[82] W. Wang et al. Superparamagnetic iron oxide nanoparticles for full-color photonic materials with tunable properties. *Results Phys.*, 14:102366, 2019.

[83] R. Díaz-Pardo and R. Valenzuela. Characterization of magnetic phases in nanostructured ferrites by electron spin resonance. In S. Bashir, editor, *Advanced Electromagnetic Waves*. InTech, November 18, 2015. DOI: 10.5772/61508.

[84] S. Tajik et al. A sensor fabricated with spinel zinc ferrite nanoparticles and reduced graphene oxide for electrochemical detection of sudan i. *J IRAN CHEM SOC*, 19(7):3127–3134, July 2022. DOI: 10.1007/s13738-022-02518-7.

[85] R. Sharma et al. Ferrimagnetic ni doped mg-zn spinel ferrite nanoparticles for high density information storage. *J. Alloys Compd.*, 704:7–17, May 2017. DOI: 10.1016/j.jallcom.2017.02.021.

[86] A. A. Ibiyemi and G. T. Yusuf. Rheological investigation of strain rate and magnetic field on the magnetorheology of zinc ferrite ferrofluid. *Appl. Phys. A*, 128(7):591, July 2022. DOI: 10.1007/s00339-022-05720-9.

[87] S. O. Aisida et al. Biogenic synthesis enhanced structural, morphological, magnetic and optical properties of zinc ferrite nanoparticles for moderate hyperthermia applications. *J. Nanopart. Res.*, 23(2):47, February 2021. DOI: 10.1007/s11051-021-05149-w.

[88] P. Vinosha et al. Impact of dysprosium doped (dy) zinc ferrite (ZnFe2o4) nanocrystals in photo- fenton exclusion of recalcitrant organic pollutant. *Environ. Res.*, 203:111913, January 2022. DOI: 10.1016/j.envres.2021.111913.

[89] P. Dave et al. Effect of nanosize zinc ferrite on thermolysis of ammonium perchlorate. *J. Electron. Mater.*, 51(2):785–792, February 2022. DOI: 10.1007/s11664-021-09335-3.

[90] C. Yang et al. The effect of ZnFe2o4/activated carbon adsorbent photocatalytic activity on gas-phase desulfurization. *Chem. Eng. J.*, 423:130255, November 2021. DOI: 10.1016/j.cej.2021.130255.

[91] M. P. Tsvetkov et al. Catalytic and photocatalytic properties of zinc-nickel ferrites. *J. Chem. Sci.*, 133(1):24, March 2021. DOI: 10.1007/s12039-020-01882-2.

[92] A. C. Ulpe et al. Photoelectrochemistry of ferrites: theoretical predictions vs. experimental results. *Zeitschrift für Physikalische Chemie*, 234(4):719–776, April 28, 2020. DOI: 10.1515/zpch-2019-1449.

[93] M. Sultan and R. Singh. Fmr studies on nanocrystalline zinc ferrite thin films. In *Journal of Physics: Conference Series*, volume 200 of number 7, page 072090. IOP Publishing, 2010.

[94] R. Soohoo. Surface anisotropy energies of thin magnetic films. *Journal of Applied Physics*, 34(4):1149–1150, 1963.

[95] E. Hsieh and R. Soohoo. Domain boundary configuration for head-on magnetization in thin films. In *AIP Conference Proceedings*, volume 5 of number 1, pages 727–731. American Institute of Physics, 1972.

[96] K. Wu, J. Li, and C. Zhang. Zinc ferrite based gas sensors: a review. *Ceram. Int.*, 45(9):11143–11157, June 2019. DOI: 10.1016/j.ceramint.2019.03.086.

[97] X. Bo et al. Magnetic diphase nanostructure of ZnFe2O4/γ-Fe2O3. *J. Solid State Chem.*, 180(3):1038–1044, March 2007. DOI: 10.1016/j.jssc.2006.12.034.

[98] L. El Mir, Z. B. Ayadi, M. Saadoun, K. Djessas, H. Von Bardeleben, and S. Alaya. Preparation and characterization of n-type conductive (al, co) co-doped zno thin films deposited by sputtering from aerogel nanopowders. *Applied Surface Science*, 254(2):570–573, 2007.

[99] S. Bonomi, M. Patrini, G. Bongiovanni, and L. Malavasi. Versatile vapor phase deposition approach to cesium tin bromide materials cssnbr 3, cssn 2 br 5 and cs 2 snbr 6. *RSC advances*, 10(48):28478–28482, 2020.

[100] L. I. Granone et al. Effect of the degree of inversion on optical properties of spinel ZnFe $_2$ O_4. *Phys. Chem. Chem. Phys.*, 20(44):28267–28278, 2018. DOI: 10.1039/C8CP05061A.

[101] P. Galinetto et al. Raman spectroscopy in zinc ferrites nanoparticles. In G. M. d. Nascimento, editor, *Raman Spectroscopy*. InTech, April 18, 2018. DOI: 10.5772/intechopen.72864.

[102] B. Albini. *Raman Spectroscopy and Nanostructured Complex Systems: A satisfactory win to win game?* PhD thesis, University of Pavia, Pavia, Italy.

[103] B. Albini, S. Restelli, M. Ambrosetti, M. Bini, F. D'Amico, M. Mozzati, and P. Galinetto. Raman spectroscopy in pure and doped zinc ferrites nanoparticles. *Journal of Materials Science: Materials in Electronics*, 34(12):1030, 2023.

[104] B. S. Yadav, A. K. Vishwakarma, A. K. Singh, and N. Kumar. Oxygen vacancies induced ferromagnetism in rf-sputtered and hydrothermally annealed zinc ferrite (znfe2o4) thin films. *Vacuum*, 207:111617, 2023.

[105] B. Sahu, A. S. Doshi, R. Prabhu, N. Venkataramani, S. Prasad, and R. Krishnan. Temperature dependence of fmr and magnetization in nanocrystalline zinc ferrite thin films. *AIP Advances*, 6(5), 2016.

[106] M. Sultan and R. Singh. Magnetic and optical properties of rf-sputtered zinc ferrite thin films. *Journal of Applied Physics*, 105(7), 2009.

[107] V. Zviagin, M. Grundmann, and R. Schmidt-Grund. Impact of defects on magnetic properties of spinel zinc ferrite thin films. *physica status solidi (b)*, 257(7):1900630, 2020.

[108] L. Fu, Z. Wu, X. Ai, J. Zhang, Y. Nie, S. Xie, G. Yang, and B. Zou. Time-resolved spectroscopic behavior of fe 2 o 3 and znfe 2 o 4 nanocrystals. *The Journal of chemical physics*, 120(7):3406–3413, 2004.

[109] D. L. A. de Faria, S. Venâncio Silva, and M. T. de Oliveira. Raman microspectroscopy of some iron oxides and oxyhydroxides. *J. Raman Spectrosc.*, 28(11):873–878, November 1997. DOI: 10.1002/(SICI)1097-4555(199711)28:11<873::AID-JRS177>3.0.CO;2-B.

[110] R. J. C. Fernandes et al. Magnetic nanoparticles of zinc/calcium ferrite decorated with silver for photodegradation of dyes. *Materials*, 12(21):3582, October 31, 2019. DOI: 10.3390/ma12213582.

[111] X. Cao et al. Spinel ZnFe2o4 nanoplates embedded with ag clusters: preparation, characterization, and photocatalytic application. *Mater. Chem. Phys.*, 106(2):175–180, December 2007. DOI: 10.1016/j.matchemphys.2007.05.033.

[112] I. M. Kolthoff. Theory of Coprecipitation. The Formation and Properties of Crystalline Precipitates. *J. Phys. Chem.*, 36(3):860–881, March 1, 1932. DOI: 10.1021/j150333a008.

[113] *Ceramic Science and Engineering*. Elsevier, 2022. DOI: 10.1016/C2020-0-03121-X.

[114] M. Virji and A. Stefaniak. A Review of Engineered Nanomaterial Manufacturing Processes and Associated Exposures. In *Comprehensive Materials Processing*, pages 103–125. Elsevier, 2014. DOI: 10.1016/B978-0-08-096532-1.00811-6.

[115] H. Al-Madhagi et al. Magnetite Nanoparticle Co-precipitation Synthesis, Characterization, and Applications: Mini Review. *BioNanoSci.*, 13(2):853–859, June 2023. DOI: 10.1007/s12668-023-01113-1.

[116] Y. I. Kim, D. Kim, and C. S. Lee. Synthesis and characterization of CoFe2O4 magnetic nanoparticles prepared by temperature-controlled co-precipitation method. *Physica B: Condensed Matter*, 337(1):42–51, September 2003. DOI: 10.1016/S0921-4526(03)00322-3.

[117] P. A. Vinosha et al. Synthesis and properties of spinel ZnFe2o4 nanoparticles by facile co-precipitation route. *Optik*, 134:99–108, April 2017. DOI: 10.1016/j.ijleo.2017.01.018.

[118] C. Selvaraju, R. Karthick, and R. Veerasubam. The modification of structural, optical and antibacterial activity properties of rare earth gadolinium-doped ZnO nanoparticles prepared by co-precipitation method. *J. Inorg. Organomet. Polym. Mater.*, 29(3):776–782, May 2019. DOI: 10.1007/s10904-018-1051-0.

[119] M. Zikriya et al. Luminescent characterization of rare earth Dy3+ ion doped TiO2 prepared by simple chemical co-precipitation method. *J. Rare Earths*, 37(1):24–31, January 2019. DOI: 10.1016/j.jre.2018.05.012.

[120] E. Curti. Coprecipitation of radionuclides during cement degradation: a preliminary modeling study for the Swiss L/ILW repository. *MRS Proc.*, 506:313, 1997. DOI: 10.1557/PROC-506-313.

[121] H. W. Stockman. Neutron activation determination of noble metals in rocks: a rapid radiochemical separation based on tellurium coprecipitation. *J. Radioanal. Chem.*, 78(2):307–317, September 1983. DOI: 10.1007/BF02530441.

[122] M. Haruta. Gold catalysts prepared by coprecipitation for low-temperature oxidation of hydrogen and of carbon monoxide. *J. Catal.*, 115(2):301–309, February 1989. DOI: 10.1016/0021-9517(89)90034-1.

[123] A. I. Petrov, D. V. Volodkin, and G. B. Sukhorukov. Protein-calcium carbonate coprecipitation: a tool for protein encapsulation. *Biotechnol. Prog.*, 21(3):918–925, September 5, 2008. DOI: 10.1021/bp0495825.

[124] F. Shi. Introductory chapter: basic theory of magnetron sputtering. In *Magnetron Sputtering [Working Title]*. IntechOpen, November 5, 2018. DOI: 10.5772/intechopen.80550.

[125] R. J. Burt, S. F. Meyer, and E. J. Hsieh. Radio frequency magnetron sputtering of thick film amorphous beryllium. *J. Vac. Sci. Technol. A*, 17(1):407–410, January 1980. DOI: 10.1116/1.570467.

[126] S. Meyer, E. Hsieh, and R. Burt. R.F. magnetron sputtering of thick platinum coatings on glass microspheres. *Thin Solid Films*, 72(2):373–378, October 1980. DOI: 10.1016/0040-6090(80)90020-6.

[127] A. Dagamseh et al. ZnO:al films prepared by rf magnetron sputtering applied as back reflectors in thin-film silicon solar cells. *Thin Solid Films*, 516(21):7844–7850, September 2008. DOI: 10.1016/j.tsf.2008.05.009.

[128] J. Fischer et al. Development of thin film cathodes for lithium-ion batteries in the material system li–mn–o by r.f. magnetron sputtering. *Thin Solid Films*, 528:217–223, January 2013. DOI: 10.1016/j.tsf.2012.08.058.

[129] A. Nagata and H. Okayama. Characterization of solid oxide fuel cell device having a three-layer film structure grown by RF magnetron sputtering. *Vacuum*, 66(3):523–529, August 2002. DOI: 10.1016/S0042-207X(02)00126-4.

[130] G. Sberveglieri et al. Methods for the preparation of NO, NO2 and H2 sensors based on tin oxide thin films, grown by means of the r.f. magnetron sputtering technique. *Sens. Actuators B: Chem.*, 8(1):79–88, April 1992. DOI: 10.1016/0925-4005(92)85012-L.

[131] S.-H. Jeong et al. Characterization of SiO2 and TiO2 films prepared using rf magnetron sputtering and their application to anti-reflection coating. *Vacuum*, 76(4):507–515, November 2004. DOI: 10.1016/j.vacuum.2004.06.003.

[132] J.-H. Lee et al. Deposition of multi-period low-emissivity filters for display application by RF magnetron sputtering. *Surf. Coat. Technol.*, 158-159:477–481, September 2002. DOI: 10.1016/S0257-8972(02)00293-1.

[133] P. Kondaiah, H. Shaik, and G. Mohan Rao. Studies on RF magnetron sputtered HfO2 thin films for microelectronic applications. *Electron. Mater. Lett.*, 11(4):592–600, July 2015. DOI: 10.1007/s13391-015-4490-6.

[134] Y. Zeng et al. Superhard TiAlCN coatings prepared by radio frequency magnetron sputtering. *Thin Solid Films*, 584:283–288, June 2015. DOI: 10.1016/j.tsf.2015.02.068.

[135] T. Vuchkov et al. Synthesis, microstructural, and mechano-tribological properties of self-lubricating w-s-c(h) thin films deposited by different RF magnetron sputtering procedures. *Coatings*, 10(3):272, March 14, 2020. DOI: 10.3390/coatings10030272.

[136] P. Carvalho et al. Structural stability of decorative ZrNxOy thin films. *Surf. Coat. Technol.*, 200(1):748–752, October 2005. DOI: 10.1016/j.surfcoat.2005.02.100.

[137] A. C. Popa et al. Submicrometer hollow bioglass cones deposited by radio frequency magnetron sputtering: formation mechanism, properties, and prospective biomedical applications. *ACS Appl. Mater. Interfaces*, 8(7):4357–4367, February 24, 2016. DOI: 10.1021/acsami.6b00606.

[138] D. A. Long. *The Raman effect: a unified treatment of the theory of Raman scattering by molecules*. Wiley, Chichester ; New York, 2002. 597 pages.

[139] R. P. Prasankumar and A. J. Taylor, editors. Optical Techniques for Solid-State Materials Characterization. CRC Press, April 19, 2016. DOI: 10.1201/b11040.

[140] G. Gouadec and P. Colomban. Raman spectroscopy of nanomaterials: how spectra relate to disorder, particle size and mechanical properties. *Prog. Cryst. Growth Charact. Mater.*, 53(1):1–56, March 2007. DOI: 10.1016/j.pcrysgrow.2007.01.001.

[141] A. K. Arora et al. Raman spectroscopy of optical phonon confinement in nanostructured materials. *J. Raman Spectrosc.*, 38(6):604–617, June 2007. DOI: 10.1002/jrs.1684.

[142] H. Richter, Z. Wang, and L. Ley. The one phonon raman spectrum in microcrystalline silicon. *Solid State Communications*, 39(5):625–629, 1981.

[143] M. M. Roessler and E. Salvadori. Principles and applications of EPR spectroscopy in the chemical sciences. *Chem. Soc. Rev.*, 47(8):2534–2553, 2018. DOI: 10.1039/C6CS00565A.

[144] M. Brustolon and E. Giamello, editors. Electron Paramagnetic Resonance: A Practitioner's Toolkit. 1st edition. Wiley, 1st edition, January 29, 2009. DOI: 10.1002/9780470432235.

[145] V. Chechik and D. M. Murphy, editors. Electron Paramagnetic Resonance: Volume 25. Volume 25. Electron Paramagnetic Resonance. Royal Society of Chemistry, Cambridge, 2016. DOI: 10.1039/9781782629436.

[146] W. R. Hagen. *Biomolecular EPR Spectroscopy*. CRC Press, December 22, 2008. DOI: 10.1201/9781420059588.

[147] R. L. Fagaly. Superconducting quantum interference device instruments and applications. *Rev. Sci. Instrum.*, 77(10):101101, October 2006. DOI: 10.1063/1.2354545.

[148] M. Buchner et al. Tutorial: basic principles, limits of detection, and pitfalls of highly sensitive SQUID magnetometry for nanomagnetism and spintronics. *J. Appl. Phys.*, 124(16):161101, October 28, 2018. DOI: 10.1063/1.5045299.

[149] J. Bardeen, L. N. Cooper, and J. R. Schrieffer. Theory of superconductivity. *Phys. Rev.*, 108(5):1175–1204, December 1, 1957. DOI: 10.1103/PhysRev.108.1175.

[150] B. Josephson. Possible new effects in superconductive tunnelling. *Phys. Lett.*, 1(7):251–253, July 1962. DOI: 10.1016/0031-9163(62)91369-0.

[151] P. W. Anderson and J. M. Rowell. Probable observation of the josephson superconducting tunneling effect. *Phys. Rev. Lett.*, 10(6):230–232, March 15, 1963. DOI: 10.1103/PhysRevLett.10.230.

[152] C. D. Tesche and J. Clarke. Dc SQUID: noise and optimization. *J. Low. Temp. Phys.*, 29(3):301–331, November 1977. DOI: 10.1007/BF00655097.

[153] K. K. Kefeni, T. A. M. Msagati, T. T. Nkambule, and B. B. Mamba. Spinel ferrite nanoparticles and nanocomposites for biomedical applications and their toxicity. *Materials Science and Engineering C*, 107:110314, 2020. DOI: 10.1016/j.msec.2019.110314.

[154] B. D. Hosterman. *Raman Spectroscopic Study of Solid Solution Spinel Oxides*. PhD thesis, University of Nevada, Las Vegas. DOI: 10.34917/2476131.

[155] T. Yamanaka and M. Ishii. Raman scattering and lattice vibrations of ni2sio4 spinel at elevated temperature. *Phys. Chem. Minerals*, 13(3):156–160, May 1986. DOI: 10.1007/BF00308157.

[156] M. Virumbrales-del Olmo et al. Effect of composition and coating on the interparticle interactions and magnetic hardness of MFe $_2$ o $_4$ (m = fe, co, zn) nanoparticles. *Phys. Chem. Chem. Phys.*, 19(12):8363–8372, 2017. DOI: 10.1039/C6CP08743D.

[157] Z. Ž. Lazarević et al. Characterization of partially inverse spinel ZnFe2o4 with high saturation magnetization synthesized via soft mechanochemically assisted route. *J. Phys. Chem. Solids*, 75(7):869–877, July 2014. DOI: 10.1016/j.jpcs.2014.03.004.

[158] M. Benz. Superparamagnetism: theory and applications. *Superparamagnetism Theory Appl*:1–27, 2012.

[159] J. A. Gomes et al. Structural, chemical, and magnetic investigations of core–shell zinc ferrite nanoparticles. *J. Phys. Chem. C*, 116(45):24281–24291, November 15, 2012. DOI: 10.1021/jp3055069.

[160] O. N. Shebanova and P. Lazor. Raman study of magnetite (fe3o4): laser-induced thermal effects and oxidation. *J. Raman Spectrosc.*, 34(11):845–852, November 2003. DOI: 10.1002/jrs.1056.

[161] Y. El Mendili et al. Insights into the mechanism related to the phase transition from γ-fe $_2$ o $_3$ to α-fe $_2$ o $_3$ nanoparticles induced by thermal treatment and laser irradiation. *J. Phys. Chem. C*, 116(44):23785–23792, November 8, 2012. DOI: 10.1021/jp308418x.

[162] B. Lafuente, R. T. Downs, H. Yang, and N. Stone. 1. the power of databases: the rruff project. *Highlights in mineralogical crystallography*:1–30, 2015.

[163] I. V. Chernyshova, M. F. Hochella Jr, and A. S. Madden. Size-dependent structural transformations of hematite nanoparticles. 1. phase transition. *Phys. Chem. Chem. Phys.*, 9(14):1736, 2007. DOI: 10.1039/b618790k.

[164] P. C. Ricci et al. Surface effects and phase stability in metal oxides nanoparticles under visible irradiation. In FUNDAMENTALS AND APPLICATIONS IN SILICA AND ADVANCED DIELECTRICS (SIO2014): X International Symposium on SiO2, Advanced Dielectrics and Related Devices, pages 104–110, Cagliari, Italy, 2014. DOI: 10.1063/1.4900464.

[165] A. Manikandan, L. J. Kennedy, M. Bououdina, and J. J. Vijaya. Synthesis, optical and magnetic properties of pure and co-doped znfe2o4 nanoparticles by microwave combustion method. *Journal of magnetism and magnetic materials*, 349:249–258, 2014.

[166] X. Xu, A. K. Azad, and J. T. Irvine. Photocatalytic h2 generation from spinels znfe2o4, znfegao4 and znga2o4. *Catalysis Today*, 199:22–26, 2013.

[167] Y.-C. Liang and H.-Y. Hsia. Growth and crystallographic feature-dependent characterization of spinel zinc ferrite thin films by rf sputtering. *Nanoscale Research Letters*, 8:1–8, 2013.

[168] D. Gao, Z. Shi, Y. Xu, J. Zhang, G. Yang, J. Zhang, X. Wang, and D. Xue. Synthesis, magnetic anisotropy and optical properties of preferred oriented zinc ferrite nanowire arrays. *Nanoscale research letters*, 5:1289–1294, 2010.

[169] V. Ziaei and T. Bredow. Ab-initio optical properties and dielectric response of open-shell spinel zinc ferrite. *The European Physical Journal B*, 90:1–4, 2017.

[170] J. Tauc and A. Menth. States in the gap. *Journal of non-crystalline solids*, 8:569–585, 1972.

[171] J. Tauc. Optical properties and electronic structure of amorphous ge and si. *Materials research bulletin*, 3(1):37–46, 1968.

[172] W. Hellenthal. Superparamagnetic effects in thin films. *IEEE Transactions on Magnetics*, 4(1):11–14, 1968.

[173] M. Bohra et al. Large room temperature magnetization in nanocrystalline zinc ferrite thin films. *Applied Physics Letters*, 88:262506, 2006. DOI: 10.1063/1.2206990.

[174] S. Nakashima, K. Fujita, K. Tanaka, and K. Hirao. High magnetization and the high-temperature superparamagnetic transition with intercluster interaction in disordered zinc ferrite thin film. *Journal of Physics: Condensed Matter*, 17:137–149, 2005. DOI: 10.1088/0953-8984/17/1/016.

[175] L. Raghavan et al. Room temperature ferrimagnetism and low temperature disorder effects in zinc ferrite thin films. *Journal of Magnetism and Magnetic Materials*, 385:265–271, 2015. DOI: 10.1016/j.jmmm.2015.03.014.

[176] D. Fritsch. Electronic and optical properties of spinel zinc ferrite: ab initio hybrid functional calculations. *Journal of Physics: Condensed Matter*, 30(9):095502, 2018.

[177] D. Peeters, D. H. Taffa, M. M. Kerrigan, A. Ney, N. Jöns, D. Rogalla, S. Cwik, H.-W. Becker, M. Grafen, A. Ostendorf, et al. Photoactive zinc ferrites fabricated via conventional cvd approach. *ACS Sustainable Chemistry & Engineering*, 5(4):2917–2926, 2017.

[178] Z. Wang, D. Schiferl, Y. Zhao, and H. S. C. O'Neill. High pressure raman spectroscopy of spinel-type ferrite znfe2o4. *Journal of Physics and Chemistry of Solids*, 64(12):2517–2523, 2003.

[179] V. Zviagin, Y. Kumar, I. Lorite, P. Esquinazi, M. Grundmann, and R. Schmidt-Grund. Ellipsometric investigation of znfe2o4 thin films in relation to magnetic properties. *Applied Physics Letters*, 108(13), 2016.

[180] A. Moskvin and R. Pisarev. Optical spectroscopy of charge transfer transitions in multiferroic manganites, ferrites, and related insulators. *Low Temperature Physics*, 36(6):489–510, 2010.

[181] J. Chen, H.-S. Hsu, Y.-H. Huang, and D.-J. Huang. Spin-dependent optical charge transfer in magnetite from transmitting optical magnetic circular dichroism. *Physical Review B*, 98(8):085141, 2018.

[182] A. Schlegel, S. Alvarado, and P. Wachter. Optical properties of magnetite (fe3o4). *Journal of Physics C: Solid State Physics*, 12(6):1157, 1979.

[183] W. Fontijn, P. Van der Zaag, M. Devillers, V. Brabers, and R. Metselaar. Optical and magneto-optical polar kerr spectra of fe 3 o 4 and mg 2+-or al 3+-substituted fe 3 o 4. *Physical Review B*, 56(9):5432, 1997.

[184] K. J. Kim, H. S. Lee, M. H. Lee, and S. H. Lee. Comparative magneto-optical investigation of d–d charge–transfer transitions in fe 3 o 4, cofe 2 o 4, and nife 2 o 4. *Journal of applied physics*, 91(12):9974–9977, 2002.

[185] E. J. Choi, Y. Ahn, and E. J. Hahn. Size dependence of the magnetic properties in superparamagnetic zinc-ferrite nanoparticles. *Journal of the Korean Physical Society*, 53:2090–2094, 2008. DOI: 10.3938/jkps.53.2090.

[186] L. Afremov, S. Anisimov, and I. Iliushin. Modeling of the blocking temperature of a system of core/shell nanoparticles. *Chinese Journal of Physics*, 70:324–335, 2021. DOI: 10.1016/j.cjph.2021.07.024.

[187] J. M. Hastings and L. M. Corliss. An antiferromagnetic transition in zinc ferrite. *Physical Review*, 102:1460–1463, 1956. DOI: 10.1103/PhysRev.102.1460.

[188] Y. Liang et al. Co3o4 nanocrystals on graphene as a synergistic catalyst for oxygen reduction reaction. *Nat. Mater.*, 10:780–786, 2011.

[189] A. Waris et al. Green fabrication of co and co3o4 nanoparticles and their biomedical applications: a review. *Open Life Sci.*, 16:14–30, 2021.

[190] J. M. Xu and J. P. Cheng. The advances of co3o4 as gas sensing materials: a review. *J. Alloys Compd.*, 686:753–768, 2016.

[191] K. Momma and F. Izumi. Vesta 3 for three-dimensional visualization of crystal, volumetric and morphology data. *Journal of applied crystallography*, 44(6):1272–1276, 2011.

[192] W. L. Smith and A. D. Hobson. The structure of cobalt oxide, co3o4. *Acta Crystallogr. B*, 29:362–363, 1973.

[193] R.-P. Wang et al. Analyzing the local electronic structure of co3o4 using 2p3d resonant inelastic x-ray scattering. *J. Phys. Chem. C*, 126:8752–8759, 2022.

[194] L. Qiao, H. Y. Xiao, H. Meyer, J. Sun, C. M. Rouleau, A. A. Puretzky, D. B. Geohegan, I. N. Ivanov, M. Yoon, W. J. Weber, et al. Nature of the band gap and origin of the electro-/photo-activity of co 3 o 4. *Journal of Materials Chemistry C*, 1(31):4628–4633, 2013.

[195] K. M. E. Miedzinska, B. R. Hollebone, and J. G. Cook. An assignment of the optical absorption spectrum of mixed valence co3o4 spinel films. *J. Phys. Chem. Solids*, 48:649–656, 1987.

[196] K. J. Kim and Y. R. Park. Optical investigation of charge-transfer transitions in spinel co3o4. *Solid state communications*, 127(1):25–28, 2003.

[197] N. Mironova, V. Skvortsova, and U. Ulmanis. Near-infrared absorption spectra in co3o4. *Solid State Commun.*, 91:731–733, 1994.

[198] P. Cossee. Structure and magnetic properties of co3o4 and znco2o4. *Recl. Trav. Chim. Pays-Bas*, 75:1089–1096, 2010.

[199] Z. Seidov, M. Açıkgöz, S. Kazan, and F. Mikailzade. Magnetic properties of co3o4 polycrystal powder. *Ceram. Int.*, 42:12928–12931, 2016.

[200] L. M. Khriplovich, E. V. Kholopov, and I. E. Paukov. Heat capacity and thermodynamic properties of co3o4 from 5 to 307 k low-temperature transition. *J. Chem. Thermodyn.*, 14:207–217, 1982.

[201] C.-M. Jiang, L. R. Baker, J. M. Lucas, J. Vura-Weis, A. P. Alivisatos, and S. R. Leone. Characterization of photo-induced charge transfer and hot carrier relaxation pathways in spinel cobalt oxide (co3o4). *The Journal of Physical Chemistry C*, 118(39):22774–22784, 2014.

[202] M. M. Waegele, H. Q. Doan, and T. Cuk. Long-lived photoexcited carrier dynamics of d–d excitations in spinel ordered co3o4. *The Journal of Physical Chemistry C*, 118(7):3426–3432, 2014.

[203] T. J. Smart, T. A. Pham, Y. Ping, and T. Ogitsu. Optical absorption induced by small polaron formation in transition metal oxides: the case of co3o4. *Phys. Rev. Mater.*, 3:102401, 2019.

[204] Y. Zhang and et al. Barrierless self-trapping of photocarriers in co3o4. *J. Phys. Chem. Lett.*, 12:12033–12039, 2021.

[205] A. Zong, A. Kogar, and N. Gedik. Unconventional light-induced states visualized by ultrafast electron diffraction and microscopy. *MRS Bull.*, 46:720–730, 2021.

[206] S. Gerber and et al. Femtosecond electron-phonon lock-in by photoemission and x-ray free-electron laser. *Science*, 357:71–75, 2017.

[207] F. Glerean and et al. Quantum model for impulsive stimulated raman scattering. *J. Phys. B At. Mol. Opt. Phys.*, 52:145502, 2019.

[208] H. J. Zeiger and et al. Theory for displacive excitation of coherent phonons. *Phys. Rev. B*, 45:768–778, 1992.

[209] J. G. Cook and M. P. Van Der Meer. The optical properties of sputtered co3o4 films. *Thin Solid Films*, 144:165–176, 1986.

[210] C.-S. Cheng, M. Serizawa, H. Sakata, and T. Hirayama. Electrical conductivity of co3o4 films prepared by chemical vapour deposition. *Mater. Chem. Phys.*, 53:225–230, 1998.

[211] S. Yao, H. Uchida, and Z. Kozuka. A closed-system potentiostatic technique employing a solid electrolyte for the investigation of co3o4 <-> 3coo + 1/2o2. *Int. J. Mater. Res.*, 82:402–407, 1991.

[212] K. Koumoto and H. Yanagida. Decomposition pressure of co3o4 determined from electrical conductivity measurements. *Jpn. J. Appl. Phys.*, 20:445, 1981.

[213] R. Dietsch, T. Holz, and H. Mai. Pulsed laser deposition (pld) — an advanced state for technical applications. *Opt Quant Electron*, 27:1385–1396, 1995.

[214] M. J. Aziz. Film growth mechanisms in pulsed laser deposition. *Appl. Phys. A*, 93:579–587, 2008.

[215] G. K. Hubler. Pulsed laser deposition. *MRS Bull.*, 17:26–29, 1992.

[216] D. N. Basov, R. D. Averitt, D. van der Marel, M. Dressel, and K. Haule. Electrodynamics of correlated electron materials. *Rev. Mod. Phys.*, 83:471–541, 2011.

[217] F. Barantani. Dynamics of dispersive collective modes in correlated matter. *Archives ouvertes (HAL)*, 2023. DOI: 10.13097/ARCHIVE-OUVERTE/UNIGE:167272.

[218] R. Kubo. Statistical-mechanical theory of irreversible processes. i. general theory and simple applications to magnetic and conduction problems. *J. Phys. Soc. Jpn.*, 12:570–586, 1957.

[219] A. B. Kuzmenko. Kramers–kronig constrained variational analysis of optical spectra. *Rev. Sci. Instrum.*, 76:083108, 2005.

[220] B. C. Smith. Fundamentals of fourier transform infrared spectroscopy, 2011. DOI: 10.1201/b10777.

[221] J. B. Bates. Fourier transform infrared spectroscopy: the basic principles and current applications of a rapidly expanding technique are reviewed. *Science*, 191:31–37, 1976.

[222] C. Berthomieu and R. Hienerwadel. Fourier transform infrared (ftir) spectroscopy. *Photosynth. Res.*, 101:157–170, 2009.

[223] H. Hedayat and et al. Investigation of the non-equilibrium state of strongly correlated materials by complementary ultrafast spectroscopy techniques. *New J. Phys.*, 23:033025, 2021.

[224] R. R. Alfano and S. L. Shapiro. Optical phonon lifetime measured directly with picosecond pulses. *Phys. Rev. Lett.*, 26:1247–1251, 1971.

[225] E. Baldini and et al. Real-time observation of phonon-mediated σ - π interband scattering in mgb 2. *Phys. Rev. Lett.*, 119:097002, 2017.

[226] S. Borroni and et al. Coherent generation of symmetry-forbidden phonons by light-induced electron-phonon interactions in magnetite. *Phys. Rev. B*, 96:104308, 2017.

[227] M. F. DeCamp, D. A. Reis, P. H. Bucksbaum, and R. Merlin. Dynamics and coherent control of high-amplitude optical phonons in bismuth. *Phys. Rev. B*, 64:092301, 2001.

[228] T. E. Stevens, J. Kuhl, and R. Merlin. Coherent phonon generation and the two stimulated raman tensors. *Phys. Rev. B*, 65:144304, 2002.

[229] J. Shah. *Coherent Spectroscopy of Semiconductors*. Springer Berlin Heidelberg, 1999.

[230] P. T. Landsberg. *Recombination in Semiconductors*. Cambridge University Press, 1992. DOI: 10.1017/CBO9780511470769.

[231] G. C. Cho, W. Kütt, and H. Kurz. Subpicosecond time-resolved coherent-phonon oscillations in gaas. *Phys. Rev. Lett.*, 65:764–766, 1990.

[232] R. Merlin. Generating coherent thz phonons with light pulses. *Solid State Commun.*, 102:207–220, 1997.

[233] G. Auböck and et al. Femtosecond pump/supercontinuum-probe setup with 20 khz repetition rate. *Rev. Sci. Instrum.*, 83:093105, 2012.

[234] E. Baldini and et al. A versatile setup for ultrafast broadband optical spectroscopy of coherent collective modes in strongly correlated quantum systems. *Struct. Dyn.*, 3:064301, 2016.

[235] C. Slavov, H. Hartmann, and J. Wachtveitl. Implementation and evaluation of data analysis strategies for time-resolved optical spectroscopy. *Anal. Chem.*, 87:2328–2336, 2015.

[236] I. H. M. van Stokkum, D. S. Larsen, and R. van Grondelle. Global and target analysis of time-resolved spectra. *Biochim. Biophys. Acta BBA - Bioenerg.*, 1657:82–104, 2004.

[237] F. J. Harris. On the use of windows for harmonic analysis with the discrete fourier transform. *Proc. IEEE*, 66:51–83, 1978.

[238] J. O. Smith. *Mathematics of the discrete Fourier transform (DFT): with audio applications*. BookSurge, 2007.

[239] P. Glatzel and U. Bergmann. High resolution 1s core hole x-ray spectroscopy in 3d transition metal complexes—electronic and structural information. *Coord. Chem. Rev.*, 249:65–95, 2005.

[240] J. A. Van Bokhoven and C. Lamberti. *X-ray absorption and X-ray emission spectroscopy: theory and applications*, volume 1. John Wiley & Sons, 2016.

[241] R. D. Cowan. *The Theory of Atomic Structure and Spectra*. University of California Press, 1981. DOI: 10.1525/9780520906150.

[242] C. Bacellar and et al. Spin cascade and doming in ferric hemes: femtosecond x-ray absorption and x-ray emission studies. *Proc. Natl. Acad. Sci.*, 117:21914–21920, 2020.

[243] D. Kinschel and et al. Femtosecond x-ray emission study of the spin crossover dynamics in haem proteins. *Nat. Commun.*, 11:4145, 2020.

[244] M. W. Mara and et al. Metalloprotein entatic control of ligand-metal bonds quantified by ultrafast x-ray spectroscopy. *Science*, 356:1276–1280, 2017.

[245] W. Zhang and et al. Tracking excited-state charge and spin dynamics in iron coordination complexes. *Nature*, 509:345–348, 2014.

[246] C.-Y. Ruan, D.-S. Yang, and A. H. Zewail. Structures and dynamics of self-assembled surface monolayers observed by ultrafast electron crystallography. *J. Am. Chem. Soc.*, 126:12797–12799, 2004.

[247] F. A. Lima and et al. A high-repetition rate scheme for synchrotron-based picosecond laser pump/x-ray probe experiments on chemical and biological systems in solution. *Rev. Sci. Instrum.*, 82:063111, 2011.

[248] A. Galler and et al. Scientific instrument femtosecond x-ray experiments (fxe): instrumentation and baseline experimental capabilities. *J. Synchrotron Radiat.*, 26:1432–1447, 2019.

[249] G. Palmer and et al. Pump–probe laser system at the fxe and spb/sfx instruments of the european x-ray free-electron laser facility. *J. Synchrotron Radiat.*, 26:328–332, 2019.

[250] M. Altarelli. The european x-ray free-electron laser facility in hamburg. *Nucl. Instrum. Methods Phys. Res. Sect. B Beam Interact. Mater. At.*, 269:2845–2849, 2011.

[251] D. Khakhulin and et al. Ultrafast x-ray photochemistry at european xfel: capabilities of the femtosecond x-ray experiments (fxe) instrument. *Appl. Sci.*, 10:995, 2020.

[252] A. Mozzanica and et al. The jungfrau detector for applications at synchrotron light sources and xfels. *Synchrotron Radiat. News*, 31:16–20, 2018.

[253] A. Bordage, V. Trannoy, O. Proux, H. Vitoux, R. Moulin, and A. Bleuzen. In situ site-selective transition metal k-edge xas: a powerful probe of the transformation of mixed-valence compounds. *Physical Chemistry Chemical Physics*, 17(26):17260–17265, 2015.

[254] H. Baumgartel. Exafs, sexafs, xanes: x-ray absorption - principles, applications, techniques of exafs, sexafs and xanes. von d. koningsberger und r. prins. john wiley & sons ltd., chichester 1988. 673 s., abb., tab., formeln. isbn 0-471-87547-3. *Nachrichten Aus Chem. Tech. Lab.*, 36:650–650, 1988.

[255] A. Mahmood and J.-L. Wang. A review of grazing incidence small-and wide-angle x-ray scattering techniques for exploring the film morphology of organic solar cells. *Solar RRL*, 4(10):2000337, 2020.

[256] J. A. Steele, E. Solano, D. Hardy, D. Dayton, D. Ladd, K. White, P. Chen, J. Hou, H. Huang, R. A. Saha, et al. How to giwaxs: grazing incidence wide angle x-ray scattering applied to metal halide perovskite thin films. *Advanced Energy Materials*:2300760, 2023.

[257] G. F. Mancini and et al. Design and implementation of a flexible beamline for fs electron diffraction experiments. *Nucl. Instrum. Methods Phys. Res. Sect. Accel. Spectrometers Detect. Assoc. Equip.*, 691:113–122, 2012.

[258] X. Liu and C. T. Prewitt. High-temperature x-ray diffraction study of co3o4: transition from normal to disordered spinel. *Phys. Chem. Miner.*, 17, 1990.

[259] A. Ichimiya and P. I. Cohen. *Reflection High-Energy Electron Diffraction*. Cambridge University Press, 2004. DOI: 10.1017/CBO9780511735097.

[260] V. Zviagin et al. Control of magnetic properties in spinel $ZnFe_2$ O_4 thin films through intrinsic defect manipulation. *J. Appl. Phys.*, 128(16):165702, October 28, 2020. DOI: 10.1063/5.0019712.

[261] P. R. Athey, F. K. Urban, M. F. Tabet, and W. A. McGahan. Optical properties of cobalt oxide films deposited by spray pyrolysis. *J. Vac. Sci. Technol. Vac. Surf. Films*, 14:685–692, 1996.

[262] C. Duke and G. Mahan. Phonon-broadened impurity spectra. i. density of states. *Physical Review*, 139(6A):A1965, 1965.

[263] K. W. Blazey and H. Rohrer. Antiferromagnetic phase diagram and magnetic band gap shift of nacr s 2. *Phys. Rev.*, 185:712–719, 1969.

[264] D. Bossini and et al. Exchange-mediated magnetic blue-shift of the band-gap energy in the antiferromagnetic semiconductor mnte. *New J. Phys.*, 22:083029, 2020.

[265] E. Baldini and et al. Lattice-mediated magnetic order melting in tbmno 3. *Phys. Rev. B*, 97:125149, 2018.

[266] H. Shirai, Y. Morioka, and I. Nakagawa. Infrared and raman spectra and lattice vibrations of some oxide spinels. *J. Phys. Soc. Jpn.*, 51:592–597, 1982.

[267] E. M. Malone, S. C. Petitto, and M. A. Langell. Fuchs–kliewer phonon spectrum of co3o4(110) single crystal surfaces by high resolution electron energy loss spectroscopy. *Solid State Commun.*, 130:571–575, 2004.

[268] V. G. Hadjiev, M. N. Iliev, and I. V. Vergilov. The raman spectra of co 3 o 4. *J. Phys. C Solid State Phys.*, 21:L199–L201, 1988.

[269] A. Mock and et al. Anisotropy, band-to-band transitions, phonon modes, and oxidation properties of cobalt-oxide core-shell slanted columnar thin films. *Appl. Phys. Lett.*, 108:051905, 2016.

[270] T. Yu and et al. Controlled growth and field-emission properties of cobalt oxide nanowalls. *Adv. Mater.*, 17:1595–1599, 2005.

[271] P. E. Blöchl. Projector augmented-wave method. *Phys. Rev. B*, 50:17953–17979, 1994.

[272] J. P. Perdew and et al. Restoring the density-gradient expansion for exchange in solids and surfaces. *Phys. Rev. Lett.*, 100:136406, 2008.

[273] G. Kresse and J. Furthmüller. Efficient iterative schemes for ab initio total-energy calculations using a plane-wave basis set. *Phys. Rev. B*, 54:11169–11186, 1996.

[274] K. Parlinski, Z. Q. Li, and Y. Kawazoe. First-principles determination of the soft mode in cubic zro 2. *Phys. Rev. Lett.*, 78:4063–4066, 1997.

[275] K. Parlinski. Phonon software. *Comput. Mater.*, 2013.

[276] T. Kaewmaraya, W. Luo, X. Yang, P. Panigrahi, and R. Ahuja. A new, layered monoclinic phase of co 3 o 4 at high pressure. *Phys. Chem. Chem. Phys.*, 17:19957–19961, 2015.

[277] Z. Zhang, J. Koppensteiner, W. Schranz, and M. A. Carpenter. Variations in elastic and anelastic properties of co3o4 due to magnetic and spin-state transitions. *Am. Mineral.*, 97:399–406, 2012.

[278] P. L. Meena, R. Kumar, and K. Sreenivas. Structural, elastic and magnetic properties of spinel co3o4. *Indian J. Pure Appl. Phys. IJPAP*, 56:890–895, 2018.

[279] U. D. Wdowik and K. Parlinski. Lattice dynamics of coo from first principles. *Phys. Rev. B*, 75:104306, 2007.

[280] J. Sakurai, W. J. L. Buyers, R. A. Cowley, and G. Dolling. Crystal dynamics and magnetic excitations in cobaltous oxide. *Phys. Rev.*, 167:510–518, 1968.

[281] P. J. Gielisse and et al. Infrared properties of nio and coo and their mixed crystals. *J. Appl. Phys.*, 36:2446–2450, 1965.

[282] W. Kappus. Lattice dynamics of sapphire (corundum): part ii: calculations of the phonon dispersion. *Z. Für Phys. B Condens. Matter Quanta*, 21:325–331, 1975.

[283] H. Bialas and H. J. Stolz. Lattice dynamics of sapphire (corundum): part i: phonon dispersion by inelastic neutron scattering. *Z. Für Phys. B Condens. Matter Quanta*, 21:319–324, 1975.

[284] S. P. S. Porto and R. S. Krishnan. Raman effect of corundum. *J. Chem. Phys.*, 47:1009–1012, 1967.

[285] A. S. Barker. Infrared lattice vibrations and dielectric dispersion in corundum. *Phys. Rev.*, 132:1474–1481, 1963.

[286] R. Heid, D. Strauch, and K.-P. Bohnen. Ab initio lattice dynamics of sapphire. *Phys. Rev. B*, 61:8625–8627, 2000.

[287] M. L. Bortz and R. H. French. Optical reflectivity measurements using a laser plasma light source. *Appl. Phys. Lett.*, 55:1955–1957, 1989.

[288] R. H. French, H. Müllejans, and D. J. Jones. Optical properties of aluminum oxide: determined from vacuum ultraviolet and electron energy-loss spectroscopies. *J. Am. Ceram. Soc.*, 81:2549–2557, 2005.

[289] T. V. Perevalov and et al. Electronic structure of α-al2o3: ab initio simulations and comparison with experiment. *JETP Lett.*, 85:165–168, 2007.

[290] S. Brivio, D. Polli, A. Crespi, R. Osellame, G. Cerullo, and R. Bertacco. Observation of anomalous acoustic phonon dispersion in srtio3 by broadband stimulated brillouin scattering. *Applied Physics Letters*, 98(21), 2011.

[291] C. Thomsen and et al. Coherent phonon generation and detection by picosecond light pulses. *Phys. Rev. Lett.*, 53:989–992, 1984.

[292] Y. J. Bae and et al. Exciton-coupled coherent magnons in a 2d semiconductor. *Nature*, 609:282–286, 2022.

[293] J. Zhang and et al. Spin-phonon coupling and two-magnons scattering behaviors in hexagonal nias-type antiferromagnetic mnte epitaxial films. *J. Raman Spectrosc.*, 51:1383–1389, 2020.

[294] A. V. Chubukov and D. M. Frenkel. Resonant two-magnon raman scattering in antiferromagnetic insulators. *Phys. Rev. Lett.*, 74:3057–3060, 1995.

[295] D. Bossini and et al. Femtosecond phononic coupling to both spins and charges in a room-temperature antiferromagnetic semiconductor. *Phys. Rev. B*, 104:224424, 2021.

[296] S. Sugai, H. Suzuki, Y. Takayanagi, T. Hosokawa, and N. Hayamizu. Carrier-density-dependent momentum shift of the coherent peak and the lo phonon mode in p-type high-tc superconductors. *Phys. Rev. B*, 68:184504, 2003.

[297] W. H. Weber and R. Merlin. *Raman scattering in materials science*, volume 42. Springer Science & Business Media, 2000.

[298] S. Kim. Ultrafast magneto-optical measurements for probing magnon–phonon interactions in nanomagnets. *Nat. Rev. Phys.*, 4:288–288, 2022.

[299] S. Baierl and et al. Terahertz-driven nonlinear spin response of antiferromagnetic nickel oxide. *Phys. Rev. Lett.*, 117:197201, 2016.

[300] T. Kampfrath and et al. Coherent terahertz control of antiferromagnetic spin waves. *Nat. Photonics*, 5:31–34, 2011.

[301] E. Möhr-Vorobeva and et al. Nonthermal melting of a charge density wave in tise 2. *Phys. Rev. Lett.*, 107:036403, 2011.

[302] K. Okazaki and et al. Antiphase fermi-surface modulations accompanying displacement excitation in a parent compound of iron-based superconductors. *Phys. Rev. B*, 97:121107, 2018.

[303] E. Golias and J. Sánchez-Barriga. Observation of antiphase coherent phonons in the warped dirac cone of bi 2 te 3. *Phys. Rev. B*, 94:161113, 2016.

[304] B. He and et al. Coherent optical phonon oscillation and possible electronic softening in wte2 crystals. *Sci. Rep.*, 6:30487, 2016.

[305] M. Cammarata and et al. Charge transfer driven by ultrafast spin transition in a cofe prussian blue analogue. *Nat. Chem.*, 13:10–14, 2021.

[306] F. Cova, M. V. Blanco, M. Hanfland, and G. Garbarino. Study of the high pressure phase evolution of co 3 o 4. *Phys. Rev. B*, 100:054111, 2019.

[307] O. M. Sousa, J. S. Lima, A. F. Lima, and M. V. Lalic. Theoretical study of structural, electronic and magnetic properties of the spinel co3o4 under the pressure from 0 to 30 gpa. *J. Magn. Magn. Mater.*, 484:21–30, 2019.

[308] S. Hirai and W. L. Mao. Novel pressure-induced phase transitions in co 3 o 4. *Appl. Phys. Lett.*, 102:041912, 2013.

[309] N. O. Golosova and et al. High pressure effects on the crystal and magnetic structures of co3o4. *J. Magn. Magn. Mater.*, 508:166874, 2020.

[310] L. Rettig, J.-H. Chu, I. R. Fisher, U. Bovensiepen, and M. Wolf. Coherent dynamics of the charge density wave gap in tritellurides. *Faraday Discuss*, 171:299–310, 2014.

[311] P. Dutta, M. S. Seehra, S. Thota, and J. Kumar. A comparative study of the magnetic properties of bulk and nanocrystalline co 3 o 4. *J. Phys. Condens. Matter*, 20:015218, 2008.

[312] M. G. Herrera-Yáñez, J. A. Guerrero-Cruz, M. Ghiasi, H. Elnaggar, A. de la Torre-Rangel, L. A. Bernal-Guzmán, R. Flores-Moreno, F. M. de Groot, and M. U. Delgado-Jaime. Fitting multiplet simulations to l-edge xas spectra of transition-metal complexes using an adaptive grid algorithm. *Inorganic Chemistry*, 62(9):3738–3760, 2023.

[313] Q. Chen, A. J. Rondinone, B. C. Chakoumakos, and Z. John Zhang. Synthesis of superparamagnetic mgfe2o4 nanoparticles by coprecipitation. *J. Magn. Magn. Mater.*, 194:1–7, 1999.

[314] Y. Tamaura and H. Kaneko. Oxygen-releasing step of ZnFe2O4/(ZnO+Fe3O4)-system in air using concentrated solar energy for solar hydrogen production. *Sol. Energy*, 78(5):616–622, May 2005. DOI: 10.1016/j.solener.2004.10.012.

[315] C. Bárcena et al. Zinc ferrite nanoparticles as MRI contrast agents. *Chem. Commun.*, (19):2224, 2008. DOI: 10.1039/b801041b.

[316] M. Bini et al. Superparamagnetic ZnFe2O4 nanoparticles: The effect of Ca and Gd doping. *Mater. Chem. Phys.*, 204:72–82, January 2018. DOI: 10.1016/j.matchemphys.2017.10.033.

[317] V. D'Ippolito et al. Raman fingerprint of chromate, aluminate and ferrite spinels: raman fingerprint of chromate, aluminate and ferrite spinels. *J. Raman Spectrosc.*, 46(12):1255–1264, December 2015. DOI: 10.1002/jrs.4764.

[318] P. Chandramohan, M. Srinivasan, S. Velmurugan, and S. Narasimhan. Cation distribution and particle size effect on raman spectrum of CoFe2o4. *J. Solid State Chem.*, 184(1):89–96, January 2011. DOI: 10.1016/j.jssc.2010.10.019.

[319] J. P. Singh et al. Micro-raman investigation of nanosized zinc ferrite: effect of crystallite size and fluence of irradiation. *J. Raman Spectrosc.*, 42(7):1510–1517, July 2011. DOI: 10.1002/jrs.2902.

[320] D. Varshney, K. Verma, and A. Kumar. Structural and vibrational properties of ZnxMn1-xFe2o4 (x=0.0, 0.25, 0.50, 0.75, 1.0) mixed ferrites. *Mater. Chem. Phys.*, 131(1):413–419, December 2011. DOI: 10.1016/j.matchemphys.2011.09.066.

[321] K. Kombaiah et al. Optical, magnetic and structural properties of ZnFe2o4 nanoparticles synthesized by conventional and microwave assisted combustion method: a comparative investigation. *Optik*, 129:57–68, January 2017. DOI: 10.1016/j.ijleo.2016.10.058.

[322] B. Lafuente et al. 1. the power of databases: the RRUFF project. In T. Armbruster and R. M. Danisi, editors, *Highlights in Mineralogical Crystallography*, pages 1–30. DE GRUYTER, November 13, 2015. DOI: 10.1515/9783110417104-003.

[323] J. Philip et al. Effect of thermal annealing under vacuum on the crystal structure, size, and magnetic properties of ZnFe2o4 nanoparticles. *J. Appl. Phys.*, 102(5):054305, September 2007. DOI: 10.1063/1.2777168.

[324] S. Ayyappan et al. Room temperature ferromagnetism in vacuum annealed ZnFe2o4 nanoparticles. *Appl. Phys. Lett.*, 96(14):143106, April 5, 2010. DOI: 10.1063/1.3374332.

[325] R. Blake et al. Refinement of the hematite structure. *Am. Mineral.*, 51(1):123–129. 1966.

[326] L. Pauling and S. B. Hendricks. THE CRYSTAL STRUCTURES OF HEMATITE AND CORUNDUM. *J. Am. Chem. Soc.*, 47(3):781–790, March 1925. DOI: 10.1021/ja01680a027.

[327] O. N. Shebanova and P. Lazor. Raman spectroscopic study of magnetite (FeFe2o4): a new assignment for the vibrational spectrum. *J. Solid State Chem.*, 174(2):424–430, September 2003. DOI: 10.1016/S0022-4596(03)00294-9.

[328] G. Nandhini and M. Shobana. Role of ferrite nanoparticles in hyperthermia applications. *J. Magn. Magn. Mater.*, 552:169236, June 2022. DOI: 10.1016/j.jmmm.2022.169236.

[329] Y. Köseoglu, H. Yıldız, and R. Yilgin. Synthesis, characterization and superparamagnetic resonance studies of ZnFe $_2$ O $_4$ nanoparticles. *J. Nanosci. Nanotechnol.*, 12(3):2261–2269, March 1, 2012. DOI: 10.1166/jnn.2012.5718.

[330] E. Rösler and A. Föhlisch. *X-Ray Absorption and X-Ray Emission Spectroscopy: Theory and Applications*. John Wiley & Sons, Ltd, 2016. DOI: 10.1002/9781118844243.

[331] R. P. Prasankumar and A. J. Taylor. *Optical techniques for solid-state materials characterization*. CRC press, 2016.

[332] E. Baldini. *Nonequilibrium dynamics of collective excitations in quantum materials*. Springer, 2018.

[333] *Raman scattering in materials science*. Springer, 2000.